

Dissertation zur Erlangung des Doktorgrades der Fakultät
für Chemie und Pharmazie der
Ludwig-Maximilians-Universität München

**The Function of KANK2 and KANK4 in Murine
Development and in a Breast Cancer
Mouse Model**



Andrea Seiwert

aus

Schweinfurt, Deutschland

2025

Erklärung

Diese Dissertation wurde im Sinne von §7 der Promotionsordnung vom 28. November 2011 von Herrn Prof. Dr. Reinhard Fässler betreut.

Eidesstattliche Versicherung

Diese Dissertation wurde selbstständig und ohne unerlaubte Hilfe erarbeitet.

München, 13.02.2025

.....

Andrea Seiwert

Dissertation eingereicht am: 13.02.2025

1. Gutachter: Prof. Dr. Reinhard Fässler

2. Gutachter: Prof. Dr. Markus Sperandio

Mündliche Prüfung am: 03.06.2025

Schwachkopf, Schwabbelspeck, Krimskrams, Quiek¹

¹Albus P. W. B. Dumbledore – Harry Potter und der Stein der Weisen

Table of Contents

TABLE OF CONTENTS	I
SUMMARY	V
ABBREVIATIONS	VIII
PUBLICATIONS	XII
1 INTRODUCTION	1
1.1 INTEGRINS AND INTEGRIN-MEDIATED SIGNALING	1
1.1.1 Integrin structure	2
1.1.2 Integrin conformations and activation	4
1.1.3 The model of the molecular clutch	7
1.1.4 Integrin-based adhesions	10
1.2 THE KANK FAMILY	12
1.2.1 <i>In vitro</i> functions of KANKs	14
1.2.2 <i>In vivo</i> functions of KANKs	21
1.2.3 KANKs in cancer	23
1.3 TGF β SUPERFAMILY	24
1.3.1 TGF β	25
1.3.1.1 Activation of TGF β	27
1.3.2 TGF β receptors and signaling	29
1.3.2.1 Smad signaling	30
1.3.2.2 Non-canonical TGF β signaling	34
1.3.3 TGF β in cancer	35
1.3.4 TGF β 1 induced KANK4 expression	37
1.4 EPITHELIAL-TO-MESENCHYMAL TRANSITION (EMT)	38
1.4.1 EMT-TFs	40
1.4.1.1 Snail family	42
1.4.1.2 Zeb homeobox family	43
1.4.1.3 TWIST family	43
1.4.2 EMT in cancer	44
1.4.3 TGF β -induced EMT	47
1.5 RHO GTPASE FAMILY	48
1.5.1 Cdc42, Rac1 and RhoA in filopodia, lamellipodia and invadopodia formation	49
1.6 CORONIN	53
1.6.1 Coro1A	54
1.6.2 Coro1B	58
1.7 CANCER DEVELOPMENT	59
1.7.1 The tumor microenvironment (TME)	60
1.7.2 Cancer cell migration, invasion, and metastases	65
1.7.2.1 Importance of Rac1 in cancer cell invasion	71
1.8 MURINE DEVELOPMENT	74
1.8.1 Early embryonic development	74
1.8.1.1 VCAM-1 and α_4 integrin in chorioallantoic fusion	76
1.8.2 MG development	78
1.8.2.1 Embryonic MG development	79
1.8.2.2 Sexual dimorphism in MG development	80
1.8.2.3 Pubertal MG development	81
1.8.2.4 MG development during pregnancy, lactation and involution	83
1.8.3 Breast cancer	84
1.8.4 MMTV-PyMT mouse model	86
2 AIMS OF THE THESIS	90

3	MATERIALS AND METHODS.....	91
3.1	ANIMALS	91
3.1.1	Generation of KANK2-KO and KANK4-KO mice	91
3.1.2	Genotyping of mice.....	92
3.1.3	Urine albumin assay.....	93
3.1.4	KANK2 embryo preparation.....	93
3.1.5	Whole mount MG staining.....	93
3.1.6	MG isolation at different developmental stages.....	94
3.1.7	Tissue isolation for WB	94
3.1.8	Analysis of tumor development	94
3.1.9	Quantification of lung metastasis.....	95
3.1.10	Cryo embedding of tissues	95
3.1.11	Paraffin embedding of tissues	95
3.1.12	Immunofluorescence microscopy of cryo-embedded sections.....	96
3.1.13	H&E staining.....	96
3.1.14	Determining tumor proliferation and apoptosis.....	97
3.2	ANTIBODIES	97
3.2.1	Primary antibodies	97
3.2.2	Secondary antibodies	100
3.2.3	Generation of anti-human KANK4 antibody	100
3.3	<i>IN VITRO</i> CELL CULTURE METHODS.....	101
3.3.1	Cell culture of MCF10A cells	101
3.3.2	Cell culture of HMLE-Twist1-ER cells	102
3.3.3	Cell culture of MKF cells.....	102
3.3.4	Cytokine treatment.....	103
3.3.5	Transient transfection.....	103
3.3.6	Viral transduction.....	105
3.3.7	CRISPR/Cas9-mediated deletion of <i>KANK4</i> gene	105
3.3.8	KD of Smad proteins and coronins	106
3.4	CELL BIOLOGY-BASED METHODS.....	107
3.4.1	Immunofluorescence microscopy of cells.....	107
3.4.1.1	BrdU staining	108
3.4.2	2D migration assay.....	108
3.4.3	Analysis of lamellipodia formation.....	109
3.4.4	Detection of invadopodia	109
3.4.5	3D collagen/Matrigel invasion assay	110
3.4.5.1	Inhibition and KD in 3D collagen/Matrigel invasion assay	111
3.4.6	Gelatin zymography assay	111
3.4.7	GTPase activity assay	112
3.4.8	Contraction assay	113
3.5	NUCLEIC ACID-BASED METHODS.....	114
3.5.1	RNA-isolation and qRT-PCR	114
3.5.2	PCR.....	115
3.5.3	Plasmids and primers	117
3.6	PROTEIN-BASED METHODS.....	120
3.6.1	SDS-PAGE	120
3.6.2	Western Blot (WB)	120
3.7	PROTEOMIC TECHNIQUES.....	121
3.7.1	Proteomics.....	121
3.7.2	GFP-IP	121
3.7.3	Endogenous IP	122
3.7.4	Mass spectrometry	123
3.7.4.1	Interaction proteomics.....	123
3.7.4.2	Total proteome	125

3.8	DATA MINING.....	127
3.8.1	TCGA database mining.....	127
3.8.2	Public ChIP databases	127
3.9	STATISTICS AND QUANTIFICATION	128
4	RESULTS.....	129
4.1	KANK2 AND KANK4 IN NORMAL DEVELOPMENT	129
4.1.1	Generation of KANK2-KO mice.....	129
4.1.2	Generation of KANK4-KO mice.....	129
4.1.3	KANKs are non-essential in normal development	130
4.2	KANK2 IN FVB MOUSE DEVELOPMENT	132
4.2.1	KANK2 deficiency results in early embryonic death in FVB background	132
4.2.2	KANK2 deficiency impairs chorioallantoic fusion	132
4.2.3	KANK2 expression in chorion and allantois	134
4.3	KANK2 AND KANK4 IN BREAST CANCER DEVELOPMENT	136
4.3.1	KANK2 does not affect tumor development.....	137
4.3.2	KANK4 promotes tumor development in a MMTV-PyMT mouse model.....	137
4.3.3	KANK4 in murine MG.....	140
4.3.3.1	KANK4 is expressed in myoepithelial cells of normal MG	140
4.3.3.2	KANK4 is <i>de novo</i> expressed in transformed LECs of mammary tumor tissues	141
4.3.3.3	Validation of <i>de novo</i> expression of KANK4.....	143
4.3.4	Induction of <i>de novo</i> expression of KANK4	145
4.3.4.1	TGF β , TNF α and IL6 are expressed in TME	146
4.3.4.2	TGF β superfamily induces KANK4 expression.....	146
4.3.4.3	TGF β 1-Smad signaling induces KANK4 expression.....	149
4.3.5	TGF β 1-induced EMT	150
4.3.5.1	TGF β 1 induces EMT in MCF10A and HMLE-Twist1-ER cells.....	150
4.3.5.2	KANK4 expression is independent of EMT-TFs	152
4.3.6	Function of TGF β 1-induced KANK4 expression.....	154
4.3.6.1	KANK4 promotes individual cell migration in 2D	154
4.3.6.2	KANK4 promotes 3D cell invasion.....	156
4.3.6.3	Recruitment of CMSC and MMPs is independent of KANK4.....	159
4.3.6.4	KANK4 promotes TGF β 1-induced lamellipodia and invadopodia formation	162
4.3.6.5	KANK4 promotes TGF β 1-induced Rac1 activation	164
4.3.6.6	KANK4 interacts with Coro1A/B to facilitate lamellipodia formation and 3D invasion	169
4.3.7	KANK4 acts as tumor promoter in several human cancers.....	172
4.3.8	Human breast cancer patients show KANK4 expression in LECs	173
5	DISCUSSION.....	175
5.1	KANK2 AND KANK4 ARE NON-ESSENTIAL IN NORMAL MURINE DEVELOPMENT (C57BL/6)....	176
5.2	ROLE OF KANK2 IN NORMAL DEVELOPMENT IS BACKGROUND-SPECIFIC	178
5.3	KANK4 PROMOTES CANCER DEVELOPMENT AND METASTASIS.....	182
5.4	TGFB1-INDUCES <i>DE NOVO</i> EXPRESSION OF KANK4 IN PARALLEL TO EMT	185
5.5	KANK4 FACILITATES 3D INVASION.....	186
5.6	KANK4 DOES NOT PLAY A SIGNIFICANT ROLE IN CMSC RECRUITMENT OR MMP SECRETION ..	188
5.7	KANK4 PROMOTES TGFB1-MEDIATED RAC1 ACTIVATION	190
5.8	KANK4 FINDINGS CAN BE APPLIED IN HUMAN.....	192
6	SHORT SUMMARY OF MANUSCRIPTS	193
6.1	PAPER I – TISSUE DISTRIBUTION AND SUBCELLULAR LOCALIZATION OF THE FAMILY OF KIDNEY ANKYRIN REPEAT DOMAIN (KANK) PROTEINS	193
6.2	PAPER II – LFC SUBCELLULAR LOCALIZATION AND ACTIVITY IS CONTROLLED BY AV-CLASS INTEGRIN	195

7	REFERENCES	197
8	APPENDIX	225
8.1	MOUSE DATA	225
8.2	GENERATION OF HUMAN KANK4 ANTIBODY	227
8.3	GENERATION OF MCF10A ^{KANK4-KO} CELLS.....	228
8.4	PAPER I – TISSUE DISTRIBUTION AND SUBCELLULAR LOCALIZATION OF THE FAMILY OF KIDNEY ANKYRIN REPEAT DOMAIN (KANK) PROTEINS	229
8.5	PAPER II – LFC SUBCELLULAR LOCALIZATION AND ACTIVITY IS CONTROLLED BY AV-CLASS INTEGRIN	248

Summary

The four proteins of the KANK family (KANK1-4) are novel members of integrin-interacting proteins found in focal adhesions. It was demonstrated that KANKs activate talin, an integrin adaptor protein, by binding to the talin-R7 domain via their N-terminal KN motif within the force-transduction layer of integrin. This interaction results in the disruption of actin-binding to talin at its actin-binding site II ranging from R4 to R8. Subsequently, this leads to reduced force transmission from the cytoskeleton to the integrins. Conversely, KANKs are integral to the cortical microtubule stabilizing complex, which connects the microtubule cytoskeleton to focal adhesions and thus affects focal adhesion turnover by orchestrating secretory processes. Besides extensive *in vitro* studies on especially KANK1 and KANK2, little is known about their *in vivo* functions. Initially identified in renal cell carcinoma, KANKs have since been associated with a number of diseases, including kidney malfunctions and cancer. However, the mechanism by which KANKs exert tumor-promoting or -suppressing functions remains unclear. This thesis aimed to elucidate the *in vivo* function of KANKs, with a particular focus on KANK4 and its role in breast cancer development.

First, we analyzed KANK expression in a range of murine tissues, including kidney, lung, skin, brain, esophagus, and vasculature (aorta and retina) (paper I). KANKs not only showed differential expression levels across the various tissues, but were also expressed by discrete cell types; KANK1 and KANK2 were detected in all analyzed tissues and were expressed in epithelial and mesenchymal cells, respectively, while KANK3 expression was limited to endothelial cells.

KANK4 displayed overlapping expression with KANK2 in contractile mesenchymal cells of lung and kidney and in myoepithelial cells of the mammary gland.

In my research project, I investigated the role of KANK2 and KANK4 in murine development. I found that despite KANK2 and KANK4 being irrelevant for normal development in C57BL/6 background, KANK2-KO-FVB mice were embryonically lethal at E8.5, due to impaired fusion of the chorion and allantois. This shows that KANK2 has a different significance depending on the genetic background.

To investigate the role of KANK2 and KANK4 in a stress situation, I induced breast cancer via the MMTV-PyMT model in KANK2-KO- and KANK4-KO-C57BL/6 mice. While KANK2 did not impact tumor development, tumor formation, progression, and lung metastasis were enhanced in the presence of KANK4. I observed that KANK4 was *de novo* expressed in luminal epithelial cells under pathological conditions. *In vitro* MCF10A cell-based analyses demonstrated that KANK4 expression is induced by the TGF β 1-Smad3/4 signaling pathway and that KANK4 promotes invasion by enhancing Rac1 activity, lamellipodia and invadopodia formation through Coro1A/B interaction. My findings assign a tumor-promoting function to KANK4 by elevating cancer metastasis.

Furthermore, I contributed to a project examining the function of $\alpha_v\beta_3$ and $\alpha_5\beta_1$ in Lfc activation following fibronectin binding (paper II). Our findings revealed that while $\alpha_v\beta_3$ integrin binding resulted in Lfc^{S151} phosphorylation, leading to dissociation from microtubules and subsequent RhoA activation, no such effect was observed with $\alpha_5\beta_1$ integrin. This suggests the existence of distinct signaling mechanisms underlying integrin function upon ligand binding.

Altogether, the studies provide valuable insights into the *in vitro* and *in vivo* functions of

KANK2 and KANK4, while also underscoring the distinct roles of different KANK family members.

Abbreviations

4T1 cells	Human breast cancer stage IV cells	CHK2	Checkpoint-kinase 2
Å	Ångström	CI	Confidence interval
aa	Amino acid	CK	Casein kinase
ABS	Actin binding site	CK5/8/14/18	Cytokeratin 5/6/8/14/18
ACR	albumin-creatinine ratio	CKIa	Casein kinase Ia
ADAM	A disintegrin and metalloproteinase	CLASP	Cytoplasmic linker associated protein
ADMIDAS	Adjacent to MIDAS	clCasp3	Cleaved caspase 3
AFM	Atomic force microscopy	CMSC	Cortical microtubule stabilizing complex
AIB1	Amplified in breast cancer 1	c-myc	Cellular-myelocytomatosis
AIF	apoptosis-inducing factor	CNS	Central nervous system
ALK	Activin receptor-like kinase	Coro1A/1B	Coronin1 A/1B
AMH	Anti-Müllerian hormone	COS1 cells	Monkey fibroblast-like cells from kidney
Ank	Ankyrin	Co-Smad	Common mediator Smad
AP1 family	Activator protein-1 family	CRIB	Cdc42- and Rac-interactive binding
APC	Adenomatous Polyposis Coli	c-Ski	Cellular-Sloan-Kettering institute
ARHGDIa	RhoGDP dissociation inhibitor alpha	c-src	Cellular-sarcoma
ArhGEF2/7	Rho guanine nucleotide exchange factor 2/7	CTC	Circulating tumor cells
Arp2/3	Actin-related protein 2/3	CXCL10	C-X-C motif chemokine ligand 10
BALB/c	Bagg and albino	Dab2	Disabled homolog 2
BC	Bent closed	dKO	Double KO
BCA assay	Bicinchoninic acid assay	DMSO	Dimethyl sulfoxide
BFP	Blue fluorescent protein	dsDNA	Double strand DNA
bHLH family	Basic helix-loop-helix family	DSR	Double strand repair
Bim	Bcl-2 interacting mediator of cell death	DTT	Dithiothreitol
BMP	Bone morphogenetic protein	E	Embryonic day
BrdU	Bromodeoxyuridine	EB1	End-binding protein 1
BSA	Bovine serum albumin	EC	Extended closed
C57BL/6	C57 black 6	E-Cad	Epithelial cadherin
CA	Constitutive active	ECM	Extracellular matrix
CAF	Cancer-associated fibroblasts	EGF	Epidermal growth factor
cAMP	Cyclic adenosine-monophosphate	EGFR	EGF receptor
CBP	cAMP response element-binding (CREB)-binding protein	ELKS	Glutamic acid-leucine-lysine-serine
CD	Circular dichroism	EMT	Epithelial-to-mesenchymal transition
CD4/24/44	Cluster of differentiation 4/24/44	EndMT	Endothelial-to-mesenchymal transition
Cdc42	Cell division cycle 42	EO	Extended open
CDK1/2	Cyclin-dependent kinase 1/2	EPHA2	Ephrin type-A receptor 2
CFEOM1	Congenital fibrosis of the extraocular muscles	ER	Estrogen receptor
ChIP-Exo	Chromatin immunoprecipitation exonucleases	Erk	Extracellular signal-regulated kinase
ChIP-Seq	Chromatin immunoprecipitation DNA-Sequencing	ES cell	Embryonic stem cell
		FA	Focal adhesion
		F-actin	Filamentous actin
		FAK	Focal adhesion kinase
		Fast-1	=Foxh1
		FBS	Fetal bovine serum
		FERM domain	4.1 protein-ezrin-radixin-moesin domain

FGF	Fibroblast growth factor	iPALM	Interferometric photo-activated localization microscopy
FGFR	FGF receptor	IR	Irradiation
Foxh1	Forkhead box H1	IRSp53	Insulin receptor substrate p53
FRET	Fluorescence resonance energy transfer	I-Smad	Inhibitory Smad
Fsp1	Fibroblast-specific protein 1	Jak	Janus kinase
FVB	Friend leukemia virus B	JNK	c-Jun N-terminal kinase
Fwd	Forward	JUN	Ju-nana (=17)
G3BP2	Ras GTPase-activating protein-binding protein 2	KANK	Kidney Ankyrin repeat containing protein
G-actin	Globular actin	KD	Knockdown
GAP	GTPase-activating protein	Ki67	Kiel-67
GDF	Growth differentiation factor	KIF21A	Kinesin-like protein
GDI	Guanine nucleotide dissociation inhibitor	KN motif	KANK N-terminal motif
GEF	Guanine nucleotide exchange factor	KO	Knockout
GEM	Genetically engineered mouse	LAP	Latency-associated peptide
GFP	Green fluorescent protein	LATS	Long-acting stimulator
Gpm6A	Glycoprotein M6A	LD motif	Leucin-aspartate motif
Grb2	Growth factor receptor-bound protein 2	LEC	Luminal epithelial cell
GRIP1	Glutamate receptor interacting protein 1	Lef1	Lymphoid enhancer-binding factor 1
gRNA	Guide RNA	LFA-1	Lymphocyte function-associated antigen 1
GSK3	Glycogen synthase kinase 3	Lfc	= ArhGEF2
GST	Glutathione S-transferase	LIF	Leukemia inhibitory factor
GTP	Guanosine-triphosphate	LIM domain	Lin-11 – Isl-1 – Mec3 domain
H&E	Hematoxylin and eosin	LL5β	Pleckstrin homology-like domain family B member 2
Ha-Ras	Harvey rat sarcoma	LLC	Large latent complex
HEK293T cells	Human embryonic kidney 293 tumor cells	LLPS	Liquid-liquid phase separation
HeLa cells	Human cervical cancer cell	LN-332	Laminin 332
HER2	Human epidermal growth factor receptor 2	LOH	Loss of heterozygosity
Het	Heterozygous	LOX	Lysyl oxidases
HGF	Hematopoietic growth factor	LRP5/6	Lipoprotein receptor-related protein 5/6
HIF	Hypoxia-inducible factor	LTR	Long terminal repeat
HL-60 cells	Human acute myeloid leukemia cells	LTBP	latent TGFβ binding protein
HMLE cells	Human mammary epithelial cells	Lyn	Lck/Yes novel tyrosine kinase
HT-1080 cells	Human epithelial fibrosarcoma cells	MAPK	Mitogen-activated protein kinase
I-BAR domain	Inverse-Bin-Amphiphysin-Rvs domain	MCF10A cells	Human Michigan Cancer Foundation 10A cells
ICAM	Intercellular adhesion molecule	MCF7 cells	Human Michigan Cancer Foundation 7 cells
ICM	Inner cell mass	MDA-MB-231 cells	Human MD Anderson-Metastatic Breast-231 cells
IF	Immunofluorescence	MDCK cells	Dog Madin-Darby Canine kidney cells
IFNγ	Interferon gamma	MEK	MAP-Erk-kinase
IGF1	Insulin-like growth factor 1	MET	Mesenchymal-to-epithelial transition
IL	Interleukin	MG	Mammary gland
ILK	Integrin-linked kinase	MH1/2	Mad homology 1/2
IMC	Inner membrane clasp	MIDAS	Metal-ion-dependent adhesion site
IP	Immunoprecipitation		

MIN	Mammary intraepithelial neoplasia	PR	Progesterone receptor
miR-200	MicroRNA-200	PTEC cells	Proximal-tubule epithelial cells
MKF cells	Mouse kidney fibroblast cells	PTGS2	Prostaglandin-endoperoxide synthase 2
MKK	Mitogen-activated protein kinase kinase	PTH1H	Parathyroid hormone like hormone
MMP	Matrix metalloprotease	PyMT	Polyoma middle T
MMTV	Mouse mammary tumor virus	qRT-PCR	Quantitative real-time PCR
MS	Mass spectrometry	qSMCL	quantitative single-molecule colocalization analysis
MT	Microtubule	Rac1	Ras-related C3 botulinum toxin substrate 1
MTLn3 cells	Rat mammary adenocarcinoma cells	Raf	Rapidly accelerated fibrosarcoma
(N-)WASP or WASp	(Neural-)Wiskoot-Aldrich syndrome protein	RANKL	Receptor activator of NF- κ B ligand
NA	Nascent adhesion	Ras	Rat sarcoma
NBT-II cells	Rat epithelial urinary bladder cancer cells	RBD-Pak1	Rac1 binding domain-Pak1
N-Cad	Neural cadherin	RCC	Renal cell carcinoma
NEAA	Non-essential amino acid	RFP	Red fluorescent protein
NIH3T3 cells	Mouse embryo fibroblast cells	RGD motif	Arginine-glycine-aspartate motif
NMR	Nuclear magnetic resonance	Rho	Ras homologue
NOS1AP	Nitric oxide synthase 1 adaptor protein	RhoGDIα	=ARHGDIA
NSCLC cells	Human non-small-cell lung cancer cells	RNAseq	RNA sequencing
OCT4	Octamer-binding transcription factor 4	ROCK	Rho-associated protein kinase
OMC	Outer membrane clasp	R-Smad	Receptor regulated Smads
OSM	Oncostatin M	RT	Room temperature
p53	Tumor protein P53	Rvs	Reverse
pA	Polyadenylation	S100A4	S100 calcium binding protein A4
PAI-1	Plasminogen-activator-inhibitor type 1	SA	Splice acceptor
Pak1	P21 activated kinase 1	SARA	Smad anchor for receptor activation
Pak1-PBD	Pak1-Rac/Cdc42 (p21) binding domain	SCRIB	Scribble
Pan-Cad	Pan cadherin	SD	Standard deviation
PANC-1 cells	Human pancreatic carcinoma cells	SDS	Sodium dodecyl sulfate
PBS	Phosphate-buffered saline	SERM	selective estrogen receptor modulator
PCR	Polymerase chain reaction	Shc	Src homology and collagen
PDAC cells	Human pancreatic ductal adenocarcinoma cells	SIP	SRC interacting protein
PDGF	Platelet-derived growth factor	siRNA	Small interfering RNA
Pen/Strep	Penicillin/Streptomycin	SKIL	Ski-like proto-oncogene
PFA	Paraformaldehyde	SLC	Small latent complex
PGM1	Phosphoglucomutase 1	Smad	Small mother against decapentaplegic homolog
PH domain	Pleckstrin homology domain	Sox2/9	Sex-determining region Y-box 2/9
pH3	Phospho-Histone 3	SP	Somite pairs
PI3K	Phosphoinositide 3-kinase	Sra1	Steroid receptor RNA activator 1
PIP2	Phosphatidylinositol-4,5-bisphosphate	SRC	Steroid receptor coactivator
PIP3	Phosphatidylinositol-3,4,5-trisphosphate	STAT3	Signal transducer and activator of transcription 3
PKA/C	Protein kinase A/C		
pN	Piconewton		

SyMBS	Synergistic metal-ion binding site	WDR26	WD repeat domain 26
T47D cells	Human epithelial breast carcinoma cells	Wnt	Wingless and Int-1
TAGLN	Transgelin	WT	Wildtype
TAK1	TGF β -activated kinase 1	YAP	Yes-associated protein
TAM	Tumor-associated macrophage	Zeb1	Zinc finger E-box binding homeobox 1
TAN	Tumor-associated neutrophil	αSMA	Alpha smooth muscle actin
TAZ	Transcriptional co-activator with PDZ-binding motif	β-gal	Beta-galactosidase
Tbx3	T-box transcription factor 3	β-TrCP	Beta-transducin repeat-containing protein 1
TCF	Transcription factor		
TCGA	The Cancer Genome Atlas Program		
TEAD	TEA domain family member		
TEB	Terminal end bud		
TF	Transcription factor		
TGFBR	TGF β receptor		
TGFβ	Transforming-growth factor beta		
THP-1 cells	Human acute monocytic leukemia cells		
Tiam1	T-lymphoma invasion and metastasis-inducing protein 1		
TIRF microscopy	Total internal reflection fluorescence microscopy		
TKS5	Tyrosine kinase substrate with 5 SH3 domains		
TLNRD1	Talin rod domain-containing protein 1		
TMD	Transmembrane domain		
TME	Tumor microenvironment		
TNBC	Triple-negative breast cancer		
TNFα	Tumor necrosis factor alpha		
Tpm	Tropomyosin		
TRAF4/6	TNF receptor associated factor 4/6		
U2OS cells	Human epithelial osteosarcoma cells		
UTSCC38 cells	Human laryngeal squamous cell carcinoma cells		
VASP	Vasodilator-stimulated phosphoprotein		
VCAM-1	Vascular cell adhesion molecule 1		
VE-Cad	Vascular endothelial cadherin		
VEGF	Vascular endothelial growth factor		
VEGFR	VEGF receptor		
VMRC-RCW cells	Human renal cell carcinoma cells		
Wap	Whey acidic protein		
WAVE	WASP family verprolin homologous protein		
WB	Western blot		
WD40	Tryptophan-aspartate 40 aa		

Publications

- I. Guo, S. S., **Seiwert, A.**, Szeto, I. Y. Y. & Fässler, R. Tissue distribution and subcellular localization of the family of Kidney Ankyrin Repeat Domain (KANK) proteins. *Exp. Cell Res.* **398**, 112391 (2021). doi: 10.1016/j.yexcr.2020.112391.
- II. Coló, G. P., **Seiwert, A.** & Haga, R. B. Lfc subcellular localization and activity is controlled by α v-class integrin. *J. Cell Sci.* **136**, (2023). doi: 10.1242/jcs.260740.

1 Introduction

1.1 Integrins and integrin-mediated signaling

Integrins have been found in 1987 as essential heterodimeric transmembrane receptors ubiquitously expressed in cells mediating cell adhesions (Hynes, 1987). Their function of bridging the exterior to the interior of the cell is resembled in the name integrin (Van der Flier and Sonnenberg, 2001). Here, integrins can either interact with extracellular matrix (ECM) proteins like collagens, fibronectin or laminin, regulating cell-ECM adhesion, or with receptors like VCAM, ICAM or cadherins, mediating cell-cell adhesion (Kammerer, Aretz and Fässler, 2017). Structurally, they comprise of a non-covalent complex of an α - and a β -subunit (Hynes, 1987). In total, there are 18 α - and eight β -subunits in mammals, resulting in 24 functional receptor combinations, which recognize specific peptide motifs depending on the composition of subunits (Figure 1) (Sun, Guo and Fässler, 2016).

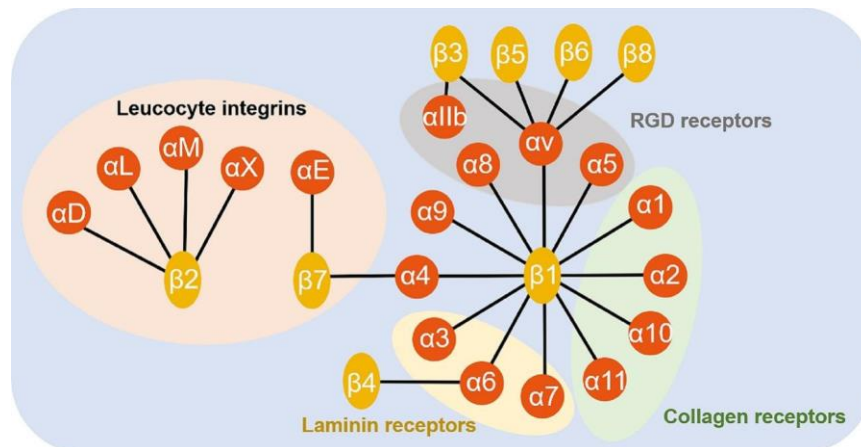


Figure 1: Integrin family. Integrins are classified into RGD-receptor binding, collagen-binding, laminin-binding or leucocyte-specific integrins, depending on the combination of α and β subunits (Liu *et al.*, 2023).

The importance of integrins is demonstrated in mice depleted of specific integrins: For example, lack of α ₄ integrin or its counter-receptor VCAM-1 result in defective chorioallantoic fusion as well as impaired epicardium development and subsequent

embryonic death at E11.5 (Gurtner *et al.*, 1995; Kwee *et al.*, 1995; Yang, Rayburn and Hynes, 1995). α_5 integrin KO embryos show decreased blood vessel complexity, less fibronectin expression, and mesodermal defects causing embryonic lethality (Francis *et al.*, 2002). Disruption of β_1 integrin leads to embryonic death shortly after the blastocyst stage (E3.5) and implantation (Fässler and Meyer, 1995).

1.1.1 Integrin structure

Integrins are type I transmembrane proteins: Both α - and β -subunits contain a large ligand binding extracellular domain of around 800 aa (ectodomain), a single transmembrane segment of around 25 aa and a short cytoplasmic tail of 10-70 aa (Moser *et al.*, 2009) (Figure 2).

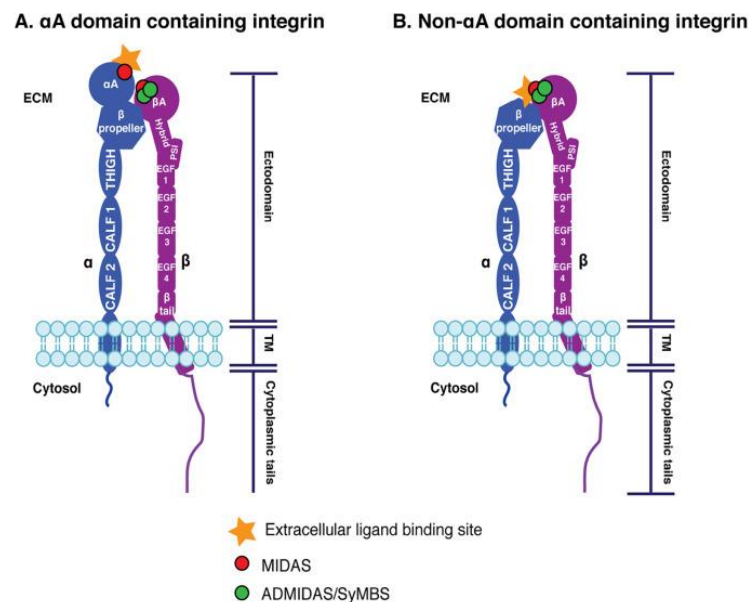


Figure 2: Integrin structure. α - and β -integrins contain a large extracellular ectodomain and a short cytoplasmic tail, connected via a TMD. The head-domain differs in the presence (A) and absence (B) of an α A domain (Kadry and Calderwood, 2020).

The extracellular ectodomain of the α -subunit contains four domains which are linked together: Two CALF domains (CALF2 and CALF1) are linked to a THIGH domain, followed by a β propeller. Some α -subunits, namely α_1 , α_2 , α_{10} , α_{11} , α_L , α_M , α_X , α_D and α_E ,

contain an additional α I (or α A domain), also called von-Willebrand-factor A domain, binding to a loop in the β propeller. It has around 200 aa, forming a Rossmann fold with five alternating α -helices and β -sheets respectively. In integrins containing an α I domain, this is the only ligand binding site. Here, a metal-ion dependent adhesion site (MIDAS) within the α I domain, which ligates Mg^{2+} ions via five aa residues, is important for ligand binding.

The β -subunit contains a β -tail, four EGF domains (EGF1-4), a hybrid and a PSI (plexin-semaphorin-integrin) domain and a β I (or β A) domain, which is structurally similar to the α I domain (Kadry and Calderwood, 2020). The subunits interact with each other via the β -propeller of the α -subunit and the β I domain of the β -subunit.

Ligand binding to integrin head is mediated by divalent cations. The β I domain contains a MIDAS, adjacent MIDAS (ADMIDAS) and a synergistic metal-ion binding site (SyMBS) to coordinate Mg^{2+} and Ca^{2+} in a Asp-X-Ser-X-Ser motif (J. Zhu *et al.*, 2008). The cations interact with negatively charged acidic side chains of the ligand and facilitate ligand binding.

The transmembrane domains (TMD) of the α - and β -subunit is directly involved in integrin activation, as they associate and disassociate according to inactive and active integrin state, respectively. TMDs assembly is mediated by electrostatic interactions within two interfaces, the so-called inner and outer membrane clasps (IMC, OMC). NMR studies showed that the TMD of the α -subunit of $\alpha_{IIb}\beta_3$ integrin contains a short α -helix, whereas the TMD of the β -subunit is larger and thus lays in the membrane with a tilted angle by 25° (Lau *et al.*, 2009). The interaction of TMDs within the OMC is mediated by a GxxxG motif and G708 of the α_{IIb} - and β_3 -subunit, respectively (Lau *et al.*, 2009). Within the IMC,

hydrophobic interactions of F992/F993 in α_{IIb} and W715/I719 in β_3 occur, as well as the formation of a salt bridge between R995 in α_{IIb} and D723 in β_3 (Lau *et al.*, 2009). Molecular dynamics simulations revealed that TMDs of different integrins differ in their number of contacts and association strength, with $\alpha_{IIb}\beta_3$ integrin showing more contacts and a higher tendency to associate compared to $\alpha_5\beta_1$ or $\alpha_v\beta_3$ (Pagani and Gohlke, 2018). Mutations that force the dissociation of the TMDs have been shown to promote integrin activation (Ginsberg, 2014).

The cytoplasmic tails are rather short and interact with various intracellular proteins. An exception is the tail of the β -subunit of β_4 integrin, which contains around 1000 aa and is therefore unusually long. The β_1 tail contains a membrane-proximal NPxY and a membrane-distal NxxY motif, which bind the integrin-adaptor proteins talin and kindlin, respectively. Talin and kindlin are highly required for integrin activation and KO of either proteins abolishes integrin binding to the ECM and thus cell attachment (Theodosiou *et al.*, 2016).

1.1.2 Integrin conformations and activation

After synthesis, the α - and β -subunits heterodimerize in the endoplasmic reticulum by interaction of the β -propeller of the α -subunit with the β I-domain, allowing for proper folding and integration into the plasma membrane (Bachmann *et al.*, 2019; Kechagia, Ivaska and Roca-Cusachs, 2019). Hereby, the β -subunit is expressed in excess, thus the presence of a specific α -subunit determines the fate of the integrin (Heino *et al.*, 1989). Once at the plasma membrane, integrins are present in three distinct conformations (Figure 3): (1) In the bent-closed (BC) conformation, which has a low affinity for ligands, both subunits are closely together with bent legs, which are stabilized by the ADMIDAS Ca^{2+}

ion of the β I-domain (Luo and Springer, 2006; Bachmann *et al.*, 2019). (2) The extended-closed (EC) conformation requires the straightening of the legs, which transforms into the (3) active extended-open (EO) conformation by TMD and thus leg separation (Luo and Springer, 2006). In the extended-open conformation, integrins are able to bind ligands, as the ligand binding site becomes accessible by a piston-like swing out of an α -helix. Conformational-specific antibodies recognizing native epitopes are useful tools to distinguish between these distinct conformations (Byron *et al.*, 2009; Su *et al.*, 2016).

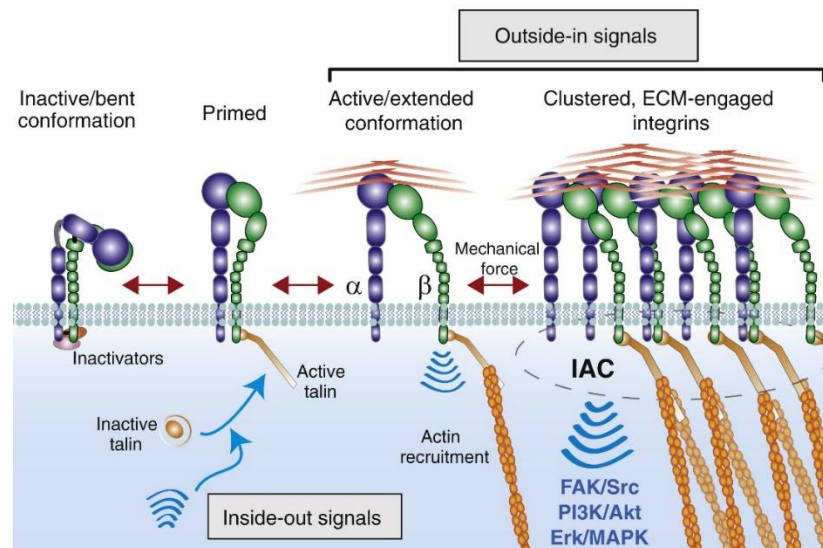


Figure 3: Integrin conformations and activation. Integrins exist in three different states: Bent closed (BC), extended closed (EC) and extended open (EO) conformation. In the EO conformation, integrins bind ligands of the ECM. In the cytoplasm, talin and kindlin interact with the β -tail to stabilize the EO conformation. As force-transmitting protein, talin binds to F-actin to transmit force generated by the cytoskeleton to the integrin head and to further enhance ligand binding. Upon integrin clustering, additional proteins of the integrin adhesome are recruited and mature FAs develop (Chastney, Conway and Ivaska, 2021).

Conformational change from the inactive BC to the active EO conformation results in ligand binding and initial cell adhesion. Upon binding, integrins assemble and cluster to recruit several proteins for integrin-ligand linkage stabilization and efficient signal transduction. In integrin activation it is distinguished between inside-out and outside-in signaling. The inside-out activation is triggered by the binding of integrin adaptor proteins talin and kindlin to the proximal and distal NPxY motifs of the integrin cytoplasmic tail,

respectively (Ripamonti, Wehrle-Haller and de Curtis, 2022). Talin is a force-sensing protein and contains an N-terminal FERM domain (F0, F1, F2, F3), a linker domain and a C-terminal rod domain, consisting of 13 helical bundles (R1-R13). The rod domain is folded and can unfold in a sequential manner, when force is applied. Talin gets released from its autoinhibitory conformation by PIP2, which allows the FERM-like head domain to bind to integrin's cytoplasmic tail (Moser *et al.*, 2009). Kindlin also contains a FERM domain (F0, F1, F2, PH, F3) and recruits the PINCH-Parvin complex, paxillin and Arp2/3 to integrins upon binding. Via its PH domain, kindlin binds to PIP2 and PIP3 in the plasma membrane (J. Liu *et al.*, 2011). Talin and kindlin form ternary adhesion complexes with active β_1 integrin. This has been visualized by quantitative single-molecule colocalization analysis (qSMCL), which can resolve the location of the individual molecules in cells (Fischer *et al.*, 2021). NMR studies also demonstrated that talin and kindlin directly interact with each other to simultaneously bind to integrins and form a transient ternary complex and that kindlin increases the affinity of talin to integrins, resulting in integrin activation and cell adhesion (Aretz *et al.*, 2023). By binding to integrins, talin and kindlin trigger a conformational change in the TMD of the β -subunit, resulting in leg separation. Additionally, talin and kindlin transduce mechanical forces to integrins to stabilize the EO conformation and facilitate ligand binding (Sun, Costell and Fässler, 2019). Via paxillin, kindlin interacts with the talin-rod domain to promote integrin activation, as disruption of paxillin-kindlin interaction strongly impairs integrin activation, ligand binding and cell adhesion (Lu *et al.*, 2022). Paxillin also activates FAK upon kindlin binding and overexpressing FAK in kindlin-deficient cells can rescue cell spreading defects (Theodosiou *et al.*, 2016).

Outside-in activation requires the spontaneous binding of integrins to ligands. Integrins exist predominantly in the BC conformation (97.75%), as this is thermodynamically favored. However, they fluctuate to EC (0.1%) and EO (0.15%) conformations, in which they have the highest ligand affinity (Li *et al.*, 2017). However, the low-affinity conformations (BC and EC) show faster ligand binding, determined by measuring the ligand on-rate, compared to the high-affinity EO conformation (Li, Yan and Springer, 2021). Prompt ligand binding to the BC conformation results in integrin leg separation and head opening converting integrins into the high-affinity EO conformation, which allows talin binding to stabilize the EO conformation by tensile forces transduced from the actin cytoskeleton (Li *et al.*, 2024).

1.1.3 The model of the molecular clutch

Once integrins are in the active EO conformation and bind ligands, integrins cluster and form adhesion complexes to transmit signals from the ECM. One important feature of integrins hereby is the sensing of ECM stiffness, which follows the principle of the molecular clutch and determines migration efficiency (Figure 4). Cell migration requires strong anchoring of the cells to the ECM and simultaneously applying opposing traction forces exerted by rapid actin polymerization at the barbed end, also called the actin retrograde flow. The actin cytoskeleton consists of polarized helical polymers, which are decorated with myosin (Pollard and Borisy, 2003). Actin polymerization happens by gradually adding actin globular monomers to the barbed end of the filaments pointing towards the plasma membrane. This results in a filament movement towards the cell center. This actin dynamic was demonstrated by fluorometric labelling of actin monomers in

epithelial keratinocytes, demonstrating that the cell pushes itself forward by constant actin polymerization (Theriot and Mitchison, 1991).

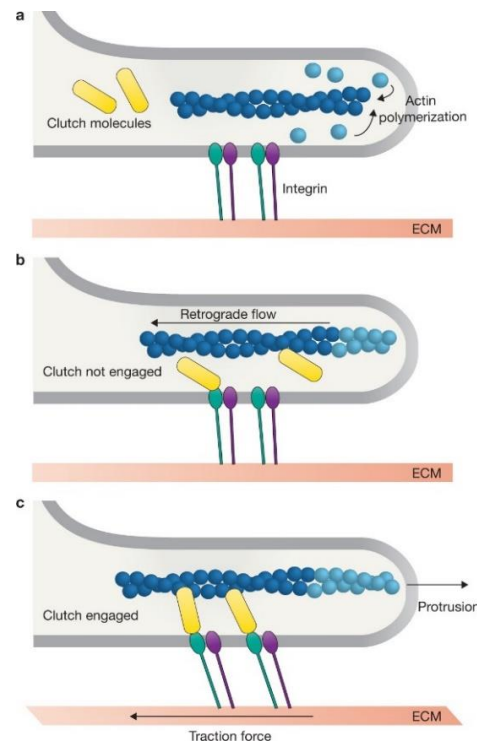


Figure 4: The model of the molecular clutch. The molecular clutch includes ECM proteins, integrins, clutch molecules, like talin and vinculin, and the actin cytoskeleton (a). If the molecular clutch is not engaged, the actin retrograde flow is fast and force transmission is low (b). If the molecular clutch is engaged, the actin retrograde flow is coupled to the ECM via integrins, resulting in slow retrograde flow, high force transmission and protrusion formation (Case and Waterman, 2015).

Integrins bridge the ECM anchoring with the polymerizing actin cytoskeleton via force-sensitive proteins like talin and vinculin. In a non-engaged molecular clutch, the actin retrograde flow is not connected to integrins. Thus, the retrograde flow is fast and does not exert pushing forces on the plasma membrane. The molecular clutch is engaged, when the actin-cytoskeleton interacts with integrins mediated by talin, vinculin and α -actinin. The retrograde flow is now anchored to the ECM, which slows down the actin flow speed, but increases traction forces. Continuous actin polymerization at the barbed end results in pushing forces against the plasma membrane, protrusion formation and cell migration (Case and Waterman, 2015). Exertion of pulling forces by the actin retrograde flow on talin

leads to unfolding of the talin rod (Yamashiro *et al.*, 2023). Encrypted actin and vinculin binding sites become available to further strengthen the interaction of talin and actin cytoskeleton.

The molecular clutch is mechanosensitive, meaning it senses substrate rigidity and responds accordingly. Different substrate stiffnesses regulate the force transmission and engagement of the molecular clutch. On soft substrates, the rate at which force that is applied to the clutch increases (=loading rate) is slower than the lifetime of the integrin-ligand bond. Integrins form so-called slip-bonds, which break with increasing force before talin unfolding.

On stiff substrates, the loading rate is faster than the lifetime of the integrin-ligand bond, thus allowing talin unfolding. The unfolded talin enables vinculin binding and additional actin recruitment to reinforce the integrin-ligand bond lifetime (Elosegui-Artola *et al.*, 2016). Integrins form so-called catch bonds, which strengthen with increasing force. This is facilitated by conformational changes in the extracellular integrin head domain which make additional fibronectin binding sites, the synergy sites, accessible (Swaminathan and Waterman, 2016).

KANKs, which will be introduced in chapter 1.2, have been identified to regulate the molecular clutch by competing with actin to talin binding (Sun *et al.*, 2016). By binding to talin, KANK weakens the actin-integrin force transmission, which results in reduced molecular clutch engagement, focal adhesion (FA) sliding into the cell center, and decreased cell migration speed (Sun *et al.*, 2016).

1.1.4 Integrin-based adhesions

Integrin-based adhesions are dynamic structures. In order to interact with the ECM, integrins form adhesive structures containing specific and distinct proteins. The adhesive structures are divided into three classes (Figure 5): (1) Dot-shaped nascent adhesions (NAs, also called focal complexes) are formed in filopodia and lamellipodia at the leading edge of migrating cells and are rather small (0.5-1 μm diameter) and short-lived (1 min lifespan). They can mature into (2) elongated FAs via integrin clustering, binding to the actin cytoskeleton, talin unfolding, and force transmission. FAs are 3-10 μm big and have a lifespan of several minutes. However, FA proteins are highly dynamic and exchange within 30 sec (Case and Waterman, 2015). In fibroblasts, FAs further develop into (3) fibrillar adhesions, which are long and thin structures that locate in the cell center to enable fibronectin fibrillogenesis and contain tensin (Chastney, Conway and Ivaska, 2021).

Upon integrin activation, integrins interact with and recruit more than 200 proteins to form mature FAs (=integrin adhesome) (Schiller *et al.*, 2011). In 2010, the nanoscale architecture of $\alpha_v\beta_3$ integrin forming FAs was solved using the super-resolution microscopy method iPALM in U2OS (Kanchanawong *et al.*, 2010). They distinguished three separate layers in z-direction: (1) At the plasma membrane (<30 nm above the plasma membrane), they identified the integrin signaling layer, in which FAK, paxillin, and ILK bind the integrin cytoplasmic tail. Paxillin can directly bind integrins via its four LIM domains and recruits FAK to FAs. Via autophosphorylation of FAK^{Y397}, FAK phosphorylates paxillin to facilitate interaction with other proteins like Src (Legerstee and Houtsmuller, 2021). Hereby, increased force results in increased paxillin phosphorylation by FAK. (2) In the middle, Kanchanawong, *et al.* describe the force transduction layer, in

which talin, vinculin and KANKs transmit signals in a force-dependent manner. Vinculin directly binds to actin and talin and promotes the activation and clustering of integrins (Legerstee and Houtsmuller, 2021). (3) On top of the force transduction layer (>50 nm above the plasma membrane) lays the actin regulatory layer, which contains actin, zyxin, VASP and α -actinin and connects the actin cytoskeleton with integrins (Kanchanawong *et al.*, 2010; Case and Waterman, 2015) (Figure 5). Zyxin binds actin via its LIM domains and recruits VASP to FAs. VASP interacts with zyxin, vinculin and GEFs to promote actin polymerization (Legerstee and Houtsmuller, 2021).

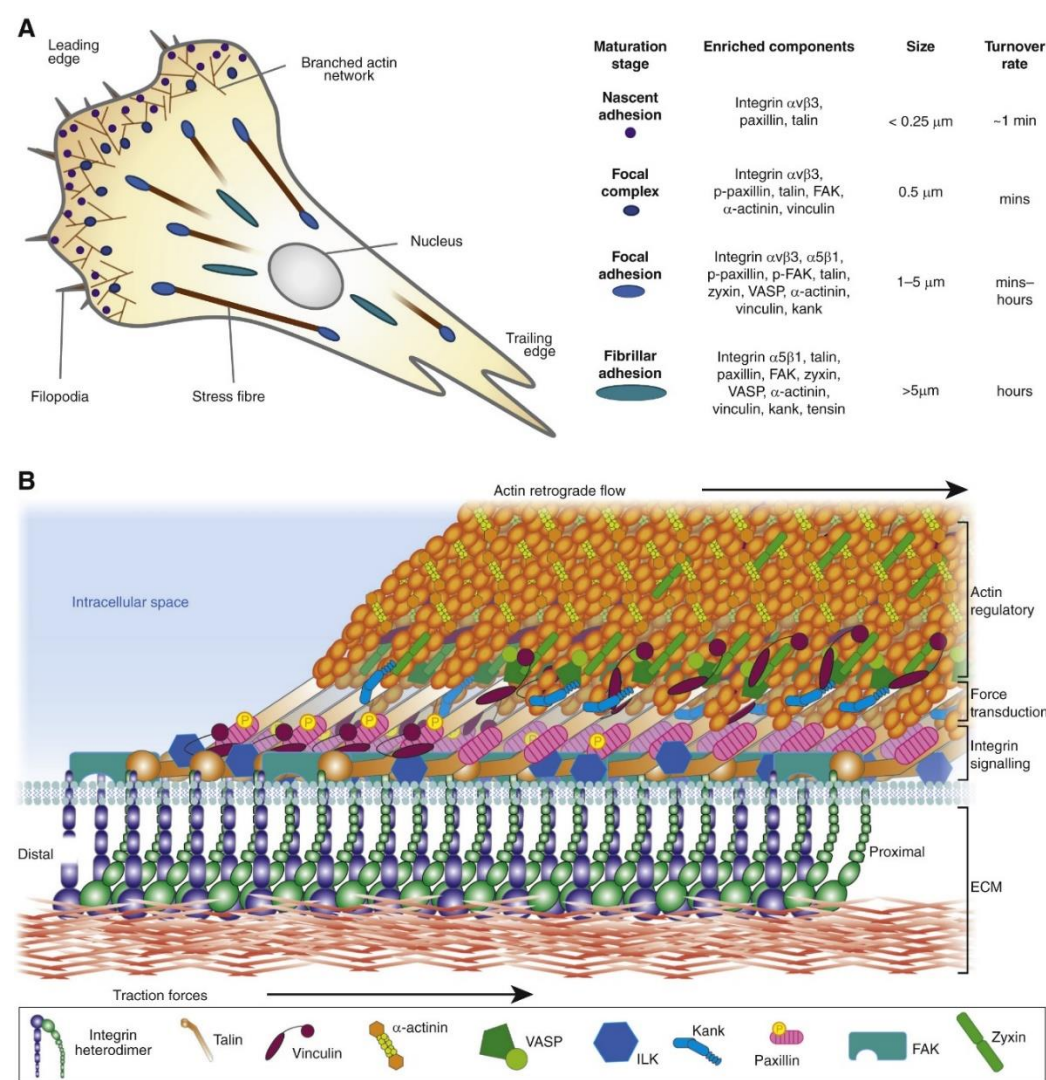


Figure 5: Integrin based adhesions. (Caption continued on next page)

Figure 5: Integrin-based adhesions. Integrins mature from NAs to FAs and fibrillar adhesions. Different maturation states show different protein compositions and physical properties (A). In z-direction, adhesive structures are divided into integrin signaling layer, a force transduction layer, and an actin regulatory layer (B) (Chastney, Conway and Ivaska, 2021).

In order to migrate successfully, FA disassembly is required. This is mediated by microtubule (MT) targeting to FAs. Paxillin and FAK have been shown to regulate MT-dependent FA disassembly. MT regulate RhoA activity through the guanine nucleotide exchange factor (GEF-H1), which cycles between MT and cytosolic localization. Whereas MT depolymerization is associated with enhanced RhoA activity, cell contractility and FA assembly, MT polymerization is associated with FA disassembly. On the other hand, MT recruit matrix metalloproteases (MMPs), which promotes FA turnover (Stehbens *et al.*, 2014). Interestingly, Chen *et al.* showed that at mitotic entry, FAs disassembly is driven by CDK1-cyclin B1-mediated phosphorylation of kindlin (Chen, Aretz and Fässler, 2022). Phosphorylated kindlin was ubiquitinated and degraded, reducing the kindlin levels by 80%. Inhibition of kindlin phosphorylation and thus degradation blocked mitotic rounding and FA disassembly resulting in apoptosis, highlighting the importance of FA turnover during cell cycle (Chen, Aretz and Fässler, 2022).

Other integrin-based adhesions are clathrin plaques, which contain β_5 integrin, clathrin, Numb and Dab2, but are not connected to the actin cytoskeleton, or hemidesmosomes, which are formed by $\alpha_6\beta_4$ integrin in epithelial monolayers and are connected to cytokeratin intermediate filaments (Chastney, Conway and Ivaska, 2021).

1.2 The KANK family

KANKs were first identified in 2002 by Sarkar *et al.*. They studied loss of heterozygosity (LOH) in renal cell carcinoma (RCC) tissues and identified 9p24 locus displaying high incidence of LOH (Sarkar *et al.*, 2002). Via gene research in the respective DNA region,

Sarkar *et al.* identified KANK as a novel kidney tumor related protein containing three coiled-coil motifs and several C-terminal ankyrin repeats. Due to its structure and relevance in the kidney, the name KANK derives from **k**idney **a**nkyrin repeat-containing protein. By using additional *in vitro* studies with HEK293T cells, the authors summarize KANK as tumor suppressing protein, which leads to growth arrest in G0/G1 phase (Sarkar *et al.*, 2002). Two alternative splicing isoforms of human KANK were found in normal and RCC tissue, which differ in the presence or absence of a 158 aa long sequence at the N-terminus (Wang *et al.*, 2005). Whereas kidney cancer cells express KANK-S, which lacks the N-terminal sequence, normal kidney tissue express the slightly larger form KANK-L, as well as KANK-S. KANK-L was also shown to contain one nuclear localization signal and three nuclear export signals, facilitating a nuclear-cytoplasmic shuttling and enhancing β -catenin nuclear localization and β -catenin-dependent transcription in human kidney cell lines (Wang *et al.*, 2006).

Via domain and phylogenetic analysis, a family of in total four KANK proteins were identified, namely KANK1, KANK2, KANK3, and KANK4 (Y. Zhu *et al.*, 2008). The paralogues share five C-terminal ankyrin-repeat motifs and an N-terminal KN (KANK N-terminal) motif. Additionally, they contain a unique set of at least one coiled-coil motif (Figure 6). Structural similarities suggest overlapping functions of the different KANKs.

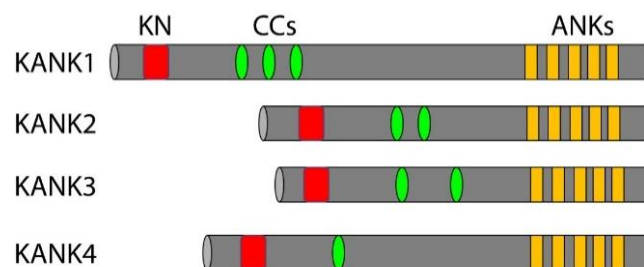


Figure 6: The KANK family. The four KANKs share an N-terminal KN motif and five C-terminal Ankyrin (Ank) repeats, but distinct coiled-coil (CC) domains (Guo and Fässler, 2022).

Two orthologs of KANK were found, called VAB-19 in *C. elegans*, and *dkank* in *Drosophila* (Ding *et al.*, 2003; Clohisey, Dzhindzhev and Ohkura, 2014; Gee *et al.*, 2015). VAB-19 has been reported to be important in epidermal elongation by properly organizing the epidermal actin cytoskeleton, as well as proper muscle attachment to the epidermis during the twofold stage of *C. elegans* embryos (Ding *et al.*, 2003). Depletion of VAB-19 resulted in embryonic death or death shortly after hatching. *Drosophila* KANK interacts with EB1, a MT plus end regulating protein, to localize to MTs and to mature muscle-tendon attachment sites (Clohisey, Dzhindzhev and Ohkura, 2014).

1.2.1 *In vitro* functions of KANKs

KANKs have been associated with several different intracellular functions (Figure 7). In cells, overexpression of the four different KANKs in NIH3T3 cells showed that actin stress fiber formation was impaired (Kakinuma *et al.*, 2008; Y. Zhu *et al.*, 2008). Kakinuma *et al.* identified KANK1 to interact with 14-3-3 via its coiled-coil domain upon PI3K/Akt-mediated phosphorylation at S167. This interaction was demonstrated to block actin stress fiber formation, as well as insulin-stimulated activation of RhoA in rat adipocytes and NIH3T3 cells resulting in decreased cell migration (Kakinuma *et al.*, 2008). KANK1 was also shown to interact with insulin receptor substrate (IRS) p53 in VMRC-RCW cells via its coiled-coil domain (Roy, Kakinuma and Kiyama, 2009). IRSp53 binds small GTPases like Rac1 and Cdc42, and WAVE2 to stimulate lamellipodia and filopodia formation. KANK1 colocalized with IRSp53 and WAVE2 at the cell periphery and at the tips of lamellipodia and filopodia. The authors found that Rac1 and KANK1 binding domains in IRSp53 were overlapping, resulting in a competitive binding of the two proteins to IRSp53. KANK1 could also partially block binding between Cdc42 and IRSp53. On the other hand,

KD of KANK1 could increase the binding between IRSp53 and active Rac1. KANK1-mediated inhibition of Rac1-IRSp53 interaction led to impaired lamellipodia formation and insulin-induced membrane ruffling. By seeding NIH3T3 cells on fibronectin, the authors could study integrin-mediated cell adhesion and spreading and examine the effect of KANK1 on integrin-Rac1 signaling. They found that KANK1 diminishes cell spreading by interacting with IRSp53 in a Rac1-independent manner, possibly by preventing IRSp53-actin association.

Via its ankyrin repeats, KANK1 can interact with the MT-associated protein KIF21A and both colocalized in membrane ruffles and cell bodies of VMRC-RCW and HeLa cells (Kakinuma and Kiyama, 2009; van der Vaart *et al.*, 2013). Interestingly, the CFEOM1-associated mutation R954W and M947T in KIF21A further enhanced the interaction of KIF21A with KANK1. Kakinuma *et al.* demonstrated that KD of KIF21A highly impaired subcellular localization of KANK1 resulting in decreased amounts of KANK1 at the cell membrane. Interestingly, while Kakinuma *et al.* showed that KIF21A localization is independent of KANK1, van der Vaart *et al.* observed an impaired localization of KIF21A to the cell cortex in the absence of KANK1 (Kakinuma and Kiyama, 2009; van der Vaart *et al.*, 2013). Van der Vaart *et al.* further showed that KANK1, together with scaffolding proteins liprin- α 1 and liprin- β 1, and the LL5 β -ELKS complex inhibit MT growth at the cell cortex (van der Vaart *et al.*, 2013). Depletion of KIF21A and KANK1, not KANK2, resulted in dense MT bundle formation and MT outgrowth at the cell periphery (van der Vaart *et al.*, 2013).

LL5 β interacts with PIP3 in the cell membrane and directly binds to CLASPs, which in turn recruits MT to the leading cell edge. Bouchet *et al.* termed the cortical assembly of

LL5 β , liprins and ELKS as cortical microtubule stabilizing complex (CMSC) and proposed a crosstalk between MT network and FA complexes (Bouchet *et al.*, 2016). Pulldown experiments revealed that KANK1 and KANK2 interact with liprin- α 1 and even more with liprin- β 1 via their first coiled-coil domain. KANK1-coiled-coil domain and the N-terminal helical region of liprin- β 1 show a strong interaction with an affinity of $0.032 \pm 0.012 \mu\text{M}$ (Guo *et al.*, 2023).

On the other hand KANK1 interacts with talin-1-R7 domain in FA complexes via its KN motif (Bouchet *et al.*, 2016; Sun *et al.*, 2016). The KANK1-KN motif consists of an LDLD motif, which provides hydrophobic residues important for talin-1 binding. NMR chemical shift mapping revealed that the KN motif interacts with the talin-1 R7 domain, and only weakly with R8 domain, which contains an LD-recognition box. The R7 domain is formed by five helices from which α 2 and α 5 form a hydrophobic groove that serves as docking station for the KANK1-KN motif. Thereby α 2^{Y1369} and α 5^{W1630} force the two helices to separate by around 8 Å. The positively charged residues R7^{K1401} and R7^{R1652} are important for binding to the negatively charged Asp residues of KN-LDLD motif. Crystallization of the KN/R7 complex identified a β -hairpin and α -helical structure of the KN motif, which amphipathic characteristics enable close interaction to the hydrophobic talin-1 R7 domain (Guo *et al.*, 2023). The sterically demanding KN^{Y48} was found to localize to a hydrophobic pocket of R7^{G1404} and a mutation to block the pocket (G1404L) abolished KANK binding completely (Bouchet *et al.*, 2016). Alternatively, mutating KN^{L41} or KN^{F45} to glutamine blocked hydrophobic interactions and thus KN/R7 binding (Guo *et al.*, 2023). As both interaction sites on talin-1 and KANK1 are conserved in talin-2 and the other KANKs it was assumed that talin and KANK are conserved binding partners. This was later

confirmed by pulldown assays, showing that talin-1 was pulled down by all four KANKs (Zhang *et al.*, 2022).

The KANK1-talin-1 interaction is crucial to localize KANK1 to FAs and to recruit the CMSC in proximity to the adhesion sites, mediated by KANK1-liprin- β 1 binding. Further it was shown that depletion of KANK1 or KANK2 resulted in MT uncoupling from FAs and subsequent increased formation of myosin II filaments accompanied by FA growth in HT-1080 and THP-1 cells (Rafiq *et al.*, 2019). This phenotype was suggested to be a consequence of increased RhoA and ROCK activity upon KANK KD, due to elevated cytoplasmic localization and hence the activation of GEF-H1 (Rafiq *et al.*, 2019). By using an optogenetic construct of KANK1, Aureille *et al.* showed that light-induced activation of KANK1 targets MTs to FAs, resulting in an GEF-H1/Rho/ROCK-mediated increased accumulation of myosin II and actin filaments and finally leading to FA sliding and disassembly (Aureille *et al.*, 2024).

CLASP, which is recruited to the proximity of FAs by LL5 β , stabilizes MT close to FAs, thereby regulating FA turnover (Stehbens *et al.*, 2014). The authors showed that CLASP regulates RAB6A-mediated exocytosis at FAs and that the exocytosis of the MT-cargo proteins MMPs close to FAs is dependent on CLASP. The secretion of MMPs close to FAs results in ECM degradation and subsequent disassembly of FAs. KD of LL5 β or CLASP, as well as inhibition of MMP resulted in an increased size and lifetime of FAs, highlighting that LL5 β recruits CLASP for targeted MMP secretion at FAs to regulate FA turnover (Stehbens *et al.*, 2014).

Crystal structure of the KANK1-KIF21A complex showed that KANK-ankyrin repeats bind to a short aa sequence (~30 aa) localized in the middle of KIF21A via polar and

hydrophobic interactions (Guo *et al.*, 2018; Pan *et al.*, 2018; Weng *et al.*, 2018). The KANK1 residues involved in KIF21A binding were conserved in KANK2, leading to comparable affinities of KANK1-KIF21A and KANK2-KIF21A binding ($K_{d_{KANK1}} 0.58 \pm 0.05 \mu\text{M}$; $K_{d_{KANK2}} 0.18 \pm 0.01 \mu\text{M}$), whereas KANK3 and KANK4 showed sequence alterations and were not able to interact with KIF21A (Guo *et al.*, 2018; Weng *et al.*, 2018). This was further supported by Zhang *et al.*, which could only pulldown KIF21A, as well as the other CMSC member liprin- β 1 by using KANK1 and KANK2, but did not detect any interaction with KANK3 and KANK4 (Zhang *et al.*, 2022). These data suggest that KANKs display different functions in recruiting the CMSC to FAs.

KANKs as FA proteins were further studied by Sun *et al.*. The authors found KANKs to be localized around mature FAs and central adhesions in the so-called FA belt in a KN-motif-dependent manner (Sun *et al.*, 2016). They showed that the presence of the coiled-coil domain is crucial to exclude KANK from the center of FAs, which was later confirmed by Guo *et al.* (Sun *et al.*, 2016; Guo *et al.*, 2023). The presence of KANK2 in the FA belt resulted in adhesion sliding and disassembly, and decreased migration speed of mouse kidney fibroblasts (MKF). Sun *et al.* linked KANK-talin interaction to integrin activation and force transduction, by applying the model of the molecular clutch. They observed that by binding to talin-R7 domain, KANK2 prevents the interaction of F-actin to talin-ABS2, a major actin binding site (ABS) covering R7 domain. This results in less force transmission generated by actomyosin contractility, converting integrin-ligand catch bonds to slip bonds, adhesion sliding and reduced migration velocity (Sun *et al.*, 2016). Magnetic tweezer experiments using the R7/KN complex showed a mechanical stability of several pNs for up to minutes, with a maximum lifetime at forces of around 6 pN (Yu *et al.*, 2019).

Interestingly, Sun *et al.* found that the role of KANK2 in FAs was not impaired by disturbing the CMSC, suggesting that it might function independently in FAs and the CMSC (Sun *et al.*, 2016).

Guo *et al.* showed that the KANK1-KN-talin-1-R7 interaction is crucial for both KANK1 and talin-1 localization to the FA belt (Guo *et al.*, 2023). As talin-1 both interacts with KANK1 (in the FA belt) and vinculin (in the FA center), they further map down the respective binding sites and show that vinculin-talin-1 binding inhibits KN binding to talin-1, by requiring R7R8 unfolding to expose the buried vinculin-binding sites. This unfolding is triggered by mechanical forces. Interestingly, interaction of KN with R7 enhanced the stability of the R7R8 domain, shown in temperature-dependent circular dichroism (CD) spectroscopy. Vinculin on the other hand lead to R7R8 unfolding and tight association of the vinculin-head domain to R8 (Guo *et al.*, 2023), providing an explanation for the exclusion of KANK1 from the focal adhesion center with high mechanical force. The ability of the KANK1 to undergo liquid-liquid phase separation (LLPS), mediated by its loop region (L1), which connects the KN motif and the coiled-coil region, turned out to be essential for KANK1's localization at the FA belt and its function in regulating FA disassembly, as well as recruitment of liprin- β 1 and MT and actin cytoskeleton organization (Guo *et al.*, 2023).

Using the super-resolution technology iPALM, Kumari *et al.* examined the vertical axis of FAs and showed that the actin-regulating proteins Tropomyosin 3.2 (Tpm3.2) and Tropomyosin 1.6 (Tpm1) form additional actin-binding layers located between the talin-positive force transduction layer close to the plasma membrane and the α -actinin-positive actin-regulating layer (Kumari *et al.*, 2024). They found that KO of Tpm3 impaired

KANK2, CMSC and CLASP localization to FAs, resulting in disorganized and less aligned MTs that bypass FAs (Kumari *et al.*, 2024).

KANK1-KN also interacts with TLNRD1, a structural similar protein to talin R7R8 that has been shown to promote tumor development in hepatocellular carcinoma and bladder cancer and correlates with poor prognosis of lung cancer patients (Tatarano *et al.*, 2012; Wu *et al.*, 2017; Nagy *et al.*, 2018; Cowell *et al.*, 2021). The authors determined a lower affinity of KANK1-KN to TLNRD1 compared to talin R7R8 (K_d 11.6 μ M vs. K_d 0.35 μ M) (Cowell *et al.*, 2021). Interestingly, they proposed a role of TLNRD1 dimerization in actin filament cross-linking and actin-bundling, thus promoting myosin X-positive filopodia formation and migration velocity in U2OS cells cultured on fibronectin (Cowell *et al.*, 2021).

Some publications refer to KANK2 as steroid receptor coactivator (SRC) interacting protein (SIP) (Zhang *et al.*, 2007; Wang *et al.*, 2012; Ramot *et al.*, 2014; Hudson, McArdle and Bernal, 2016). As stated in the name, SIP was identified to interact with SRC coactivators SRC-1, AIB1, and GRIP1 via its ankyrin repeats and colocalized in the cytoplasm of MCF7 cells (Zhang *et al.*, 2007). The SRC family is important in transcription and translation processes, especially in estrogen receptor (ER)-mediated gene transcription and proliferation. Upon estrogen stimulation, SRC-1 shuttled into the nucleus, whereas SIP retained its cytoplasmic localization. Via KD experiments, the authors concluded that SIP sequesters SRC coactivators in the cytoplasm, to prevent ER-mediated gene transcription. They propose a model in which estrogen-activated casein kinase (CK) II phosphorylates SIP, which facilitates SRC-1 release and nuclear translocation to stimulate ER-regulated gene transcription (Zhang *et al.*, 2007). SIP is also involved in apoptosis-inducing factor

(AIF)-mediated cell death (Wang *et al.*, 2012). AIF translocates from mitochondria into the nucleus upon various apoptosis stimuli, resulting in AIF-triggered chromatin condensation and DNA fragmentation. Wang *et al.* reported that KANK2 interacts with AIF in the mitochondria via its coiled-coil domain to inhibit AIF release and thus inhibits apoptosis (Wang *et al.*, 2012). Another study suggests that SIP is phosphorylated upon EGF stimulation in human myometrial cells, and regulates prostaglandin-endoperoxide synthase 2 (PTGS2) expression (Hudson, McArdle and Bernal, 2016).

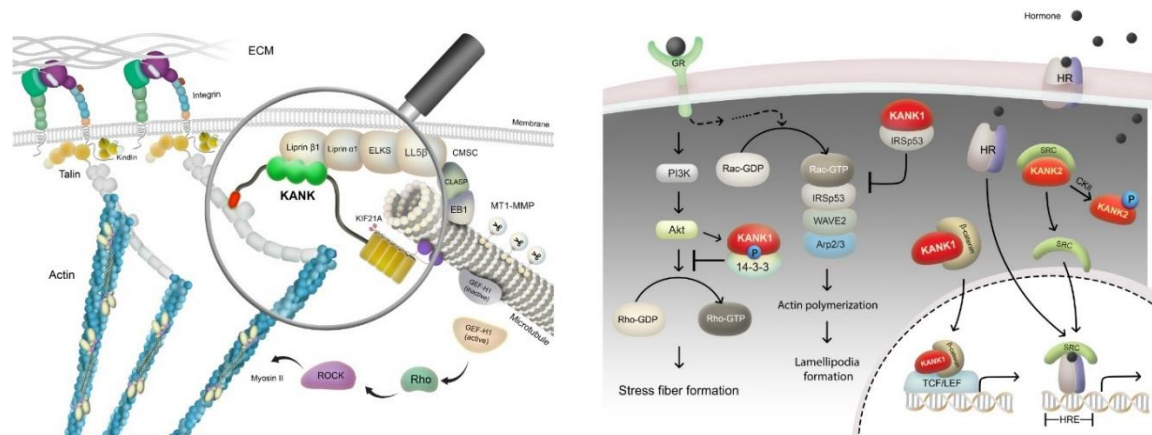


Figure 7: *In vitro* functions of KANKs. KANKs interact with talin and liprin-β1 to connect FAs and MT cytoskeleton (left panel). KANKs were shown to be involved in several intracellular signaling pathways (right panel) (Guo and Fässler, 2022).

1.2.2 *In vivo* functions of KANKs

In vivo functions of KANKs are less intensively studied compared to their *in vitro* functions. An expression pattern study of the four KANKs in zebrafish showed that KANKs are predominantly expressed in embryonic vascular development (Hensley *et al.*, 2016). Homozygous missense mutations in human KANK1 (p.E454K), KANK2 (p.S181G, p.S684F), and KANK4 (p.Y801H) genes have been associated to nephrotic syndrome (Sarkar *et al.*, 2002; Gee *et al.*, 2015). KD of the drosophila ortholog dkank in cardiac nephrocytes highly impaired nephrotic cellular structure and function and depletion of KANK2 in zebrafish resulted in disorganized podocyte foot processes, decreased slit

membranes, and impaired glomerular basement membrane, leading to increased proteinuria (Gee *et al.*, 2015). The authors observed an interaction of KANK2 and ARHGDI1 and RhoA, which was strongly increased by KANK2-p.S181G mutation, linking GTPase signaling and nephrotic syndrome. On the other hand, mice lacking KANK1 specifically in podocytes did not show defects in kidney functions, evaluated by determining the urinary albumin-creatinine ratio (ACR), blood urea nitrogen, or serum creatinine levels (Oda *et al.*, 2024). Also, the morphology of the kidney was not affected in the absence of KANK1 (Oda *et al.*, 2024). However, upon kidney injury induced by adriamycin, lack of KANK1 in podocytes resulted in less dense foot processes at the glomerular basement membrane, leading to increased urinary ACR (Oda *et al.*, 2024).

The missense mutation p.A670V in the first ankyrin repeat of KANK2 was found in patients suffering from keratoderma and woolly hair, disturbing the interaction between KANK2 and SRC-1 (Ramot *et al.*, 2014). Deletion of KANK1 at 9p24.3 has been associated with familial cerebral palsy (Lerer *et al.*, 2005).

KANK4 has been studied in the context of arteriogenesis. By using a KANK4-EGFP reporter mouse, Zhang *et al.* suggest that KANK4 is expressed in endothelial cells. The authors report that KANK4-KO mice develop normally without affecting vessel development. However, upon induction of an ischemic injury in the hindlimb, KANK4 is important to regulate collateral artery arteriogenesis by enhancing the vessel diameter, endothelial cell proliferation and enlarging the vessel lumen to facilitate an alternative blood circulation and enable sufficient blood supply of the hindlimb despite ischemia. KANK4-KO mice formed smaller arteries and thus showed slower recovery of blood perfusion of the hindlimb. Mechanistically, the authors suggest that KANK4 interacts with

VEGF receptor 2 (VEGFR2) and talin-1 to couple VEGFR2 to integrins and thus potentiate VEGF signaling (Zhang *et al.*, 2022). Haydont and colleagues detected KANK4 expression in aged and photo-damaged skin by qRT-PCR and high KANK4 expression positively correlated with the age of papillary fibroblasts (Haydont *et al.*, 2019). In multiple sclerosis patient brain tissues, KANK4 was shown to be downregulated in chronic active demyelinating lesions in the CNS, but the function of KANK4 remains unknown (Hendrickx *et al.*, 2017).

RNAseq and immunohistochemical analysis of keloid tissue forming around wounds revealed an TGF β -dependent upregulation of KANK4 in TAGLN-positive activated myofibroblasts and α SMA-positive fibroblasts (Oishi *et al.*, 2024). Overexpression of KANK4 enhanced, whereas KANK4-KD impaired cell motility in a transwell migration assay, suggesting a promoting role of KANK4 in keloid expansion and thus pathologic wound healing (Oishi *et al.*, 2024).

1.2.3 KANKs in cancer

KANK was first identified as a growth suppressor in renal cell carcinoma (Sarkar *et al.*, 2002). Since then, overexpression, mutations or deletions of KANK genes have been reported in different cancers (Tadijan *et al.*, 2021). Whereas KANK1 and KANK3 are thought to be tumor suppressing, KANK2 and KANK4 might act as tumor promoters (Tadijan *et al.*, 2021). Nevertheless, extensive studies on the function of KANKs in cancers are missing.

Recently, Guo *et al.* identified KANK1 as tumor promoting protein. They showed that KANK1 was expressed in breast cancer luminal epithelial cells (LECs), which resulted in faster tumoroid growth and proliferation (Guo *et al.*, 2024). MCF7-based cell studies

revealed that KANK1 interacts with NOS1APc at cell-cell junctions via its ANK repeats together with the preceding unstructured region. This interaction outcompetes NOS1APc-SCRIB binding, resulting in compromised SCRIB function in Hippo pathway activation and results in higher nuclear TAZ localization. Mechanistically, KANK1-KO cells showed increased activity of LATS kinase, mediating an increased TAZ^{S89} and TAZ^{S311} phosphorylation and subsequent TAZ cytoplasmic retention and degradation. KANK1-WT cells on the other hand showed enhanced TAZ stabilization with nuclear translocation. The correlation of KANK1 expression and nuclear TAZ accumulation was confirmed *in vivo* via IF stainings of breast cancer tissues derived from mouse and human patients (Guo *et al.*, 2024).

1.3 TGF β superfamily

The TGF β superfamily is a well characterized family of ubiquitously expressed growth factors that have been widely studied in embryogenesis, tissue formation, immune response, and disease context. The superfamily contains more than 30 members, subgrouped in TGF β -like (including TGF β s, activins, nodal, lefty, and myostatin) and BMP-like (including BMPs, GDFs and AMH) molecules (Massagué, 2008). The subgroups differ in their mode of signaling by interacting with different type I and type II receptors, resulting in the activation of distinct Smad proteins (Figure 8) (Weiss and Attisano, 2013; Trelford, Dagnino and Di Guglielmo, 2022).

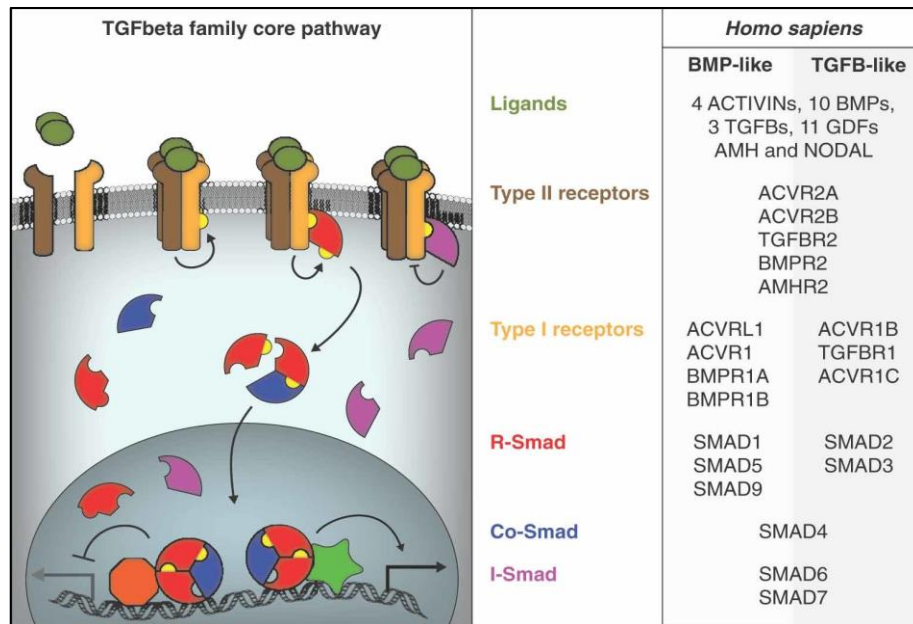


Figure8: The TGFβ superfamily. The members of the TGFβ superfamily are divided into BMP- and TGFβ-like proteins. They differ in the use of type II and type I receptors and signal transduction via different Smads (Weiss and Attisano, 2013).

The superfamily members show distinct expression patterns as well as temporal expression differences (Massagué, 2008). TGFβ superfamily signaling strongly depends on cell type and cell context. The cell response is hereby determined by (1) the presence or absence of certain TGFβ signaling members, like extracellular ligands, cell surface receptors or intracellular signaling molecules, (2) the presence or absence of transcription factors (TFs) regulating, enhancing or inhibiting Smad binding to the DNA, and (3) the epigenetic features of the DNA, like DNA methylation or histone modifications (Massagué, 2012).

One widely described paradox is the antiproliferative effect of TGFβ during development and embryogenesis, versus its proliferation and metastases promoting function during late tumor development, which will be discussed in chapter 1.3.3.

1.3.1 TGFβ

In mammals, three TGFβ isoforms are expressed (*TGFB1*, *TGFB2*, and *TGFB3*), located on different chromosomes (Ch 19, 1, and 14, respectively). In addition, avians where shown

to express *TGFB4*, an orthologue to mammalian *TGFB1*, whereas *TGFB5* was found in *X. Laevis* (Kondaiah *et al.*, 1990; Halper, Burt and Romanov, 2004). Structurally alike, the three mammalian TGF β isoforms share 71-79% sequence similarity and act via the same set of TGF β -receptors (TGFBR) (Huang, Schor and Hinck, 2014). TGF β 2 however has a decreased affinity to TGFBR2, as it lacks R25 and R94, which are present in TGF β 1 and TGF β 3 and form hydrogen bonds with E119 and D32 of TGFBR2 (Baardsnes *et al.*, 2009). On the other hand, TGF β 2 shows an increased affinity for the co-receptor TGFBR3 compared to TGF β 1 and TGF β 3. This results in lower biological activity of TGF β 2 in cells lacking TGFBR3, which is equalized by the presence of TGFBR3 (Baardsnes *et al.*, 2009).

Despite overlapping expression patterns, the TGF β isoforms show specific and non-redundant functions, as mice lacking either of the isoforms all die around birth, caused by distinct phenotypes: Several TGF β 1-KO mice have been generated, all showing impaired immune functions and enhanced inflammatory responses induced by infiltrating leukocytes and macrophages in different organs developing shortly after birth. Eventually, the mice die at the age of one month (Shull *et al.*, 1992; Kulkarni *et al.*, 1993; Bottinger, Letterio and Roberts, 1997). Defects in the yolk vasculature and the hematopoietic system result in death of 50% TGF β 1-KO embryos at E10.5 (Dickson *et al.*, 1995). TGF β 2-KO on the other hand was shown to be lethal shortly before or after birth due to heavy malformations in heart, lung, craniofacial structures, fore-and hind limbs, neural tube, eye, spiral limbus of the inner ear, and urogenital tracts (Sanford *et al.*, 1997). Finally, disruption of TGF β 3 resulted in death within 24 hours after birth, caused by defective palatal shelf fusion at

E14.5 leading to cleft palate and subsequent problems of suckling (Proetzel *et al.*, 1995; Koo *et al.*, 2001).

1.3.1.1 Activation of TGF β

Expressed and secreted by many cell types, TGF β has a tightly controlled mechanism of getting activated. It is stored in the ECM in an inactive form. TGF β functions in form of an active dimer, which undergoes several steps of precursor forms to get activated (Figure 9). In a first step, TGF β is translated as pre-pro TGF β protein and translocates to the Golgi. The 12.5 kDa mature ligand is connected to a signal peptide, as well as to the so-called large amino-terminal latency-associated peptide (LAP) sequence (Aashaq *et al.*, 2021; Trelford, Dagnino and Di Guglielmo, 2022). After the proteolytic removal of the short signal peptide in the rough ER, two pro-proteins dimerize via two disulfide bonds between the two LAPs and one disulfide bond between two mature ligands, mediated by disulfide isomerases, forming the characteristic 'cysteine knot' of the pro-TGF β (Weiss and Attisano, 2013; Trelford, Dagnino and Di Guglielmo, 2022).

Furins and convertases cleave the LAP in the Golgi membrane, forming a small latent complex (SLC) containing a mature TGF β -dimer non-covalently bound to two LAPs, but lacking bioactivity. The SLC is secreted into the ECM via secretory vesicles and interacts with extracellular glycoproteins called latent TGF β binding proteins (LTBP1-4, of which LTBP2 shows no TGF β binding (Robertson *et al.*, 2015)), to form a large latent complex (LLC), which further reduces bioactivity. Thereby, one LTBP molecule covalently binds two LAPs with its C-terminal TGF β -binding domain forming disulfide bonds (Shi *et al.*, 2011; Lockhart-Cairns *et al.*, 2022). In addition, LTBPs bind to fibrillin, connecting the LLC to the ECM, which was shown to play an important role in TGF β activation

(Yoshinaga *et al.*, 2008). The LLC remains inactive until the mature TGF β dimer is released from the complex.

The dimer release is mediated by proteases like MMPs and furins, which cleave off the LAP-binding domains of LTBPs to release active TGF β (Trelford, Dagnino and Di Guglielmo, 2022). LAP-binding transmembrane receptors like thrombospondin-1, mannose 6-phosphate, or $\alpha_v\beta_6$ and $\alpha_v\beta_8$ integrins also mediate activation of TGF β . Here, the α_v -chain of $\alpha_v\beta_6$ and $\alpha_v\beta_8$ integrins contain RGD-binding motifs, which specifically recognize the RGD flanked by a helical motif in LAPs of TGF β dimers. Contractile force generated by the actin cytoskeleton is transported via $\alpha_v\beta_6$ integrin to induce conformational changes of LAP (Bachmann *et al.*, 2019; Deng *et al.*, 2024). This results in decreased binding affinity of LAP to the TGF β dimer and the subsequent release of mature TGF β from its inactivating complex. $\alpha_v\beta_8$ integrin, which does not bind the actin cytoskeleton requires e.g. MMPs to activate TGF β . Interestingly, TGF β 2 lacks the RGD motif in its LAPs and is thus thought to be activated independent of integrins. However, Le *et al.* demonstrated that $\alpha_v\beta_6$ integrin can activate TGF β 2 in HEK293 cells (Le *et al.*, 2023). The authors show that TGF β 2 contains a SGDQKTI motif instead of the RGD motif, which is recognized specifically by $\alpha_v\beta_6$ integrin (Le *et al.*, 2023).

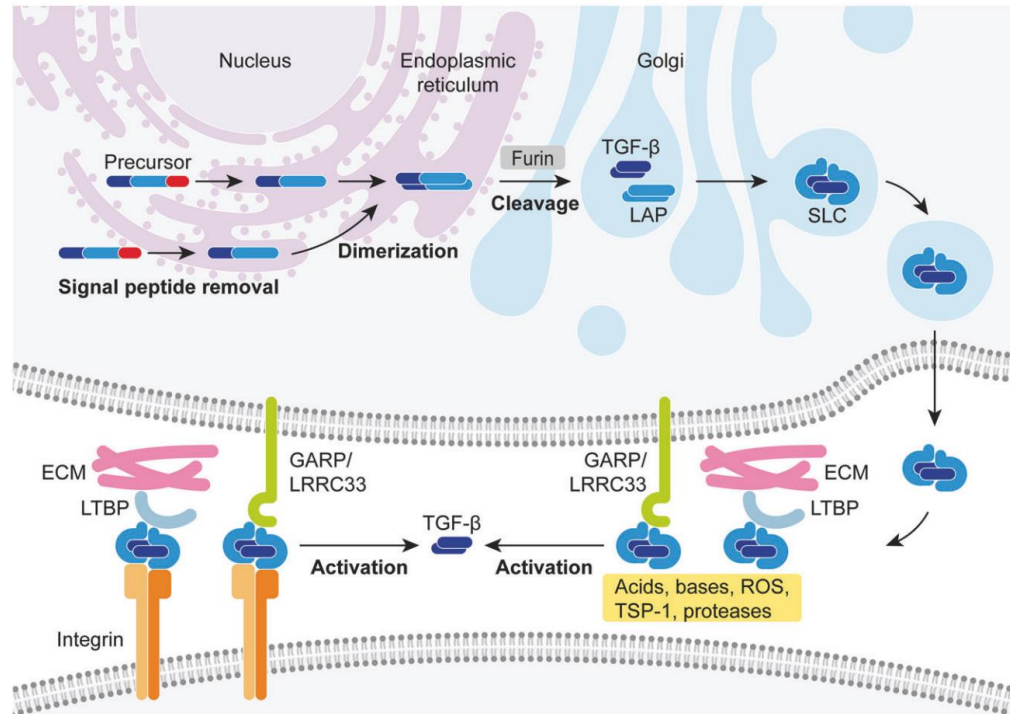


Figure 9: TGFβ activation. TGFβ is synthesized and activated in several steps. After translation and signal peptide removal, two pro-TGFβ ligands associate with two LAP sequences via disulfide bonds. The SLC is secreted and interacts with LTBP, where it remains inactive upon activation via proteases or integrins (Deng *et al.*, 2024).

1.3.2 TGFβ receptors and signaling

The TGFβ superfamily signals by binding to distinct sets of receptors, which in turn activate different intracellular pathways. There are in total seven type I receptors (also called ALK1-7 = activin-like kinase1-7) and 5 type II receptors (TβRII, ActRII, ActRIIB, AMHRII, and BMPRII) in mammals (Weiss and Attisano, 2013). All contain a short cysteine-rich extra-cellular domain, a single transmembrane domain and an intracellular domain showing serine/threonine kinase activity (Heldin, Miyazono and Ten Dijke, 1997). Receptors and ligands can interact in various combinations to transduce different intracellular signals (Weiss and Attisano, 2013; David and Massagué, 2018). In general, the dimeric ligand firstly binds to a specific constitutively active homodimer of type II receptors, which then forms a complex with a type I receptor homodimer (Yamashita *et*

al., 1994; Aashaq *et al.*, 2021). Co-receptors like type III receptor betaglycan or endoglin, which lack kinase activity, may mediate this binding, by enhancing ligand-receptor binding (Huynh, Hipolito and Dijke, 2019). The type II receptor phosphorylates S/T residues in the GS juxtamembrane domain of type I receptor, inducing canonical and non-canonical signaling pathways (Gilbert, Vickaryous and Vilorio-Petit, 2016; Huynh, Hipolito and Dijke, 2019). The active hetero-tetrameric ligand-receptor complex stays active for 30-60 min upon TGF β binding (Wrana *et al.*, 1994).

1.3.2.1 Smad signaling

Smads are ubiquitously expressed in cells and are the main signaling molecules in the canonical TGF β signaling pathway. These so-called signal-driven transcription factors interact with various other transcription factors to specifically drive gene expression and cell fate (David and Massagué, 2018).

The importance of Smads is demonstrated in several animal KO studies. Lack of Smad2 resulted in embryonic lethality at E7.5 in C57BL/6J background, showing defects in assembling and organizing the primitive germ layers (Nomura and Li, 1998; Liu *et al.*, 2016). In contrast, Smad3 lacking mice are viable and fertile, but show defects in the immune response and have a higher predisposition to form tumors (Liu *et al.*, 2016). Smad4-deficient C57BL/6 mice die between E6.5 and E8.5 due to epiblast proliferation defects and defective endoderm differentiation (Yang *et al.*, 1998). These studies highlight that although structurally highly similar, Smads do not share equivalent functions.

The Smad family consists of eight Smads in mammals, which are sub-grouped into receptor regulated Smads (R-Smad; Smad1, 2, 3, 5, and 8), common mediator Smad (Co-Smad; Smad4) and inhibitory Smads (I-Smad; Smad6 and 7) (L. Attisano, 2001; Aashaq *et al.*,

2021). The R-Smads are further separated in BMP receptor-activated Smads (Smad1, 5, and 8) and TGF β receptor-activated Smads (Smad2 and 3). R-Smads and Co-Smad Smad4 are 40-60 kDa proteins containing mad-homology domains (MH1 and MH2) connected with a proline-rich linker (Figure 10). It is suggested that Smads rest in an inactive state, in which MH1 and MH2 are intramolecular connected (Hata *et al.*, 1997; Wrans and Pawson, 1997). I-Smads only contain a MH2 domain. The N-terminal MH1 domain enables active transport of Smads into the nucleus and facilitates DNA binding via a β -hairpin DNA interaction motif, whereas the C-terminal MH2 domain mediates receptor binding, oligomerization and interaction with other proteins (Miyazono, Kamiya and Morikawa, 2010; Liu *et al.*, 2016; Aashaq *et al.*, 2021). Interestingly, Smad2 contains a 30 aa insertion (E3 insert) in the MH1 domain, which supposedly abolishes DNA binding ability of Smad2 (Shi *et al.*, 1998; Hill, 2016). However, it was shown that Smad2 does bind DNA but with reduced affinity (Aragón *et al.*, 2019).

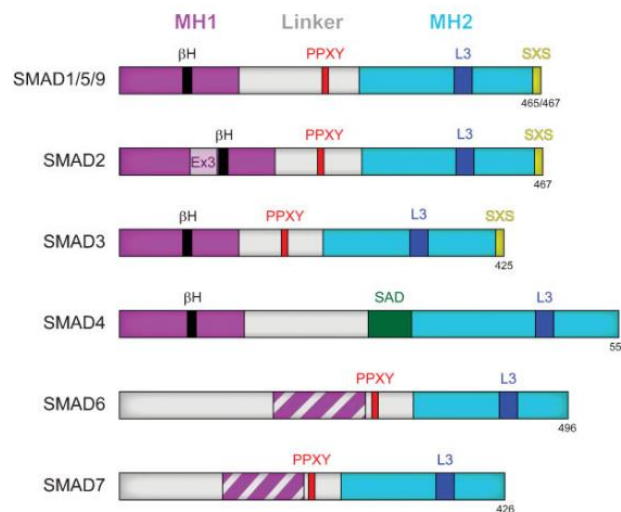


Figure 10: The structure of Smad proteins. Smads contain an MH1 and MH2 domain, which are connected via a proline-rich (PPXY) linker. I-Smads (Smad6/7) lack the MH1 domain (Weiss and Attisano, 2013).

Upon ligand binding to its respective receptor and receptor dimerization, the type I receptors phosphorylate R-Smads at their C-terminal SS(M/V)S motif. Hereby, the L45

loop of the respective type I receptors interacts with the L3 loop within the MH2 domain of Smads (Weiss and Attisano, 2013). Binding of R-Smads to the receptor is mediated by Smad anchor for receptor activation (SARA) (L. Attisano, 2001). Buwaneka *et al.* recently showed that Smad2 binds PIP2 in the plasma membrane via its MH2 domain. They demonstrate that PIP2 is enriched around the receptor complex and Smad2-PIP2 binding is required for Smad2 phosphorylation and thus activation (Buwaneka *et al.*, 2021).

Phosphorylated R-Smads form a complex with Smad4 in the cytoplasm and subsequently translocate into the nucleus to activate gene expression (Weiss and Attisano, 2013; Aashaq *et al.*, 2021). The R-Smad/Co-Smad complex is thought to exist as heterodimers or heterotrimers with a stoichiometry of R-Smads:Co-Smad 1:1 or 2:1 (Chacko *et al.*, 2001, 2004; Inman and Hill, 2002). Sanz *et al.* show the existence of three possible heterotrimer formation during neurogenesis of vertebrates, namely (1) Smad2-Smad2-Smad4, (2) Smad3-Smad3-Smad4, and (3) Smad2-Smad3-Smad4 heterotrimer, which target different DNA regulatory sequences (Míguez *et al.*, 2013; Sanz and Míguez, 2014).

DNA binding is mediated by the MH1 domain. Here, an eleven aa β -hairpin in the MH1 domain of Smad3 and Smad4 recognize the canonical Smad-binding element GTCT, which is directly or palindromic repeated *in vivo* to achieve Smad complex binding (Shi *et al.*, 1998; Hill, 2016). The low DNA binding affinity of Smads ($K_d \sim 1 \times 10^{-7}$ M) is compensated by the interaction with high-affinity DNA binding co-factors like Foxh1 (Fast-1), AP1 family (FOS, JUN), OCT4 or Sox2 (Hill, 2016). Smad-binding to the DNA leads to the recruitment of co-regulators, which can either be activators (e.g. CBP and p300) or repressors (e.g. p107, c-Ski and SKIL) (Akiyoshi *et al.*, 1999; Hill, 2016; Miller and Hill, 2023). The histone acetyl transferases CBP and p300 remodel the chromatin structure by

acetylating lysine-residues and thus making the DNA more accessible for transcription. On the other hand, p107, c-Ski, and SKIL associate with histone deacetylases to inhibit transcription.

Studies have shown that Smads regulate distinct sets of genes and can act independently of each other. For example, TGF β -induced MMP2 upregulation in human PTECs has been shown to be dependent on Smad2, but not on Smad3, whereas the expression of VEGF, which promotes angiogenesis, is Smad3-dependent (Phanish *et al.*, 2006). On the other hand, Smad2 and Smad3 were shown to gain oncogenic functions in the absence of Smad4, giving them the ability to promote cell migration and invasion by Rac1-dependent lamellipodia formation upon TGF β treatment in Smad4-deficient pancreatic cancer cells (Bertrand-Chapel *et al.*, 2022).

Smad signaling is regulated on several layers. I-Smads like Smad6/7 block Smad phosphorylation, complex formation, or DNA binding (Miller and Hill, 2023). I-Smads lack the C-terminal SSXS motif and bind to type I receptors to prevent R-Smad-receptor interaction (L. Attisano, 2001). Recruiting of Smurf1 and Smurf2, an E3 ubiquitin-protein ligase, to the TGF β receptors by Smad7 results in ubiquitination and degradation of R-Smad proteins (Zhang *et al.*, 2001; David and Massagué, 2018). Further posttranslational modifications like acetylation, which releases Smad from its inactive conformation (Hata *et al.*, 1997), PARylation, which releases Smad3/4 from DNA binding (Lönn *et al.*, 2010), and sumoylation, which stabilizes Smad4, have been also shown to play important roles in regulating Smad activity (Lee *et al.*, 2003).

1.3.2.2 Non-canonical TGF β signaling

Besides Smad signaling, TGF β activates several other cellular pathways like Erk, p38 MAPK, JNK or PI3K/Akt (Figure 11). The mitogen-activated protein kinase (MAPK) cascades are one of the major pathways activated by TGF β . Phosphorylation of a MAPK kinase kinase phosphorylates and activates a MAPK kinase, which in turn phosphorylates a MAPK (Gui *et al.*, 2012).

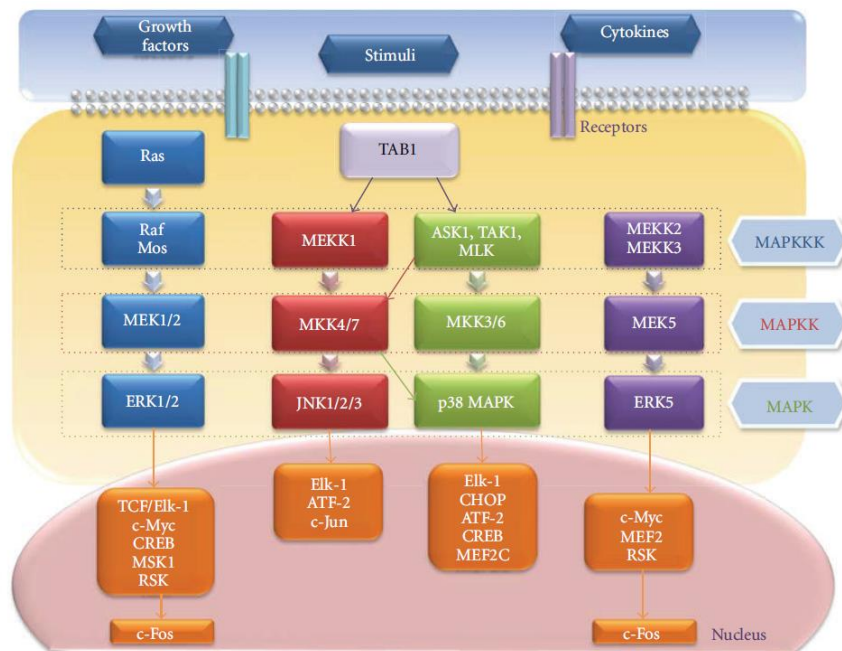


Figure 11: Non-canonical TGF β -signaling pathways. Besides Smads, TGF β has been shown to activate MAPK pathways Erk1/2, JNK, p38 MAPK and Erk5 (Gui *et al.*, 2012).

The TGF β receptors recruit Shc and Grb2 adaptor proteins to the plasma membrane to activate Ras GTPase and the downstream Raf-MEK-Erk signaling cascade (Zhang, 2009). To activate p38 MAPK or JNK, TGF β receptors recruit TRAF4 and TRAF6 and induce polyubiquitination at K63 (Deng *et al.*, 2024). This results in activation of TAK1 and several MAPKKs, like MKK3 and MKK6 to trigger p38 MAPK, or MKK4 to activate p38 MAPK and JNK. It was shown that TGF β activates p38 MAPK signaling within 15 min and inhibition of p38 MAPK blocked TGF β -induced EMT and impaired the migration

capacity of mammary epithelial cells (Bakin *et al.*, 2002).

PI3K/Akt signaling is also activated by TGF β -dependent TRAF6. PI3K is polyubiquitinated at its p85 α regulatory subunit by TRAF6 and can then phosphorylate PIP2 to PIP3 and subsequently activate Akt (Hamidi *et al.*, 2017).

Rho GTPase signaling via Rac1, Cdc42 or RhoA is also induced by TGF β to regulate actin cytoskeleton arrangement, cell migration, and EMT (Ungefroren, Witte and Lehnert, 2018).

The non-canonical TGF β signaling pathways interact with the canonical Smad pathway in a complex and context-dependent manner. For example it has been shown that TGF β activates JNK within 5 min of treatment, which in turn mediates Smad3 phosphorylation resulting in nuclear translocation (Engel *et al.*, 1999). On the other hand, Erk-dependent phosphorylation of linker region of Smad1, 2 and 3 inhibits nuclear translocation of Smad, giving a possible explanation why Ras-hyperactive cells might not respond to TGF β (Kretzschmar *et al.*, 1999).

Thus, the activation of several different but interacting pathways results in a vast variety of cellular response to TGF β treatment.

1.3.3 TGF β in cancer

TGF β has a dual role in cancer development. Whereas in premalignant stages, TGF β acts as a tumor suppressor, it switches to a tumor promoting role in late stages.

As suppressor, TGF β was shown to reduce cell proliferation by interfering with cell cycle progression from G1 to S phase by inhibiting CDK2 activity and to trigger apoptosis by e.g. inducing expression of pro-apoptotic protein Bim (Mazars *et al.*, 1995; Ramesh, Wildey and Howe, 2009). TGF β also inhibits expression of c-myc, an oncogene that acts

as a TF to trigger cell growth and differentiation (Chen *et al.*, 2002). In normal development, this is of utmost importance to control proper tissue formation, e.g., during mammary gland (MG) development.

Tumorigenic cell lines like MCF7, have been shown to lose responsiveness to TGF β by downregulating TGFBR2 to escape the growth inhibitory effects (Mazars *et al.*, 1995). Also, KD of TGFBR2 in cancer-associated fibroblasts (CAFs) enhanced MCF7 cell growth and gave rise to bigger primary tumors in xenograft models (Busch *et al.*, 2014). Mutations in TGFBR2, Smad2 or Smad4 have been observed in colorectal, gastric, pancreatic and ovarian cancer to inhibit TGF β signaling and overcome its suppressive function (Weiss and Attisano, 2013). Overexpression of TGF β or TGFBR reduces tumor progression in mammary epithelia (Pierce *et al.*, 1995).

On the other hand, TGF β switches to a tumor promoter predominantly by inducing EMT (see chapter 1.4.3), as well as by reducing the immune response of CD4⁺ T-cells (Liu *et al.*, 2020), acting as communicator between cancer and stromal cells (Liao *et al.*, 2024), and promoting angiogenesis, e.g. via endothelial-to-mesenchymal transition (EndMT) in breast cancer stem-like cells (Li *et al.*, 2022). TGF β 1 and TGF β 3 levels are enhanced in breast cancer tissues compared to normal breast tissue (Hachim *et al.*, 2018). In primary human mammary carcinomas, TGF β was shown to be highly expressed in the stroma close to the tumor edge and high TGF β staining correlated with an advanced and metastatic tumor stage (Dalal, Keown and Greenberg, 1993).

Studies using four cell lines derived from the normal human mammary epithelial cell line MCF10A resembling increasing stages of cancer development (M1-M4) demonstrated the tumor suppressing role of TGF β 1 in the less malignant cell lines M2 and M3, but clearly

showed a metastasis promoting role in the highly malignant M4 cell line (Tang *et al.*, 2003; Sato *et al.*, 2014). KD of Smad3 in M3 cells and subsequent orthotopic implantation in mice resulted in increased tumor formation, while KD of Smad2 did not alter the tumor formation, suggesting that Smad3 is responsible for the tumor suppressing role of TGF β 1 in M3 cells (Sato *et al.*, 2014). Wiercinska *et al.* showed that 5 ng/mL TGF β 3 induces invasion of MCF10A-M1 cells embedded in a 3D collagen/methylcellulose matrix and further increases invasion of M2 cells (Wiercinska *et al.*, 2011). They observed that the invasion was TGF β 3-Smad3/4-dependent, which induced the expression of MMP2 and MMP9. Inhibition of MMPs using GM6001 significantly reduced TGF β 3-mediated invasion (Wiercinska *et al.*, 2011). Kim *et al.* reported a TGF β 1-p38 MAPK-dependent upregulation of MMP2 and MMP9 (Kim, Kim and Moon, 2004).

Thus, *in vivo* and *in vitro* studies demonstrate the dual nature of TGF β in cancer progression.

1.3.4 TGF β 1 induced KANK4 expression

The influence of TGF β 1 on gene transcription has been widely studied in different established cell lines. Several projects focus on the altered gene expression upon TGF β 1 treatment. These whole cell genome-based approaches further elucidate the influence of TGF β 1 on promoting migration and invasion by upregulating related genes. Treatment of MCF10A cells with 5 ng/mL TGF β 1 for up to three days revealed an upregulation of 1166 genes using RNA sequencing, with the majority being associated with FAs, as well as cancer-regulating and actin-cytoskeleton controlling pathways (Liu *et al.*, 2019). Interestingly, they identified KANK4 as one of the strongest induced proteins showing a 40-fold increase in expression after 24, 48, and 72 hours of TGF β 1 treatment, whereas

KANK2 only showed a 1.7-fold increase after 24 and 48 hours of TGF β 1 treatment (Liu *et al.*, 2019). KANK1 and KANK3 were not detected. Similar, Du *et al.* observed KANK4 upregulation in TGF β 1/OSM (10 ng/mL and 50 ng/mL) treated MCF10A cells after seven days via microarray-based gene expression profiling (Du *et al.*, 2016). KANK4 was among the top three genes with a fold change of >200, which expression was significantly induced by TGF β 1 (Du *et al.*, 2016). By treating MCF10A cells with several different ligands (EGF, HGF, OSM, IFN γ , TGF β , and BMP2) for 24 and 48 h, Gross *et al.* performed a multi-omic analysis to map differentially regulated proteins (Gross *et al.*, 2022). RNAseq data showed that KANK4 was significantly upregulated upon treatment with the TGF β -superfamily members BMP2 and TGF β 1 with a fold change of 5, but not upon treatment with the other ligands (Gross *et al.*, 2022). Further evidence of TGF β 1-dependent KANK4 upregulation is provided by Sato *et al.*, which performed promoter-wide chromatin IP in four MCF10A-related Ras-transformed cell lines (M1-M4) (Strickland *et al.*, 2000; Santner *et al.*, 2001) using a Smad3 antibody to identify genes targeted by TGF β 1-Smad3 (Sato *et al.*, 2014). By comparing TGF β 1-untreated and treated cells they found 404 TGF β 1-Smad3-specific regulated genes among the four cell lines, with only 9% of these genes being commonly found in all four cell lines. KANK3 and KANK4 were both detected in all cell lines as TGF β 1-Smad3 regulated genes (Sato *et al.*, 2014). These genome-wide studies consistently demonstrate the correlation between TGF β 1 signaling and KANK4 expression in MCF10A cells.

1.4 Epithelial-to-mesenchymal transition (EMT)

The concept of EMT was first introduced in 1968, when Elisabeth Hay characterized the EMT process in remodeling epithelial tissues during chick embryogenesis and soon the

possible consequences of EMT in a pathological context, e.g. for invading carcinoma cells, were discussed (Hay, 1968, 1995). Since then, EMT has been of wide interest and many publications have aimed to further understand the EMT process in a variety of different contexts. Broadly speaking, EMT is necessary for cells to acquire the ability to disseminate and migrate into distant tissue. It describes the highly dynamic conversion of cobblestone and non-motile epithelial cells into spindle-like and highly motile mesenchymal cells. These changes are driven by the expression of EMT-related pleiotropic transcription factors (EMT-TF), which either directly or indirectly regulate the downregulation and upregulation of epithelial and mesenchymal genes, respectively (Figure 12). Due to the variety of contexts and outcomes, in which EMT was observed, one distinguishes between three different classes of EMT: (1) Type 1 EMT is related to normal embryogenesis, which is essential during development to form mesenchymal cells. (2) Type 2 EMT is observed in the context of wound healing and tissue regeneration. (3) Type 3 EMT describes tumor development and is required for establishing an invasive phenotype leading to distant metastasis formation (Kalluri and Weinberg, 2009; Thiery *et al.*, 2009). Although EMT is observed in different contexts, the underlying mechanism is similar and no difference between developmental- and cancer-related EMT is observed.

EMT is not a one-way, but rather a highly dynamic process. Indeed, complete conversion of epithelial cells into mesenchymal cells is hardly observed. This dynamic is reflected in the term partial EMT plasticity, indicating that cells show both epithelial and mesenchymal markers (Stemmler *et al.*, 2019; Brabletz *et al.*, 2021). The EMT plasticity is necessary for the cells to perfectly adapt to their changing microenvironments.

Due to the inflationary use of the term "EMT" in research, several authors wrote a

consensus statement in 2020 with the aim to correctly define EMT (Yang *et al.*, 2020). They recommend using several molecular markers to check EMT-signaling, EMT-TFs and mesenchymal or epithelial cell state. Additionally, the gene expression profile of a cell has to be complemented with morphological analysis, to confidently describe EMT (Yang *et al.*, 2020).

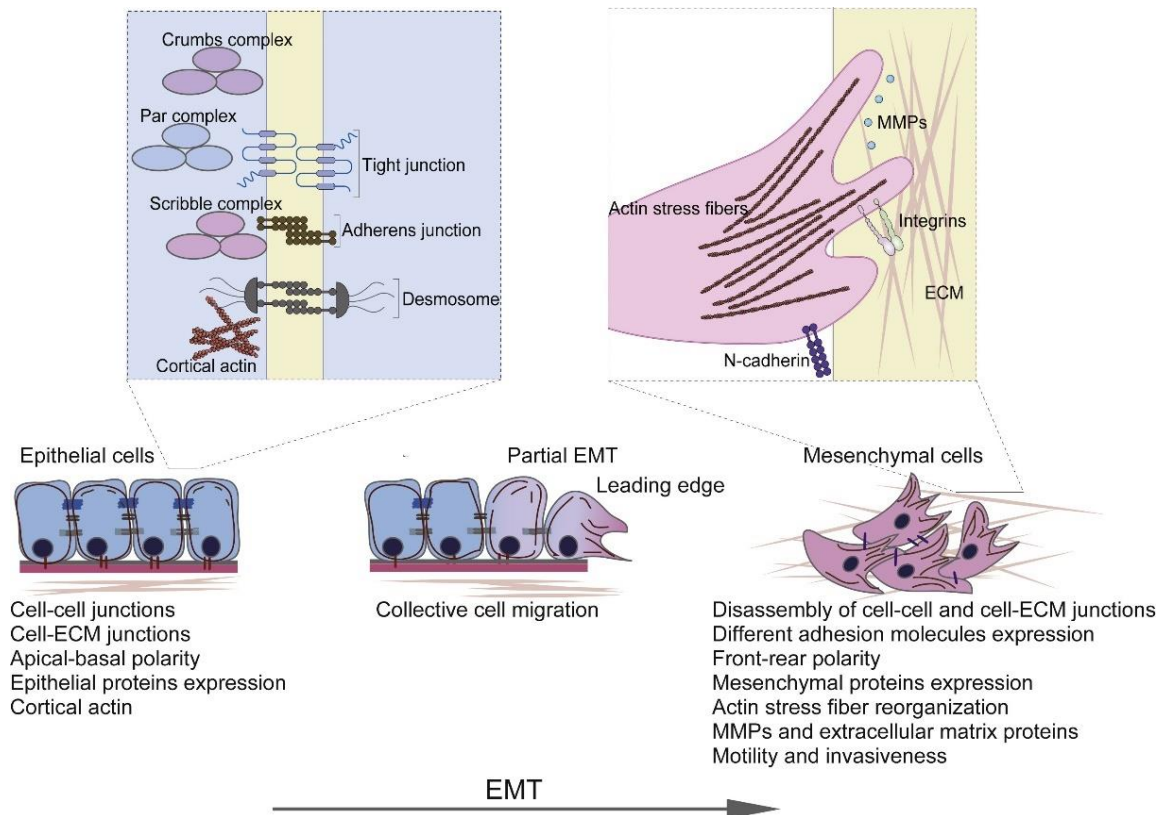


Figure 12: The EMT process. Expression of EMT-TFs induces morphological changes, enhances the expression of mesenchymal proteins, and represses epithelial proteins (Katsuno and Derynck, 2021).

1.4.1 EMT-TFs

EMT is characterized by the upregulation of a core set of TFs. The major EMT-TFs are Snail, Zeb and Twist (Figure 13), which also crosstalk to induce or repress the expression of each other. The pleiotropic functions of EMT-TFs are related to maintenance of stemness properties, tumorigenicity, dsDNA repair, proliferation, cytokine upregulation and escape from senescence (Brabletz *et al.*, 2018). The induction of EMT-TF expression

is triggered by growth factors like HGF, EGF, PDGF, or TGF β secreted by stroma cells, as well as other factors like hypoxia, UV-light, tension and shear stress force (Kalluri and Weinberg, 2009; Stemmler *et al.*, 2019).

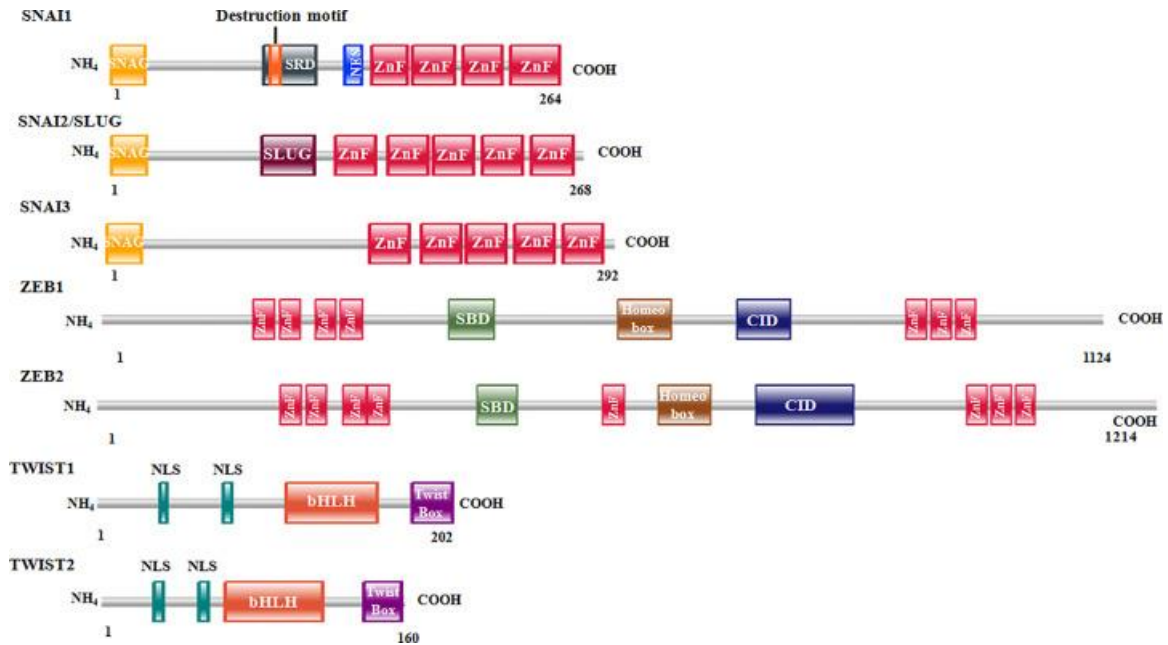


Figure 13: EMT-TFs. The master regulators of EMT are the Snail family (Snai1, Snai2/Slug, Snai3/Smuc), Zeb homeobox family (Zeb1, Zeb2), and TWIST family (Twist1, Twist2) (Debnath *et al.*, 2021).

EMT-TFs regulate the suppression of epithelial proteins like E-Cadherin (E-Cad), claudin, or occluding and the induction of mesenchymal proteins like N-Cadherin (N-Cad), vimentin and fibronectin. EMT-TFs can either directly or indirectly regulate the expression of E-Cad: Directly regulating TFs belong to the Snail and Zeb family and bind to the E-box (CAGGTG) in the E-Cad promoter to repress activity, whereas indirectly regulating TFs are Twist, GSC, SIX1, E2.2 and FOXC2 (Thiery *et al.*, 2009; Puisieux, Brabletz and Caramel, 2014).

It has been shown that expression of the EMT-TFs Snail or Twist in HMLE cells leads to stem-cell-like features like high CD44 and low CD24 expression (Mani *et al.*, 2008). EMT-undergoing cancer cells induced by Snail or Twist showed increased tumorigenicity and

stemness, determined by soft agar and tumor sphere assay, respectively (Mani *et al.*, 2008). The three main EMT-TFs will be described in the following.

1.4.1.1 Snail family

The Snail family consists of three members in vertebrates, namely Snail, Slug and Smuc. They are zinc finger proteins, containing one zinc finger cluster (Figure 13). Snails are important for embryonic development, as Snail-deficient mouse embryos display impaired mesodermal germ layer formation due to retained E-Cad expression and are embryonically lethal at E8.5 (Carver *et al.*, 2001). Slug is expressed in migrating neural crest cells and epiblast cells of chick embryos before mesenchymal cells arise, suggesting a role of Slug in EMT (Nieto *et al.*, 1994). First studies on Slug showed that FGF-1 treatment of NBT-II cells upregulates Slug within three hours and Slug expression results in less cell-cell contacts and reduced desmosome formation, inducing the first step of EMT (Savagner, Yamada and Thiery, 1997). Slug is expressed in myoepithelial cells of normal MG. Transient co-expression of Slug together with Sox9 induces mammary stem cell differentiation of luminal cells, resulting in the ability to form complete MGs in fat pads, highlighting Slug's function in stemness (Guo *et al.*, 2012).

It was shown that Snail and Slug bind to the E-pal element of the E-box motif in the promoter of E-Cad. This inhibited E-Cad expression and resulted in a spindle-like cell morphology and enhanced migration of MDCK cells (Bolós *et al.*, 2016). Snail was detected in invasive carcinoma cell lines that lack E-Cad expression, and inhibition of Snail restores E-Cad expression (Batlle *et al.*, 2000; Cano *et al.*, 2000). The Snail family was linked to EMT in cancer, invasiveness and tumor aggressiveness.

1.4.1.2 Zeb homeobox family

The Zeb homeobox family consists of two members, namely Zeb1 and Zeb2, which are zinc finger and E-box binding proteins. The function of Zeb1 in tumor development is very well studied and Zeb1 expression correlates with poor patient outcome. Zeb1 is expressed in response to TGF β , TNF α and IGF1 (Andrews, Kim and Hens, 2012) and interacts with histone acetyltransferase p300/pCAF or Smads to regulate gene expression (Stemmler *et al.*, 2019). Gene profiling of NSCLC cell lines expressing Zeb1 showed that vimentin and N-Cad were significantly upregulated, while E-Cad was downregulated (Gemmell *et al.*, 2011). Zeb1 directly binds to two E-boxes of the E-Cad promoter via its two zinc finger clusters (Figure 13), repressing the expression of E-Cad (Grooteclaes and Frisch, 2000). Zeb1 is not only induced in EMT undergoing tumor cells, but is also expressed in tumor stroma to further promote cancer formation. Fu *et al.* showed that Zeb1 levels were significantly increased in tumor compared to normal stroma of luminal, HER2⁺ and triple-negative tumor samples and high stromal Zeb1 expression was related to poor patient outcome (Fu *et al.*, 2019). Deletion of Zeb1 in the stroma of MMTV-PyMT tumor mice delayed tumor onset reduced tumor growth, as well as impaired formation of CK14⁺ invasive cell strands (Fu *et al.*, 2019).

1.4.1.3 TWIST family

The TWIST family consists of Twist1 and Twist2 and is part of the basic-helix-loop-helix (bHLH) family (Figure 13). As a dimer, Twist can bind two E-box sequences with a distance of five nucleotides (Stemmler *et al.*, 2019).

In cancer, Twist was associated with EMT and metastasis formation, as it is strongly upregulated in invasive cell lines and inhibition of Twist reduced the amount of circulating

tumor cells (CTCs) and the metastatic potential of 4T1 cells injected into the fat pad of mice (Yang *et al.*, 2004). In patients, high Twist expression correlated with reduced E-Cad expression and more invasive tumor state (Yang *et al.*, 2004). However, downregulation of Twist and subsequent mesenchymal-to-epithelial transition (MET) were important for metastasis formation. Twist was also shown to inhibit tumor suppressive programs by interacting with p53 and promote p53 degradation (Puisieux, Brabletz and Caramel, 2014).

1.4.2 EMT in cancer

Type 3 EMT is related to cancer and undergoing EMT is associated with poor patient outcome due to a highly progressive and invasive phenotype. EMT gives the cancer cells the required plasticity to optimally adapt to tumorigenic microenvironments. The major role of EMT during cancer development is its function in metastasis formation. The invasion-metastasis cascade can be divided into five steps (Figure 14) (Scheel and Weinberg, 2012): (1) Invasion – Here, primary tumor cells undergo (partial) EMT to gain migratory capacities by reduced E-Cad expression and to be able to escape the primary tumor site. (2) Intravasation and (3) systemic dissemination – The CTCs intravasate into the lymphatic and blood system and are transported through the body. (4) Extravasation – At distant sites, the tumor cells extravasate the vasculature. (5) Colonization – The cancer cells must adapt to the new microenvironment to successfully form metastases.

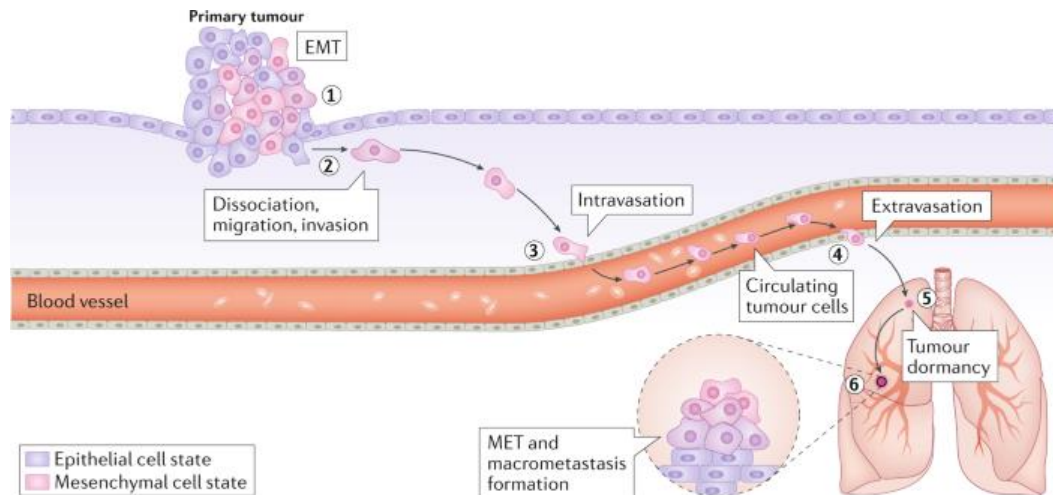


Figure 14: The invasion-metastasis cascade. Tumor cells disseminate from the primary tumor (1), dissociate (2), intravasate into the blood circulation (3), extravasate at distant sites (4) and colonize to form secondary tumors (5, 6) (Yang *et al.*, 2020).

An important marker for EMT is the downregulation of E-Cad. E-Cad interacts with β -catenin, which stabilizes the polarized epithelial cell morphology and enables the formation of normal epithelial architecture (Andrews, Kim and Hens, 2012). β -catenin hereby connects the cytoplasmic tail of E-Cad with the actin cytoskeleton through which the nuclear translocation of β -catenin and the transcription of downstream genes of Wnt signaling like FGF are prevented (Andrews, Kim and Hens, 2012).

E-Cad suppression during EMT correlates with the upregulation of the non-epithelial cadherin N-Cad. Association of N-Cad with FGFR has been shown to prolong FGF-mediated activation of MAPK/Erk pathway, which induces MMP9 expression and results in enhanced cell motility (Nieman *et al.*, 1999; Hazan *et al.*, 2000; Cavallaro *et al.*, 2001). Expressing N-Cad in MCF7 cells showed increased migration and invasion compared to E-Cad expressing MCF7 cells and also formed more metastases when transplanted into mammary fat pad of mice (Hazan *et al.*, 2000).

Several studies demonstrate the importance of EMT, but also MET for the formation of metastases: Here, cells need to regain epithelial characteristics to enable proper

colonization (Brabletz *et al.*, 2018; Eichelberger *et al.*, 2020). Additionally, KD of E-Cad in a non-migrative cell population significantly reduced metastases formation, whereas over-expression of E-Cad in migrative cell population increased metastases formation by promoting the clustering of CTCs (Hapach *et al.*, 2021).

Nevertheless, the role of EMT in invasion is not uncontroversial. Indeed, EMT *in vivo* is rarely detected. Mouse models have been established to track EMT undergoing cancer cells using a fluorescent color-switching system in breast cancer mice (Fischer *et al.*, 2015; Li *et al.*, 2020; Lüönd *et al.*, 2022). Fischer *et al.* generated an EMT reporter mouse in the MMTV-PyMT breast cancer model using Fsp1 as EMT marker to challenge the importance of EMT in metastases formation (Fischer *et al.*, 2015). They introduced an RFP-GFP Cre-switchable fluorescent marker to label cancer cells and introduced Cre recombinase behind the Fsp1 promoter. Upon Fsp1-Cre expression in EMT undergoing cells, Cre alters the RFP to GFP expression, providing a convenient EMT-tracking system. At the primary tumor site, only 2% of cells underwent EMT, whereas lung metastases did not show any EMT event. Additionally, inhibition of EMT using miR-200 did not alter lung metastases incidences, suggesting an EMT-independent metastases formation. Instead they found an increased resistance of EMT-undergoing cells to chemotherapy (Fischer *et al.*, 2015). The study was promptly criticized by leading scientists of the field, who questioned the suitability of the used mouse model as well as miR-200 as efficient EMT inhibitor (Ye *et al.*, 2017).

Lüönd *et al.* established two mouse lines that carry either GFP-tagged Tenascin C or N-Cad as indicators for partial EMT or full EMT, respectively (Lüönd *et al.*, 2022). Initially, PyMT-transformed cancer cells are labelled with mCherry upon Tamoxifen application.

Cells that undergo EMT start to express Tenascin C or N-Cad, leading to an irreversible fluorescent switch from red to green. Interestingly, whereas partial EMT was observed in all tumor stages, full EMT only occurred in 0.002% of cancer cells, indicating the low frequency of full EMT *in vivo* (Lüönd *et al.*, 2021). Partial EMT undergoing cells had a mesenchymal morphology, migrated collectively with cancer cells and formed invasive protrusions as leader cells in a 3D collagen I matrix. Full EMT undergoing cells also had a mesenchymal morphology but were less migrative, migrated as mesenchymal single-cells, and showed impaired invasion in 3D (Lüönd *et al.*, 2021). TGF β -induced EMT *in vitro* induced partial EMT in 90% of cells, whereas full EMT was induced in only 30% of the cells after 20 days of treatment. Finally, partial EMT undergoing cells showed higher potential to form lung metastasis compared to full EMT undergoing cells, demonstrating the importance of EMT plasticity for cell survival at distant sites (Lüönd *et al.*, 2021).

By labelling PyMT-transformed luminal cancer cells with ZsGreen and using tdTomato-labelled vimentin (full EMT) or N-Cad (partial EMT) as EMT markers, Li *et al.*, detected that around 2-10% of cancer cells undergo EMT at late stages of tumor (Li *et al.*, 2020). The authors demonstrate the importance of N-Cad, but not vimentin, in lung metastasis, as KO of N-Cad decreased metastasis formation (Li *et al.*, 2020).

1.4.3 TGF β -induced EMT

TGF β is a well-known inducer of EMT. By activating the EMT program via canonical and non-canonical signaling pathways in cancer cells, TGF β exerts its tumor promoting functions and enhances cell migration capacity.

Depletion of Smad signaling was shown to prevent TGF β -induced EMT (Xu, Lamouille and Derynck, 2009). Giampieri *et al.* showed via pSmad3 staining in human breast cancer

tissues that TGF β signaling pathway was heterogeneously active especially at tumor edges *in vivo*. Furthermore, they demonstrated that Smad2 was predominantly cytoplasmic in non-moving or collectively moving cells, whereas individually moving cells showed nuclear Smad2 together with an enhanced TGF β -dependent transcription (Giampieri *et al.*, 2009). Cell-based experiments using MTLn3 cells showed that TGF β 1 induced single-cell movement in these otherwise collectively migrating cells and enhanced actin stress fiber formation. Individually migrating cells were more efficiently entering the blood circulation, compared to collectively migrating cells, but showed a diminished capacity to form lung metastases (Giampieri *et al.*, 2009).

Beside Smad, TGF β was shown to activate MAPK pathways, Rho GTPases and PI3K/Akt signaling, promoting EMT by rearranging the actin cytoskeleton, cell survival and invasion (Xu, Lamouille and Derynck, 2009).

MCF10A cells are widely used to study TGF β -induced EMT (Kim, Kim and Moon, 2004; Djomehri *et al.*, 2019). Here, cells treated with TGF β 1 start to express N-Cad, vimentin and PAI-1 within 48 h, show enhanced Erk signaling, upregulated MMP2/9 secretion and invade into a Matrigel-coated transwell chamber (Mori *et al.*, 2015). Cells respond to TGF β with morphological changes, upregulation of EMT-TFs Snail and Zeb1 as well as mesenchymal markers like vimentin (Zhang *et al.*, 2014). Cells could either enter a reversible partial- or irreversible full-EMT state, depending on TGF β concentration (Zhang *et al.*, 2014).

1.5 Rho GTPase family

The family of Rho GTPases consists of 20 members with the most prominent members being RhoA, Rac1 and Cdc42. Characteristic for all the members is their regulation via

guanine nucleotide-exchange factors (GEFs) and GTPase-activating proteins (GAPs). GEFs induce the exchange of GDP (inactive form) with GTP (active form), resulting in activation of the small GTPases and their downstream signaling pathways. GAPs on the other hand result in inactivation of the small GTPases by enhancing the intrinsic GTP hydrolysis rate to convert GTP to GDP (Hodge and Ridley, 2016). Guanine nucleotide dissociation inhibitors (GDIs) inhibit GTPase activation by preventing membrane translocation or GEF activation. Rho GTPases are posttranslationally modified by lipids, phosphorylation, sumoylation or ubiquitination, to regulate membrane localization, activation or degradation.

Rac1 binds and hydrolyses GTP via its N-terminal G-domain. The G-domain contains two switches (I and II), which undergo conformational changes to either promote the GTP- or GDP-binding of Rac1. The C-terminal region of Rac1 enables the subcellular localization to the plasma membrane. Here, the CAAX motif undergoes three subsequent posttranslational modifications, which increase the hydrophobicity and thus facilitate interaction with the plasma membrane: (1) isoprenylation of the cysteine-residue, (2) endoproteolytic cleavage of the AAX motif, and (3) methylation of the prenylated cysteine (Ma *et al.*, 2023).

Rho GTPases are involved in cell contractility, actin cytoskeleton rearrangement and cell migration.

1.5.1 Cdc42, Rac1 and RhoA in filopodia, lamellipodia and invadopodia formation

Cdc42, Rac1 and RhoA have essential functions in development and are ubiquitously expressed. KO of Cdc42 or Rac1 in mice are embryonically lethal and embryos die around E7.5 and E9.5, respectively (Sugihara *et al.*, 1998; Chen *et al.*, 2000). Conditional KO of

RhoA in neuroepithelial cells of the spinal cord results in late embryonic stage lethality (Herzog *et al.*, 2011).

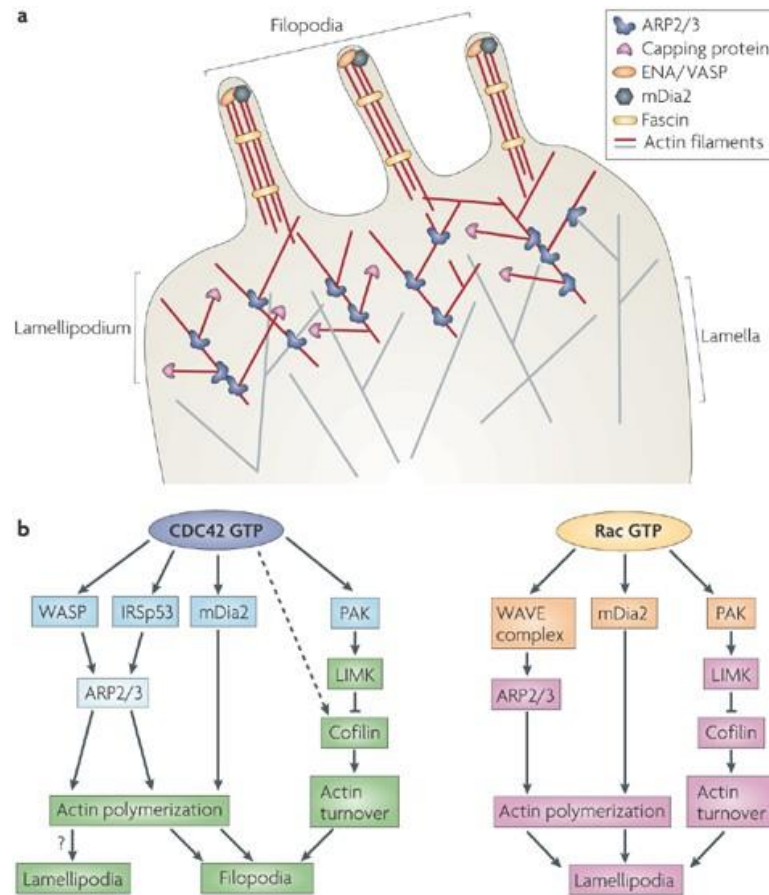


Figure 15: Lamellipodia and filopodia formation. Cdc42 is important for filopodia formation, whereas Rac 1 regulates lamellipodia formation (Heasman and Ridley, 2008).

Cdc42 is important in filopodia formation, thin actin-rich and finger-like protrusions at the leading edge of migrating cells (Figure 15). In filopodia, the F-actin is arranged in tight parallel bundles, with the barbed ends facing the plasma membrane (Théry and Blanchoin, 2024). F-actin polymerization results in protrusion formation and cell migration (Mattila and Lappalainen, 2008). The antennae-like structures are useful tools to sense the microenvironment via integrins and facilitate directed cell migration. Besides integrins, filopodia contain actin-regulating proteins like Ena/VASP proteins, formins, myosin X, fascin and I-BAR domain proteins, which all regulate filopodia formation (Mattila and

Lappalainen, 2008). In NAs forming in filopodia tips, integrins assemble talin, FAK and paxillin to eventually mature into FAs and strengthen adhesions. Cdc42 interacts with WASP and N-WASP or IRSp53 to activate Arp2/3 and stimulate actin nucleation and branching. Via the formin mDia2, Cdc42 regulates polymerization of unbranched actin. Inhibition of Cdc42 activity impairs filopodia formation, cell spreading and migration (Heasman and Ridley, 2008).

Filopodia can convert into lamellipodia, which requires integrin-mediated adhesions and Rac1 activity (Figure 15) (Guillou *et al.*, 2008). Lamellipodia are sheet-like actin filament-based protrusions with a diameter of 0.1-0.2 μm , which extend 2-4 μm at the leading edge of migrating cells (Pollard and Borisy, 2003). The actin network is branched and equal to filopodia, the barbed ends face the plasma membrane (Théry and Blanchoin, 2024). Formin-mediated stress fiber formation at the back of lamellipodia, consisting of actin and myosin bundles, generates contractile forces, required for cell migration (Mattila and Lappalainen, 2008). Rac1 binds to the WAVE regulatory complex subunit Sra1 in the lamellipodia tip (Chen *et al.*, 2017; Mehidi *et al.*, 2019). WAVE2 then interacts with the actin nucleation complex Arp2/3 to facilitate actin stress fiber formation (Paňková *et al.*, 2010). Additionally, Rac1 removes capping proteins that prevent actin polymerization and inhibits cofilin-mediated severing of actin filaments (Heasman and Ridley, 2008). Inhibition of Rac1 impairs lamellipodia formation and membrane ruffling.

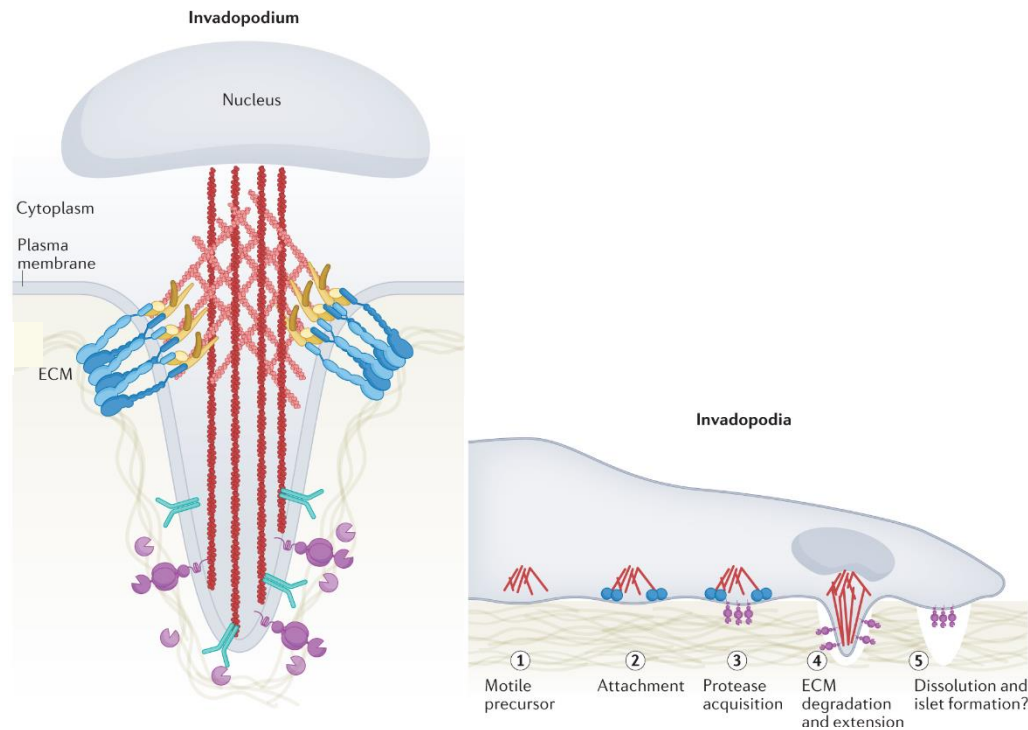


Figure 16: The structure of invadopodia. The invadopodia core contains unbranched actin filaments which are connected to the ECM via integrins (left panel). Invadopodia formation occurs in several steps (right panel) (adapted from Linder *et al.*, 2023).

Invadopodia are matrix degrading structures predominantly formed by cancer cells for invasion and are essential for metastasis formation (Figure 16) (Yamaguchi, 2012). In contrast to filopodia and lamellipodia, invadopodia facilitate invasion through the basement membrane (Krause and Gautreau, 2014). Invadopodia localize close to the nucleus, from which they acquire mechanical stability by pushing against the nucleus (Revach *et al.*, 2015), have dot-like shapes and can last from several minutes to hours. Invadopodia formation can be triggered by growth factors like TGF β , EGF, or TNF, which induces the attachment of a branched actin precursor to the plasma membrane via TKS5-binding to PIP2. The invadopodia core contains unbranched actin filaments, which are anchored to the ECM via adhesion rings containing integrins, FAK, paxillin, vinculin and ILK. The adhesion rings form shortly after invadopodia initiation and are essential for invadopodia maturation and proteolytic activity (Branch, Hoshino and Weaver, 2012).

Inhibition of FAK, for example, was shown to impair invadopodia formation and matrix degradation (Pignatelli *et al.*, 2012). Secretion of MMPs, like MMP2, MMP9, and MMP14, ADAM, and serine proteases allow the degradation of ECM proteins like collagen, gelatin, fibronectin or laminin, enabling further extension of the protrusion into the matrix (Revach *et al.*, 2016; Linder *et al.*, 2023). Cdc42 activates WASP/Arp2/3 actin polymerization and branching in the invadopodia core (Yamaguchi *et al.*, 2005). TGF β treatment of MCF10A cells enhanced formation of invadopodia and gelatin degradation (Pignatelli *et al.*, 2012). Functional blocking analyses with chemical inhibitors (Rac1) or siRNA-mediated KD (RhoA) suggested that Rac1 but not RhoA is required for TGF β -mediated invadopodia formation and matrix degradation (Pignatelli *et al.*, 2012). In contrast, using a Rac1-FRET biosensor, it was shown that Rac1 is active during invadopodia disassembly via a TrioGEF-Rac1-Pak1 cascade, suggesting that Rac1 is important for invadopodia turnover (Moshfegh *et al.*, 2014). RhoA is required for MMP exocytosis in invadopodia (Alexander *et al.*, 2008; Jerrell and Parekh, 2014). Enhanced myosin II activity via Rho-ROCK signaling increases actomyosin contractility, which promotes ECM degradation (Alexander *et al.*, 2008). Altogether, small GTPases are important for the formation of adhesive and protrusive structures, which is relevant in cell migration and invasion.

1.6 Coronin

Coronins were identified as actin-myosin binding proteins in *Dictyostelium discoideum*, localizing to crown-shaped and F-actin containing lamellipodia, giving it the name coronin (de Hostos *et al.*, 1991). Seven mammalian Coronin genes are known: Coro1A, Coro1B, Coro1C, Coro6, Coro2A, Coro2B, and Coro7 (Chan, Creed and Bear, 2011). They are divided into three types, Type I, II and III. Structurally similar, they contain N-terminal

β -propeller-like WD40 repeats and C-terminal coiled-coil domains, which are connected via a unique region (Figure 17). Type III Coronins (Coro7) differ structurally, as they lack the coiled-coil domain, but possess two β -propeller domains. Much less is known about type II Coronins that include Coro2A and Coro2B. Coro1A, as well as Coro1B, are type I Coronins, which interact with the F-actin cytoskeleton and the Arp2/3 complex via their β -propeller and coiled-coil domain, respectively (Humphries *et al.*, 2002). Especially the conserved residue R30 in the β -propeller was shown to be essential for F-actin binding of Coro1A, 1B and 1C (Chan, Creed and Bear, 2011).

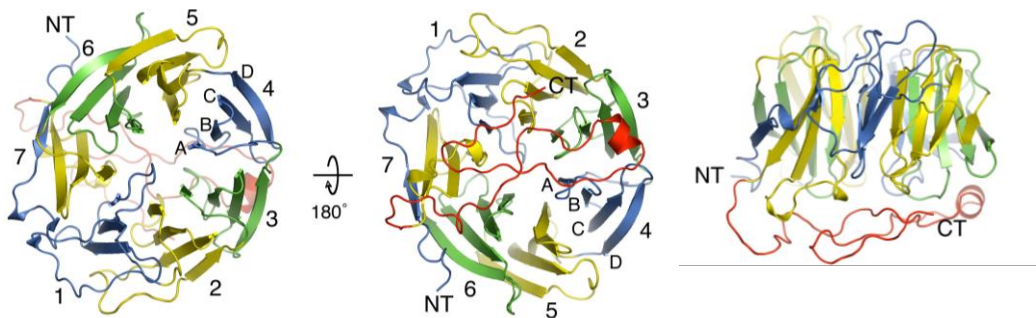


Figure 17: Structure of Coronin. Coronins contain seven N-terminal β -propeller-like WD40 repeats and C-terminal coiled-coil domains (Appleton, Wu and Wiesmann, 2006).

1.6.1 Coro1A

Coronins are involved in actin depolymerization by enhancing the severing activity of cofilin. During actin assembly, profilin induces a nucleotide exchange from ADP to ATP G-actin to facilitate the formin-mediated actin nucleation, which assembles the actin filament in length by blocking the capping at the plus end (barbed end). The actin nucleator complex Arp2/3 enables branching of the actin filaments by mimicking an actin dimer or trimer and thus serving as template for further nucleation (Goley and Welch, 2006; Ben Zablah, Merovitch and Jia, 2020). Cofilin, as an actin-depolymerizing protein, mediates actin filament severing by binding to ADP-actin filaments. Additionally, cofilin regulates

debranching of Arp2/3 nucleated filaments. Coronins might promote cofilin's severing function, by inducing a conformational change in F-actin so that the nucleotide-binding cleft of actin switches to an open position, which enhances cofilin binding to F-actin (Mikati *et al.*, 2015). In yeast, it was shown that Coro1A regulates cofilin depending on the nucleotide state of actin-filaments (Gandhi *et al.*, 2009). The authors show that Coro1A antagonizes the cofilin-mediated disassembly of ATP/ADP+P_i-actin, but promotes cofilin severing of ADP-actin. By binding to actin via its coiled-coil domain, additionally to the β -propeller, Coro1A competes with cofilin for actin binding and does so more effectively for ATP/ADP+P_i-actin compared to ADP-actin. Off note, this additional actin-binding site in yeast has not been confirmed.

Coro1A directly binds the p35 subunit of Arp2/3 via its coiled-coil domain to impair Arp2/3 function by locking the complex in an open conformation (Rodal *et al.*, 2005). The interaction of yeast Coro1A and Arp2/3 complex results in inhibition of the Arp2/3 activity in a Coro1A-concentration-dependent manner (Humphries *et al.*, 2002; S.-L. Liu *et al.*, 2011). Low Coro1A concentrations resulted in activation of Arp2/3 to increase filament binding. High Coro1A concentrations on the other hand resulted in inhibition of Arp2/3 to abolish filament binding and thus inhibits filament branching in budding yeast (S.-L. Liu *et al.*, 2011).

The proper localization of Coro1A to the plasma membrane is mediated by Coro1A binding to PIP₂ at the plasma membrane (Tsujita *et al.*, 2010). Coro1A then dissociates from PIP₂ in order to disassemble actin branches and to increase actin-cytoskeleton turnover. This disassembly is essential for efficient lamellipodia formation.

It was shown that Coro1A interacts with the β subunit of β_2 integrins in HL-60 cells and

colocalizes to cortical F-actin cytoskeleton to enable rolling leukocyte adhesion, LFA-1 clustering and F-actin accumulation (Pick *et al.*, 2017; Thome *et al.*, 2018). Coro1A was found to interact with actin-crosslinking filamins in HL-60 cells, but neither the interaction, nor filamins were essential for proper cell migration, spreading, or adhesion (Roth *et al.*, 2017).

Via genome-wide functional screens using HEK293T-cells as well as IF stainings of GFP-tagged Coro1A overexpressing COS1 cells, Coro1A was identified as a Rac1 translocating protein to the plasma membrane (Figure 18) (Castro-Castro *et al.*, 2011). Ectopic expression of GFP-tagged Coro1A enhanced endogenous Rac1 levels in the membrane fractions of COS1 cells, as well as in Rac1-rich lamellipodia (Castro-Castro *et al.*, 2011, 2016). Off note, an influence of Coro1A on the translocation of RhoA or Cdc42 to the plasma membrane was not observed (Castro-Castro *et al.*, 2011). Interestingly, expression of Coro1A did not only affect Rac1 localization, but also enhanced its activity, shown by a GFP-tagged RBD-Pak1 bioreporter assay and active Rac1 pulldowns in response to EGF stimulation. It was suggested that Coro1A interacts with WDR26, ArhGEF7 and Pak1 to mediate Pak1-dependent phosphorylation of RhoGDI α . This induces the dissociation of RhoGDI α and Rac1 to enhance Rac1 activity by GDP-GTP exchange (Castro-Castro *et al.*, 2011, 2016). Coro1A's function of regulating Rac1 was demonstrated to be dependent on Coro1A binding to F-actin. Deficiency of Coro1A additionally reduced EGF-induced lamellipodia formation (Castro-Castro *et al.*, 2011). The importance of Coro1A in Rac1 translocation and activation was also shown in rat hippocampal neurons. Here, Coro1A interacts with the membrane glycoprotein Gpm6A and Rac1, and, together with Rac1

downstream effector Pak1, ensures proper Gpm6A-induced filopodia formation (Alvarez Juliá, Frasch and Fuchsova, 2016).

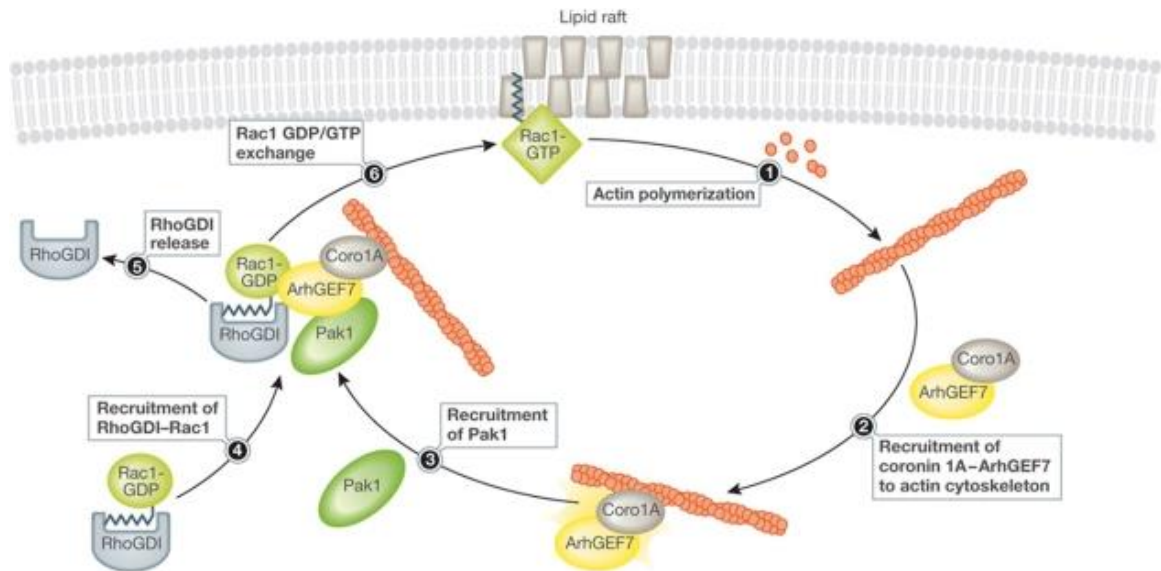


Figure 18: Rac1 activation by Coro1A. Coro1A directly binds actin filaments and recruits Pak1 to translocate and activate Rac1 by releasing Rac1 inhibitor RhoGDI α (Symons, 2011).

The human Coro1A gene locus on chromosome 16 is highly associated with neurobehavioral dysfunction (Horev *et al.*, 2011). Thus, Coro1A has been subject of neuronal studies. Studies on the role of Coro1A during maternal exposure to the toxic metal pollutant Cadmium showed that neurons express reduced levels of Coro1A, Rac1 and Pak1, resulting in defective neurodevelopment in rats (Feng *et al.*, 2019). Loss of Coro1A is also associated with loss of excitatory synapses and defects in neurobehavior. Here, Coro1A enhances cAMP production and PKA activation in excitatory synapse, enabling synaptic plasticity.

It has been shown that Coro1A besides other numerous actin-binding proteins is upregulated by 2-fold in MCF10A cells upon TGF β 1 treatment after 24, 48 and 72 hours (Liu *et al.*, 2019). In Th17 CD4⁺ T cells, it was shown that Coro1A deficiency resulted in decreased Smad3 phosphorylation and hence, less Smad3 DNA binding activity. The

impaired TGF β -Smad signaling in Coro1A-deficient cells lead to increased IL-17 and IFN γ production, and hence increased experimental autoimmune encephalomyelitis (Kaminski *et al.*, 2011).

Although Coro1A-KO mice are viable and fertile, specific deletion of Coro1A in T-cells leads to decreased number of peripheral T-cells as a consequence of impaired cell survival and migration (Chan, Creed and Bear, 2011).

Hattori *et al.* aimed to identify methylation-silenced genes in rat mammary carcinomas via expression microarray analysis and found that among other genes, Coro1A was highly methylated in different carcinoma cell lines, but not in normal MGs (Hattori *et al.*, 2011). Evaluating the expression level of Coro1A in breast samples revealed that Coro1A was significantly upregulated in breast cancer patients, especially triple negative cancers, compared to normal breast tissue (Zhao *et al.*, 2021).

1.6.2 Coro1B

Whereas Coro1A is mainly expressed in cells of hematopoietic lineage, Coro1B is ubiquitously expressed (Chan, Creed and Bear, 2011). Coro1B is structurally similar to Coro1A and also localizes to lamellipodia of fibroblasts in an Arp2/3-dependent manner (King *et al.*, 2022). The interaction of Coro1B and Arp2/3 is negatively regulated by PKC-dependent phosphorylation of Coro1B^{S2}, and inhibits Arp2/3-mediated filament nucleation (Cai *et al.*, 2005, 2007). Lack of Coro1B results in decreased cell migration and lamellipodia formation with densely branched actin filaments and reduced retrograde actin flow (Cai *et al.*, 2005, 2007). It was also shown that Coro1B-KD reduces protrusion rates with enhanced duration times of protrusions (King *et al.*, 2022).

Coro1B is located at apical junctions in MCF7 cells to regulate the F-actin and E-Cad

organization at the junctions. Coro1B was required to properly localize RhoA and ROCK1 to the junctions, and Coro1B-dependent stabilization of non-muscle myosin II at junctions resulted in deactivated p190B RhoGAP pathway, and thus, enhanced RhoA activation (Priya *et al.*, 2016). In endothelial cells, Coro1B co-localizes with F-actin and VE-Cad in lamellipodia and cell-cell junctions, respectively, and loss of Coro1B results in decreased stress fiber formation, impaired cortical actin and disorganized VE-Cad (Werner *et al.*, 2020). The number of junction-associated intermittent lamellipodia was reduced upon Coro1B-KD. Coro1B was shown to interact with Arp2/3, cofilin and ILK (Werner *et al.*, 2020). Coro1B was essential for the proper assembly of endothelial networks and vessel formation (Werner *et al.*, 2020).

1.7 Cancer development

Cancer describes the abnormal behavior of cells regarding proliferation, differentiation and survival. Depending on the cell type, cancers are classified into carcinomas, arising from epithelial cells, sarcomas, arising from cells of the connective tissues, and leukemias or lymphomas, arising from blood cells. The following chapters focus on carcinomas. Cancer is divided into (1) benign tumors, which are incapable of migration and invasion and do not spread within the body, and (2) malignant tumors – commonly referred to as cancer – which are highly invasive, comprising the risk for metastasis formation and resulting in bad survival prognosis. In order for a cell to transform into a highly proliferative and resistant cancer cell, human epithelial cells must acquire at least five distinct alterations (Weinberg, 2013). Off note, rodent epithelial cells must acquire only two distinct alterations. Additional to genetic alterations, clonal selection results in the outgrowth of cells that show proliferative, survival and invasive advantages. Increased secretion of

growth factors like EGF, TGF β , IL and HGF by the cancer cells themselves or by surrounding stromal cells like fibroblasts, endothelial cells and inflammatory cells further promote cell proliferation.

Metastasis requires highly migrative and invasive cancer cells that can rapidly adapt to new environments. Due to the formation of secondary tumors at distant sites in the body, metastases correlate with poor survival and are the main cause for cancer deaths (Seyfried and Huysentruyt, 2013; Fares *et al.*, 2020). EMT, tissue stem cells and tumor-associated macrophages (TAMs) or myeloid cells are considered as causes for metastases formation (Seyfried and Huysentruyt, 2013; Fares *et al.*, 2020). Phylogenetic relationship analyses of individual tumor cells using a Cas9-based single-cell lineage tracer system showed that tumor cells are highly heterogeneous in their ability to metastasize. Highly metastatic cells inherited and developed differential gene expressions over time, and these altered genes are associated with metastases (Quinn *et al.*, 2021). Thus, the authors found that different metastatic nodules often descend from a few highly metastatic cell clones (Quinn *et al.*, 2021).

1.7.1 The tumor microenvironment (TME)

Stromal cells and the ECM are important factors to drive tumor progression. Stromal cells like fibroblasts, immune cells (macrophages), or endothelial cells get activated and start to secrete signaling factors like growth factors (TGF β , EGF, HGF), interleukins (IL6, IL9, IL17) or TNF α , as well as ECM components like collagens or fibronectin (Friedl and Alexander, 2011). Thus, the relationship between cancer cells and the TME is highly dynamic and interactive. The TME enables tumor cell survival and promotes tumor

progression, by providing oxygen and nutrient supply via angiogenesis, stimulating proliferation and facilitating invasion via matrix degradation (Figure 19).

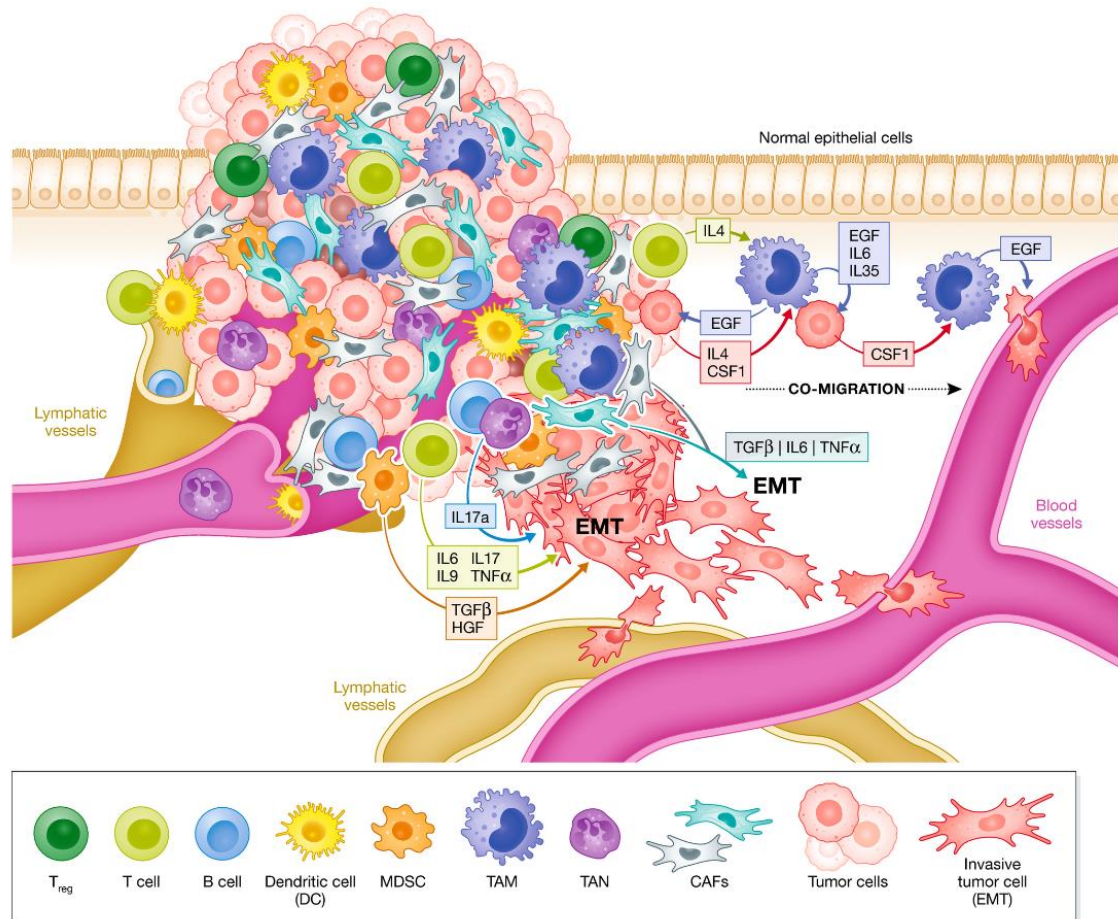


Figure 19: The tumor microenvironment. Cancer and stromal cells interact in a dynamic manner by secreting different growth factors, which promotes cell proliferation, migration, invasion, and tumor progression (Brabletz *et al.*, 2021).

CAFs are the major source for secreting signaling factors involved in EMT (Brabletz *et al.*, 2021). They derive from local fibroblasts, but can also derive from other cell types like adipocytes or endothelial cells (Anderson and Simon, 2020). Factors like TGF β , PDGF and FGF2 activate these cells and convert them into CAFs. CAFs in turn can transform normal epithelial cells into cancer cells. Studies of CAFs isolated from different stages of murine breast cancer showed that with increasing tumor stage, CAFs show enhanced expression of α SMA and S100A4 and form more FAs and stress fibers (Calvo *et al.*, 2013).

Consequently, the ability to contract collagen of CAFs is positively correlated to the disease stage and CAFs remodel collagen gels to increase matrix stiffness from 120 Pa to >1 kPa (Calvo *et al.*, 2013). The authors showed that cancer cells cultured in CAF-remodeled matrices were highly invasive, whereas normal fibroblast-remodeled matrices did not enable cancer cell invasion, indicating that fibroblasts, once activated, promote tumor progression. Mechanistically, they show that increased nuclear YAP in CAFs is required to achieve efficient matrix remodeling and matrix contraction (Calvo *et al.*, 2013).

The interaction between different cell types is shown by mixing MCF7-ras cells with normal human mammary fibroblasts, which results in the activation of the fibroblasts and the conversion into CAFs, indicated by an increased expression of α SMA (Kojima *et al.*, 2010). The authors showed that CAFs contained elevated TGF β mRNA levels and increased TGF β secretion in comparison to normal fibroblasts, which exerted an autocrine effect on CAFs (Kojima *et al.*, 2010). This ultimately lead to increased tumor growth, when CAFs and MCF7-ras mixed cells were injected into nude mice, compared to mixed normal fibroblasts and MCF7-ras cells, suggesting a tumor promoting function of CAFs (Kojima *et al.*, 2010). On the other hand, culturing MCF7, T47D, or MDA-MB-231 cells in the presence of CAF conditioned medium, secreted TGF β by CAFs resulted in upregulation of fibronectin and vimentin, morphological changes, and enhanced migrating and invading capacity in cancer cells (Yu *et al.*, 2014).

However, Özdemir *et al.* showed that depletion of α SMA⁺ myofibroblasts in mouse pancreas cancer lead to poorly differentiated tumors and decreased survival (Özdemir *et al.*, 2014). Myofibroblast-depleted tumors showed decreased amount of collagen and reduced stiffness, decreased angiogenesis and increased tumor hypoxia. Cancer cells

displayed increased mesenchymal features like expression of α SMA and EMT-TFs like Twist, Snail and Slug and had a higher invasive grade. This highlights the diversity of different tumors and their interaction with stromal cells.

Co-culture of ovarian cancer cells and CAFs showed that CAFs induce activation of PGM1 in cancer cells (Curtis *et al.*, 2019). PGM1 is important to degrade glycogen for glucose production and thus provides energy by enhancing glycogenolysis and glycolysis (Curtis *et al.*, 2019). Mechanistically, it was shown that cancer cells secrete TGF β , which upregulates p38 α MAPK pathway in CAFs. The p38 signaling in CAFs is required to secrete cytokines like IL6, IL8 and CXCL10, which act back on cancer cells by inducing STAT3, MEK1/2 and Rac1 signaling and promoting glycogenolysis in cancer cells to increase cell proliferation, invasion, and tumor growth (Curtis *et al.*, 2019). Staining of human ovarian metastasis samples showed that late metastases had low levels of glycogen, indicating that high glycogen mobilization in cancer cells correlates with a higher grade of metastasis (Curtis *et al.*, 2019). This highlights the importance of feedback loops between cancer cells and CAFs to promote tumor progression.

The secretion of matrix degrading proteinases like MMPs enables cell invasion via degrading the basement membrane, activation of growth factors like TGF β or other MMPs, and degradation of adhesion molecules (Cichon *et al.*, 2010). Increased levels of MMPs in the tumor stroma is often observed in advanced tumor stages.

The excess deposition of ECM, namely collagen, fibronectin, elastin and laminin, is another hallmark of cancer progression. Increase in the tumor stroma stiffness often correlates with poor prognosis. Normal breast tissue shows a stiffness of 0.1 kPa – 0.5 kPa, whereas invasive carcinomas can reach stiffnesses of 2 – 6 kPa, which strongly promotes

cancer progression (Paszek *et al.*, 2005; Lopez *et al.*, 2011; Lee *et al.*, 2019; Pratt, Lee and Martin, 2020). An increased stiffness is achieved by accumulated ECM deposition or enhanced crosslinking of collagens. The crosslinking is mediated by lysyl oxidases (LOX), which catalyze the oxidative deamination of lysin and hydroxylysine residues of collagen fibers (Tanzer, 1973). The allysines of different fibers then spontaneously condensate to generate a highly interconnected collagen network.

By using AFM, Lopez *et al.* measured the stiffness of MMTV-PyMT breast cancer mice and observed that increasing malignancy correlated with enhance collagen disposition and ECM stiffening. Cancer cells showed increased cell tension with increasing stiffness and were consequently stiffer compared to normal epithelial cells (Lopez *et al.*, 2011).

Cells cultured on stiff surfaces showed flattening of the nucleus mediated by stress fibers, which leads to a mechanical opening of nuclear pores and the accumulation of the transcription regulator YAP in the nucleus (Elosegui-Artola *et al.*, 2017). YAP is a known tumor promoting protein that interacts with the TF TEAD to trigger the gene expression involved in cell proliferation, differentiation, survival and invasion (Böttcher, Sun and Fässler, 2017).

Stiff tumor tissue alters integrin levels. Culturing non-malignant MCF10A cells in increasing amounts of collagen showed that acinus formation was impaired with inhibited lumen formation and eventually loss of basal polarity (Paszek *et al.*, 2005). The authors observed an increased $\alpha_3\beta_1$ integrin clustering and signaling, marked by enhanced FAK^{pY397} and vinculin levels and increased FA size, when the matrix was stiffer. Additionally, they saw an increase in Rho/ROCK signaling resulting in enhanced cytoskeletal tension and Erk signaling, highlighting the influence of matrix stiffness on cell

behavior (Paszek *et al.*, 2005).

Twist can sense ECM stiffness (Wei *et al.*, 2015). On low stiffness, Twist1 is cytosolic. On high stiffness, Twist is nuclear. Lyn phosphorylates Twist on a stiff surface (5700 Pa). Lyn interacts with EPHA2 only at high stiffnesses. Inhibiting Lyn via Bafetinib results in no phosphorylation of Twist1 on stiff surface. When Twist1 is phosphorylated, interaction of Twist and G3BP2, which is a cytosolic protein, is decreased, resulting in nuclear translocation of Twist1, to induce EMT (Wei *et al.*, 2015). The authors show how the EMT event is induced by increased ECM stiffness. EMT was needed for cells to enter the blood. Induction of EMT increased CTCs. Nevertheless, EMT plasticity was necessary to eventually form macro-metastases in lung.

1.7.2 Cancer cell migration, invasion, and metastases

Cancer cell migration is essential for further tumor development and eventual metastases formation. Three different migration modes are generally distinguished (Figure 20): (1) Cells migrate collectively as clusters, (2) cells migrate individually with a mesenchymal cell shape, and (3) cells migrate individually with roundish cell shape (amoeboid migration).

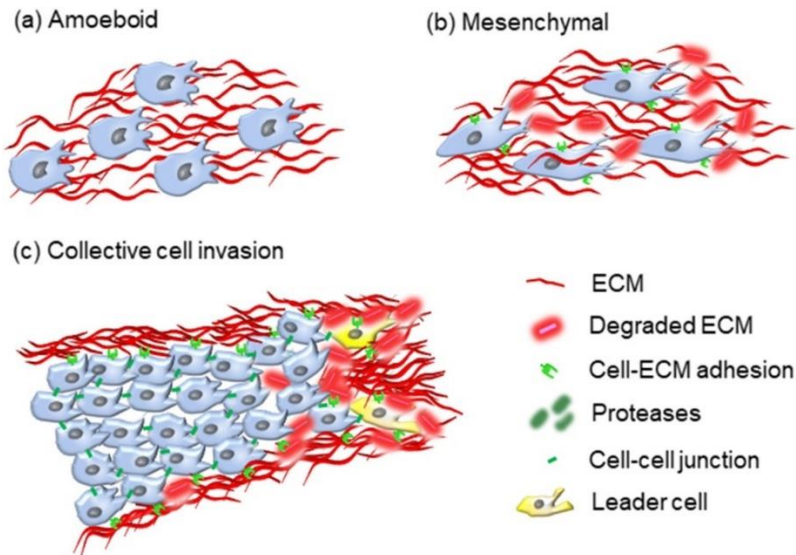


Figure 20: Cell migration modes. Cells can migrate individually in an amoeboid (a) or mesenchymal (b) fashion, or as collective strands (c) (Wu *et al.*, 2021).

Collective cell migration requires cell-cell interactions. Collectively migrating strands show a leader cell at the front, which form tracks through the stroma by proteolysis and guide the follower cells through the tissue. These leader cells show an increased glucose uptake and energy consumption than follower cells (Zhang *et al.*, 2019). A dynamic replacement of leader cells by follower cells was observed, when the leader cell ran out of energy (Zhang *et al.*, 2019). By using an Erk-activity FRET biosensor, Hino *et al.* showed that HGF induced continuous Ras-Erk activation in lamellipodia of leader cells, which propagates towards follower cells (Hino *et al.*, 2022). Follower cells showed oscillatory Erk activation, which was EGFR-dependent. The authors show that leader cells encounter less confinement, which enables the formation of protrusions via talin-1-mediated focal complex formation. This protrusion formation was critical for HGF-dependent Erk activation, explaining why densely packed follower cells were non-responsive to HGF (Hino *et al.*, 2022). Continuous Erk activity resulted in a positive-feedback loop, in which Erk enhances lamellipodia formation and traction force generation in leader cells. Thus, the authors provide a mechanism for leader and follower cell specification in collectively

migrating cells (Hino *et al.*, 2022).

Mesenchymal individual migration requires a polarized cell shape with lamellipodia and filopodia forming at the leading edge, driven by Rac1 and Cdc42. FAs are necessary to interact with the ECM and to facilitate guided secretion of MMPs to remodel the ECM. In a first step, lamellipodia form via interaction of Rac1/Cdc42 with WASP/WAVE complex to activate Arp2/3 and thus the nucleation of actin filaments to form the actin-based protrusion (=lamellipodia). Small NAs containing well-known proteins like integrins, talin, vinculin, paxillin and FAK form around 1-2 μm away from the leading edge with a rapid turnover rate of $t_{1/2} \sim 60$ sec, which require actin polymerization (Nobes and Hall, 1995; Beningo *et al.*, 2001; Vicente-Manzanares and Horwitz, 2011). The formation of mature FAs via integrin assembly further stabilizes the lamellipodia and enables a strong attachment of the cell to the ECM. Rho/ROCK signaling-dependent phosphorylation of myosin light chain and assembly of myosin II filaments further promotes actin stress fiber formation. Contraction of stress fibers and the cortical actin result in retraction of the cell rear and forward movement. Via interaction of FAs with the CMSC complex, the MT cytoskeleton is guided in proximity to FAs and enables localized recruitment and secretion of MMPs to degrade the ECM (Paňková *et al.*, 2010).

Amoeboid individual migration on the other hand requires myosin II-dependent contractility of the cell driven by Rho/Rock signaling pathway, resulting in a round cell shape and the ability to move through the ECM with weak ECM attachment by either squeezing through ECM gaps or remodeling the ECM with force (Paňková *et al.*, 2010). Ezrin, radixin and moesin link actin to the membrane to generate a cell tension and generating an intracellular hydrostatic pressure. This pressure leads to the formation of

so-called membrane blebs (spherical protrusions), which facilitate cell migration.

Haeger *et al.* showed that HT-1080 sarcoma xenografts predominantly invade collectively into the dermis (Haeger *et al.*, 2020). Irradiation of the tumor led to increased nuclear fragmentation, dsDNA breaks and cell death in the tumor core, whereas collectively migrating cells (=invasive zone) were radioresistant. The authors show that the tumor core had a prolonged phosphorylation of CHK2, a protein regulating double strand repair (DSR) outcome, compared to the invasive zone, indicating that DSR was efficient in the invasive zone but not in the tumor core, subsequently leading to apoptosis in the latter. Downregulation of β_1 , $\alpha_v\beta_3$ and $\alpha_v\beta_5$ integrin showed that integrins are responsible for the IR resistance in collective migrating cells. This was also demonstrated by increased survival and abolished metastasis formation in mice treated with a combination of IR and integrin inhibitors compared to IR only (Haeger *et al.*, 2020).

Cancer cell migration is highly dynamic, and cells switch between different migration modes to perfectly adapt to the surrounding environment. Mesenchymal-amoeboïd transition and collective-individual transition, as well as the respective inverted processes have been observed, depending on the matrix stiffness, activity of RhoA, Rac1 and Cdc42, integrin-mediated adhesion and MMP function (Wu *et al.*, 2021). Law *et al.* showed that physical confinement led to single-cell dissociation from collectively migrating cells by destabilizing E-Cad and thus cell-cell interactions (Law *et al.*, 2023). Confinement enhanced MT destabilization, resulting in GEF-H1 release and activation and RhoA activation. Increased actomyosin contractile forces mediated by RhoA/myosin IIA in the cell anterior induced stress on cell-cell junctions, resulting in E-Cad mobilization and subsequent leader cells detachment (Law *et al.*, 2023). The detached cells migrated faster

and penetrated further into the channels compared to collectively migrating follower cells. The dependence of migration mode on tissue density was also shown by seeding MCF7 cells in increasing collagen density (Ilina *et al.*, 2020). Matrices with sufficient space or matrices that were remodeled by MMP-secreting fibroblasts to form guiding trails allowed MCF7 cells to invade collectively. Collective migration was again dependent on E-Cad and β -catenin expression. Inhibiting E-Cad expression increased single-cell detachment at low collagen densities, whereas it increased fluid-like or uncoordinated collective sheet migration at high collagen densities (Ilina *et al.*, 2020). Although downregulation of E-Cad resulted in increased primary tumor formation of MCF7-tumors, metastases were not induced (Ilina *et al.*, 2020). Both primary tumor growth and lung metastases were reduced in 4T1-tumors upon E-Cad downregulation (Ilina *et al.*, 2020).

Seeding HT-1080 cells in micro-tracks of different diameters generated of collagen revealed that the cells migrate collectively or individually with similar migration speed, which increased from 0.5 $\mu\text{m}/\text{min}$ to 0.7 $\mu\text{m}/\text{min}$ measured in 7 μm^2 and 460 μm^2 wide tracks, respectively (Beunk *et al.*, 2022). The cells were thereby either pushing against the tracks to widen the narrow diameter or pulling wide tracks in an actomyosin-dependent manner to achieve diameters of the cell body. Inhibition of myosin II or ROCK with Y-27632 or Blebbistatin impaired cell contractility, resulted in cell elongation and reduced cell migration speed. Treated cells were still able to widen narrow tracks while passing through, but the tracks shrank to their original diameters after the cells migrated, indicating that cell contractility is essential to stably rearrange collagen matrices (Beunk *et al.*, 2022). This demonstrates how migrating cells interact and remodel their surrounding for optimal migration.

Hypoxia is often present in tumors because of enhanced tumor cell proliferation and outgrowth of the tissue vasculature. Lack of oxygen and nutrients due to insufficient blood supply leads to the survival of cells that adapt to the hypoxic tumor microenvironment. These cells often are highly aggressive as they express genes associated with stem cell maintenance, migration and invasion, proliferation, and ECM remodeling (Martin *et al.*, 2011). Lehmann *et al.* showed that hypoxia promotes amoeboid single-cell detachment and invasion of 4T1 cells cultured in a 3D fibrillar collagen matrix (Lehmann *et al.*, 2017). This was accompanied by an increase of EMT signature in detached cells, e.g., decreased E-Cad levels and increased levels of Snail and Twist. The hypoxia-mediated amoeboid cell detachment was independent of MMP secretion. They found that hypoxic conditions resulted in an increased metastatic burden, highlighting the importance of hypoxia in cancer development (Lehmann *et al.*, 2017).

Integrins have been shown to play an important function in regulating the migration mode in 3D. Elevated activation of β_1 integrins in 4T1 and UTSCC38 cells resulted in reduced amoeboid, but increased elongated cell migration with pseudopodal protrusion formation (te Boekhorst *et al.*, 2021). Focusing on hypoxia induced stabilization of HIF, the authors showed that increased calpain-2 activity in hypoxic conditions correlated with decreased levels of active β_1 due to cleavage of talin-1, leading to cell rounding and amoeboid migration. In addition, hypoxia-induced blebbing-amoeboid migration resulted in decreased oxidative respiration and glycolysis and was thus the most energy efficient migration mode. *In vivo* metastatic studies revealed higher metastatic incidences in hypoxic conditions, which could be reversed by inhibiting calpain-2 and thus inhibiting the transition from elongated to blebbing-amoeboid migration (te Boekhorst *et al.*, 2021).

Hapach *et al.* aimed to elucidate the difference in metastatic potential of strongly and weakly migratory subpopulations of MDA-MB-231 cancer cells (Hapach *et al.*, 2021). By implanting the two subpopulations into mice, they showed that, although strongly migratory cells showed enhanced invasion and circulation, they form less metastases than weakly migratory cells. The primary tumor formation and cell proliferation was comparable between the subpopulations. Strongly migratory cells had a strong expression of EMT-associated genes and predominantly migrated as single-cells, whereas weakly migratory cells were high in E-Cad expression and migrated collectively. In a mixture of strongly and weakly migratory cells, predominantly strongly migratory cells served as leader cells, which enabled weakly migratory cells to follow. Interestingly, implanted into mice, the mixed population showed the highest metastatic incidence. This suggests that strongly migratory cells guide weakly migratory cells to invade in surrounding matrix, whereas weakly migratory cells are required to colonize at distant sites in a E-Cad-dependent manner (Hapach *et al.*, 2023).

Additional studies suggest that tumor cells interact with CAFs as epithelial-mesenchymal couple to invade into 3D. Here, CAFs take the function as leader cells and remodel the ECM in an α_3/α_5 integrin and RhoA-dependent manner, so that epithelial cancer cells collectively follow the provided tracks (Gaggioli, 2008).

1.7.2.1 Importance of Rac1 in cancer cell invasion

The small GTPase Rac1 has been shown to play a crucial role in tumor cell migration and invasion and thus has been a potential target of antitumor therapies (Ma *et al.*, 2023). Rac1 is often overexpressed or hyperactive in cancer, and high expression correlates with poor patient outcome. Rac1 regulates migration by establishing a front-rear polarity by

localizing to the migration front and forming lamellipodia. Disrupting this targeted localization of Rac1 and thus having Rac1 homogenously localized within the cell results in impaired directionality (Jain *et al.*, 2020). The Rac1 polarity is thereby controlled by localization of e.g., Tiam1, a Rac1 GEF, to the leading edge, resulting in polarized Rac1 activation.

The TGF β -Smad4 signaling cascade was shown to be important to stimulate expression of mesenchymal markers like vimentin and repressing expression of E-Cad in PDAC organoids cultured in collagen I, resulting in the change from collective cell invasion to mesenchymal invasion pattern (Huang *et al.*, 2020). Clinical outcome studies revealed that expression of Smad4 and the ability of tumors to invade in a mesenchymal fashion correlates with poor patient outcome and survival (Huang *et al.*, 2020). In addition, the authors showed that TGF β activates Rac1 and Cdc42 in a Smad4-independent manner (Huang *et al.*, 2020).

TGF β -induced Rac1 activation was also shown to be crucial for the EMT process in mouse transformed keratinocytes (Santibáñez *et al.*, 2010). Introducing a dominant-active form of Rac1 decreased the expression of E-Cad and had disrupted cell-cell junctions. TGF β -mediated enhanced Snail expression, increased migration capacity, and MMP9 secretion was blocked by a dominant-negative Rac1, whereas dominant-active Rac1 increased Snail expression, cell motility, and MMP9 secretion even in the absence of TGF β . Interfering with the MAPK signaling pathway by inhibiting MEK using PD98059 impaired TGF β -induced Snail expression and MMP9 secretion and also reversed the effects seen with dominant-active Rac1, concluding that TGF β leads to Rac1 activation, which contributes to EMT-marker expression and enhanced motility in a MAPK-dependent manner

(Santibáñez *et al.*, 2010).

Complementary to that, Hage *et al.* showed that expression of a dominant-negative Rac1 (N17), or Rac1 inhibition by NSC23766 in the pancreatic carcinoma cell line PANC-1 increased the protein levels of E-Cad and β -catenin, whereas the dominant-active form of Rac1 (V12), or activation of Rac1 via PDGF reduced the protein levels of E-Cad and α -catenin (Hage *et al.*, 2009). The latter could be prevented by inhibiting the proteolytic machinery by MG132. Immunoprecipitation experiments of β -catenin revealed a Rac1-dependent complex formation of E-Cad, α -catenin and β -catenin. They demonstrate that Rac1 activity increases proteolytic degradation of E-Cad. Active Rac1 correlated with enhanced cell migration, as well as cell invasion through a collagen I gel.

By using a FRET-based biosensor, Floerchinger *et al.* could monitor live Rac1 activity in growing breast cancer of MMTV-PyMT transgenic mice (Floerchinger *et al.*, 2021). They detected an increased Rac1 activity in mammary tumors and especially in cancer cells adjacent to blood vessels. During metastasis formation in lung, they detected high Rac1 activity during the extravasation and colonization process. Inhibition of Rac1 affected 2D migration of cancer cells and impaired 3D invasion of tumor cells seeded on fibroblast remodeled matrix. Treating MMTV-PyMT transgenic mice with Rac1 inhibitor NSC23766 slightly reduced tumor burden and enhanced overall survival, whilst the metastatic burden was significantly decreased, demonstrating the importance of active Rac1 during tumor progression (Floerchinger *et al.*, 2021).

Rac1 was also shown to induce amoeboid-mesenchymal transition in melanoma cells. Activation of Rac1 induces mesenchymal migration mode via WAVE2 to direct mesenchymal movement and to suppress amoeboid movement by inhibiting actomyosin

contractility (Sanz-Moreno *et al.*, 2008). The transition was a reversible process, in which Rho signaling inhibited Rac1 by activating Rac1 GAP ARHGAP22 and thus promoting amoeboid movement. This highlights the dynamic in migration mode and the ability of cells to quickly adapt to cellular surroundings and orchestrate their migration mode accordingly.

Yoon *et al.* discovered that *Lama3*, encoding for LN-332, was expressed in collectively migrating 4T1 cells, whereas its promoter was methylated and thus repressed in individually migrating 4T1 cells (Friedl and Zegers, 2024; Yoon *et al.*, 2024). Although both, collective and single-cells, bind LN-332 via $\alpha_6\beta_4$ integrins, the authors show that LN-332 secreted by collectively migrating cells activates Rac1 in single-cells to enhance cell detachment, velocity, and directionality and thus promotes invasiveness of individually migrating cells (Yoon *et al.*, 2024).

Taking together, Rac1 plays an essential role in cancer cell migration and drives metastasis formation.

1.8 Murine development

1.8.1 Early embryonic development

Mouse development starts with the cell division of the zygote, before the embryo polarizes into an inner cell mass (ICM) and an outer layer of trophectoderm (trophoblast) (Figure 21, preimplantation). During this blastocyst stage, the inner cell mass differentiates into the epiblast and the primitive endoderm (hypoblast), which eventually surrounds the epiblast. At E4.5-6.0, the blastocyst implants, the egg cylinder forms and differentiates into an extra-embryonic part, such as the trophoblast, which expands to form the ectoplacental cone (extra-embryonic ectoderm) with trophoblast giant cells invading into maternal tissue, and

an embryonic part, namely the epiblast (embryonic ectoderm) (Figure 21, peri-implantation). At E5.0, the pro-amniotic cavity forms within the epiblast. During the primitive streak stage, epiblast cells differentiate into mesoderm, also called the primitive streak, at the posterior side of the embryo. The distal node appears on the anterior side of the embryo. The primitive streak elongates along the embryo and divides the pro-amniotic cavity into the amniotic and exocoelom cavities, separated by the amniotic ectoderm and amniotic mesoderm cell layer. At E7.5, the posterior extra-embryonic mesoderm forms the allantois that extends into the exocoelom cavity. At E8.5, the allantois fuses with the chorion, which forms along the ectoplacental cone, eventually forming the umbilical cord, connecting the maternal placental tissue with the embryo and facilitating blood and nutrient supply (Figure 21, organogenesis). Now, the heart differentiates and irregular contractions of the heart are visible. The extra-embryonic exocoelom forms the yolk sack, which subsequently fully surrounds the turning embryo. By E9.5, the turning process is completed, the heart is beating regularly and the embryo is vascularized with blood circulating.

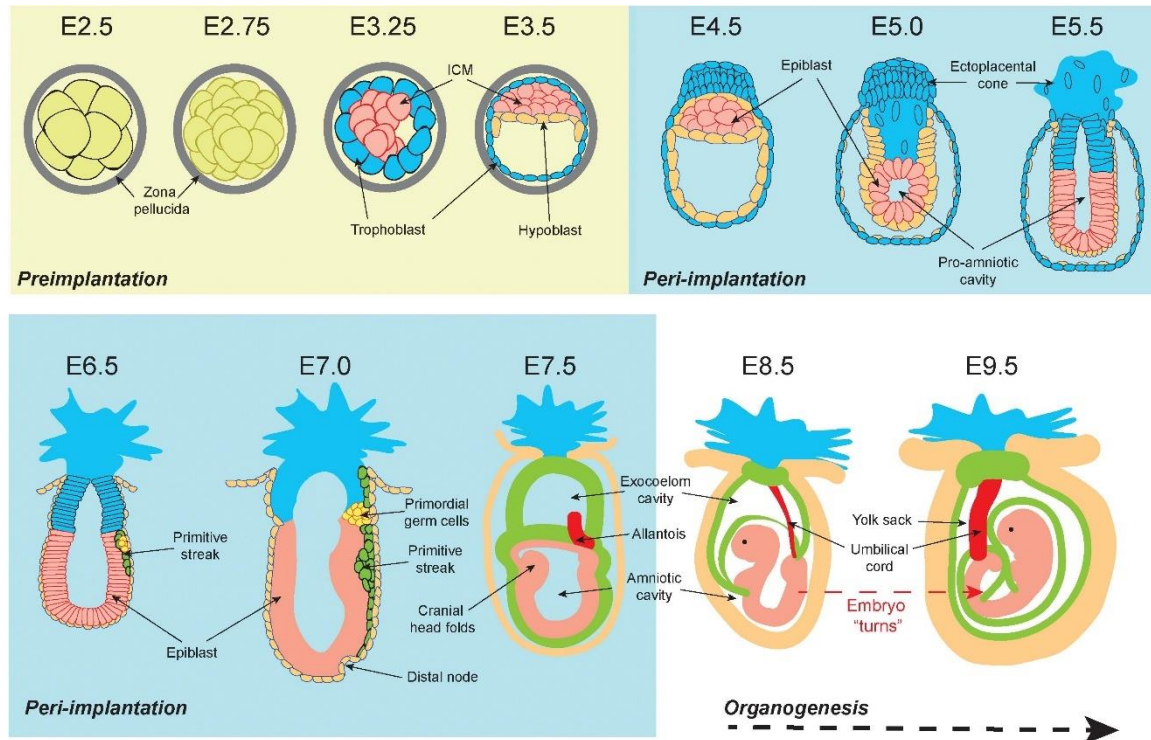


Figure 21: Schematic depiction of murine embryonic development. The ICM (pink) differentiates into the embryonic epiblast and the primitive endoderm (yellow). The trophoblast (blue) forms the extra-embryonic part and differentiates into the ectoplacental cone. During the primitive streak stage, the mesoderm (green) arises and forms the allantois (red), which eventually forms the umbilical cord by fusing with the chorion. (Kafer and Cesare, 2020).

1.8.1.1 VCAM-1 and α_4 integrin in chorioallantoic fusion

The allantois derives from epiblast cells that differentiates into extra-embryonic mesodermal cells. It contains an outer layer of a simple squamous epithelium, called mesothelium, filled with roundish inner core cells. While the proximal inner cells are densely packed, the distal inner cells are arranged in a loose configuration (Inman and Downs, 2007). BMPs (BMP2, 4, 5, 7) and Smads (Smad1) among other proteins are required for proper allantoic development (Watson and Cross, 2005). The elongation of the allantois is a combination of adding new cells from the primitive streak, allantoic cell proliferation, and cavitation to increase the hydroptic space (Inman and Downs, 2007). Increased surface area maximizes the contact area of the allantois with its opposing partner, the chorion. The chorion derives from the extra-embryonic ectoderm and the chorionic

mesothelium.

The fusion of both parts requires VCAM-1, which is gradually expressed at the distal end of the elongating allantoic mesothelium and at the contact site with the chorionic plate, and its receptor α_4 integrin, which is expressed in the chorionic mesothelium (Gurtner *et al.*, 1995; Yang, Rayburn and Hynes, 1995; Downs, 2002; Watson and Cross, 2005). Upon fusion, the allantois *de novo* vascularizes the chorion, thereby forming a placental labyrinth. The umbilical artery and vein form within the chorioallantois that facilitates gas and nutrient exchange between the mother and the embryo.

Both KO of VCAM-1 and α_4 integrin in mice is embryonically lethal between E10.5 and E13.5 (Gurtner *et al.*, 1995; Kwee *et al.*, 1995; Yang, Rayburn and Hynes, 1995). During embryogenesis, VCAM-1 is expressed in the myocytes of the myocardium in the heart, the yolk sac and the allantois. In the latter, VCAM-1 is detected early on in allantoic differentiation and then distributes to the distal end (Downs, 2002). α_4 integrin is expressed in epicardial cells, the yolk sac and in the chorionic plate (Sheppard *et al.*, 1994). Here, α_4 integrin is expressed in the chorionic mesoderm. Both, VCAM-1 and α_4 integrin are particularly highly expressed at the edges of chorioallantoic contact points, whereas they show a spotted and discontinuous distribution along the chorioallantoic interface, demonstrating that chorionic and allantoic tissues merged (Downs, 2002).

The VCAM-1-KO embryos die because of either heart defects or due to failure of the chorioallantoic fusion before E13.5 (Gurtner *et al.*, 1995; Kwee *et al.*, 1995). Around 50% of VCAM-1-KO embryos were unable to fuse the allantois with the chorion and died before E11.5. Here, the allantois predominantly appeared as large and swollen sac and exhaustion of embryonic nutrient and oxygen resources results in death. However, the other half of

VCAM-1-KO embryos that survived E11.5 were able to establish a functional chorioallantoic connection with umbilical vessel formation, suggesting that other proteins are involved that can compensate for VCAM-1 loss during the initial fusion step. Nevertheless, these embryos showed blood in the pericardial sac, lacked an epicardium, showed defects in the ventricular myocardium and lacked an intraventricular septum, resulting in heart failure and death at latest E13.5 (Gurtner *et al.*, 1995; Kwee *et al.*, 1995). Similarly, α_4 integrin-KO embryos died between E9.5 and E14.5 (Yang, Rayburn and Hynes, 1995). Comparable to VCAM-1-KO, α_4 integrin-KO embryos dying around E11 were unable to fuse chorion and allantois at E8.75, which hindered placenta development, resulting in a delayed development around E10.5 and eventually death. α_4 integrin-KO embryos that were able to form a chorioallantoic connection showed severe hemorrhage at the heart, due to a missing epicardium and had an impaired facial and cranial development, resulting at death at E12.5, but latest at E14.5 (Yang, Rayburn and Hynes, 1995).

Besides VCAM-1 and α_4 integrin, mutations in other proteins like LPP3, Smad1, Edd, Fgfr2, or TGF β can result in impaired chorioallantoic fusion and thus result in embryonic death (Dickson *et al.*, 1995; Inman and Downs, 2007; Arora and Papaioannou, 2012).

1.8.2 MG development

The mouse MG is a highly dynamic tissue that first starts developing at E10 to form a rudimentary duct system before entering a dormant state at birth and finally undergoing extensive proliferation at puberty with enhanced remodeling during pregnancy (Figure 22). The overall tree-like structure consists of ducts formed by an inner layer of luminal epithelial cells surrounded by a basal layer of myoepithelial cells and stem cells. This branched epithelial structure deriving from the ectoderm is surrounded by the stroma,

consisting of fibroblasts and fat cells deriving from the mesoderm. The MG development is tightly regulated by hormones and undergoes massive structural changes during pregnancy.

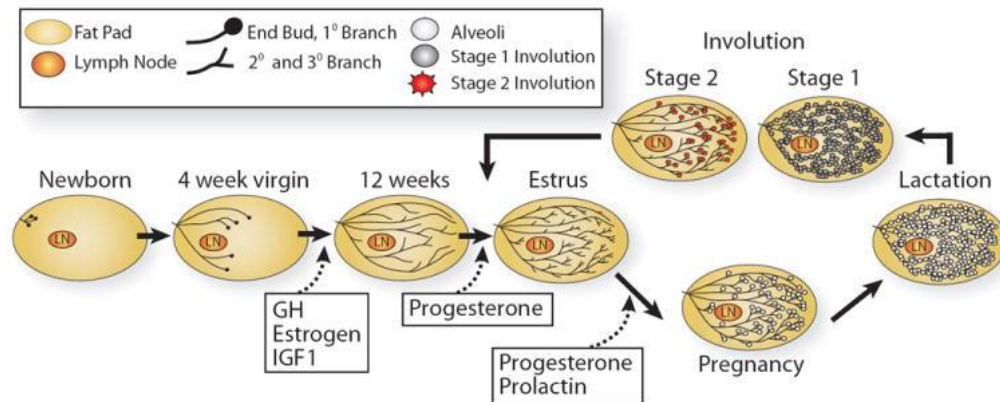


Figure 22: MG development. The MG undergoes drastic morphological changes during pregnancy and involution (Macias and Hinck, 2012).

1.8.2.1 Embryonic MG development

At E10, the milk lines start to form within the ectoderm between fore-and hindlimb bud on the ventral side (Hinck, 1978). The milk line formation is tightly regulated by the mammary mesenchyme, expressing Tbx3. Tbx3 controls Wnt10B and subsequent Lef1 expression to define the milk line (Propper, 1978). Hereby, BMP4 inhibits the expression of Tbx3 at the ventral border of the milk line to further define the location of the milk line (Cho *et al.*, 2006).

The canonical Wnt signaling pathway is activated by Wnt binding to Frizzled receptors and LRP5/LRP6 co-receptors resulting in the inactivation of the β -catenin degrading protein complex of GSK3, APC, Axin, and CK1 α . This complex regulates β -catenin ubiquitination by the E3 ubiquitin ligase β -TrCP for proteasomal degradation. Wnt binding inhibits β -catenin phosphorylation by GSK3, and the unphosphorylated β -catenin can now translocate into the nucleus, where it interacts with TCF/LEF to regulate gene expression

(Patel *et al.*, 2019). Expression of FGF10 at E10.5 in the thoracic somites further regulates Wnt signaling and is involved in the correct dorsal-ventral placement of the five mammary placode pairs. These mammary placodes derive from migrating ectodermal cells, which accumulate in clusters along the milk line (Propper, 1978). By E11.5, the third, fourth, first and fifth, and finally the second mammary placode pair formed asynchronously along the milk line.

The importance of Wnt signaling in mammogenesis is demonstrated by (1) over-activating Wnt using WNT3A-conditioned medium leading to enhanced mammary placode formation and (2) overexpressing the Wnt inhibitor DKK1, resulting in suppressed mammary placode formation (Chu *et al.*, 2004).

At E13.5, the mammary placodes invade into the mammary mesenchyme and form so-called mammary buds (Paine and Lewis, 2017). These buds then start to elongate and the so-called sprouts penetrate into the fat pad to form a tree-like gland containing 10-15 branches (Watson and Khaled, 2008). The nipple starts to form as a result of epidermis thickening induced by PTHLH. The embryonic MG then enters a resting phase at E18.5 and continues to develop during puberty.

1.8.2.2 Sexual dimorphism in MG development

Up to day E13, male and female MG development is the same. However, at E13.5, a sexual dimorphism is observed (Figure 23): While female embryos show further penetration of the mammary buds into the mesenchyme, male embryos show regression of the mammary buds with a densely packed mesenchyme around the gland epithelium as a consequence of androgens like testosterone (Kratochwil, 1971). By using testosterone-insensitive epithelium or mesenchyme, respectively, Kratochwil *et al.* could show that testosterone

hereby predominantly acts on the mesenchyme, which then triggers necrosis and degradation of the mammary buds (Kratochwil and Schwartz, 1976). The mammary buds start to detach from the epidermis and are completely absorbed after 60 hours of testosterone exposure. Interestingly, female embryos also respond to androgens with regression of the mammary buds, while withdrawal of testosterone on male mammary buds results in recovery and female-like MG development, demonstrating that the sexual genetic background alone does not influence the MG development (Hoshino, 1965; Kratochwil, 1971, 1977). However, mammary buds that developed until E15 or later stages lose their responsiveness to androgens and continue in their development (Hoshino, 1965; Kratochwil, 1971, 1977).

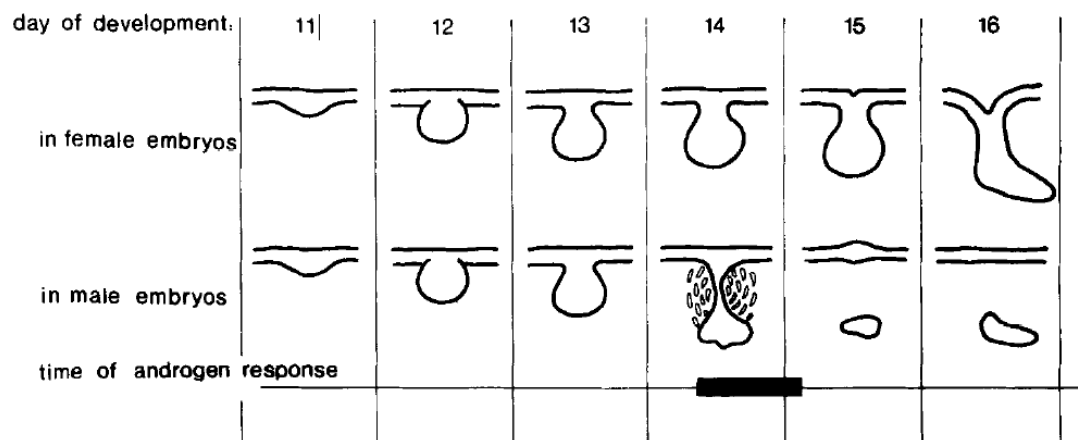


Figure 23: Sexual dimorphism. At E14 of development, male androgens destroy mammary buds. After E15, cells lose the responsiveness to androgens (Kratochwil, 1977).

1.8.2.3 Pubertal MG development

After entering puberty, the MG continues to develop to eventually form a branched epithelial network of ducts that can support alveolar development and milk production during pregnancy and lactation. Increased production of estrogen promotes the formation of terminal end buds (TEB) at the tips of mammary ducts, which are specific structures for

pubertal development and are responsible for driving the elongation and branching of the mammary ductal tree by producing the mature cell types that make up the ducts (Figure 24). TEBs form by multiple divisions of luminal epithelial cells to generate a bulb-like structure. Cap cells at the outer layer of the TEB are pluripotent with high regenerative potential and are highly proliferative and eventually differentiate into myoepithelial cells with continuous duct elongation (Paine and Lewis, 2017). Body cells in the inner compartment of TEBs are progenitor cells of luminal and alveolar cells and develop into the luminal layer of the ducts.

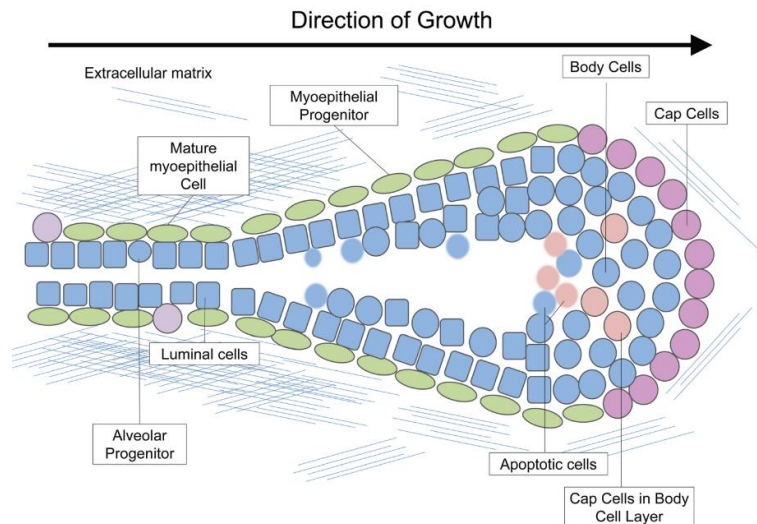


Figure 24: The terminal end bud. The TEB penetrates into the fat pad and gives rise to the mature ductal tree (Paine and Lewis, 2017).

Fibroblasts, which assemble at the tip of TEBs, are getting activated by estrogen and secrete growth factors, like FGF, HGF, and IGF-1, produce ECM, like laminin, collagen and fibronectin, and facilitate ECM degradation by secreting MMPs to promote luminal cell proliferation and invasion (Paine and Lewis, 2017).

TGF β 1 is produced by the epithelium during MG development and inhibits cell proliferation of cap cells, as well as side branching and bifurcation, while simultaneously stimulating the production and secretion of ECM in fibroblasts (Wiseman and Werb, 2002;

Paine and Lewis, 2017). A proper balance between proliferation or branching stimulating and inhibiting factors is important to acquire the correct mammary morphogenesis.

Given that TEBs are specific for puberty, at the age of 10-12 weeks in mouse, TEBs start to regress once they reached the end of the MG fat pad and the growth of the MG stops, leaving behind the mature ductal tree (Watson and Khaled, 2008).

1.8.2.4 MG development during pregnancy, lactation and involution

Pregnancy induces strong morphological changes and remodeling of the MG to form a high number of milk secreting ducts important for pup feeding (see chapter 1.8.2, Figure 22). This is achieved by coordinated changes in proliferation, differentiation and apoptosis. Enhanced levels of progesterone and prolactin lead to rapid proliferation and differentiation of mammary epithelial cells, resulting in secondary and tertiary branching of the ducts and giving rise to spherical and grape-shaped alveoli, which synthesize and secrete milk (alveologensis) (Oakes, Hilton and Ormandy, 2006; Wang and Scherer, 2019). KO of prolactin or its receptor impairs alveolar development and milk production (Briskin *et al.*, 1999). Progesterone further induces RANKL expression, which regulates calcium release and stimulates cell growth (Hannan *et al.*, 2023). KO of RANKL shows defects in alveoli formation, similar to prolactin-KO (Fata *et al.*, 2000). Prolactin-dependent activation of Jak and Stat5 leads to expression of β -casein and Wap, the milk proteins (Buser *et al.*, 2007; Macias and Hinck, 2012).

Contractile myoepithelial cells surround each alveolus in a discontinuous manner, enabling direct contact of alveoli epithelial cells to the basement membrane and mediating milk transport. The alveoli are connected to the ductal system via small ducts. In parallel, the stromal adipocytes lose their lipid content and undergo de-differentiation and apoptosis to

give space to the growing milk secreting ducts (Wang and Scherer, 2019). Also, the glands increasingly become vascularized.

After parturition, progesterone levels decrease to stimulate milk secretion and tight junction closure of mammary epithelial cells, allowing milk proteins to move into the alveolar lumen, whereas prolactin stimulates the expression of milk synthesis promoting genes (Hannan *et al.*, 2023). Suckling, olfactory and auditory stimuli of the pups enables continuous synthesis and secretion of milk by increasing oxytocin production. Oxytocin increases the calcium levels in myoepithelial cells, resulting in enhanced cell contraction which leads to milk ejection (Hannan *et al.*, 2023).

Involution and regression of the lactating MG happens in two steps. The first step of involution is reversible and starts within the first 12 hours after suckling. It is marked by alveolar cell detachment and apoptosis, mediated by TGF β 3 and LIF activated Stat3 (Macias and Hinck, 2012; Hannan *et al.*, 2023). Continued suckling of pups reverses this step of involution. 48 hours after pup weaning, the second step of involution starts, which is irreversible and results in the collapse of the alveoli and heavy apoptosis. Increased levels of estradiol and decreased levels of prolactin dominate these morphological changes (Hannan *et al.*, 2023). Proteases activate plasminogen and MMPs degrade the ECM to disrupt interactions between the ECM and cells. Adipocytes re-differentiate and replace the secretory epithelium to finally develop back to the rudimental MG tree of a virgin mouse (Macias and Hinck, 2012; Wang and Scherer, 2019).

1.8.3 Breast cancer

Breast cancer is the second most common cancer type diagnosed in women. One distinguishes between different subtypes according to histology, proliferation rate and gene

expression of the tumor. Histologically, tumors are classified into three categories according to their differentiation state with category 1 showing well-differentiated and category 3 poorly differentiated and thus more aggressive tumors (van Steenhoven *et al.*, 2020).

To determine the proliferation, tumors are examined for Ki67 or pH3 levels and the mitotic activity index is calculated. Ki67 is expressed during interphase (G1, S, G2) and mitosis and is required to stabilize the mitotic spindle. Normal breast tissue shows less than 3% of Ki67 levels. As a prognostic marker in breast cancer, levels of less than 10% of Ki67 positive cells are considered as low, whereas levels of more than 20% of Ki67 positive cells are considered as high and correlate with poor survival. On the other hand, phosphohistone H3 (pH3) is a marker to detect phosphorylation of H3^{S10/S20} during the late G2 phase and metaphase of mitosis, which is important for chromatin condensation. This makes pH3 a specific marker for mitotically active cells and is thus more specific for proliferation compared to Ki67 (Kim *et al.*, 2017).

Four different types of breast cancer are distinguished according to distinct gene expression profiles (Herschkowitz *et al.*, 2007; Orrantia-Borunda *et al.*, 2022): (1) The luminal A-like breast cancer is ER⁺, PR⁺, HER2⁻, CK8/18⁺ and shows with low levels of Ki67 (<20%). Low proliferation rates give patients with luminal A subtype the best survival prognosis. (2) The luminal B-like breast cancer is ER⁺, PR^{+/-}, HER2⁺, and CK8/18⁺, has more than 20% Ki67 levels, and shows poorer outcome than luminal A. (3) The HER2-enriched breast cancer is ER⁻, PR⁻, and HER2⁺, and is more aggressive than the luminal breast cancer. (4) The triple-negative (TNBC) or basal-like breast cancer ER⁻, PR⁻, and HER2⁻, and is the most aggressive cancer subtype.

To study breast cancer, cell lines from patients have been established to recapitulate different subtypes. Commonly used breast (cancer) cell lines have been analyzed by IHC staining to classify them according to their molecular expression profile. For example, MCF7 is both positive for ER and PR, but negative for HER2, thus resembling a luminal A breast cancer subtype. On the other hand, MDA-MB-231 and the normal breast epithelial cell line MCF10A cells are all negative for ER, PR, and HER2. These cell lines thus resemble a basal-like breast cancer subtype (Subik *et al.*, 2010).

1.8.4 MMTV-PyMT mouse model

Due to its high relevance in human, breast cancer is widely studied in mouse. Several mouse models have been established, which can be distinguished into (1) xenograft models, (2) radiation-induced models and (3) genetically engineered mouse (GEM) models (Sakamoto, Schmidt and Wagner, 2015). Xenograft models rely on the implantation of cancer cell lines into e.g., the tail vein or the mammary fat pad of immune-compromised mice. They are useful tools to study the behavior of patient-derived cancer cell lines *in vivo*, to investigate KO cell lines of proteins of interests, or to examine pre-treatments of cancer cells. Radiation-induced models are based on gamma- and X-ray irradiations, which induce tumor formation (Rivina, Davoren and Schiestl, 2016). Several generations of GEMs have been established over the years. Here, oncogenes like c-myc, Ha-Ras, HER2/neu and PyMT are expressed under the control of a MG-specific promoter. Combined with KO mouse strands, this enables the evaluation of the role of a protein of interest in spontaneous tumor formation.

A frequently used MG-specific promoter is the U3 promoter from the mouse mammary tumor virus long terminal repeat (MMTV-LTR). The virus is 9 kb in size and contains 5'

and 3' LTRs, which contain TF binding sites and transcriptional regulatory elements, important for virus infection, production, and specific expression in mammary epithelial cells (Ross, 2010). Exogenous MMTV is highly present in milk of diseased female mice and is transmitted via feeding to pups, where it infects lymphocytes and is transported to the MG (Ahmad *et al.*, 2023). Hormone-driven cell proliferation during puberty and pregnancy leads to the infection of mammary epithelial cells with virus, which replicates and integrates to activate transcription of proto-oncogenes (Ross, 2008; Ahmad *et al.*, 2023). MMTV-LTR is expressed and active in mammary luminal and basal epithelial cells, but also in salivary and vesicular glands, macrophages and lymphocytes (Grimm and Nordeen, 1998; Sakamoto, Schmidt and Wagner, 2015). This can cause leaking cancer development additionally to mammary cancer. The MMTV-LTR promoter is highly dependent on steroid hormones and the presence of glucocorticoids and progesterone strongly increases gene transcription (Sonnenberg *et al.*, 1987; Grimm and Nordeen, 1998; Ross, 2008).

The polyomavirus middle T antigen (PyMT) is a potent oncogene to drive epithelial cell transformation and proliferation by e.g. interacting with PI3K, Ras, as well as activating c-src family members (Guy, Cardiff and Muller, 1992).

The MMTV-PyMT transgenic mouse model displays characteristics of a human luminal B breast cancer sub-type, but shows mainly ER⁻ and PR⁻ tumor cells at later cancer stages (Herschkowitz *et al.*, 2007; Fluck and Schaffhausen, 2009; Attalla *et al.*, 2021). It preferably metastasizes into the lung and to a lesser extent to the bone marrow. The tumor progression is divided in four different stages (Figure 25): (1) In the hyperplasia stage, a single lesion arises close to the nipple and several new lesions appear along the ducts. It is

characterized by an intact and normal looking ductal morphology, although myoepithelial cells are more roundish and the nuclear/cytoplasmic ratio is slightly increased. (2) In the Adenoma/MIN stage, intraluminal epithelial cell proliferation happens, myoepithelial cells start to disappear, and the basement membrane breaks open. This results in the infiltration of immune cells like leukocytes or macrophages. The stage is characterized by mass producing (Adenoma) and premalignant (MIN) features. (3) In the early carcinoma stage, the basement membrane is scattered, leading to enhanced stromal invasion, increasing cell heterogeneity and new vessel formation. (4) In the late carcinoma stage, acinar structures have disappeared and solid sheets of densely packed, highly heterogeneous and polynuclear epithelial cells dominate (Lin *et al.*, 2003; Fluck and Schaffhausen, 2009).



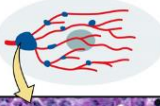

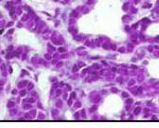
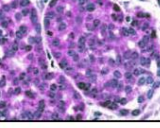
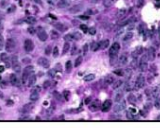
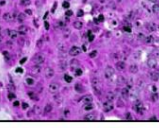
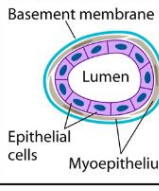
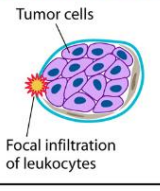
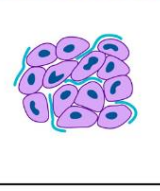
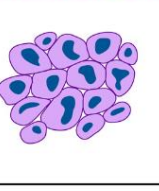
Stage	Hyperplasia	Adenoma/MIN	Early carcinoma	Late carcinoma
Gross				
H&E				
Cellular morphology				
Biomarkers	ER++ PR++ Neu (T/D) ~ 1 Cyclin D1 + Integrin β ±	ER+++ PR++ Neu (T/D) ↑ Cyclin D1 + Integrin β ±	ER++ PR± Neu (T/D) ↑↑ Cyclin D1 ++ Integrin β -	ER± PR- Neu (T/D) ↑↑↑ Cyclin D1 +++ Integrin β -

Figure 25: The MMTV-PyMT breast cancer model. The PyMT-driven cancer progresses from the hyperplasia state via Adenoma/MIN and early carcinoma into late carcinoma. The different states are characterized by enhanced cell proliferation, disruption of the basement membrane, and expression of distinct biomarkers (Fluck and Schaffhausen, 2009).

Depending on the used oncogene and the mouse background, tumor latency varies from three weeks to 18 months and the formation of lung metastases differs in its incidence.

Whereas female MMTV-PyMT-C57BL/6 mice develop breast cancer after 90 days and

rarely form lung metastases, MMTV-PyMT-FVB mice develop tumors after 50 days with faster tumor growth kinetics and form lung metastases within three months (Davie *et al.*, 2007).

Several studies aimed to address the comparability of mouse breast cancer models and human breast cancer patients. Histologically, the MMTV-PyMT model shares many similarities with human luminal breast cancer. Additionally, loss of ER and PR and overexpression of cyclin D1 and HER2 during tumor progression, which correlates with poor prognosis, is both observed in MMTV-PyMT mice and human (Attalla *et al.*, 2021). Loss of β_1 integrin is also associated with tumor progression and is observed in the center of MMTV-PyMT tumors (Lin *et al.*, 2003). Furthermore, the MMTV-PyMT cancer shows genetic aberrations like amplification of chromosome 11, deletions of chromosome 4 and mutations, as well as epigenetic changes like histone methylation that can be also found in human cancer suggesting that mouse studies can be applied to human (Attalla *et al.*, 2021). Overall, the MMTV-PyMT mouse model is a powerful tool to resemble human breast cancer and study cancer progression with human relevance.

2 Aims of the thesis

KANKs have been widely studied in different cell-based systems and have been identified as FA proteins, as well as members of the CMSC. Despite the presence of analogous functional domains within the four distinct KANK family members, they exhibit unique functional characteristics that are specific to each individual member. However, *in vivo* studies on KANKs remain scarce.

Accordingly, the **first aim** of the doctoral research was to examine the expression levels and patterns of the four KANKs in diverse murine tissues through the use of qRT-PCR, WB analysis, and immunofluorescent staining. Based on these experiments, we were able to discern cell-type and organ-specific expression patterns for each KANK (paper I).

Following up on the distinct expression pattern of KANKs *in vivo* evaluated in aim 1, I sought to elucidate the function of KANK2 and KANK4 in murine development in the **second aim**. To this end, we generated KANK2-KO, KANK4-KO and KANK2/4-dKO mice and looked for developmental defects.

The **third aim** of this thesis was to evaluate the function of KANK2 and KANK4 in a breast cancer model. Therefore, I crossed KANK2-KO and KANK4-KO mice with the widely used mouse mammary tumor model MMTV-PyMT and compared the tumor development and metastasis formation in female KANK-WT^{PyMT} and KANK-KO^{PyMT} mice. To complement the *in vivo* studies, I generated a constitutive KO of KANK4 in MCF10A cells, and examined TGF β 1-driven invasion capacities in a 3D collagen/Matrigel matrix.

Parts of the thesis were taken from the yet unpublished manuscript (Seiwert *et al.*), which is currently submitted to *PNAS* for consideration.

3 Materials and Methods

3.1 Animals

C57BL/6 and FVB mice were bred in the animal facility at the Max Planck Institute of Biochemistry, Martinsried, Germany. The MMTV-*PyMT* (stock number 022974) mouse strain was obtained from the Jackson Laboratory. Mice were bred in a special pathogen-free mouse facility and all animal experiments were conducted according to the protocol approved by the government of Upper Bavaria, Germany.

3.1.1 Generation of KANK2-KO and KANK4-KO mice

KANK2-KO-C57BL/6 mice were generated by Dr. Zhiqi Sun using the *Cre/lox* system (Sun, 2015). The targeting construct consisted of a loxP-flanked exon 4 and 5. The KANK2 targeting construct was electroporated into R1-129/Sv embryonic stem (ES) cells followed by G418 selection and isolation of individual ES cell clones that were tested for homologous recombination by Southern Blots using an external DNA probe amplified using the following primers:

- 5'-TGCTTATCTGTGGATTCTAG-3'
- 5'-CCAGCATGCCTGCTATTGTC-3'

Five independent ES cell clones that underwent homologous recombination were used to generate germline chimeras. Homologous loxP-flanked mice were crossed with a cre transgenic mouse strain to obtain KANK2-het mice. KANK2-het mice were backcrossed onto the C57BL/6 and the FVB background for ten generations and then used in this study. Generation of KANK4-KO-C57BL/6 mice was performed by Dr. Shiny Shengzhen Guo. KANK4-KO mice were generated using KO-first allele strategy by EUCOMM ("tm1a"). The KANK4 targeting construct obtained from EuMMCR consisted of a 16.4 kb modified

fragment with a 4.8 kb-recombination 5' arm, a splice acceptor (SA) site followed by promoterless lacZ-neo fusion gene and a polyadenylation (pA) sequence, a loxP-flanked exon 3, and a 5.2 kb-recombination 3' arm (<https://www.eummc.org/products/cassettes>). The KANK4 targeting construct was electroporated into R1-129/Sv embryonic stem (ES) cells followed by G418 selection and isolation of individual ES cell clones that were tested for homologous recombination by Southern Blots using an external DNA probe amplified using the following primers:

- 5'-TTACTAACCCTGACCCCGCC-3'
- 5'-TGCCACCTTATACACCGTCACC-3'

Briefly, genomic DNA was digested with BstEII, separated via 0.8% agarose gel electrophoresis, transferred onto a microcellulose membrane and hybridized with the radioactively labelled cDNA probe. Three independent ES cell clones that underwent homologous recombination were used to generate germline chimeras. The F1 heterozygous offspring from the three independent founders exhibited no apparent phenotype. KANK4-het mice were backcrossed onto the C57BL/6 background for ten generations and then used in this study.

3.1.2 Genotyping of mice

Tail biopsies were taken from mice at weaning age (P21), boiled in 50 mM NaOH for 30 min, neutralized with 0.5 mM Tris-HCl, centrifuged for 5 min at maximum speed, and stored at 4°C.

KANK2 embryos of different developmental stages were genotyped by carefully dissecting the yolk sac. DNA was extracted from the yolk sac like described above.

Genotype was determined via PCR (chapter 3.5.2).

3.1.3 Urine albumin assay

Urine was collected from KANK2-WT and KANK2-KO, KANK4-WT and KANK4-KO, and KANK2/4-WT and KANK2/4-KO mice at the age of 3-6 months. 10 μ L fresh urine were mixed with 10 μ L 2x Laemmli buffer (5% β -mercaptoethanol, 30% glycerol, 10% SDS, 250 mM Tris, pH 6.8, 0.02% bromophenol blue) and boiled at 95°C for 5 min. Samples were loaded on an 8% SDS gel. Proteins were stained overnight using Coomassie Quick Stain (Serva, 35081.01). A BSA control was used to identify the correct size of albumin.

3.1.4 KANK2 embryo preparation

Time matings of KANK2-het mice were set and plug formation was checked every day. Pregnant mice were sacrificed and embryos were carefully dissected under the stereomicroscope MZFLIII (Leica, 15209) at E8.5, E9.5, E11.5 and E14.5. Yolk sacs were stored for genotyping (chapter 3.1.2). Somite pairs were counted to enable exact comparison of the developmental stages. Light microscope images were taken, before embryos were fixed, sectioned and stained (chapters 3.1.10 - 3.1.13).

3.1.5 Whole mount MG staining

MGs from KANK4-WT and KANK4-KO mice were dissected, carefully spread on a glass slide, fixed with Carnoy's fixative (60% pure ethanol, 30% chloroform, 10% glacial acetic acid) for 4 h at RT, gradually rehydrated, stained with carmine alum solution (2.5 g alum potassium sulfate, 1.0 g carmine, 500 mL ddH₂O) overnight at RT, and then gradually dehydrated, washed with xylene, and mounted with EntellanTM (Merck KGaA, 1.07961).

3.1.6 MG isolation at different developmental stages

To isolate MG at pregnancy (E14.5), lactation (D14) and involution (1 m after weaning), time matings of KANK4-WT mice were set and plug formation was checked every day. Pregnant mice were sacrificed at 14.5 days after plug formation (E14.5), 14 days after pup delivery (D14), or one month after weaning and MG were dissected, fixed, sectioned and stained (chapters 3.1.10, 3.1.12).

3.1.7 Tissue isolation for WB

KANK4-WT, KANK4-het and KANK4-KO mice were sacrificed and lungs, MGs, hearts, and kidneys were isolated. The tissues were washed with ice cold PBS (Sigma Aldrich, P4417), suspended in 300 μ L RIPA buffer (150 mM NaCl, 5 mM EDTA, pH 8.0, 50 mM Tris, pH 8.0, 10% NP-40, 10% Na-deoxycholate, 10% SDS) supplemented with protease inhibitors (Roche, 04693159001) and homogenized. After incubation on ice for 10 min, tissue lysates were cleared by centrifugation for 20 min at 4°C. Protein concentration of the supernatants was determined via PierceTM BCA protein assay (ThermoFisher Scientific, 23223) and used for WB analysis (chapter 3.6).

3.1.8 Analysis of tumor development

Tumor onset and growth were monitored in female mice by weekly palpation and measurement of tumor size with a caliper. Tumor volume was calculated as described before (Faustino-Rocha *et al.*, 2013), using the following equation (1).

$$V_{\text{Tumor}} = \frac{\text{width}^2 \times \text{length}}{2} \quad (1)$$

At experimental end point 60 days after tumors were palpated, mice were sacrificed and tumor tissues as well as lungs collected. Total tumor mass was weighed, fixed, sectioned and stained (chapters 3.1.10, 3.1.12). Mice analyzed for tumor growth, tumor weight and metastasis formation are listed in chapter 9.1, Table 14, Table 15, Table 16, and Table 17.

3.1.9 Quantification of lung metastasis

60 days after tumors were palpated, lungs were recovered and the numbers of superficial metastasis were counted under the stereomicroscope MZFLIII (Leica, 15209). Lungs were fixed, embedded in paraffin (ThermoFisher Scientific, 8336) and H&E stained (chapters 3.1.11, 3.1.13).

3.1.10 Cryo embedding of tissues

To obtain MG and embryo tissue sections, tissues were isolated, fixed in 4% PFA (VWR, 1.04005.1000) for 4 h and 1 h, respectively, at 4°C, washed three times with ice cold PBS (Sigma Aldrich, P4417) for 10 min, rotated in 30% sucrose in PBS overnight at 4°C, embedded in Cryomatrix™ (ThermoFisher Scientific, 6769006) and cryo-sectioned using the CryoStar NX70 (epredia) with a thickness of 7 µm.

Snap-frozen clinical human cancer tissue samples were obtained from the Institute of Pathology, University of Cologne, Cologne, Germany, embedded in Cryomatrix™ and sectioned with a thickness of 7 µm. Sections were fixed in 4% PFA for 15 min at RT immediately before IF staining (chapter 3.1.12).

3.1.11 Paraffin embedding of tissues

Lungs (chapter 9.1, Table 16, Table 17) and embryos were isolated, fixed in 4% PFA (VWR, 1.04005.1000) for 4 h and 1 at 4°C, washed three times with ice cold PBS (Sigma

Aldrich, P4417) for 10 min and postfixed in 70% ethanol overnight at 4°C. Tissues were dehydrated in sequential ethanol and xylene steps, incubated in paraffin (ThermoFisher Scientific, 8336) overnight, embedded in fresh paraffin, and cut using the Microm HM355S (ThermoFisher Scientific) with a thickness of 5 µm. Slides with paraffin-embedded sections were incubated at 57°C overnight before dewaxing in xylene, rehydration in sequential ethanol washing steps and H&E staining (chapter 3.1.13).

3.1.12 Immunofluorescence microscopy of cryo-embedded sections

Slides with cryo-embedded sections were washed with PBS (Sigma Aldrich, P4417), permeabilized with 0.1% Triton X-100 in PBS for 15 min, blocked with 3% BSA (PAN Biotech, P06-1391100) in PBS for 1 h at RT, incubated with primary antibodies in 3% BSA overnight at 4°C, washed five times with PBS, and incubated with secondary antibodies for 2 h at RT. After washing with PBS, nuclei were counterstained with DAPI for 10 min at RT and sections were mounted with Elvanol (2.4 g Mowiol 4-88, Roth, 0713.2; 25 mg/mL DABCO, Sigma Aldrich, D27802; 6 g Glycerol; 12 mL 0.2 M Tris, pH 8.5). Confocal images were taken on a Zeiss (Jena) LSM780 confocal laser scanning microscope and images were analyzed using the Zen 2.6 lite (blue edition) software.

Antibodies are listed in chapter 3.2.

3.1.13 H&E staining

Dewaxed slides with paraffin-embedded sections were rinsed with water, incubated with filtered hematoxylin solution (Sigma Aldrich, 1.05174) for 3 min, rinsed with 0.1% HCl solution, washed with water and counterstained with EosinY solution (Sigma Aldrich, 1.02439) for 3 min. Tissues were dehydrated in sequential ethanol washing steps and incubated in xylene for 5 min before mounting with Entellan™ (Merck KGaA, 1.07961).

3.1.14 Determining tumor proliferation and apoptosis

To assess the *in vivo* tumor proliferation rate or apoptosis, MG tumor tissue cryo-sections of KANK4-WT^{PyMT} and KANK4-KO^{PyMT} mice were IF-stained for Ki67 and pH3, or clCasp3, respectively. Ki67⁺, pH3⁺, or clCasp3⁺ transformed LECs were manually counted and normalized to DAPI.

Antibodies are listed in chapter 3.2.

3.2 Antibodies

3.2.1 Primary antibodies

1 st Antibody	Species	Source	Cat. number	Application	Remark
α_4 integrin	Rat	PharMingen	01271D	1:200 (IF)	
Arp3	Mouse	Merck	A5979	1:200 (IF)	
α SMA-FITC	Mouse	Sigma Aldrich	F3777	1:800 (IF)	
β -galactosidase	Rabbit	5'-3'	7-063100	1:100 (IF)	
BrdU	Rat	Abcam	Ab6326	1:1000 (IF)	Denature DNA with 2 M HCl for 30 min at 37°C
Cdc42	Mouse	Cell signaling	8747	1:167 (WB)	
CK8/TROMA-I	Rat	DSHB		1:400 (IF)	
Cleaved Caspase 3	Rabbit	Cell signaling	#9661	1:100 (IF)	
Coro1A	Mouse	Santa Cruz	sc-100925	1:1000 (WB)	
Coro1B	Rabbit	Sigma Aldrich	HPA070456	1:1000 (WB, IF)	
DAPI		ThermoFisher Scientific	D1306	1:10000 (IF)	

1 st Antibody	Species	Source	Cat. number	Application	Remark
E-Cadherin	Rat	Invitrogen	13-1900	1:400 (IF) 1:1000 (WB)	
F-actin (Phalloidin ^{Alexa647})		ThermoFisher Scientific	A22287	1:200 (IF)	
Fibronectin	Rabbit	Home-made		1:500 (IF)	For human cells
GAPDH	Mouse	Sigma Aldrich	CB1001	1:1000 (WB)	
GFP	Mouse	Sigma Aldrich	11814460001	1:200 (WB)	
hKANK4	Rabbit	Home-made		1:1000 (WB)	For human cell lysate
hKANK4	Rabbit	Sigma Aldrich	HPA014030	1:1000 (IF)	For human patient samples
IL6	Rabbit	Abcam	Ab6672	1:400 (IF)	
Ki67	Rabbit	Abcam	Ab15580	1:600 (IF)	pH6 antigen retrieval
KIF21A	Rabbit	Proteintech	27276-1-AP	1:1000 (WB)	
mKANK2	Rabbit	Home-made		1:2000 (IF)	
mKANK4	Rabbit	Home-made		1:1000 (IF)	For mouse tissue
MMP14	Rabbit	Abcam	AB6004	1:200 (IF)	
N-Cadherin	Mouse	Transduction Lab	610920	1:400 (IF) 1:1000 (WB)	
Nidogen	Rat	Chemicon	MAB1946	1:2000 (IF)	
Pan-Cadherin	Goat	Santa Cruz	sc-1499	1:600 (IF)	
Paxillin	Mouse	Transduction Lab	610051	1:300 (IF)	

1 st Antibody	Species	Source	Cat. number	Application	Remark
PPFIBP1 (liprin β 1)	Rabbit	Sigma Aldrich	HPA001924	1:1000 (WB)	
pH3	Rabbit	Upstate	16-189	1:600 (IF)	
pSMAD1	Rabbit	Cell signaling	9511	1:1000 (WB)	
pSMAD2/3	Rabbit	Sigma Aldrich	SAB4504208	1:500 (WB)	
pSMAD3	Rabbit	Abcam	AB52903	1:200 (IF)	
pSTAT3	Rabbit	Cell signaling	9145s	1:1000 (WB)	
PyMT	Rat	Santa Cruz	sc-53481	1:400 (IF) 1:1000 (WB)	
Rac1	Mouse	Cell signaling	8631S	1:1000 (WB)	
RhoA	Rabbit	Cell signaling	8789	1:667 (WB)	
Smad2	Rabbit	Cell signaling	5339	1:1000 (WB)	
Smad3	Rabbit	Cell signaling	9523	1:1000 (WB)	
Smad2/3	Rabbit	Santa Cruz	sc-8332	1:1000 (WB)	
Smad4	Rabbit	Cell signaling	38454	1:1000 (WB)	
Snail	Rabbit	Cell signaling	3879T	1:1000 (WB)	
Talin-1	Mouse	Sigma Aldrich	T3287	1:1000 (WB)	
TGF β 1	Rabbit	ThermoFisher Scientific	PA5120329	1:100 (IF)	
TNF α	Rat	AbboMax	604-960	1:400 (IF)	
Tubulin	Rat	Sigma Aldrich	MAB1864	1:200 (IF)	
Twist1	Mouse	Santa Cruz	sc-81417	1:1000 (WB)	

1 st Antibody	Species	Source	Cat. number	Application	Remark
VCAM-1	Rat	Chemicon	Cbl1300B	1:200 (IF)	
Vimentin	Chicken	Abcam	Ab24525	1:2000 (IF, WB)	
Vinculin	Mouse	Sigma Aldrich	V9131	1:2000 (WB)	
Zeb1	Rabbit	Novusbio	NBP1-05987	1:1000 (WB)	

3.2.2 Secondary antibodies

2 nd Antibody	Source	Cat. number	Dilution
Anti-mouse ^{Alexa488}	Invitrogen	A11029	1:800 (IF)
Anti-mouse ^{Alexa647}	Invitrogen	A31571	1:500 (IF)
Anti-rabbit ^{Cy3}	Jackson Lab	711-165-152	1:800 (IF)
Anti-rat ^{Alexa488}	Life technologies	A21208	1:800 (IF)
Anti-rat ^{Alexa647}	Invitrogen	A21247	1:500 (IF)
Anti-goat ^{Alexa488}	Invitrogen	A11055	1:800 (IF)
Anti-chicken	Invitrogen	A11039	1:800 (IF)
Anti-mouse HRP	Jackson Immuno Research	715-035-151	1:10,000 (WB)
Anti-rabbit HRP	Jackson Immuno Research	711-035-152	1:10,000 (WB)
Anti-rat HRP	Jackson Immuno Research	712-035-150	1:10,000 (WB)
Anti-chicken HRP	Jackson Immuno Research	303-035-003	1:10,000 (WB)

3.2.3 Generation of anti-human KANK4 antibody

Human KANK4-specific antibody was generated with the help of the biochemistry core facility and the animal facility of the Max Planck Institute of Biochemistry, Martinsried, Germany. The human KANK4-specific peptides CGPDGCHKQGNQSPAER (aa 457-471) and CDSEAEKKCDGPDHKKH (aa 692-706) were designed using the AbDesigner

(<https://esbl.nhlbi.nih.gov/AbDesigner/>). The peptides were synthesized together with an N-terminal cysteine residue to couple the peptide with the InjectTM Maleimide Activated mcKLH Spin kit (ThermoFisher Scientific, 77666) to the maleimide-activated carrier protein. Rabbits were immunized by injecting the KANK4 peptides five times every four weeks. The peptides were suspended in TiterMax Gold Adjuvant (Sigma Aldrich, T2684) for the first injection and in incomplete Freund's Adjuvant (Sigma Aldrich, F5506) for the subsequent four injections. Final sera were tested by WB on MKF cells transiently transfected with the pcDNA3.1-hKANK4 expression construct (chapters 3.3.5, 3.5.3, and 3.6).

3.3 *In vitro* cell culture methods

3.3.1 Cell culture of MCF10A cells

MCF10A cells were cultured in DMEM/F12 medium (ThermoFisher Scientific, 11330-032) supplemented with 5% heat inactivated horse serum (ThermoFisher Scientific, 16050-122), 20 ng/mL EGF (PeproTech, AF-100-15), 0.5 mg/mL hydrocortisone (Sigma Aldrich, H-0888), 100 ng/mL cholera toxin (Sigma Aldrich, C-8052), 10 µg/mL insulin (Sigma Aldrich, I-1882) and 1x Pen/Strep (ThermoFisher Scientific, 15140-122). Cells were split using 0.5% Trypsin-EDTA (ThermoFisher Scientific, 15400-054). To induce EMT and KANK4 expression, cells were treated with TGFβ1 (PeproTech, AF-100-21C) at a final concentration of 5 ng/mL for the indicated times. Light microscopy images were taken on an inverted laboratory microscope (Leica DM IL LED).

3.3.2 Cell culture of HMLE-Twist1-ER cells

HMLE-Twist1-ER cells (gift from Dr. Christina Scheel, Institute of Stem Cell Research, Helmholtz Center Munich, Neuherberg, Germany) have been previously described (Mani *et al.*, 2008). Briefly, HMLE-Twist1-ER cells were cultured in Mammary Epithelial Cell Basal Medium (PromoCell, C-21210) supplemented with Growth Medium SupplementMix (PromoCell, C-39115), 1x Pen/Strep (ThermoFisher Scientific, 15140-122) and Blasticidin S HCl (ThermoFisher Scientific, A1113903) at a final concentration of 10 µg/mL. To activate Twist1-ER, fresh medium containing 20 nM Tamoxifen (Sigma Aldrich, H7904) was added to the cell culture every second day. To induce EMT and KANK4 expression, cells were treated with TGFβ1 (PeproTech, AF-100-21C) at a final concentration of 5 ng/mL for the indicated times. Cells were split using 0.5% Trypsin-EDTA (ThermoFisher Scientific, 15400-054). Light microscopy images were taken on an inverted laboratory microscope (Leica DM IL LED).

3.3.3 Cell culture of MKF cells

MKF cells were cultured in DMEM medium (ThermoFisher Scientific, 31966-021) supplemented with 10% heat inactivated FBS (ThermoFisher Scientific, 10270-106), 1x Pen/Strep (ThermoFisher Scientific, 15140-122), 1x NEAA (ThermoFisher Scientific, 11140-035), and 1x Primocin® (InvivoGen, ant-pm-05). Cells were split using 0.5% Trypsin-EDTA (ThermoFisher Scientific, 15400-054).

3.3.4 Cytokine treatment

Cytokines were purchased from PeproTech and the concentrations applied to the cells are listed in Table 1. MCF10A^{KANK4-WT} cells were treated with the respective cytokines for three to four days before collecting cell lysates for WB (chapter 3.6).

Table 1: Cytokines

Cytokine	Source	Cat. number	Concentration
TGFβ1	PeproTech	AF-100-21C	5 ng/mL
TGFβ2	PeproTech	100-35B	5 ng/mL
TGFβ3	PeproTech	100-36E	5 ng/mL
BMP2	PeproTech	120-02C	50 ng/mL
BMP4	PeproTech	AF-120-05ET	50 ng/mL
BMP6	PeproTech	120-06	50 ng/mL
BMP7	PeproTech	120-03P	50 ng/mL
BMP10	PeproTech	120-40	50 ng/mL
Activin	PeproTech	120-14P	50 ng/mL
TNFα	PeproTech	300-01A	50 ng/mL
IL6	PeproTech	200-06	50 ng/mL

3.3.5 Transient transfection

To confirm the specificity of the homemade KANK4 antibody, MKF were transiently transfected with pcDNA3.1-hKANK4 using LipofectamineTM 2000 (ThermoFisher Scientific, 11668019) according to the manufacturer's instructions. Briefly, cells were detached and seeded into 6-well plates. After 24 h, 1.5 µg plasmid per well in 175 µL Opti-MEMTM (ThermoFisher Scientific, 31985062) were mixed with 3 µL LipofectamineTM 2000 in 150 µL Opti-MEMTM. The plasmid mixture was incubated for 5 min, added to the cells and incubated for 5 h, before changing to fresh medium and cultured for 24 h. Cell

lysates were harvested for WB analysis (chapter 3.6).

To detect Rac1 activity, MCF10A cells ectopically expressing GFP-KANK4 were transiently transfected with tdTomato-WASp using LipofectamineTM 3000 (ThermoFisher Scientific, L3000001) according to manufacturer's instructions. CMVdel-dimericTomato-WASp(CRIB) was a gift from Dorus Gadella (Addgene plasmid #191450; <http://n2t.net/addgene:191450>; RRID: Addgene_191450) (Mahlandt *et al.*, 2023). Briefly, cells were detached and seeded onto fibronectin-coated 8-well glass bottom chamber slides (ibidi, 80827). 0.5 µg plasmid per well were diluted with 1 µL P3000 in 25 µL Opti-MEMTM and mixed with 0.75 µL LipofectamineTM 3000 reagent in 25 µL Opti-MEMTM. The plasmid mixture was incubated for 15 min, added to the cells and incubated for 5 h, before changing to fresh medium without or with TGFβ1 at a final concentration of 5 ng/mL and cultured for three days. Cells were fixed and analyzed via TIRF microscopy (SR1 Zeiss Elyra PS.1 microscope) (chapter 3.4.1).

To perform GFP-IP, MCF10A cells ectopically expressing GFP or GFP-KANK4 were transiently transfected with pCB6-CorolA-HA using LipofectamineTM 3000 according to manufacturer's instructions. pCB6-Cor1-HA was a gift from Jean Pieters (Addgene plasmid #102815; <http://n2t.net/addgene:102815>; RRID: Addgene_102815) (Gatfield *et al.*, 2005). Briefly, cells were detached and seeded into a 15-cm dish. 15 µg plasmid per dish were diluted with 30 µL P3000 in 1 mL Opti-MEMTM and mixed with 50 µL LipofectamineTM 3000 reagent in 1 mL Opti-MEMTM. The plasmid mixture was incubated for 15 min, added to the cells and incubated for 5 h, before changing to fresh medium and cultured for three days. Cells were lysed and GFP-IP was performed (chapter 3.7.2).

Plasmids are listed in Table 12 (chapter 3.5.3).

3.3.6 Viral transduction

For generating CRISPR/Cas9-KO cell lines, MCF10A^{KANK4-WT} cells were transduced with eSpCas9Plus-T2A-TagBFP2 lentiviral vector.

To perform rescue experiments, MCF10A^{KANK4-WT} and MCF10A^{KANK4-KO} cells were transduced with either pRetroQ-GFP or pRetroQ-GFP-KANK4, or HSC1-GiP-GFP or HSC1-GiP-CA-Rac1-GFP retroviral vectors. HSC1-GiP was a gift from James Ellis (Addgene plasmid #58254; <http://n2t.net/addgene:58254>; RRID: Addgene_58254) (Rival-Gervier *et al.*, 2013). HMLE-Twist1-ER cells were transduced with pRetroQ-GFP-KANK4 retroviral vector.

To induce EMT independently of TGFβ1 in MCF10A^{KANK4-WT} and HMLE-Twist1-ER cells, cells were transduced with pRetroQ-Snail retroviral vector, cloned from SnailHA_pcDNA3. SnailHA_pcDNA3 was a gift from Paul Wade (Addgene plasmid #31697; <http://n2t.net/addgene:31697>; RRID: Addgene_31697) (Kajita, McClinic and Wade, 2004).

For transforming MCF10A^{KANK4-WT} cells, cells were transduced with pBabe-hygro-PyMT retroviral vector. pBabe-hygro-PyMT was a gift from Filippo Giancotti (Addgene plasmid #22305; <http://n2t.net/addgene:22305>; RRID: Addgene_22305) (Pylayeva *et al.*, 2009).

To localize Rac1 in cells, MCF10A cells ectopically expressing GFP-KANK4 were transduced with pRetroD-Rac1-mCherry retroviral vector.

Plasmids are listed in Table 12 (chapter 3.5.3).

3.3.7 CRISPR/Cas9-mediated deletion of *KANK4* gene

The Cas9-stable expressing MCF10A cell line (MCF10A^{Cas9}) was generated by transducing the cells with eSpCas9Plus-T2A-TagBFP2 leading to stable expression of

BFP-labelled Cas9. The gRNA was designed via the ChopChop online software (<https://chopchop.cbu.uib.no/>) and was synthesized using the GeneArt™ Precision gRNA Synthesis kit (ThermoFisher Scientific, A29377). The cDNAs consisting of the gRNA sequence in the core, T7 promoter sequence for *in vitro* transcription and the crRNA/tracrRNA constant region for efficient targeting were synthesized, assembled with Phusion™ High-Fidelity PCR master mix (ThermoFisher Scientific, F531L) and then *in vitro* transcribed with the TranscriptAid™ Enzyme Mix (ThermoFisher Scientific, A29377). The purified gRNA (gRNA_KANK4: GGCCGATCACAACGGGAACACGG) was electroporated into MCF10A^{Cas9} cells followed by BFP-based cell sorting using BD FACSAria™ III Cell Sorter (BD Biosciences) for generating single-cell colonies. Disruption of the *KANK4* gene was determined by DNA sequencing. For this, DNA was isolated using DNA isolation quick kit (Macherey-Nagel, 740569.250), before amplifying the DNA via PCR (chapter 3.5.2), purifying the product via 1% agarose gel electrophoresis, extracting the band using the QIAquick® gel extraction kit (28704, Qiagen) and subsequent sequencing (TubeSeq, Eurofins). KO-score was analyzed via <https://ice.synthego.com/#/>. KANK4-KO was verified by WB analysis (chapter 3.6). The MCF10A^{KANK4-WT} parental cells, one MCF10A^{KANK4-WT} clone (Clone #1) and two MCF10A^{KANK4-KO} clones (Clone #2 and #3, both KO-score=100) were used in the experiments.

3.3.8 KD of Smad proteins and coronins

The siRNA depletion experiments were carried out with siRNA SMARTpool obtained from Dharmacon (Table 2). A non-targeting siRNA pool was used as control. siRNAs were resuspended in 1x siRNA buffer (horizon, B-002000-UB-100) to obtain 20 µM siRNA stock solutions. Transfections of siRNAs were carried out using Lipofectamine® RNAiMax

reagent (Invitrogen, 13778075) according to the manufacturer's instructions. Briefly, cells were seeded into a 6-well plate one day prior to transfection with the respective siRNA diluted in Opti-MEMTM and the appropriate amount of Lipofectamine[®] RNAiMax reagent. TGFβ1 at a final concentration of 5 ng/mL was added and the cells were incubated for three days, before morphological analysis, harvesting cell lysates for WB analysis (chapter 3.6), or 3D culture (chapter 3.4.5.1).

Table 2: siRNAs

siRNA	Source	Cat. number	Final concentration
Smad2	Dharmacon	L-003561-00-0005	50 nM
Smad3	Dharmacon	L-020067-00-0005	50 nM
Smad4	Dharmacon	L-003902-00-0005	50 nM
Coro1A	Dharmacon	L-012771-00-0005	50 nM
Coro1B	Dharmacon	L-010493-01-0005	50 nM
Control	Dharmacon	D-001810-10-05	50 nM

3.4 Cell biology-based methods

3.4.1 Immunofluorescence microscopy of cells

Cells were cultured on fibronectin-coated coverslips or 8-well glass bottom chamber slides (ibidi, 80827) without or with TGFβ1 at a final concentration of 5 ng/mL for three days. Cells were washed with PBS (Sigma Aldrich, P4417), fixed with 4% PFA (VWR, 1.04005.1000) for 15 min at RT, and washed again with PBS. Cells were permeabilized with 0.1% Triton X-100 in PBS for 15 min, blocked with 3% BSA (PAN Biotech, P06-1391100) in PBS for 1 h at RT, incubated with primary antibodies in 3% BSA overnight at 4°C, washed five times with PBS, and incubated with secondary antibodies for 2 h at RT. After washing with PBS, nuclei were counterstained with DAPI for 10 min at RT and cells

cultured in 8-well glass bottom chamber slides were stored in PBS, whereas cells cultured on coverslips were mounted with Elvanol (2.4 g Mowiol 4-88, Roth, 0713.2; 25 mg/mL DABCO, Sigma Aldrich, D27802; 6 g Glycerol; 12 mL 0.2 M Tris, pH 8.5). Confocal images were taken on a Zeiss (Jena) LSM780 confocal laser scanning microscope and TIRF images were taken at the imaging core facility of the Max Planck Institute of Biochemistry, Martinsried, Germany using SR1 Zeiss Elyra PS.1 microscope. Images were analyzed using the Zen 2.6 lite (blue edition) software.

Antibodies are listed in chapter 3.2.

3.4.1.1 BrdU staining

For BrdU staining, MCF10A^{KANK4-WT} and MCF10A^{KANK4-KO} cells treated without or with TGFβ1 at a final concentration of 5 ng/mL for three days were incubated with 10 μM BrdU (Upstate, 19-160) in DMSO (Serva, 20385.0) for 2 h at 37°C, washed with PBS (Sigma Aldrich, P4417), fixed with 4% PFA (VWR, 1.04005.1000) for 15 min at RT, washed with PBS again and incubated with 2 M HCl in H₂O solution for 30 min at 37°C followed by IF staining (chapter 3.4.1). BrdU⁺ cells were counted using CellPose. The ratio of BrdU⁺ cells to the respective DAPI⁺ total cells was calculated for each image and plotted in a graph.

Antibodies are listed in chapter 3.2.

3.4.2 2D migration assay

MCF10A^{KANK4-WT} and MCF10A^{KANK4-KO} cells were treated with TGFβ1 at a final concentration of 5 ng/mL for five days, before seeding onto collagen I-coated 0.5 kPa hydrogel plates (Cell Guidance Systems, Softwell®, SW5-Col-0.5 kPa) containing a glass cover slip in one half of the well to prevent cell adhesion to the hydrogel. After 24 h, the

cells were serum-starved with medium containing 1% horse serum (ThermoFisher Scientific, 16050-122) for 2 h and the glass cover slip was removed to generate a migration front. Fresh 1% horse serum containing medium was added and cells were imaged every 15 min for >three days using VisiScope Live Cell Imaging System (Software: VisiView Version 4.5.0.13).

3.4.3 Analysis of lamellipodia formation

To analyze lamellipodia formation, MCF10A^{KANK4-WT}, MCF10A^{KANK4-KO}, MCF10A^{KANK4-KO} cells ectopically expressing GFP-KANK4, or MCF10A^{KANK4-WT} cells siRNA-depleted of CorolA, CorolB, or CorolA/B were seeded on collagen I-coated 0.5 kPa hydrogel plates and cultured with TGFβ1 at a final concentration of 5 ng/mL for three days. The total cell number was counted using CellPose. The number of lamellipodia forming cells were counted manually and normalized to the total cell number. Circularity was determined using the Fiji ImageJ measurement tool (ImageJ 2.14.0/1.54f).

3.4.4 Detection of invadopodia

Invadopodia detection was performed as previously described (Díaz, 2013). Briefly, 8-well glass bottom chamber slides (ibidi, 80827) were coated with 50 μL of 1 mg/mL gelatin-488 (ThermoFisher Scientific, G13186). Excess liquid was carefully aspirated, the coating was dried for 10 min at RT and then 200 μL of cold 0.5% glutaraldehyde solution (Carl Roth, 4157.1) were added into each well and incubated for 15 min on ice. Wells were washed three times with PBS (Sigma Aldrich, P4417) and residual aldehyde was quenched by adding MCF10A culture medium for 30 min at 37°C. MCF10A^{KANK4-WT} and MCF10A^{KANK4-KO} cells were seeded onto the gelatin and cultured with TGFβ1 at a final

concentration of 5 ng/mL for two days. Cells were fixed and stained (chapter 3.4.1). TIRF images were taken at the imaging core facility of the Max Planck Institute of Biochemistry, Martinsried, Germany using SR1 Zeiss Elyra PS.1 microscope. Images were analyzed using the Zen 2.6 lite (blue edition) software. The number of invadopodia per cell was counted manually.

Antibodies are listed in chapter 3.2.

3.4.5 3D collagen/Matrigel invasion assay

3D culture was performed with MCF10A^{KANK4-WT} and MCF10A^{KANK4-KO} cells. For rescue experiments, MCF10A^{KANK4-WT} and MCF10A^{KANK4-KO} cells ectopically expressing pRetroQ-GFP, pRetroQ-GFP-KANK4, HSC1-GiP-GFP or HSC1-GiP-CA-Rac1-GFP were used. To investigate TGFβ1-independent EMT, HMLE-Twist1-ER cells ectopically expressing pRetroQ-GFP-KANK4 were used.

Cells were cultured in a 3D collagen/Matrigel mixture adapted as previously described (Debnath, Muthuswamy and Brugge, 2003). Briefly, 48-well plate was coated with 30 µL mixture of neutralized 2 mg/mL rat tail collagen I (Corning, 354249) and 2 mg/mL Matrigel (Corning, 354230) for at least 30 min at 37°C until gelification was completed. Subsequently, 100 µL cell suspension (5x10⁴ cells/mL) was gently mixed with 100 µL of collagen/Matrigel mixture (4 mg/mL each), from which 150 µL were seeded on top of the coated wells. The mixture was incubated for 60 min for gelification before 500 µL medium was added. After 24 h of incubation, fresh medium without or with TGFβ1 at a final concentration of 5 ng/mL was applied. Spheroid growth was monitored for up to 12 days and the respective medium was changed every two to three days. Images were taken using InvitrogenTM EVOSTM FL Auto 2 Imaging System (ThermoFisher Scientific, 15736152).

For live cell imaging of 3D cell invasion, spheroids were prepared as described above and incubated with TGF β 1 for five days prior to image acquisition. Fresh TGF β 1 in 700 μ L medium per well were added and images were taken every 30 min for five days using VisiScope Live Cell Imaging System (Software: VisiView Version 4.5.0.13), without changing medium in between.

3.4.5.1 Inhibition and KD in 3D collagen/Matrigel invasion assay

To investigate the relevance of small GTPases Rac1 and Cdc42, as well as Coro1A and Coro1B in 3D invasion, MCF10A^{KANK4-WT} cells were embedded in collagen/Matrigel like described above and chemical inhibitors (Table 3) or Coro1A/B siRNAs mixed with Lipofectamine[®] RNAiMax reagent (Invitrogen, 13778075) (see chapter 3.3.8, Table 2) were applied to the culture medium every other day.

Table 3: Small GTPase inhibitors

Inhibitor	Source	Cat. number	Final concentration
EHT1864 (Rac1)	Selleckchem	S7482	10 μ M
NSC23766 (Rac1)	Selleckchem	S8031	100 μ M
ML141 (Cdc42)	MedChemExpress	HY-12755	5 mM

3.4.6 Gelatin zymography assay

MCF10A^{KANK4-WT} and MCF10A^{KANK4-KO} cells were cultured in 10-cm dishes without or with TGF β 1 at a final concentration of 5 ng/mL for three days. At 70% confluency, cells were washed three times with PBS (Sigma Aldrich, P4417) and cultured in serum-free medium without or with TGF β 1 at a final concentration of 5 ng/mL for three days. The conditioned supernatant was collected, filtered, and concentrated using Amicon Ultra-4 Centrifugal Filters (Merck Millipore, UFC801024D) at 5000xg for 15 min to achieve a

final volume of 250 μ L. Cells were lysed with 300 μ L zymography lysis buffer (25 mM Tris, pH 7.4, 100 mM NaCl, 0.1% NP-40), incubated on ice for 15 min and centrifuged at maximum speed for 20 min at 4°C. Protein concentration was determined via PierceTM BCA protein assay (ThermoFisher Scientific, 23223). Samples were adjusted to the same protein concentration in 5x non-reducing sample buffer (125 mM Tris-HCl, pH 6.8, 4% SDS, 20% glycerol, 0.01% bromophenol blue) and loaded onto 7.5% acrylamide gels containing 4 mg/mL gelatin and separated at 120 V. The gelatin gel was briefly rinsed with ddH₂O and washed twice with washing buffer (50 mM Tris-HCl, pH 7.5, 2.5% Triton X-100, 5 mM CaCl₂, 1 μ M ZnCl₂) for 30 min each. The gel was then incubated for 5 min with incubation buffer (50 mM Tris-HCl, pH 7.5, 1% Triton X-100, 5 mM CaCl₂, 1 μ M ZnCl₂) at 37°C before replacing the buffer with fresh incubation buffer and shaking at 37°C for 24 h. The gel was stained with Coomassie Quick Stain (Serva, 35081.01).

3.4.7 GTPase activity assay

The GTPase activity assay was performed with active GTPase detection kits (Cell signaling, #8815 for Rac1, #8819 for Cdc42, and #8820 for RhoA) according to the manufacturer's instructions. Briefly, MCF10A^{KANK4-WT} and MCF10A^{KANK4-KO} cells were cultured without or with TGF β 1 at a final concentration of 5 ng/mL for four days. Cells were washed twice with cold PBS (Sigma Aldrich, P4417), lysed with 200 μ L 1x lysis buffer supplemented with protease inhibitors (Roche, 04693159001) and cleared by centrifugation. Supernatants were collected, protein concentration was determined via PierceTM BCA protein assay (ThermoFisher Scientific, 23223) and adjusted to 1 mg/mL. 700 μ L cell lysate was added to glutathione agarose beads supplemented with 20 μ g GST-Pak1-PBD (Rac1, or Cdc42), or 400 μ g GST-Rhotekin-RBD (RhoA) and incubated for 1-

3 h at 4°C under constant rotation. The beads were washed three times with 1x lysis buffer, and active GTPase was eluted with 2x SDS sample buffer, supplemented with 200 mM DTT (ThermoFisher Scientific, R0861) and analyzed by WB (chapter 3.6).

3.4.8 Contraction assay

MCF10A^{KANK4-WT} and MCF10A^{KANK4-KO} cells were treated without or with TGFβ1 at a final concentration of 5 ng/mL for four days before culturing them on fibronectin-coated 10-cm dishes for 1 day. Rat tail collagen I (Corning, 354249) was diluted to 3 mg/mL with 0.1% acetic acid and rotated overnight at 4°C. Fibronectin (1:100) was added to the diluted collagen and the mixture was rotated again for several hours at 4°C. Cells were trypsinized and the cell suspension (1.5×10^6 cells/mL) was gently mixed on ice with collagen at a final concentration of 1 mg/mL. 1 M NaOH was added to neutralize collagen. 500 µL cell-collagen mixture was added in triplicates into a prewarmed 24-well plate. As a control, collagen at a final concentration of 1 mg/mL without cells was added into the well plate. The mixture was incubated for 60 min for gelification, before carefully detaching the gels from the plastic wells using a pipette tip. 600 µL medium without or with TGFβ1 at a final concentration of 5 ng/mL were added to each well and gels were further detached until they were floating in the medium. Cells were incubated for 96 h and images of the gel area were taken every 24 h using the stereomicroscope MZFLIII (Leica, 15209). The relative gel area normalized to the control gel lacking cells was plotted.

3.5 Nucleic acid-based methods

3.5.1 RNA-isolation and qRT-PCR

Total RNA of MCF10A and HMLE-Twist1-ER cells treated without or with TGFβ1 at a final concentration of 5 ng/mL or 20 nM Tamoxifen was extracted using the RNeasy Mini extraction kit (Qiagen, 74104). cDNA was generated via the iScript cDNA Synthesis kit (Biorad, 170-8891) and qRT-PCR was performed with the Light-Cycler®480 Instrument II (Roche). Samples were measured in triplicates. The levels of *KANK4* were normalized to *GAPDH* levels. Treated samples were normalized to control samples. PCR primers are listed in Table 4. qRT-PCR protocol is listed in Table 5.

Table 4: qRT-PCR primers

Primer pair	Product length
<i>KANK4</i> Fwd: 5'-CCACTCCAACCTTCTCCATCG-3' Rvs: 5'-TGTCTTCATTGGTCTCTGCG-3'	128 bp
<i>GAPDH</i> Fwd: 5'-GTCTCCTCTGACTTCAACAGCG-3' Rvs: 5'-ACCACCCTGTTGCTGTAGCCAA-3'	131 bp

Table 5: qRT-PCR protocol

Component	Volume/reaction	Reaction setup	
cDNA	5 μL	95°C – 5 min	
ddH ₂ O	3.8 μL	95°C – 15 sec	40 cycles
Primer Fwd	0.6 μL	57°C – 15 sec	
Primer Rvs	0.6 μL	95°C – 15 sec	
SYBR green	10 μL	60°C – 15 sec	
		95°C – 15 sec	
		4°C – ∞	

3.5.2 PCR

Genotyping PCRs were performed using mi-Taq polymerase (metabion, mi-E8015S) (chapter 3.1.2). DNA amplification was performed on a thermocycler (Biometra TRIO 48, analytikjena). The amplified DNA fragments were separated via 3% agarose gel electrophoresis. PCR primers are listed in Table 6. PCR setup and cycling protocols are listed in Table 7, Table 8, and Table 9.

Table 6: Genotyping primers

Gene	Primer pair	Product length
<i>KANK2</i>	5'-CCTGAAGTCAACCAGAGGAACC-3'	WT size: 382 bp
	5'-GAACTTGCCAGATAGGCTAGG-3'	KO size: 481 bp
	5'-CGGGTAAGTAGGGGTCTGAAAT-3'	
<i>KANK4</i>	Fwd: 5'-CGCCGCCAGGTAAATATTCA-3'	WT size: 363 bp
	Rvs: 5'-CCAAGAAGGGACACCCAGGA-3'	KO size: 419 bp
<i>PyMT</i>	5'-GGAAGCAAGTACTTCACAAGGG-3'	WT allele size: 200 bp
	5'-GGAAAGTCACTAGGAGCAGGG-3'	PyMT allele: 556 bp
	5'-CAAATGTTGCTTGTCTGGTG-3'	
	5'-GTCAGTCGAGTGCACAGTTT-3'	

Table 7: KANK2 genotyping PCR

Component	Volume/reaction	Reaction setup	
DNA	3 μL	94°C – 5 min	
ddH ₂ O	12.45 μL	94°C – 30 sec	35 cycles
5x buffer	2 μL	64°C – 30 sec	
dNTP	0.5 μL	72°C – 30 sec	
Primer 1	0.6 μL	72°C – 5 min	
Primer 2	0.6 μL	4°C – ∞	
Primer 3	0.6 μL		
miTaq	0.25 μL		

Table 8: KANK4 genotyping PCR

Component	Volume/reaction	Reaction setup	
DNA	3 μ L	94°C – 5 min	
ddH ₂ O	13.75 μ L	94°C – 30 sec	30 cycles
5x buffer	2 μ L	62°C – 30 sec	
dNTP	0.5 μ L	72°C – 30 sec	
Primer Fwd	0.25 μ L	72°C – 5 min	
Primer Rvs	0.25 μ L	4°C – ∞	
miTaq	0.25 μ L		

Table 9: PyMT genotyping PCR

Component	Volume/reaction	Reaction setup	
DNA	3 μL	94°C – 2 min	
ddH ₂ O	13 μL	94°C – 20 sec	10 cycles Touchdown -0.5°C
5x buffer	2.5 μL	65°C – 15 sec	
DMSO	0.75 μL	68°C – 10 sec	
dNTP	0.5 μL	94°C – 20 sec	28 cycles
Primer 1	0.25 μL	60°C – 15 sec	
Primer 2	0.25 μL	72°C – 10 sec	
Primer 3	0.25 μL	72°C – 2 min	
Primer 4	0.25 μL	4°C – ∞	
miTaq	0.25 μL		

To verify KANK4-KO, PCR using Q5 Hot Start polymerase (New England Biolabs, M0493) was performed on DNA isolated from MCF10A^{Cas9} cells transfected with *KANK4*-specific gRNA (chapter 3.3.7). The amplified DNA fragments were separated via 1% agarose gel electrophoresis. Primers are listed in Table 10. PCR setup and cycling protocols are listed in Table 11.

Table 10: CRISPR/Cas9 primers

Gene	Primers	Product length	Comment
<i>KANK4</i>	Fwd: 5'-ACAGAGGCCAAAGCTGTCTTTC-3'	486 bp	Used for sequencing
	Rvs: 5'-GTATGCTATTTGGGTGATGGGT-3'		
	5'AAATTGCCCTGCTCTTCAAGG-3'		

Table 11: KANK4 PCR

Component	Volume/reaction	Reaction setup	
DNA	1 μL	94°C – 5 min	
ddH ₂ O	35 μL	94°C – 30 sec	30 cycles
Q5 reaction buffer 5x	10 μL	66°C – 30 sec	
dNTP	2 μL	72°C – 30 sec	
Primer Fwd	1 μL	72°C – 5 min	
Primer Rvs	1 μL	4°C – ∞	
Q5 Hot Start	1 μL		

3.5.3 Plasmids and primers

Plasmids used for transient transfection or viral transduction are listed in Table 12. Primers designed for Gibson assemblies are listed in Table 13.

The pcDNA3.1-hKANK4 plasmid was generated by amplifying hKANK4 from hKANK4-pBluescript (primers listed in Table 13) and inserted between the NheI and XhoI sites of pcDNA3.1. Correct insertions and plasmid assemblies were verified by Sanger Sequencing (Tube Ecoli NightSeq[®] Prepaid, Microsynth, or TubeSeq, Eurofins).

Table 12: Plasmids

Name	Backbone	Insert	Species	Transfection	Source	Reference
GFP	pRetroQ(EF-1a)	GFP		Viral		
GFP-KANK4	pRetroQ(EF-1a)	KANK4	Human	Viral	Home-made	Current work
Rac1-mCherry	pRetroD-mCherry	Rac1	Human	Viral	Home-made	Current work
GFP	HSC1-GiP	GFP		Viral	Addgene #58254	(Rival-Gervier <i>et al.</i> , 2013)
CA-Rac1-GFP	HSC1-GiP	CA-Rac1 (Q61L)	Human	Viral	Home-made	Current work
SnailHA	pcDNA3	SnailHA	Human		Addgene #31697	(Kajita, McClinic and Wade, 2004)
Snail	pRetroQ	Snail	Human	Viral	Home-made	Current work
Coro1A-HA	pCB6	Coro1A-HA	Mouse	Transient	Addgene #102815	(Gatfield <i>et al.</i> , 2005)
hKANK4	pcDNA3.1	KANK4	Human	Transient	Home-made	Current work
tdTomato-WASp	pEGFP-C1	WASp(CRIB)	Human	Transient	Addgene #191450	(Mahlandt <i>et al.</i> , 2023)
PyMT	pBabe-hygro	PyMT	Mouse	Viral	Addgene #22305	(Pylayeva <i>et al.</i> , 2009)
eSpCas9Plus-T2A-TagBFP2	pLenti-SFFVT7	Cas9Plus	S.pyogenes	Viral	Home-made	

Table 13: Cloning primers

Final plasmid	Primer pair
pRetroQ-GFP-KANK4	Insert Fwd: 5'-AGTCCGGACTCAGATCTCGAGAGAAGACAGATGCCAAAGACCAG-3'
	Insert Rvs: 5'-GCAGAATTCTGAAGCTTGAGCCTACAGCCCCAGGGACCTGC-3'
	Vector Fwd: 5'-GCAGGTCCCTGGGGCTGTAGGCTCAAGCTTCGAATTCTGCAGT-3'
	Vector Rvs: 5'-TCTTTGGCATCTGTCTTCTCTCGAGATCTGAGTCCGGACTT-3'
pRetroD-Rac1-mCherry	Insert Fwd: 5'-CTTCGAATTCTGCAGTCGACATGCAGGCCATCAAGTGTG-3'
	Insert Rvs: 5'-GAGCCTGGACCACTGATGGGTTACAACAGCAGGCATTTTCTCTTCCTC-3'
	Vector Fwd: 5'-GAAAATGCCTGCTGTTGTAACCCATCAGTGGTCCAGGCTCTAGT-3'
	Vector Rvs: 5'-ACACACTTGATGGCCTGCATGTCTGACTGCAGAATTCGA-3'
HSC1-GiP-CA-Rac1-GFP	Insert Fwd: 5'-AGGTGTCGTGAGAATTAGCCATGCAGGCCATCAAGTG-3'
	Insert Rvs: 5'-TAACGTCGAGGTTGGCCGCTTTACAACAGCAGGCATTTTCTCTTCC-3'
	Vector Fwd: 5'-GAAAATGCCTGCTGTTGTAAAGCGGCCAACCTCGACGT-3'
	Vector Rvs: 5'-ACACACTTGATGGCCTGCATGGCTAATTCTCACGACACCTG-3'
pRetroQ-Snail	Insert Fwd: 5'-TAGCGCTACCGGTCGCCACCATGCCGCGCTCT-3'
	Insert Rvs: 5'-TCTAGAGTCGCGGCCGCTTAGCGGGGACATCCTGAGC-3'
	Vector Fwd: 5'-GCTGCTCAGGATGTCCCCGCTAAGCGGCCGCGACTCT-3'
	Vector Rvs: 5'-ACGAGGAAAGAGCGCGGCATGGTGGCGACCGGT-3'
pcDNA3.1-hKANK4	Fwd: 5'-CAAGCTGGCTAGCATGGAGAAGACAGATGCCAAAG-3'
	Rvs: 5'-ACAGTGGCGGCCGCTCGAGCTACAGCCCCAGGGAC-3'

3.6 Protein-based methods

3.6.1 SDS-PAGE

Cells were cultured for a given time under the specified conditions. Cells were lysed on ice using RIPA buffer (150 mM NaCl, 5 mM EDTA, pH 8.0, 50 mM Tris, pH 8.0, 10% NP-40, 10% Na-deoxycholate, 10% SDS) supplemented with protease inhibitors (Roche, 04693159001), 0.1% SDS, and benzonase (Merck, E1014). Cell fragments were centrifuged for 15 min at maximum speed at 4°C and the protein concentration of the supernatant was determined via PierceTM BCA protein assay (ThermoFisher Scientific, 23223). The protein lysates were separated via SDS-PAGE under denaturing conditions in SDS running buffer (25 mM Tris, 250 mM glycine, 0.1% SDS) using 4-15% precast polyacrylamide gels (Bio-Rad, 4561086).

3.6.2 Western Blot (WB)

Proteins were transferred onto nitrocellulose membranes using the Trans-Blot[®] TurboTM transfer kit (Bio-Rad, 1704270) and the Trans-Blot[®] TurboTM Transfer System (Bio-Rad, 1704150). After transfer, the membranes were blocked with 5% BSA (PAN Biotech, P06-1391100) in 1x TBS-T (10x: 200 mM Tris, pH 7.6, 1.5 M NaCl, 1% Tween-20) for 1 h at RT and incubated with primary antibodies in 5% BSA overnight at 4°C. Membranes were washed with 1x TBS-T and incubated with secondary antibodies for 1 h at RT. The membranes were developed with Chemiluminescent HRP substrate (Millipore, P90720) using the AmershamTM Imager 600RGB (GE Healthcare). Membranes were stripped for 4 h at RT using stripping buffer (1% glycine, 1% SDS, 0.0005% NP-40, pH 2.2), before blocking and antibody decoration as described above. The protein levels were quantified

using ImageStudioLite (version 5.2.5).

Antibodies are listed in chapter 3.2.

3.7 Proteomic techniques

3.7.1 Proteomics

MCF10A^{KANK4-WT} cells were seeded in 15-cm dishes and treated without or with TGFβ1 (in triplicates each) at a final concentration of 5 ng/mL for three days. Cells were washed with PBS (Sigma Aldrich, P4417) and collected in an Eppendorf tube. Cells were centrifuged and cell pellets were submitted for total proteome analysis to the mass spectrometry core facility of the Max Planck Institute of Biochemistry, Martinsried, Germany.

3.7.2 GFP-IP

MCF10A cells stably expressing GFP or GFP-KANK4 were seeded in 15-cm dishes. To determine KANK4 interactome, cells were treated without or with TGFβ1 (in triplicates each) at a final concentration of 5 ng/mL for three days. To verify KANK4-CorolA/1B interaction, cells were transiently transfected with 15 µg CorolA-HA plasmid (see chapter 3.5.3, Table 12) for 24 h. Cells were lysed in lysis buffer (10 mM Tris, pH 8.0, 150 mM NaCl, 0.5 mM EDTA, 1% NP-40) supplemented with protease inhibitors (Roche, 04693159001). Lysates were sonicated for 10 sec with 30% intensity. Supernatant was collected and protein concentration was determined via PierceTM BCA protein assay (ThermoFisher Scientific, 23223). GFP-beads (30 µL per sample; GFP-Trap® agarose, Chromotek) were incubated with 0.5 mg protein lysate for 3 h at 4°C under constant rotation. Beads were centrifuged and washed three times with wash buffer (10 mM Tris,

pH 8.0, 150 mM NaCl, 0.5 mM EDTA).

For WB, proteins were eluted by adding 50 μ L of hot 4x Laemmli buffer (5% β -mercaptoethanol, 30% glycerol, 10% SDS, 250 mM Tris, pH 6.8, 0.02% bromophenol blue) to the beads and samples were boiled for 5 min at 95°C, before analysis by WB (chapter 3.6).

For proteomic analysis, beads were washed additionally twice with PBS (Sigma Aldrich, P4417) and samples on-beads were submitted for interaction proteomics analysis to the mass spectrometry core facility of the Max Planck Institute of Biochemistry, Martinsried, Germany.

3.7.3 Endogenous IP

MCF10A^{KANK4-WT} cells were seeded in 15-cm dishes and treated without or with TGF β 1 (in triplicates each) at a final concentration of 5 ng/mL for three days. Cells were lysed in lysis buffer (10 mM Tris, pH 8.0, 150 mM NaCl, 0.5 mM EDTA, 1% NP-40) supplemented with protease inhibitors (Roche, 04693159001). Lysates were sonicated for 10 sec with 30% intensity. Supernatant was collected and protein concentration was determined via PierceTM BCA protein assay (ThermoFisher Scientific, 23223). The home-made human KANK4 antibody was conjugated to Protein A/G agarose beads (Santa Cruz, SC-2003) in 3% BSA (PAN Biotech, P06-1391100) for 1 h at 4°C. KANK4-beads (30 μ L per sample) were incubated with 1 mg protein lysate for 3 h at 4°C under constant rotation. Beads were centrifuged and washed three times with wash buffer (10 mM Tris, pH 8.0, 150 mM NaCl, 0.5 mM EDTA) followed by additional two washing steps with PBS (Sigma Aldrich, P4417). Samples on-beads were submitted for interaction proteomics analysis to the mass

spectrometry core facility of the Max Planck Institute of Biochemistry, Martinsried, Germany.

3.7.4 Mass spectrometry

3.7.4.1 Interaction proteomics

To identify the interacting partners of KANK4 or GFP-KANK4 immunoprecipitates obtained with anti-KANK4 and anti-GFP antibodies, respectively, were submitted to the mass spectrometry core facility of the Max Planck Institute of Biochemistry, Martinsried, Germany for on-beads digestion.

Sample preparation

For the reduction and alkylation of proteins, PBS-washed beads were incubated with a buffer containing 1% sodium deoxycholate (SDC; Sigma-Aldrich), 40 mM 2-chloroacetamide (CAA; Sigma-Aldrich), 10 mM tris(2-carboxyethyl)phosphine (TCEP; ThermoFisher Scientific), and 100 mM Tris (pH 8.0). The samples were incubated for 20 min at 37°C. After incubation, they were diluted 1:1 with MS-grade water (VWR). Proteins were digested overnight at 37°C using 0.5 µg of trypsin (Promega). Following digestion, the supernatant was separated from the beads, which was then washed with buffer A (0.1% [v/v] formic acid). The supernatants were collected, combined, and acidified with trifluoroacetic acid (TFA; Merck) to a final concentration of 1% and a pH<2. The precipitated SDC was removed by centrifugation, and the peptide mixture was purified using SCX StageTips.

LC-MS/MS data acquisition

Purified and desalted peptides were loaded onto a 30-cm column (inner diameter: 75 μm ; packed in-house with ReproSil-Pur C18-AQ 1.9- μm beads, Dr. Maisch GmbH) via the autosampler of the Thermo Easy-nLC 1200 (ThermoFisher Scientific) at 60°C. Using a nanoelectrospray interface, eluted peptides were directly sprayed onto either an Orbitrap Exploris 480 mass spectrometer (ThermoFisher Scientific) or a timsTOF Pro mass spectrometer (Bruker Daltonics). Peptides were loaded in buffer A (0.1% formic acid) and separated through the column at a flow rate of 300 nL/min by increasing the percentage of buffer B (80% acetonitrile, 0.1% formic acid) as follows: from 5% to 30% buffer B over 30 min, followed by an increase to 65% buffer B over 5 min, then to 95% over the next 5 min. Buffer B was maintained at 95% for an additional 5 min.

Data acquisition on the timsTOF Pro mass spectrometer was performed using otofControl 6.0 in data-dependent PASEF mode, with one survey TIMS-MS and ten PASEF MS/MS scans per acquisition cycle. The analysis was conducted over a mass range of 100–1700 m/z and an ion mobility range from $1/K_0 = 1.6 \text{ Vs/cm}^2$ to 0.6 Vs/cm^2 , using equal ion accumulation and ramp time in the dual TIMS analyzer (100 ms each) at a spectral rate of 9.52 Hz. Suitable precursor ions for MS/MS analysis were isolated within a window of 2 Th for $m/z < 700$ and 3 Th for $m/z > 700$ by rapidly switching the quadrupole position in sync with the precursor elution from the TIMS device. Collision energy was adjusted stepwise with increasing ion mobility: starting at 52 eV for 0–19% of the TIMS ramp time, 47 eV for 19–38%, 42 eV for 38–57%, 37 eV for 57–76%, and 32 eV until the end. m/z and ion mobility data were used to exclude singly charged precursor ions via a polygon filter mask. Dynamic exclusion was applied to avoid resequencing precursors that reached a target

value of 20,000 a.u.

For the Orbitrap Exploris 480 mass spectrometer, data acquisition was performed in data-dependent mode with survey scans from 300 to 1650 m/z (resolution of 60,000 at $m/z = 200$). Up to 15 of the top precursors were selected and fragmented using higher-energy collisional dissociation (HCD) with a normalized collision energy of 28. MS2 spectra were recorded at a resolution of 15,000 (at $m/z = 200$). AGC targets for MS and MS2 scans were set to 3E6 and 1E5, respectively, with maximum injection times of 25 ms for MS scans and 28 ms for MS2 scans. Dynamic exclusion was set to 30 seconds.

Data analysis

Raw data were processed using the MaxQuant computational platform (version 2.2.0.0) (Cox and Mann, 2008). Shortly, the peak list was searched against the human database (SwissProt and TrEMBL, downloaded in 2022). Cysteine carbamidomethylation was set as static modification, and methionine oxidation and N-terminal acetylation as variable modifications. The match-between-run option was enabled, and proteins were quantified across samples using the label-free quantification algorithm in MaxQuant generating label-free quantification (LFQ) intensities.

3.7.4.2 Total proteome

To analyze the total proteome of MCF10A cells treated without or with TGF β 1, cell pellets were submitted to the mass spectrometry core facility of the Max Planck Institute of Biochemistry, Martinsried, Germany.

Sample preparation

Cell pellets were lysed by addition of 150 μ L of SDC buffer containing 1% sodium deoxycholate, 40mM 2-chloroacetamide (Sigma-Aldrich), 10mM tris(2-carboxyethyl) phosphine (TCEP; ThermoFisher Scientific) in 100mM Tris HCl at pH 8.0. The samples were incubated at 95°C for 2 min and subsequently sonicated using a Bioruptor Plus sonication system (Diagenode) for 10x30 sec at high intensity. Samples were incubated once more at 95°C for 2 min and sonicated. Then, samples were diluted 1:1 with water and digested for 1.5 h at 37°C with 1 μ g of LysC and overnight at 37°C with 1 μ g trypsin (Promega). The peptide mixture was acidified with trifluoroacetic acid (Merck) to a final concentration of 1%, followed by desalting of the peptides via SCX StageTips. Samples were vacuum dried and re-suspended in 6 μ l of buffer A (0.1% formic acid).

LC-MS/MS data acquisition

The peptides (3 μ l) were loaded onto a 30-cm column (inner diameter: 75 microns; packed in-house with ReproSil-Pur C18-AQ 1.9-micron beads, Dr. Maisch GmbH) via the autosampler of the Thermo Easy-nLC 1200 (ThermoFisher Scientific) at 60°C. Eluting peptides were directly sprayed onto the mass spectrometer Q Exactive HF (ThermoFisher Scientific). Peptides were separated with a flow rate of 250 nL/min by a gradient of buffer B (80% ACN, 0.1% formic acid) from 2% to 30%B over 120 min followed an increase to 60%B over 10 min then to 95%B over the next 5 min and finally the percentage of buffer B was maintained at 95%B for another 5 min.

The mass spectrometer was operated in a data-dependent mode with MS1 scans from 300 to 1750 m/z (resolution of 60000 at m/z =200), and up to 15 of the top precursors were selected for fragmentation using higher energy collisional dissociation (HCD with a

normalized collision energy of value of 28). The MS2 spectra were recorded at a resolution of 15000 (at $m/z = 200$). AGC target for MS1 and MS2 scans were set to 3×10^6 and 1×10^5 respectively within a maximum injection time of 100 and 25 ms for MS1 and MS2 scans respectively.

Data analysis

Raw data were processed using the MaxQuant computational platform (version 1.6.17.0) (Cox and Mann, 2008). Shortly, the peak list was searched against the Uniprot database of human (SwissProt and TrEMBL, downloaded in July 2020) with an allowed precursor mass deviation of 4.5 ppm and an allowed fragment mass deviation of 20 ppm. Cysteine carbamidomethylation was set as static modification, and methionine oxidation and N-terminal acetylation as variable modifications. The match-between-run option was enabled, and proteins were quantified across samples using the label-free quantification algorithm in MaxQuant generating label-free quantification (LFQ) intensities.

3.8 Data mining

3.8.1 TCGA database mining

To correlate KANK4 expression and survival probability in patients of different cancer, the TCGA GDC release was analyzed using the <https://kmplot.com/analysis/> (Györfy, 2023). Datasets for cancer patients were obtained from GEO and EGA repositories and implemented into the kmplot database (Györfy, 2021, 2024).

3.8.2 Public ChIP databases

Public data search was performed by Dr. Assa Yeroslaviz using the ChIP-Atlas: Peak Browser (<http://chip-atlas.org/>).

3.9 Statistics and quantification

Statistical analysis was carried out in GraphPad Prism Software (version 9) and the specific tests are indicated in the figure legends. The length of invading strands of cultured spheroids and size of FAs were measured using straight line measuring tool from Fiji (ImageJ 2.14.0/1.54f). Spheroid size was measured at the indicated dates using the oval selection from Fiji. The protein levels from WB analysis were quantified using ImageStudioLite (version 5.2.5) and normalized to loading controls.

4 Results

4.1 KANK2 and KANK4 in normal development

KANKs have been widely studied *in vitro*. However, only limited studies are available on their *in vivo* functions. To address this knowledge gap, KANK-KO mice were generated in C57BL/6 background. Given that KANK2 and KANK4 showed overlapping expression patterns in murine tissues (Guo *et al.*, 2021), both genes were either knocked-out individually or together to generate a KANK2/4 double KO (dKO).

4.1.1 Generation of KANK2-KO mice

KANK2-KO mice were generated in C57BL/6 background by using the Cre/*lox* system. Two loxP sites flanking exon 4 and exon 5 were inserted into the *KANK2* gene locus and KANK2-KO mice were obtained by crossing the loxP-flanked mice with cre transgenic mice (Figure 26). This results in deletion of exon 4 and exon 5, leading to the disruption of the *KANK2* gene.

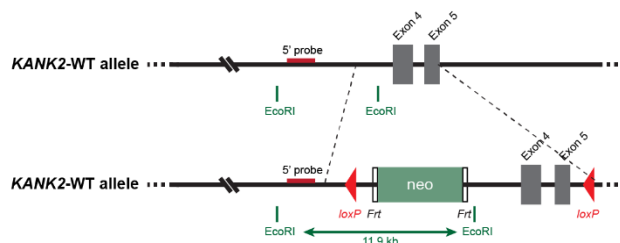


Figure 26: Scheme of KANK2 gene targeting strategy. The *KANK2* gene locus was disrupted by inserting two loxP sites flanking exon 4 and 5 and crossing the obtained mice with cre transgenic mice. Restriction enzymes and 5' probe used for Southern blot screening are indicated.

4.1.2 Generation of KANK4-KO mice

KANK4-KO mice were generated in C57BL/6 background by inserting a *lacZ* trapping cassette into the intron between exon 2 and exon 3 (Figure 27). The targeting construct consisted of a 16.4 kb fragment containing a promoterless *lacZ*-neo trapping cassette

comprising an EN2 splice acceptor (SA) and an SV40 polyadenylation sequence (pA) and two loxP sites flanking exon 3. The EN2 SA results in alternative splicing of exon 2 with the lacZ trapping cassette, leading to the disruption of the *KANK4* gene. As the reporter gene, *lacZ*, is expressed under the control of the endogenous *KANK4* promoter, expression of lacZ or β -galactosidase can be used as a control for successful *KANK4*-KO generation.

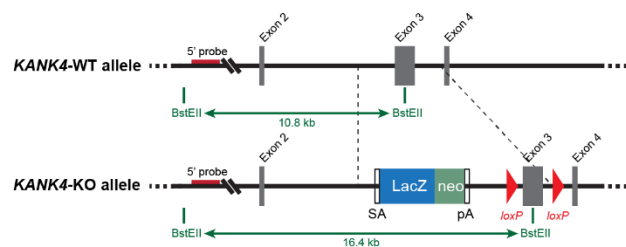


Figure 27: Scheme of *KANK4* gene targeting strategy. The *KANK4* gene locus was disrupted and replaced by LacZ in the *KANK4*-KO allele. Restriction enzymes and 5' probe used for Southern blot screening are indicated. SA: splicing acceptor. pA: poly A tail. In parts taken from a manuscript (Seiwert *et al.*) in consideration.

4.1.3 KANKs are non-essential in normal development

C57BL/6 mice were genotyped via *KANK2*- and *KANK4*-specific PCR (Figure 28A, B). The crossing of *KANK2*-het and *KANK4*-het mice resulted in *KANK2*-KO or *KANK4*-KO offspring, respectively, in accordance with the expected mendelian ratio of 25% (Figure 28C, D). The *KANK2/4*-dKO offspring was obtained with around 5%, which fits with the expected mendelian ratio of 6.25% in a heterozygous mating (Figure 28E). The successful disruption of the *KANK4* gene was additionally verified on protein lysates extracted from lung, MG, heart and kidney from *KANK4*-WT, *KANK4*-het and *KANK4*-KO mice (Figure 28F). WB analysis demonstrated that *KANK4*-het mice exhibited similar or reduced levels of *KANK4* protein, whereas it was gone in *KANK4*-KO mice. Depletion of *KANK4* did not result in compensatory upregulation of *KANK1*, *KANK2*, or *KANK3*.

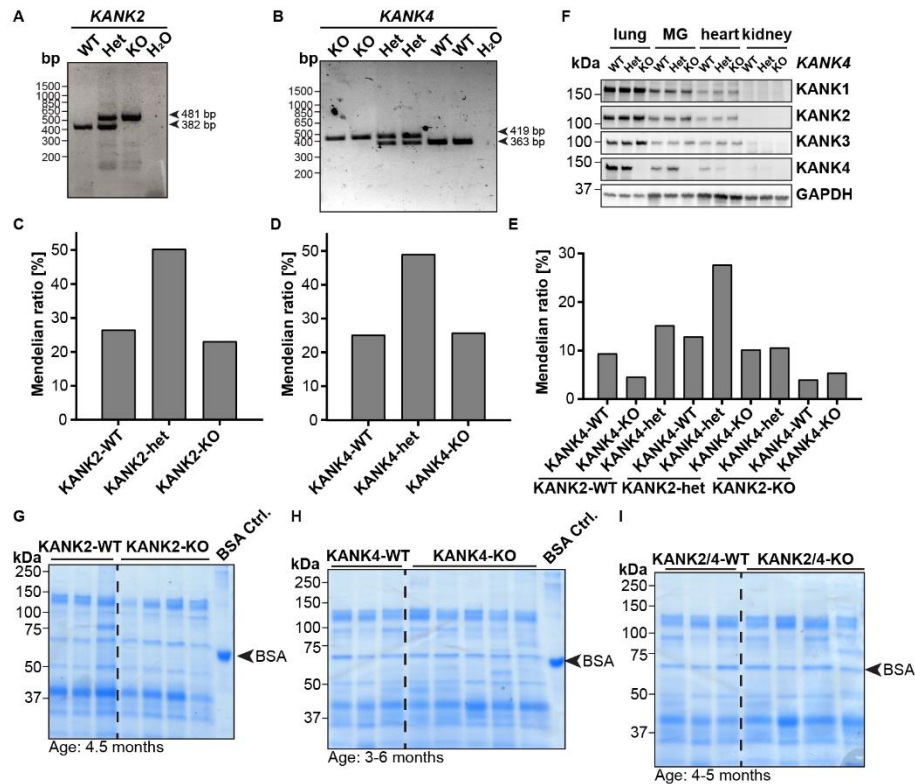


Figure 28: Development of KANK-KO mice. (A, B) Offspring were genotyped for KANK2 (A) and KANK4 (B) using specific PCRs. PCR product size of KANK2-WT allele is 382 bp and of KANK2-KO allele 481 bp. PCR product size of KANK4-WT allele is 363 bp and of KANK4-KO allele 419 bp. (C) Mendelian ratio of KANK2-WT, KANK2-het and KANK2-KO mice (n=147). (D) Mendelian ratio of KANK4-WT, KANK4-het and KANK4-KO mice (n=365). (E) Mendelian ratio of KANK2/4-WT, KANK2/4-het and KANK2/4-KO mice (n=490). (F) Lysates of indicated tissues from KANK4-WT, KANK4-het and KANK4-KO mice were analyzed by WB with indicated antibodies. (G-I) Urine samples of KANK2-WT and KANK2-KO mice (G), KANK4-WT and KANK4-KO mice (H), and KANK2/4-WT and KANK2/4-dKO mice (I) were analyzed for proteinuria by Coomassie-staining.

Given the association between KANKs and nephrotic syndrome, as well as the observation that KD of *Kank2* in zebrafish results in proteinuria (Gee *et al.*, 2015), the urine of the three different WT and KO mouse lines was analyzed for albumin levels (Figure 28G-I). Neither the absence of KANK2 or KANK4, nor the dKO result in elevated albumin levels, which would be indicative of impaired kidney function.

Altogether, the generation of complete KANK2-KO, KANK4-KO and KANK2/4-dKO mice was achieved, and the respective KO mice exhibited normal development without any obvious developmental issues.

Given that KANK2-KO and KANK4-KO mice did not show developmental defects in

C57BL/6 background and the KANK2/4-dKO was also normal, the function of KANKs were firstly evaluated within a different mouse background (see chapter 4.2), and secondly in a pathological condition, namely breast cancer (see chapter 4.3).

4.2 KANK2 in FVB mouse development

4.2.1 KANK2 deficiency results in early embryonic death in FVB background

To assess whether the mouse background affects the relevance of KANKs in normal development, KANK2-KO mice were backcrossed from C57BL/6 background to FVB background. Interestingly, an embryonic lethality of KANK2-deficient FVB mice was observed. Analysis of the mendelian ratio of pups from heterozygous intercrosses at 21 days after birth showed an abnormal ratio of approximately 66% KANK2-WT and 34% KANK2-het mice, with no KANK2-KO mice detected (Figure 29A). Similarly, genotyping of newborns and E14.5 embryos revealed the absence of KANK2-KO mice, whereas at E8.5, KANK2-KO embryos were still detected. This suggests that the absence of KANK2 results in embryonic lethality between E8.5 and E14.5 (Figure 29B, C).

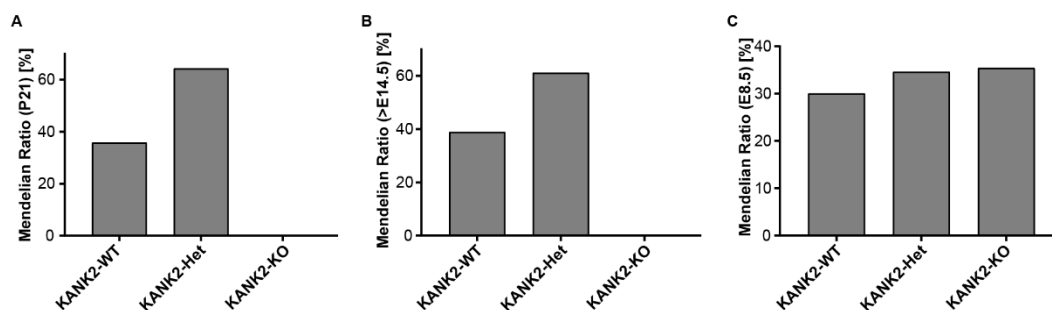


Figure 29: KANK2 deficiency is embryonically lethal. (A, B, C) Mendelian ratio of KANK2-WT, KANK2-het and KANK2-KO mice at P21 (n=291) (A), >E14.5 (n=18) (B), and E8.5 (n=130) (C).

4.2.2 KANK2 deficiency impairs chorioallantoic fusion

To examine the underlying cause of lethality, embryos were dissected at different developmental stages (E8.5, E9.5, E11.5). The yolk sac or limb buds were isolated and

used for genotyping. Embryos with the KANK2-WT and KANK2-het genotypes exhibited normal development at E11.5, displaying a properly oriented body axis, a functional circulatory system with a regular heartbeat, and an intact umbilical cord (Figure 30A). In contrast, KANK2-KO embryos were mostly reabsorbed with a reduced size and a pale appearance lacking vascularization and an umbilical cord (Figure 30A). The umbilical cord develops via fusion of the extra-embryonic allantoic mesothelium and the chorionic mesoderm, which occurs at the 4-6 somite pairs stage (E8.0) to form the chorioallantois (Arora and Papaioannou, 2012) (see chapter 1.8.1). Interestingly, KANK2-KO embryos at E8.5 and E9.5 exhibited a defect in this chorioallantoic fusion event, indicated by a balloon-like outgrowth of the allantois into the exocoelom cavity, which was detached from the chorion (Figure 30A, B). However, KANK2-WT and KANK2-het embryos had successfully established the chorioallantois at the same developmental stage. This suggests that KANK2-KO embryos most likely died due to inadequate nutrient and oxygen supply at E11.5. Further investigation is required to ascertain the potential involvement of other defects, such as heart abnormalities.

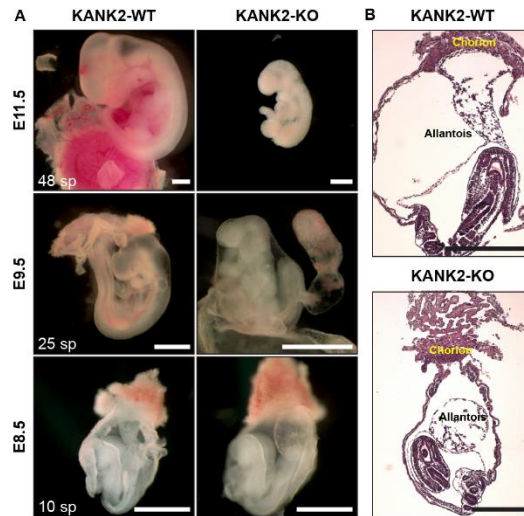


Figure 30: KANK2 deficiency impairs chorioallantoic fusion. (A) Gross viewing of KANK2-WT and KANK2-KO embryos at indicated ages. Scale bar: 0.1 cm. (B) KANK2-WT and KANK2-KO embryos were analyzed by histology at E9.5. Scale bar: 0.1 cm.

4.2.3 KANK2 expression in chorion and allantois

Previous studies have established a correlation between integrin signaling and the proper fusion of chorion and allantois (see chapter 1.8.1.1). The observation of similar phenotypes in α_4 integrin or its co-receptor VCAM-1-KO mice (Gurtner *et al.*, 1995; Kwee *et al.*, 1995; Yang, Rayburn and Hynes, 1995) suggest that KANK2 may be a necessary factor in proper integrin signaling during the fusion event. As reported in the literature, VCAM-1 was detected in distal allantoic mesothelial cells and at the allantoic mesoderm interacting with the chorionic plate, but was absent in inner core cells within the allantois. In line with this, α_4 integrin showed a discontinuous expression pattern in the chorion and was absent from the allantois. Preliminary IF stainings of KANK2 of KANK2-WT and KANK2-KO embryos at E8.5 (12 sp) demonstrated expression of KANK2 in both α_4 integrin⁺ chorionic mesoderm and VCAM-1⁺ distal allantoic mesothelial cells (Figure 31).

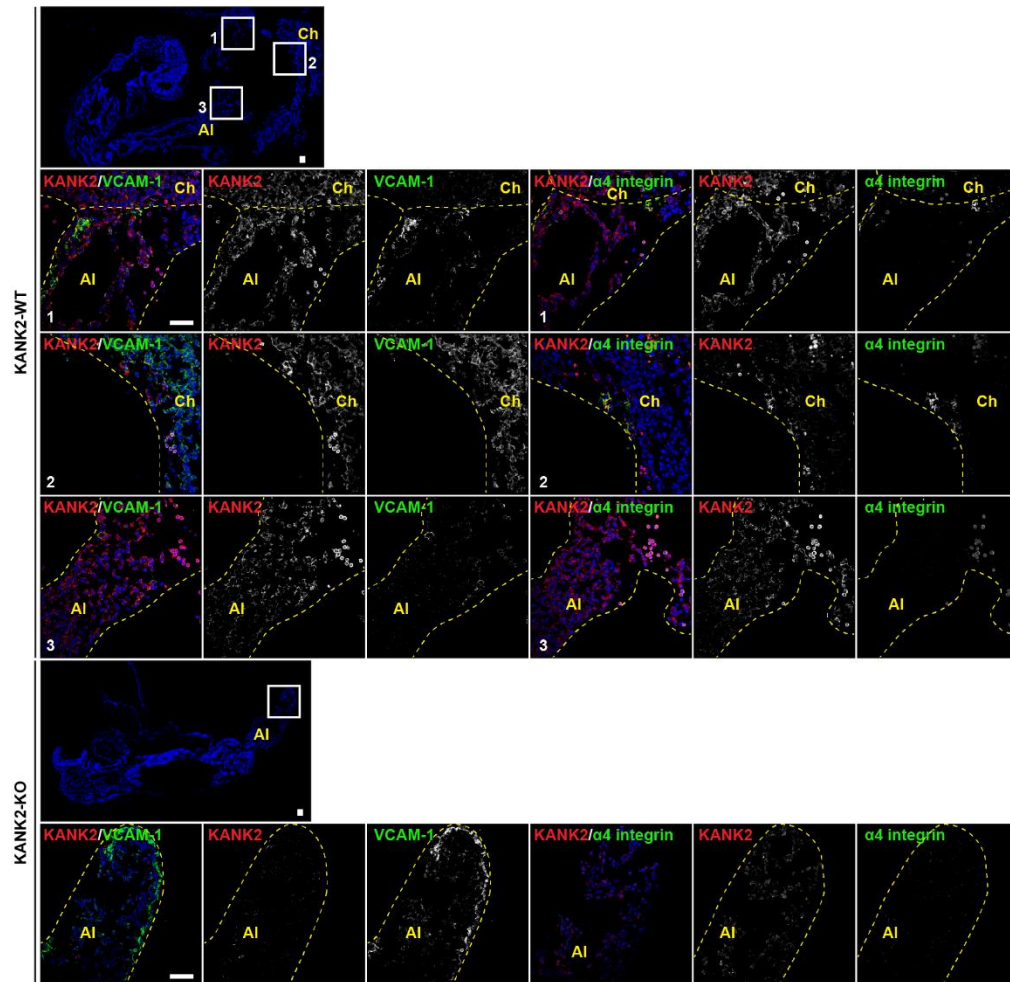


Figure 31: KANK2 expression in embryogenesis. IF staining of KANK2-WT and KANK2-KO embryos at E8.5 (12 sp) for KANK2 (red) and VCAM-1⁺ allantoic cells or α_4 integrin⁺ chorionic cells (both shown in green). Nuclei were counterstained with DAPI (blue). AI: Allantois, Ch: Chorion. Scale bar: 50 μ m.

The data collectively indicate that KANK2 plays a context-specific role in normal development. The absence of KANK2 results in embryonic lethality due to impaired chorioallantoic fusion at E8.0-E8.5. Further characterization of the phenotype is ongoing. KANK4-KO mice backcrossed from C57BL/6 for six generations to FVB background (KANK4-KO-FVB-F6) did not show developmental defects (data not shown). Further backcrossing until F10 is needed to reliably evaluate the development.

4.3 KANK2 and KANK4 in breast cancer development

Initially identified in renal cell carcinoma via loss of heterozygosity analysis, KANK1 was subsequently characterized as a tumor suppressor (Sarkar *et al.*, 2002). Despite the lack of comprehensive studies on KANKs in cancer, *in silico*-based analyses indicate that KANK1 and KANK3 may suppress tumor formation, while KANK2 and KANK4 may promote tumor formation (Kim *et al.*, 2018; Tadijan *et al.*, 2021). Given that KANK2 and KANK4 do not play a crucial role in normal murine development in C57BL/6 background (see chapter 4.1.3, Figure 28), their function in cancer was investigated. For this, the MMTV-PyMT breast cancer as well-established mouse model was chosen, due to the high relevance of breast cancer in women. This model resembles human breast cancer development and uses the PyMT-oncogene driven by the MMTV promoter to initiate pathological transformation of mammary LECs, thereby resulting in breast cancer formation (see chapter 1.8.4). The MMTV-PyMT breast cancer model was introduced into KANK2-WT and KANK2-KO, as well as KANK4-WT and KANK4-KO mice. For this, respective KANK-het mice were crossed with the MMTV-PyMT mouse strain and KANK-het female mice were crossed with KANK-het male mice positive for PyMT (KANK2-het^{PyMT} and KANK4-het^{PyMT}) to obtain female KANK2-WT^{PyMT} and KANK2-KO^{PyMT}, as well as KANK4-WT^{PyMT} and KANK4-KO^{PyMT} littermates for analysis. The presence of the PyMT oncogene was confirmed via PCR analysis (Figure 32).

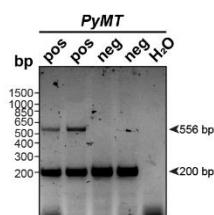


Figure 32: PyMT PCR. Offspring were genotyped for PyMT using a specific PyMT PCR. PCR product size for mice positive for PyMT is 556 bp. Control product size is 200 bp.

4.3.1 KANK2 does not affect tumor development

To evaluate the influence of KANK2 in the formation of breast cancer, tumor onset was monitored by palpation on a weekly basis in female KANK2-WT^{PyMT} and KANK2-KO^{PyMT} mice. No difference was observed between KANK2-WT^{PyMT} and KANK2-KO^{PyMT} mice, with both developing tumors after around 81 days (Figure 33A). Following tumor onset, tumor volumes were measured to enable comparison of the growth rates. Tumors developed with similar rates in KANK2-WT^{PyMT} and KANK2-KO^{PyMT} mice (Figure 33B). Finally, also the end point tumor weight was comparable in KANK2-WT^{PyMT} and KANK2-KO^{PyMT} mice (Figure 33C), suggesting that presence or absence of KANK2 does not affect tumor development.

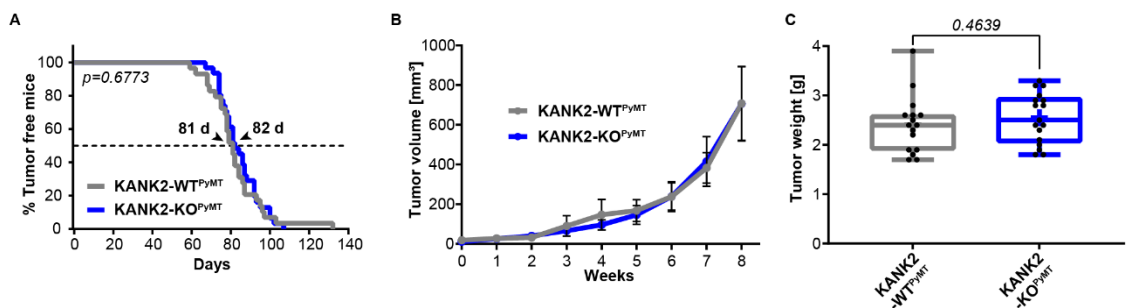


Figure 33: KANK2 does not affect tumor development. (A) Tumor incidence in KANK2-WT^{PyMT} (n=29) and KANK2-KO^{PyMT} (n=31) mice shown as tumor-free survival curve. Arrowheads indicate medium tumor latency. *P* value was calculated by Log-rank test. (B) Tumor volume in KANK2-WT^{PyMT} (n=16) and KANK2-KO^{PyMT} (n=17) mice after tumors were palpated. Mean \pm 95% CI is shown. (C) Tumor weight of KANK2-WT^{PyMT} (n=16) and KANK2-KO^{PyMT} (n=17) mice at 60 days after tumor onset. *P* value was calculated by unpaired Student's *t*-test.

Given that KANK2 seemed to have no impact on tumor formation, no further analyses were performed on KANK2-WT^{PyMT} and KANK2-KO^{PyMT} mice.

4.3.2 KANK4 promotes tumor development in a MMTV-PyMT mouse model

Similar to KANK2, the influence of KANK4 in breast cancer was determined by tumor onset, growth rate and end point tumor weight. KANK4-WT^{PyMT} mice developed tumors

after 81.5 days, whereas tumor onset was significantly delayed by 11.5 days in KANK4-KO^{PyMT} mice (93 days) (Figure 34A). The delayed tumor onset in KANK4-KO^{PyMT} mice was accompanied by a slower tumor growth, as indicated by a decrease in tumor volume compared to KANK4-WT^{PyMT} mice (Figure 34B). Consequently, the end point tumor weight was significantly less in KANK4-KO^{PyMT} mice, compared to KANK4-WT^{PyMT} mice (Figure 34C, Appendix Table 15). Staining for Ki67 and pH3 suggested that tumor cell proliferation was significantly increased in KANK4-WT^{PyMT} mice (Figure 34D-G), resulting in faster tumor growth and increased tumor burden. Slower tumor development observed in KANK4-KO^{PyMT} mice was not due to enhanced tumor cell apoptosis, as demonstrated by similar levels of cIcasp3 staining (Figure 34H, I).

Interestingly, the incidence of lung metastasis was also increased in KANK4-WT^{PyMT} mice. The formation of superficial metastatic nodules was observed in nine out of 39 KANK4-WT^{PyMT} mice that were analyzed, whereas only two out of 37 KANK4-KO^{PyMT} mice that were analyzed exhibited the formation of metastatic nodules (Figure 34J, K). Furthermore, the average number of metastatic nodules formed by metastasizing cancers was four in KANK4-WT^{PyMT} mice, but only one in KANK4-KO^{PyMT} mice at similar tumor weights (Figure 34L).

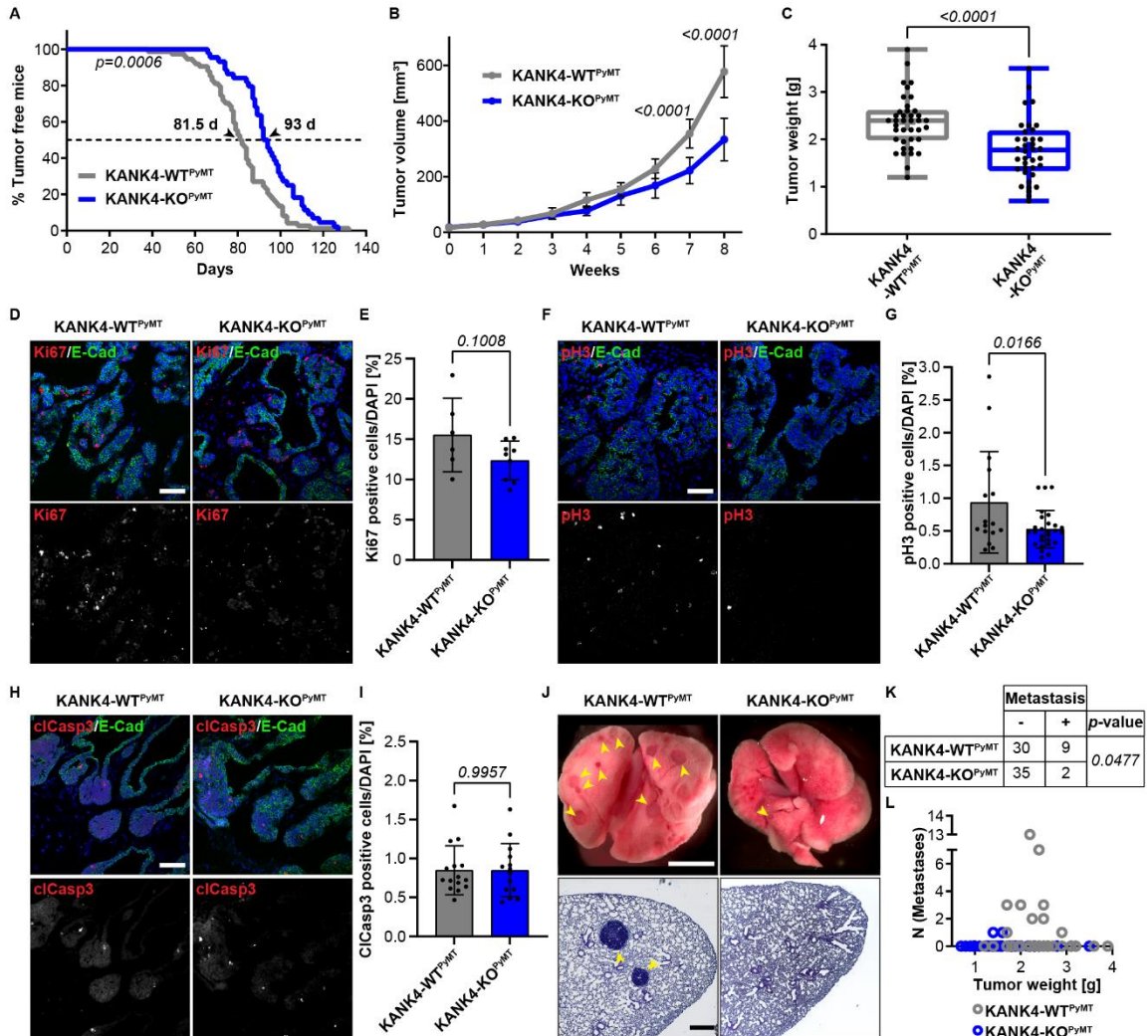


Figure 34: KANK4 promotes tumor development in KANK4-WT^{PyMT} mice. (A) Tumor incidence in KANK4-WT^{PyMT} (n=74) and KANK4-KO^{PyMT} (n=44) mice shown as tumor-free survival curve. Arrowheads indicate medium tumor latency. *P* value was calculated by Log-rank test. (B) Tumor volume in KANK4-WT^{PyMT} (n=39) and KANK4-KO^{PyMT} (n=37) mice after tumor onset. *P* values (mixed-effects analysis with multiple comparison and Sidák correction) are indicated on top of each comparison. Mean \pm 95% CI is shown. (C) Tumor weight of KANK4-WT^{PyMT} (n=39) and KANK4-KO^{PyMT} (n=37) mice at 60 days after tumor onset. *P* value was calculated by unpaired Student's *t*-test. (D, E) IF staining (D) of E-Cad⁺ (green) tumor cells analyzed for proliferation by Ki67 (red) in KANK4-WT^{PyMT} and KANK4-KO^{PyMT} tumor tissues. Nuclei were counterstained with DAPI (blue). Scale bar: 50 μ m. Quantification (E) of Ki67⁺ cells is shown from n=3 tumor regions, pooled from n=6 KANK4-WT^{PyMT} mice and n=9 KANK4-KO^{PyMT} mice. *P* value was calculated by unpaired Student's *t*-test (two-tailed). Mean \pm SD is shown. (F, G) IF staining (F) of E-Cad⁺ (green) tumor cells analyzed for their proliferation rate by pH3 (red) in KANK4-WT^{PyMT} and KANK4-KO^{PyMT} tumor tissues. Nuclei were counterstained with DAPI (blue). Scale bar: 50 μ m. Quantification (G) of pH3⁺ cells is shown from n=3 tumor regions, pooled from n=6 KANK4-WT^{PyMT} mice and n=9 KANK4-KO^{PyMT} mice. *P* value was calculated by unpaired Student's *t*-test (two-tailed). Mean \pm SD is shown. (H, I) IF staining (H) of E-Cad⁺ (green) tumor cells analyzed for their survival rate by cIcasp3 (red) in KANK4-WT^{PyMT} and KANK4-KO^{PyMT} tumor tissues. Nuclei were counterstained with DAPI (blue). Scale bar: 50 μ m. Quantification (I) of cIcasp3⁺ cells are shown from n=3 tumor regions, pooled from n=16 KANK4-WT^{PyMT} mice and n=15 KANK4-KO^{PyMT} mice. *P* value was calculated by unpaired Student's *t*-test (two-tailed). Mean \pm SD is shown. (J, K, L) Lung metastases (J) formed in KANK4-WT^{PyMT} and KANK4-KO^{PyMT} mice were analyzed by gross viewing and histology 60 days after primary tumor onset. Arrowheads indicate metastases. Scale bars: 500 μ m. Quantification (K) of lung surface nodules at day 60 after tumor onset. 23.1% of

KANK4-WT^{PyMT} mice developed metastasis (9 out of 39 mice analyzed) and 5.4% of KANK4-KO^{PyMT} mice developed metastasis (2 out of 37 mice analyzed). Number of metastatic nodules is compared with the total tumor mass (**L**). *P* value was calculated by Fisher's exact test. All data points are shown. In parts taken from a manuscript (Seiwert *et al.*) in consideration.

The data collectively indicate that KANK4, in contrast to KANK2, functions as a tumor promoter in the MMTV-PyMT breast cancer mouse model, facilitating cell proliferation and consequently accelerating tumor onset, growth, burden and metastasis formation.

4.3.3 KANK4 in murine MG

The four KANK proteins exhibit distinct expression patterns. KANK4 is predominantly expressed in mesangial cells and pericytes (Guo *et al.*, 2021). To further examine the tumor-promoting function of KANK4, the KANK4 expressing cell types in normal MG and tumor tissue were determined.

4.3.3.1 KANK4 is expressed in myoepithelial cells of normal MG

The MG undergoes a series of developmental stages during the processes of embryogenesis, puberty, and pregnancy (see chapter 1.8.2). To investigate the dynamics of KANK4 expression in the MG, MG samples from young virgin, pregnant, lactating, involuting and old virgin female KANK4-WT mice were isolated and stained for KANK4 (Figure 35A). The formation of TEB is a defining feature of MG development during puberty (see chapter 1.8.2.3). Here, KANK4 is expressed in cap cells, which subsequently give rise to myoepithelial cells, as well as in differentiated myoepithelial cells that surround CK8⁺ body cells. During pregnancy, KANK4 is expressed in myoepithelial cells of proliferating ducts. Lactation is characterized by the presence of alveoli, which are surrounded by discontinuous contractile myoepithelial cells that facilitate milk transport. Similarly, the discontinuous pattern of KANK4 expression is detected in these

myoepithelial cells, which line the CK8⁺ ductal LECs. Furthermore, the involution state, as well as the MG of old virgin mice also show KANK4 expression in myoepithelial cells. Although continuously expressed in all developmental stages of the MG, depletion of KANK4 did not alter the MG morphology or function, as indicated by whole mount MG staining and the numbers of offspring at the weaning stage, which suggests the maintenance of normal reproductive functions (Figure 35B, C).

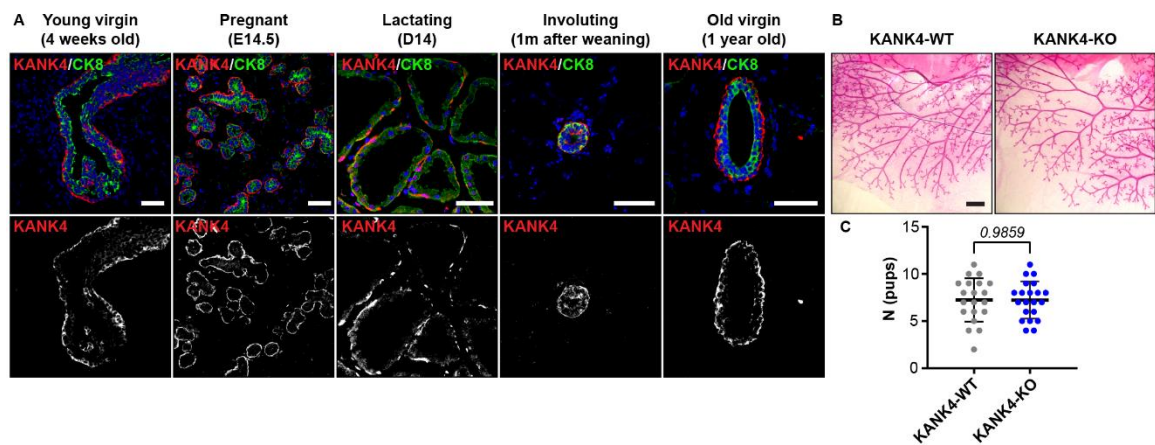


Figure 35: KANK4 expression in myoepithelial cells of murine MG during different developmental stages. (A) IF staining of MG tissues from KANK4-WT mice for KANK4 (red) and CK8⁺ LECs (green). Nuclei were counterstained with DAPI (blue). Scale bar: 50 µm. (B) Whole-mount MG staining with Carmine Alum in 6-month-old KANK4-WT (n=3) and KANK4-KO (n=3) female mice. Scale bar: 1 mm. (C) Offspring numbers from KANK4-WT x KANK4-WT (n=20 litters) and KANK4-KO x KANK4-KO (n=21 litters) intercrosses. *P* value was calculated by unpaired Student's *t*-test. Mean ± SD is shown. In parts taken from a manuscript (Seiwert *et al.*) in consideration.

The data demonstrate that KANK4 is expressed early on during MG development and throughout its subsequent progression, with expression confined to myoepithelial cells.

4.3.3.2 KANK4 is *de novo* expressed in transformed LECs of mammary tumor tissues

Following a 60-day period of tumor development, KANK4-WT^{PyMT} tissue was isolated and stained for KANK4 to compare the expression pattern in normal and pathological situation. Normal MG showed KANK4 expression in αSMA⁺ myoepithelial cells that

surrounded LECs (Figure 36A). MG from KANK4-KO mice served as a negative control to confirm the absence of KANK4 protein and to demonstrate the specificity of the KANK4 antibody. Interestingly, while KANK4 expression remained unaltered and continuous in myoepithelial cells throughout normal MG development (see chapter 4.3.3.1, Figure 35A), tumor tissues exhibited an additional *de novo* expression pattern of KANK4 in transformed LECs (Figure 36B). Marking the basement membrane with nidogen revealed that KANK4 was also expressed in transformed LECs that were breaking through the basement membrane, as indicated by discontinuous nidogen staining.

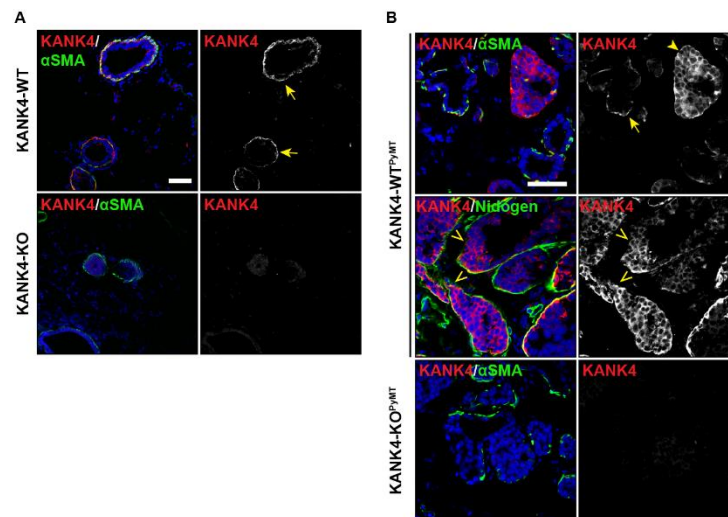


Figure 36: KANK4 is *de novo* expressed in transformed LECs of murine breast cancer tissue. (A, B) IF staining of MG tissues from KANK4-WT and KANK4-KO virgin mice (A) and of tumor tissues from KANK4-WT^{PyMT} and KANK4-KO^{PyMT} mice (B) for KANK4 (red) and αSMA⁺ myoepithelial cells or nidogen⁺ basement membrane (both shown in green). Nuclei were counterstained with DAPI (blue). Arrows indicate KANK4 expression in αSMA⁺ myoepithelial cells and arrowhead in transformed LECs grown into the MG ducts. Open arrowheads indicate cells breaking through the basement membrane. Scale bar: 50 μm.

Thus, in contrast to normal tissue, transformed and invading LECs of breast cancer tissue display *de novo* KANK4 expression. This could cause the observed enhanced tumor development and increased metastasis formation observed in KANK4-WT^{PyMT} mice.

4.3.3.3 Validation of *de novo* expression of KANK4

The intriguing *de novo* expression of KANK4 in transformed LECs was corroborated through the utilization of the *lacZ* reporter gene, which was incorporated into the targeting construct for KANK4-KO mice generation (see chapter 4.1.2, Figure 27). KANK4-WT mice express KANK4, but lack the reporter gene (KANK4⁺/β-galactosidase⁻). KANK4-KO mice express *lacZ* under the endogenous KANK4 promoter, which in turn disrupts KANK4 expression (KANK4⁻/β-galactosidase⁺). To verify the expression pattern of KANK4, normal MG and tumor tissue of KANK4-WT mice were stained for KANK4, and of KANK4-KO mice for β-galactosidase (Figure 37).

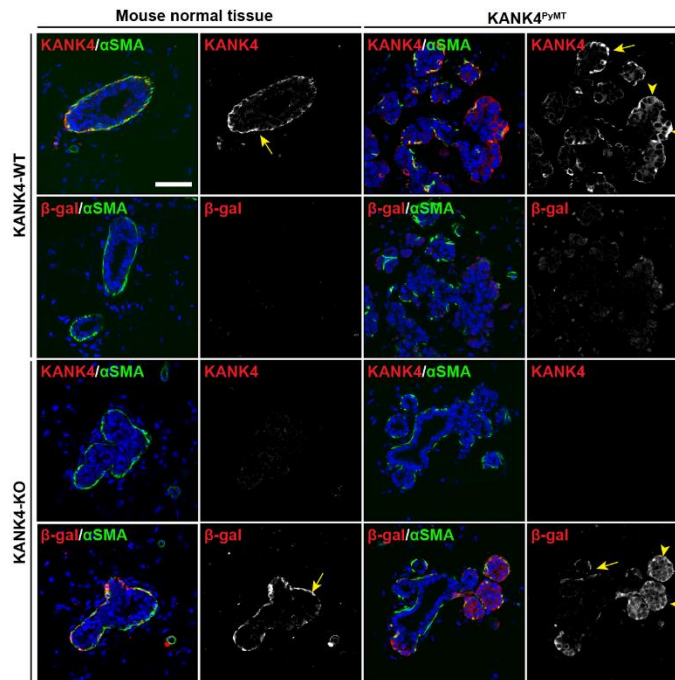


Figure 37: Validation of *de novo* expression of KANK4 in murine MG and breast cancer. IF staining of MG tissues from KANK4-WT and KANK4-KO mice and of tumor tissues from KANK4-WT^{PyMT} and KANK4-KO^{PyMT} mice for KANK4 or β-galactosidase (β-gal) (both shown in red) and αSMA⁺ myoepithelial cells (green). Nuclei were counterstained with DAPI (blue). Arrows indicate KANK4 or β-gal expression in αSMA⁺ myoepithelial cells. Arrowheads indicate KANK4 or β-gal expression in transformed LECs. Scale bar: 50 μm. In parts taken from a manuscript (Seiwert *et al.*) in consideration.

In normal MG of KANK4-WT or KANK4-KO mice, KANK4 or β-galactosidase expression was observed in myoepithelial cells. In contrast, tumor tissues of

KANK4-WT^{PyMT} or KANK4-KO^{PyMT} mice exhibited KANK4 or β -galactosidase expression not only in myoepithelial cells but also in transformed LECs. Staining of KANK4 and β -galactosidase in KANK4-KO and KANK4-WT tissue, respectively, served to confirm the specificity of expression.

To ascertain whether the *PyMT* oncogene was responsible for the *de novo* expression of KANK4 in transformed LECs, MG tumor tissues of KANK4-WT^{PyMT} mice were stained for KANK4 and PyMT (Figure 38). The MMTV promoter is responsible for driving PyMT expression specifically in mammary LECs. Consequently, these cells will eventually undergo transformation and become cancerous. PyMT was expressed in all pan-Cad⁺ LECs (Figure 38). However, KANK4 was expressed in PyMT⁻ myoepithelial cells (Figure 38, upper panel), as well as in some, but not all PyMT⁺ transformed LECs (Figure 38, middle panel). This indicates that KANK4 *de novo* expression is not directly dependent on PyMT expression. As the MMTV promoter is hormone-dependent, PyMT expression is first induced during puberty (Sonnenberg *et al.*, 1987; Grimm and Nordeen, 1998; Ross, 2008). Consequently, PyMT in LECs was not detected in MG of newborn KANK4-WT^{PyMT} mice (Figure 38, lower panel). In this instance, KANK4 expression was only detected in myoepithelial cells.

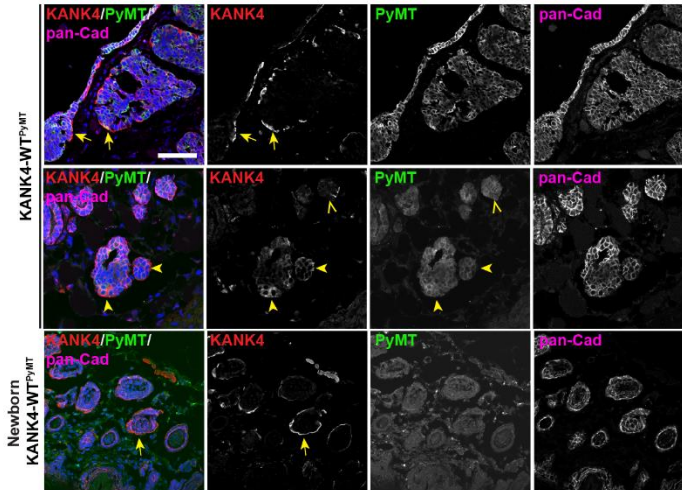


Figure 38: KANK4 expression in PyMT-transformed MG. IF staining of MG tumor tissues from KANK4-WT^{PyMT} mice and of MG tissues from KANK4-WT^{PyMT} newborn mice for KANK4 (red) and PyMT⁺ (green) and pan-Cad⁺ (magenta) (transformed) LECs. Nuclei were counterstained with DAPI (blue). Arrows indicate KANK4 expression in PyMT⁻ myoepithelial cells. Arrowheads indicate KANK4 expression in PyMT⁺ transformed LECs. Open arrowheads indicate lack of KANK4 expression in PyMT⁺ transformed LECs.

The results of the IF stainings suggest that the *de novo* expression of KANK4 is independent of PyMT.

4.3.4 Induction of *de novo* expression of KANK4

De novo expression of KANK4 in transformed LECs could be caused by an intrinsic transformation event, e.g. expression of PyMT, or by exogenous factors from the TME. Tumor is composed of cancer cells, as well as the TME, which includes infiltrating macrophages and stromal cells (see chapter 1.7.1). The tumor and TME interact with each other via the secretion of factors, which further influence each other and promote tumor development. The most prominent factors are TGF β , TNF α and IL6, which are predominantly secreted by CAFs to promote cancer cell transformation. Given that IF staining suggested a PyMT-independent KANK4 induction, and that the KANK4 expression is not homogenous across all transformed LECs, but rather occurs in specific tumor areas, the question was whether the exogenous factors TGF β , TNF α and IL6 induce KANK4 expression.

4.3.4.1 TGF β , TNF α and IL6 are expressed in TME

First, the expression pattern of TGF β 1, TNF α and IL6 was determined in KANK4-WT^{PyMT} and KANK4-KO^{PyMT} tumor tissue. All three factors were localized in vimentin⁺ stroma surrounding tumor clusters (Figure 39A, B). No difference was observed in KANK4-WT^{PyMT} and KANK4-KO^{PyMT} tumor tissue.

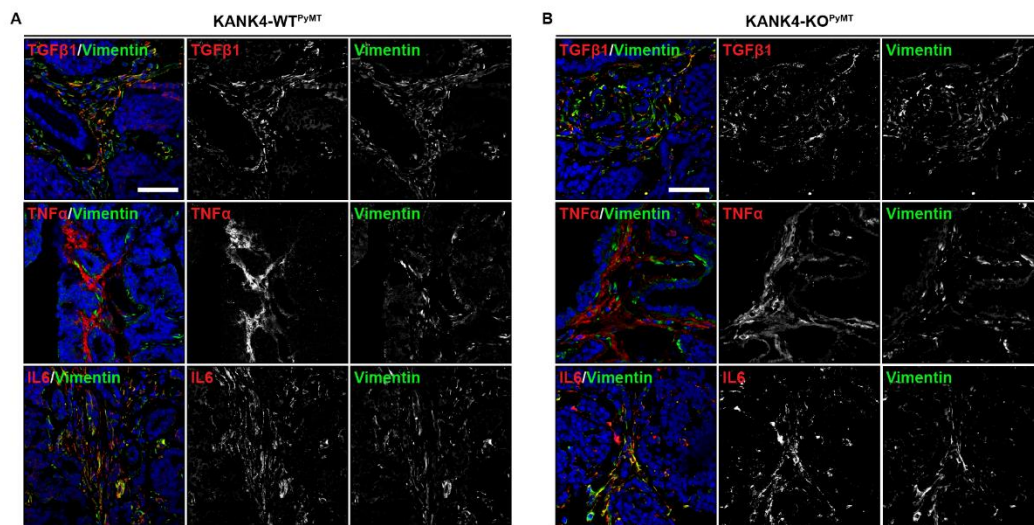


Figure 39: TGF β , TNF α and IL6 are expressed in murine breast cancer tissue. (A, B) IF staining of MG tumor tissues from KANK4-WT^{PyMT} (A) and KANK4-KO^{PyMT} (B) mice for TGF β 1, TNF α and IL6 (all shown in red) and vimentin⁺ stromal fibroblasts (green). Nuclei were counterstained with DAPI (blue). Scale bar: 50 μ m. In parts taken from a manuscript (Seiwert *et al.*) in consideration.

4.3.4.2 TGF β superfamily induces KANK4 expression

MCF10A is a well-established, non-cancerous epithelial cell line derived from benign human MG tissue (Debnath, Muthuswamy and Brugge, 2003). To answer whether KANK4 expression is induced by TGF β , TNF α and/or IL6 in LECs, MCF10A cells were treated with the different cytokines for a period of three days and analyzed for KANK4 expression via WB. Given that the TGF β superfamily comprises over 30 members, representatives of the TGF β -like subgroup (TGF β 1, 2, 3, activin) and the BMP-like subgroup (BMP2, 4, 6, 7, 10) were selected for analysis. Treatment with the nine different members of the TGF β

superfamily resulted in the *de novo* expression of KANK4 in MCF10A cells (Figure 40A). In contrast, TNF α or IL6 were unable to induce KANK4 expression (Figure 40A). Active signaling of the different ligands was confirmed by increased levels of pSmad2/3 (TGF β -like subgroup), pSmad1 (BMP-like subgroup), or pSTAT3 (TNF α or IL6). Among the TGF β superfamily, TGF β 1, β 2, β 3, BMP2, 6, 7, and 10 were found to significantly upregulate KANK4 (Figure 40B). The data demonstrate that the *de novo* expression of KANK4 is driven by the TGF β superfamily. Subsequent experiments were conducted using TGF β 1.

The use of MCF10A as a cell model allowed further verifying that the *de novo* expression of KANK4 was not caused by PyMT expression (see chapter 4.3.3.3, Figure 38) by overexpressing PyMT and examining KANK4 protein levels via WB analysis (Figure 40C). PyMT expression alone was insufficient to induce KANK4. However, TGF β 1 induced KANK4 expression, showing that KANK4 depends on TME factors rather than PyMT.

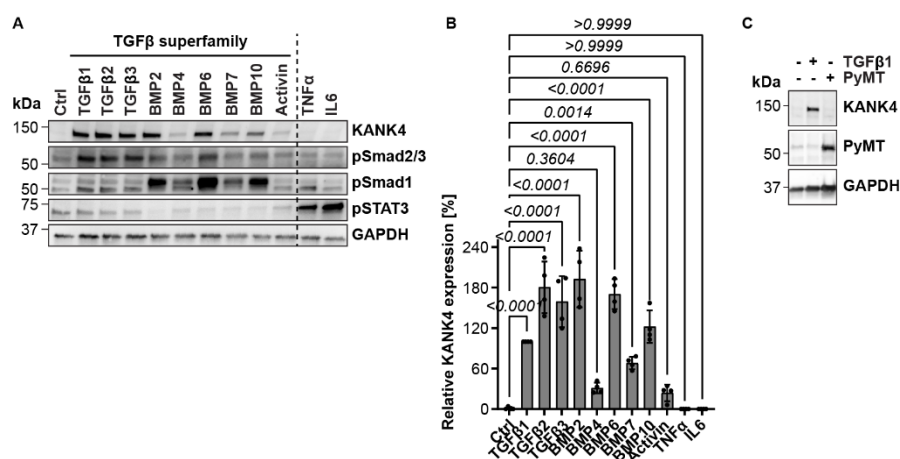


Figure 40: TGF β superfamily induces *de novo* expression of KANK4. (A, B) Lysates of MCF10A cells treated with indicated cytokines for three days were analyzed by WB with indicated antibodies (A). GAPDH served as loading control. Quantification (B) shows abundance of KANK4 protein levels normalized to GAPDH (n=4 independent experiments). *P* values (one-way ANOVA with Dunnett's multiple comparisons test) are shown on top of each comparison. Mean \pm SD is shown. (C) Lysates of MCF10A cells transfected

with PyMT were analyzed by WB with indicated antibodies. GAPDH served as loading control. In parts taken from a manuscript (Seiwert *et al.*) in consideration.

To examine the kinetics of KANK4 induction, MCF10A cells were treated with TGF β 1 for 24, 48, 72, and 96 hours. KANK4 levels were initially detected at low levels after 24 hours and reached a peak at 72 hours of TGF β 1 treatment (Figure 41A, B). Thereafter, KANK4 levels began to decline (Figure 41A, B). Based on these findings, three days of TGF β 1 treatment was established as the standard duration for following experiments, unless otherwise indicated.

The dependance of KANK4 expression on TGF β 1 was investigated by treating MCF10A cells with TGF β 1 for a period of three days (day 0 – day 3), after which the cells were washed and the medium was replaced for medium lacking TGF β 1 (Figure 41C). At days 0, 3, and 7 the cells were lysed and analyzed via WB and qRT-PCR for KANK4 expression. Both, protein and mRNA levels showed an increase at day three in comparison to day zero (Figure 41D, E). Active TGF β 1 signaling was confirmed by elevated pSmad2/3 levels at day three (Figure 41D). However, when TGF β 1 was removed, TGF β 1 signaling (pSmad2/3) and KANK4 levels were downregulated accordingly (Figure 41D, E).

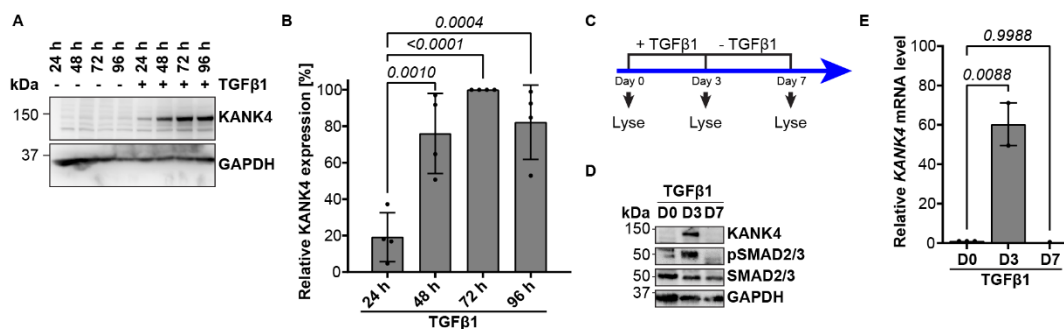


Figure 41: TGF β 1 induces KANK4 expression. (A, B) Lysates of MCF10A cells treated without or with TGF β 1 for indicated timepoints were analyzed by WB with indicated antibody (A). GAPDH served as loading control. Quantification (B) shows abundance of KANK4 protein levels upon TGF β 1 treatment normalized to GAPDH (n=4 independent experiments). *P* values (one-way ANOVA with Dunnett's multiple comparisons test) are shown on top of each comparison. Mean \pm SD is shown. (C) Scheme of TGF β 1 treatment. MCF10A cells were treated with TGF β 1 for three days (day 0 – day 3), before medium was replaced and cells were continued to be cultured without TGF β 1 (day 3 – day 7). (D) Lysates of MCF10A cells treated according to scheme (C) were analyzed by WB with indicated antibodies. GAPDH served as

loading control. (E) mRNA level of *KANK4* in MCF10A cells treated according to scheme (C) were analyzed by qRT-PCR. Fold change is shown after normalization to *GAPDH* (n=3 independent experiments). *P* values (one-way ANOVA with Dunnett's multiple comparisons test) are shown on top of each comparison. Mean \pm SD is shown. In parts taken from a manuscript (Seiwert *et al.*) in consideration.

The data show that TGF β 1 induces *KANK4* expression within three days and that *KANK4* levels are dependent on the continuous presence of TGF β 1.

4.3.4.3 TGF β 1-Smad signaling induces *KANK4* expression

The canonical TGF β 1 signaling is dependent on the Smad protein family (see chapter 1.3.2.1). Data mining of public ChIP-Seq or ChIP-exo experiments revealed that Smads of the TGF β -like subgroup (Smad2, 3) and the BMP-like subgroup (Smad1, 5), as well as Co-Smad Smad4 display binding sites at the promoter region of *KANK4*, indicating a transcriptional connection between TGF β -Smad signaling and *KANK4* (Figure 42).

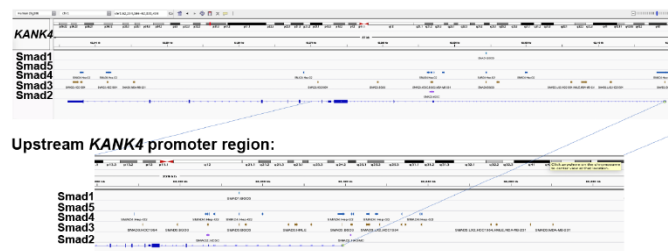


Figure 42: ChIP-analysis. Data mining of public ChIP-Seq experiments. The upstream promoter region of *KANK4* is highlighted. Peaks in the tracks of the different Smads show potential binding-sites to the *KANK4* promoter.

To verify this assumption, Smad2, 3, and 4 were knocked down in MCF10A cells using pooled siRNAs and cells were treated with TGF β 1 to induce *KANK4* expression. The TGF β 1-dependent induction of *KANK4* was significantly impaired upon KD of Smad3 and, in particular, Smad4 (Figure 43A, B). As anticipated, KD of the different Smads also downregulated E-Cad and upregulated N-Cad, indicating inhibition of EMT (Figure 43A). Staining of *KANK4* and pSmad3 in adjacent sections of *KANK4*-WT^{PyMT} tumor tissue further supported the TGF β 1-Smad-mediated *KANK4* induction, as *KANK4* expression

correlated with active TGF β 1 signaling, shown by pSmad3, in transformed LECs (Figure 43C).

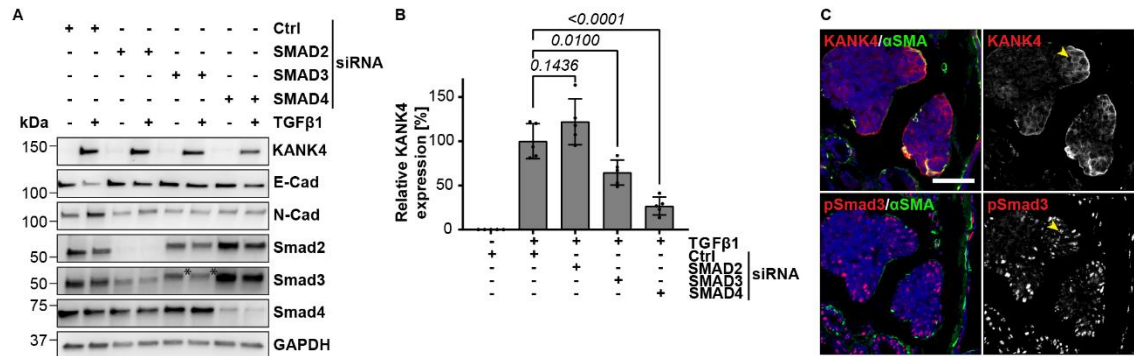


Figure 43: TGF β 1-Smad signaling induces KANK4 expression. (A, B) Lysates of MCF10A cells treated without or with TGF β 1 for three days and siRNA-depleted of indicated Smad proteins were analyzed by WB with indicated antibodies (A). Note that the two bands (marked by asterisks in the Smad3 blot) were remaining signals from the Smad2 antibody after incomplete stripping. GAPDH served as loading control. Quantification (B) shows abundance of KANK4 protein levels normalized to GAPDH (n=5 independent experiments). *P* values (one-way ANOVA with Dunnett's multiple comparisons test) are shown on top of each comparison. Mean \pm SD is shown. (C) IF staining of MG tumor tissues from KANK4-WT^{pyMT} mice for KANK4 or pSmad3 (both shown in red) and α SMA⁺ myoepithelial cells (green). Nuclei were counterstained with DAPI (blue). Arrowheads show regions with KANK4 and pSmad3 co-expression. Scale bar: 50 μ m. In parts taken from a manuscript (Seiwert *et al.*) in consideration.

4.3.5 TGF β 1-induced EMT

EMT is a process that enables cancer cells to invade and eventually form metastasis at distant sites (see chapter 1.4 and 1.4.2). TGF β is well documented as a factor that induces EMT, and extensive evidence exists demonstrating that MCF10A cells respond to TGF β treatment with EMT (Kim, Kim and Moon, 2004; Djomehri *et al.*, 2019).

4.3.5.1 TGF β 1 induces EMT in MCF10A and HMLE-Twist1-ER cells

To examine the impact of TGF β 1 on MCF10A cells, whole cell proteomic analysis was performed. This confirmed that KANK4, but not KANK1 or KANK2, was specifically upregulated in TGF β 1 treated MCF10A cells (Figure 44A). Furthermore, it clearly showed the upregulation of mesenchymal proteins involved in actin regulation and the downregulation of epithelial proteins. As previously reported in the literature, TGF β 1

changed the cellular morphology of MCF10A cells from a cobblestone morphology to an elongated and spindle-like cell shape (Figure 44B, upper panel). IF staining of MCF10A cells demonstrated the correlation between the observed change in morphology and a decrease in the epithelial marker E-Cad, accompanied by an upregulation of the mesenchymal markers N-Cad and fibronectin (Figure 44B, middle and lower panel). WB analysis showed that E-Cad expression exhibited a gradual increase in untreated cells, potentially due to an increase in confluency over the three-day culture period, leading to enhanced cell-cell contacts and adhesions (Figure 44C, D). However, TGF β 1 treatment resulted in a significant impairment of E-Cad expression (Figure 44C, D). In contrast, N-Cad expression increased after 24 hours of TGF β 1 treatment (Figure 44C, E).

To corroborate the findings in an alternative cell line, HMLE-Twist1-ER cells were employed. These cells stably express the EMT-TF Twist1 coupled to a Tamoxifen-inducible estrogen receptor and were previously established by Mani *et al.* (Mani *et al.*, 2008). This enables the onset of the EMT program via either TGF β 1 or, independently of TGF β 1, via Tamoxifen. Morphological changes similar to those observed in MCF10A cells treated with TGF β 1 were seen in HMLE-Twist1-ER cells treated with TGF β 1 or Tamoxifen, indicating that EMT was successfully induced in HMLE-Twist1-ER cells (Figure 44F).

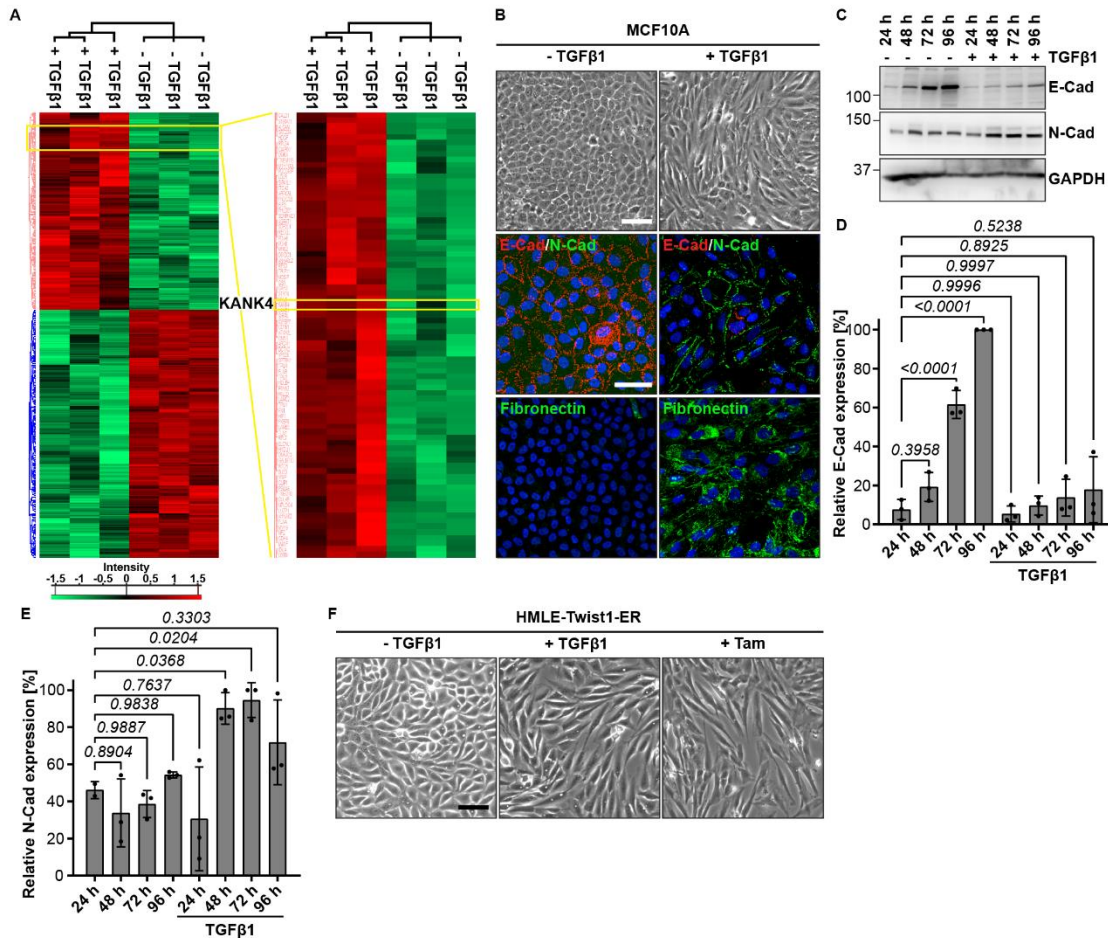


Figure 44: TGFβ1 induces EMT in MCF10A and HMLE-Twist1-ER cells. (A) Total proteome of MCF10A cells treated without or with TGFβ1. (B) Light microscopy and IF staining of MCF10A cells treated without or with TGFβ1 for three days for E-Cad (red) and N-Cad or fibronectin (both shown in green). Nuclei were counterstained with DAPI (blue). Scale bar: 50 μm. (C, D, E) Lysates of MCF10A cells treated without or with TGFβ1 for indicated timepoints were analyzed by WB with indicated antibodies (C). GAPDH served as loading control. Note that parts of the WB have been already used to show time-dependent upregulation of KANK4 in Figure 41 A. Quantification (D, E) shows abundances of E-Cad (D) or N-Cad (E) protein levels normalized to GAPDH (n=3 independent experiments). P values (one-way ANOVA with Dunnett's multiple comparisons test) are shown on top of each comparison. Mean ± SD is shown. (F) Light microscopy of HMLE-Twist1-ER cells treated without or with TGFβ1 or Tamoxifen (Tam) for three days. Scale bar: 50 μm. In parts taken from a manuscript (Seiwert *et al.*) in consideration.

Altogether, MCF10A and HMLE-Twist1-ER cells were verified as working model systems for investigating TGFβ1-dependent and -independent EMT.

4.3.5.2 KANK4 expression is independent of EMT-TFs

TGFβ1 induces *de novo* expression of KANK4 in MCF10A cells (see chapter 4.3.4.2-4.3.4.3, Figure 40-43). Moreover, TGFβ1 induces EMT in MCF10A cells (see chapter

4.3.5.1, Figure 44). To determine whether EMT is responsible for KANK4 expression, the EMT-TFs Snail, Twist and Zeb1 were tested for transient and viral transfection in MCF10A cells, of which only Snail overexpression was successfully achieved. Thus, HMLE-Twist1-ER cells were used as a second model system to evaluate Twist1. While TGF β 1 treatment induced KANK4 expression in MCF10A and HMLE-Twist1-ER cells, Snail expression alone was unable to induce KANK4 (Figure 45A). The treatment of HMLE-Twist1-ER cells with Tamoxifen activated the EMT-TF Twist1, but also proved ineffective in inducing KANK4 expression (Figure 45A). TGF β 1, Snail, or Tamoxifen treatment resulted in the characteristic upregulation of N-Cad, vimentin, and Zeb1, thereby demonstrating that EMT occurred under all three conditions (Figure 45A).

Furthermore, KANK4 mRNA levels were elevated in response to TGF β 1, but not Tamoxifen in HMLE-Twist1-ER cells (Figure 45B). To analyze whether prolonged Tamoxifen treatment would eventually induce KANK4 expression in HMLE-Twist1-ER cells via Twist1 or upregulation of Zeb1, the cells were cultured for up to 23 days in the presence of Tamoxifen. Despite the induction of Zeb1 and an EMT phenotype, Tamoxifen did not induce KANK4 expression (Figure 45C).

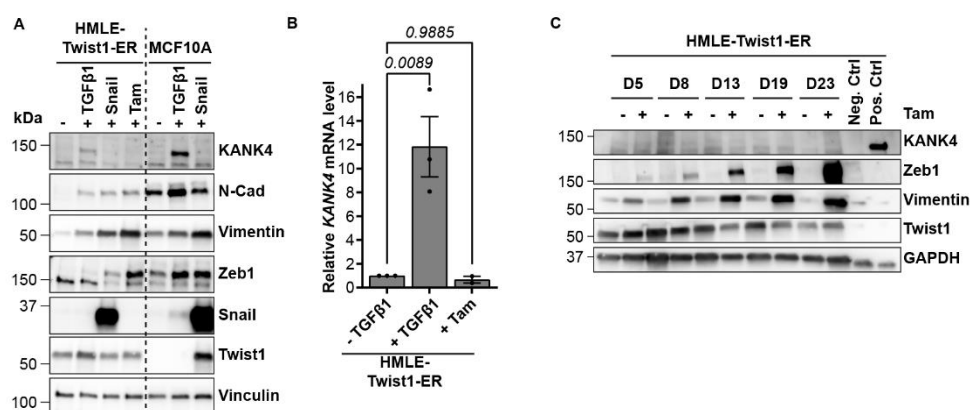


Figure 45: KANK4 expression is independent of EMT-TFs. (A) Lysates of HMLE-Twist1-ER and MCF10A cells treated either without or with TGF β 1 or Tamoxifen for three days or transfected with Snail cDNA were analyzed by WB with indicated antibodies. Vinculin served as loading control. (B) mRNA level

of *KANK4* in HMLE-Twist1-ER cells treated without or with TGF β 1 or Tamoxifen for three days were analyzed by qRT-PCR. Fold change is shown after normalization to *GAPDH* (n=3 independent experiments). *P* values (one-way ANOVA with Dunnett's multiple comparisons test) are shown on top of each comparison. Mean \pm SD is shown. (C) Lysates of HMLE-Twist1-ER cells treated without or with Tamoxifen for indicated days were analyzed by WB with indicated antibodies. GAPDH served as loading control. In parts taken from a manuscript (Seiwert *et al.*) in consideration.

The data demonstrate that TGF β 1-induced EMT in MCF10A and HMLE-Twist1-ER cells occurs concurrently with TGF β 1-induced *KANK4* expression and that EMT alone, as indicated by EMT-TFs, is insufficient to induce *KANK4*.

4.3.6 Function of TGF β 1-induced *KANK4* expression

The previous data show that TGF β 1-Smad3/4 induce *de novo* expression of *KANK4* in transformed LECs (see chapter 4.3.4.3, Figure 43), which correlates with earlier tumor onset, tumor growth, and most importantly increased metastasis formation (see chapter 4.3.2, Figure 34). The subsequent objective was to elucidate the molecular function of *KANK4* by using CRISPR/Cas9-mediated depletion of *KANK4* in MCF10A cells (see chapter 9.3, Figure 67).

4.3.6.1 *KANK4* promotes individual cell migration in 2D

Given that TGF β 1 is known to enhance cell migration and invasion capability and that the presence of *KANK4* enhances metastasis formation, the influence of *KANK4* on 2D migration was investigated. To this end, MCF10A^{KANK4-WT} and MCF10A^{KANK4-KO} cells were cultured in the absence or presence of TGF β 1 on a collagen I-coated 0.5 kPa hydrogel plate. The specific stiffness of the hydrogel was employed to emulate the *in vivo* circumstances within the breast tissue (Pratt, Lee and Martin, 2020). 2D migration showed that MCF10A^{KANK4-WT} and MCF10A^{KANK4-KO} cells exhibited collective migration in chains and sheets, and maintained a cobblestone morphology in the absence of TGF β 1 (Figure 46A two upper panels, B). However, treatment with TGF β 1 induced individual cell

migration in MCF10A^{KANK4-WT} cells, which subsequently switched into collective chain-like movement with spindle-like cell morphology. In contrast, MCF10A^{KANK4-KO} cells continued to migrate collectively with epithelial cell shape (Figure 46A two lower panels, B). The quantification of the three distinct migration modes (individual, sheet-like, and chain-like) in the presence of TGFβ1 revealed that MCF10A^{KANK4-WT} cells exhibited a significantly higher propensity for individual migration compared to MCF10A^{KANK4-KO} cells (Figure 46C).

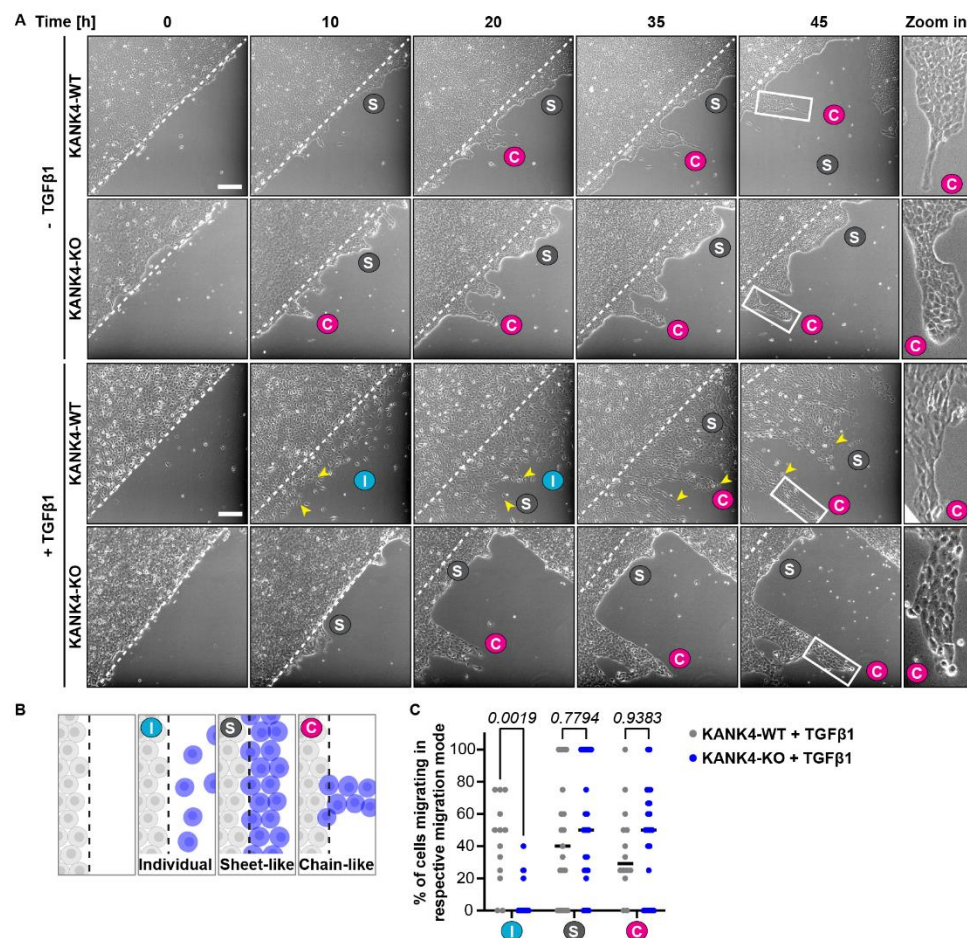


Figure 46: KANK4 promotes individual cell migration in 2D. (A) Still images of 2D migrating MCF10A^{KANK4-WT} and MCF10A^{KANK4-KO} cells cultured on collagen I-coated 0.5 kPa hydrogel plates without or with TGFβ1 for 45 hours. Dotted lines mark the initial migration front. Arrowheads indicate individually migrating cells that turn into leader cells. Boxed areas from the 45 hours timepoint are shown at higher magnification (zoom in). S: Sheet-like cell movement. C: Chain-like cell movement. I: Individual cell movement. Scale bar: 50 μm. (B) Cartoon illustrating the different migration modes detected. (C) Quantification of the respective migration modes shown in (A, B) (n=3 independent experiments). *P* values

(two-way ANOVA with multiple comparison and Šídák correction) are indicated on top of each comparison. In parts taken from a manuscript (Seiwert *et al.*) in consideration.

4.3.6.2 KANK4 promotes 3D cell invasion

To study the effect of enhanced individual cell migration on the capacity to invade 3D environments, MCF10A^{KANK4-WT} and MCF10A^{KANK4-KO} cells were embedded in a collagen/Matrigel matrix, and the formation and growth of spheroids were monitored over a 12-day period in the absence and presence of TGFβ1. In the absence of TGFβ1, the spheroids exhibited a roundish morphology and demonstrated growth over time. However, upon TGFβ1 treatment, the cells underwent elongation and invasion of cell strands into the matrix in MCF10A^{KANK4-WT} cells (Figure 47A, upper panel). Live-cell imaging showed that the cells initially detached as single-cells from the spheroid, a phenomenon that was also observed in 2D culture. Subsequently, the cells elongated and formed connections with each other to collectively invade the surrounding matrix. However, depletion of KANK4 significantly impaired 3D invasion, which could be partially rescued by stably expressing GFP-KANK4 in MCF10A^{KANK4-KO} cells (Figure 47A, three lower panels, B). Introducing GFP-KANK4 in MCF10A^{KANK4-WT} cells could further enhance invasion (Figure 47B).

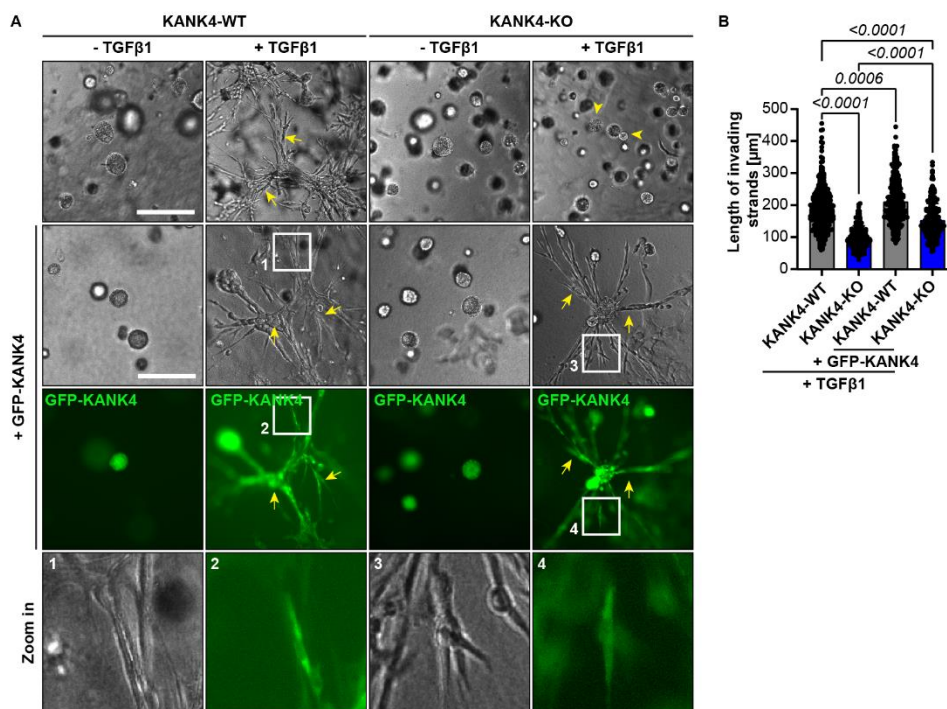


Figure 47: KANK4 promotes 3D cell invasion. (A) MCF10A^{KANK4-WT} and MCF10A^{KANK4-KO} cells without or with ectopic GFP-KANK4 expression cultured in collagen/Matrigel matrix without or with TGFβ1 for 12 days. Arrows indicate invading strands and arrowheads indicate spheroids. Inserts (1-4) highlight GFP-KANK4 expression. Scale bar: 200 μm. (B) Quantification of the invading strands shown in (A) (n>20 spheroids measured per condition and experiment, pooled from n=4 independent experiments). *P* values (one-way ANOVA with multiple comparison and Šidák correction) are indicated on top of each comparison. Mean ± SD is shown. In parts taken from a manuscript (Seiwert *et al.*) in consideration.

The expression of GFP alone failed to rescue the invasive phenotype in MCF10A^{KANK4-KO} cells (Figure 48).

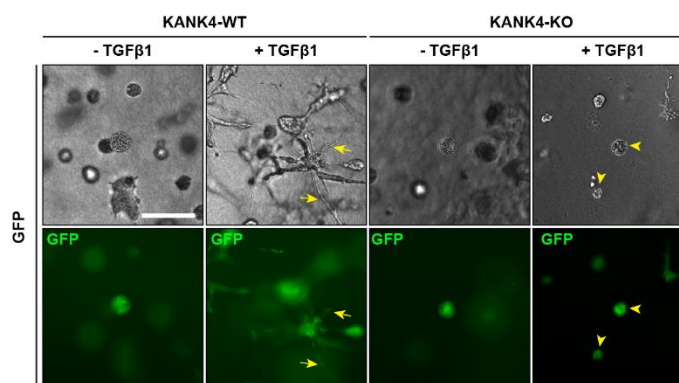


Figure 48: KANK4 in 3D invasion. MCF10A^{KANK4-WT} and MCF10A^{KANK4-KO} cells with ectopic GFP expression cultured in collagen/Matrigel matrix without or with TGFβ1 for 12 days. Arrows indicate invading strands and arrowheads indicate spheroids. Scale bar: 200 μm. In parts taken from a manuscript (Seiwert *et al.*) in consideration.

To exclude the possibility that the observed defects in invasion are due to impaired cell proliferation, the size and growth of spheroids were determined. No difference in size was observed between MCF10A^{KANK4-WT} and MCF10A^{KANK4-KO} cells, neither in the absence nor presence of TGFβ1 (Figure 49A). However, TGFβ1 treatment generally resulted in a significant reduction in spheroid growth, which is in accordance with its anti-proliferative effects reported in the literature (see chapter 1.3.3). 2D BrdU staining of MCF10A^{KANK4-WT} and MCF10A^{KANK4-KO} cells did not reveal differences in proliferation rate (Figure 49B), indicating that the reduced 3D invasion observed in the absence of KANK4 was not due to decreased cell proliferation.

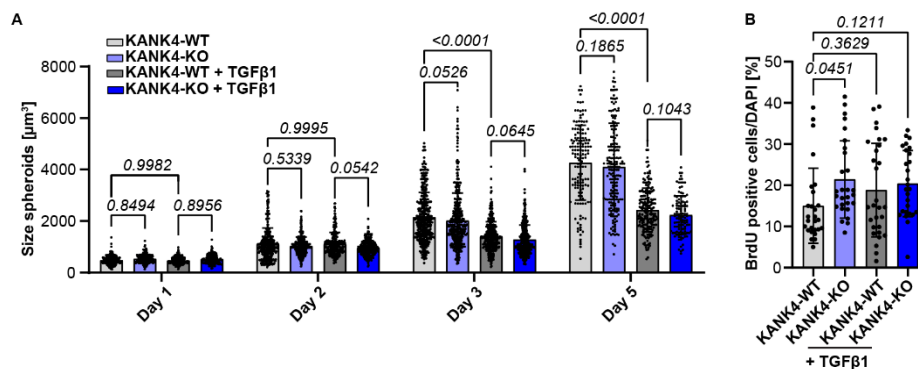


Figure 49: Spheroid growth and cell proliferation. (A) Growth monitoring of the spheroids derived from MCF10A^{KANK4-WT} and MCF10A^{KANK4-KO} cells cultured in collagen/Matrigel matrix without or with TGFβ1 over a five-day period (n>50 spheroids measured per condition, pooled from n=4 independent experiments). *P* values (two-way ANOVA with multiple comparison and Tukey correction) are indicated on top of each comparison. Mean ± SD is shown. (B) Cell proliferation analyzed by BrdU staining in MCF10A^{KANK4-WT} and MCF10A^{KANK4-KO} cells cultured on collagen I-coated 0.5 kPa hydrogel plates without or with TGFβ1 for three days (n>5 cell regions, pooled from n=3 independent experiments). *P* values (one-way ANOVA with multiple comparison and Šidák correction) are indicated on top of each comparison. Mean ± SD is shown. In parts taken from a manuscript (Seiwert *et al.*) in consideration.

Additionally, 3D invasion was observed in TGFβ1-treated HMLE-Twist1-ER cells (Figure 50). However, treatment with Tamoxifen to induce TGFβ1-independent EMT without KANK4 *de novo* expression did not result in invasion, neither with ectopic expression of GFP-KANK4. Furthermore, neither TGFβ1 nor additional GFP-KANK4 could rescue the anti-proliferative effects of Tamoxifen (Figure 50).

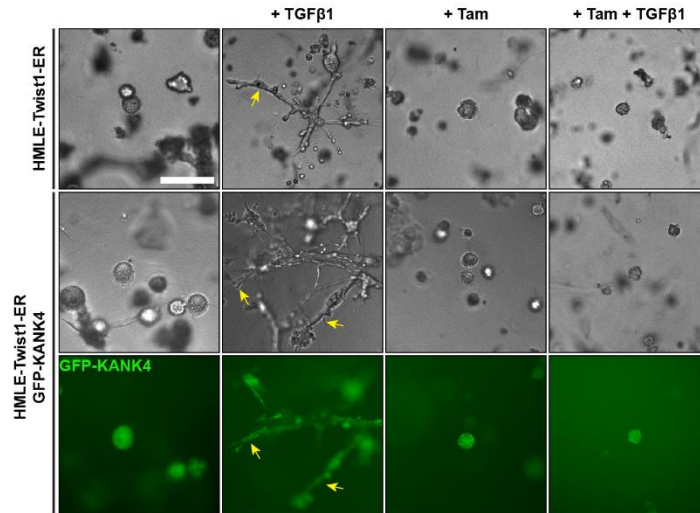


Figure 50: 3D invasion of HMLE-Twist1-ER cells. HMLE-Twist1-ER cells without or with ectopic GFP-KANK4 expression cultured in collagen/Matrigel matrix without or with TGF β 1 or Tamoxifen for 12 days. Arrows indicate invading strands. Scale bar: 200 μ m.

The data collectively show that KANK4 is indispensable for optimal 3D invasion, as it facilitates single-cell detachment and cell elongation, which are required for invasion. However, KANK4 expression alone was not able to induce the invasive process, showing that KANK4 requires the coupling with TGF β 1 signaling.

4.3.6.3 Recruitment of CMSC and MMPs is independent of KANK4

KANK1 and KANK2 interact with the CMSC via KIF21A and liprin- β 1, to direct MTs to FAs and facilitate targeted secretion of e.g., MMPs (see chapter 1.2.1). Given the essential role of matrix degradation in mesenchymal migration and invasion (see chapter 1.7.2), the hypothesis was tested whether KANK4 deficiency impairs MT targeting and the secretion of MMPs, thus affecting 3D invasion. To this end, GFP-IP/MS experiments were conducted to determine whether KANK4 interacts with the CMSC like KANK1 and KANK2. Similar to structural analysis performed on the interaction between KANKs and KIF21A, which proposed that KANK4 is unable to bind KIF21A (Guo *et al.*, 2018; Pan *et al.*, 2018; Weng *et al.*, 2018), no CMSC member was pulled down by GFP-KANK4

(Figure 51A). Instead, known interaction partners, including 14-3-3 proteins and talin, were identified and served as positive controls. The lack of interaction between KANK4 and KIF21A or liprin- β 1 was also demonstrated by WB (Figure 51B).

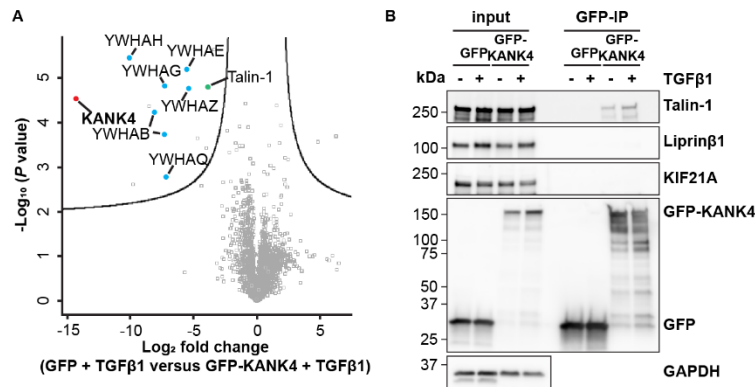


Figure 51: KANK4 does not interact with the CMSC. (A) Volcano plot of GFP-KANK4 interacting proteins in MCF10A cells treated with TGFβ1 and with ectopic GFP versus GFP-KANK4 expression. KANK4 is highlighted in red. Known KANK4 interacting partners are highlighted in blue (14-3-3) and green. Black line indicates the significance cut-off (false discovery rate of 0.05, S0: 0.5) estimated with the Perseus software. (B) Lysates of MCF10A cells with ectopic GFP or GFP-KANK4 expression treated without or with TGFβ1 for three days were used for GFP-IP and analyzed by WB with indicated antibodies. GAPDH served as loading control. In parts taken from a manuscript (Seiwert *et al.*) in consideration.

Assuming that CMSC targeting to FAs is independent of KANK4, the localization of MMPs to FAs should not be affected in MCF10A^{KANK4-KO} cells. This was corroborated by staining for the membrane-bound MMP14 in MCF10A^{KANK4-WT} and MCF10A^{KANK4-KO} cells treated with TGFβ1 (Figure 52A). MMP14 was detected at the cell edge in close proximity to FAs in both cell lines. Similarly, MT ends were observed to localize to FAs in both MCF10A^{KANK4-WT} and MCF10A^{KANK4-KO} cells.

To analyze the effect of KANK4 depletion on the secreted MMPs MMP2 and MMP9, gelatin zymography assays were conducted. This involved culturing MCF10A^{KANK4-WT} and MCF10A^{KANK4-KO} cells in the absence or presence of TGFβ1, collecting cell lysates as well as the conditioned medium, and applying the samples on a gelatin-containing gel under non-reducing conditions. The enzyme activity was restored by incubating the gel in washing buffer to remove SDS and incubation buffer to add the requisite cofactors needed

for the gelatinase reaction. The presence of white bands in the Coomassie-stained gel is indicative of gelatin degradation, which is analogous to MMP activity. As anticipated, cell lysates exhibited minimal MMP activity in samples treated with TGF β 1 (Figure 52B). However, given that TGF β 1 stimulates MMP secretion, the activity was markedly elevated in the conditioned culture medium. No discernible difference was observed in MMP2 and MMP9 activity between MCF10A^{KANK4-WT} and MCF10A^{KANK4-KO} cells treated with TGF β 1. Additionally, the size of FAs was quantified and found to be comparable between MCF10A^{KANK4-WT} and MCF10A^{KANK4-KO} cells (Figure 52C).

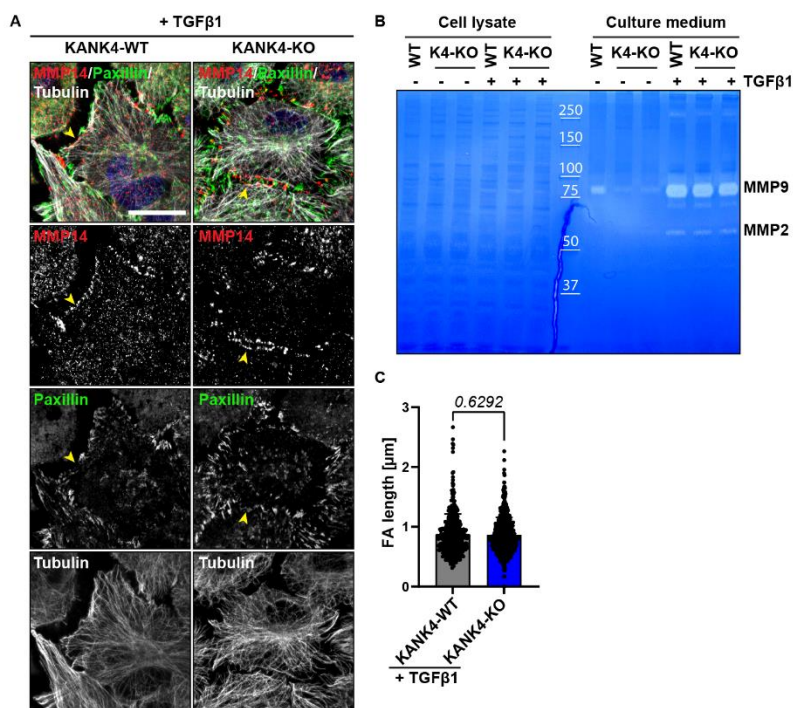


Figure 52: MMP recruitment and secretion is independent of KANK4. (A) IF staining of MCF10A^{KANK4-WT} and MCF10A^{KANK4-KO} cells treated with TGF β 1 for three days for MMP14 (red), Paxillin (green) and Tubulin (white). Nuclei were counterstained with DAPI (blue). Arrowheads indicate MMP14 signals at the vicinity of Paxillin⁺ FAs. Scale bar: 50 μ m. (B) Gelatin degradation assay of cell lysates or supernatants of MCF10A^{KANK4-WT} and MCF10A^{KANK4-KO} cells treated without or with TGF β 1 for three days. Secreted MMPs (MMP2 and MMP9) are indicated. (C) Quantification of FA length in MCF10A^{KANK4-WT} and MCF10A^{KANK4-KO} cells treated with TGF β 1 for three days (n=69 MCF10A^{KANK4-WT} and n=81 MCF10A^{KANK4-KO} cells analyzed, pooled from n=2 independent experiments). *P* value was calculated by unpaired Student's *t*-test. Mean \pm SD is shown. In parts taken from a manuscript (Seiwert *et al.*) in consideration.

The data collectively show that the absence of KANK4 does not influence the localization of CMSC to FAs nor the accurate targeting and secretion of MMPs (MMP14, MMP2, MMP9). This might be due to the lack of interaction between KANK4 and the CMSC members KIF21A and liprin- β 1. Also, the formation and size of FAs were unaffected in MCF10A^{KANK4-KO} cells, suggesting that KANK4's role in 3D invasion is independent of cell adhesion and matrix degradation.

4.3.6.4 KANK4 promotes TGF β 1-induced lamellipodia and invadopodia formation

The 2D and 3D assays demonstrated that MCF10A^{KANK4-WT} cells exhibited an elongated cell shape with single-cell detachment. Mesenchymal cell migration is dependent upon three main steps: The initial phase of cell migration involves the formation of filopodia and lamellipodia, as well as the establishment of NAs. The subsequent stage encompasses the maturation of these NAs into FAs, which facilitate robust cell-matrix adhesion. Finally, the ECM is locally degraded (see chapter 1.7.2). Given the absence of a discernible difference in FA formation and matrix degradation between MCF10A^{KANK4-WT} and MCF10A^{KANK4-KO} cells treated with TGF β 1 (see chapter 4.3.6.3, Figure 52), the initial step of lamellipodia formation was further examined. Indeed, MCF10A^{KANK4-KO} cells showed a significant diminished formation of lamellipodia compared to MCF10A^{KANK4-WT} cells in the presence of TGF β 1, which could be partially rescued by the expression of GFP-KANK4 (Figure 53A, B). As a consequence of reduced lamellipodia formation, cell circularity was increased in MCF10A^{KANK4-KO} cells, due to a rounder cell morphology (Figure 53C). In contrast, cell circularity was decreased in MCF10A^{KANK4-WT} cells or MCF10A^{KANK4-KO} cells expressing GFP-KANK4 (Figure 53C).

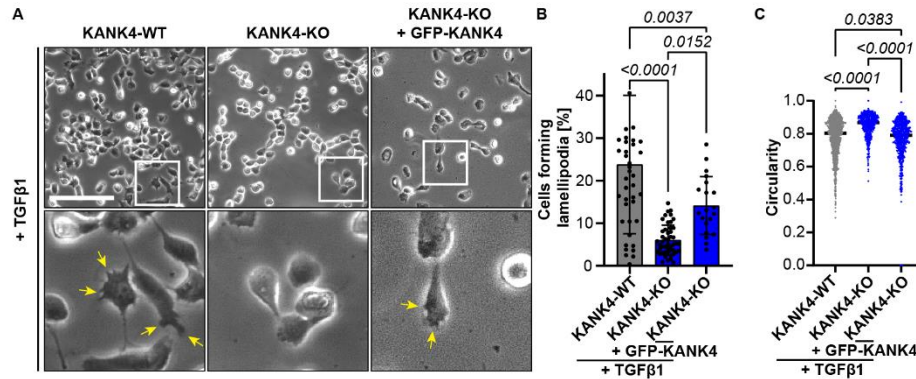


Figure 53: KANK4 promotes TGFβ1-induced lamellipodia formation. (A) Light microscopy images of MCF10A^{KANK4-WT}, MCF10A^{KANK4-KO}, and MCF10A^{KANK4-KO} cells ectopically expressing GFP-KANK4 seeded on collagen I-coated 0.5 kPa hydrogel plates treated with TGFβ1 for 48 hours. Arrows indicate lamellipodia. Scale bar: 50 μm. (B, C) Quantification of lamellipodia (B) and cell circularity (C) are shown for n>100 cells analyzed per condition, pooled from n=4 independent experiments with five images analyzed, respectively. *P* values (one-way ANOVA with multiple comparison and Tukey correction) are indicated on top of each comparison. Mean ± SD is shown. In parts taken from a manuscript (Seiwert *et al.*) in consideration.

Invadopodia are indispensable for mesenchymal 3D invasion and exhibit elevated proteolytic activity. The formation of invadopodia was observed by culturing MCF10A^{KANK4-WT} and MCF10A^{KANK4-KO} cells in the presence of TGFβ1 on 488-labelled gelatin substrate. As with the gelatin zymography assay, proteolytic activity and thus invadopodia formation were identified by the presence of black spots in the gelatin coating, indicating the degradation of gelatin. Furthermore, visualization of the F-actin-rich and dot-shaped core of invadopodia was achieved through phalloidin staining. In the presence of TGFβ1, MCF10A^{KANK4-WT} cells formed gelatin-degrading invadopodia with KANK4 localizing around the F-actin core (Figure 54A, upper panel). In contrast, MCF10A^{KANK4-KO} cells formed significantly fewer invadopodia that did not mature into proteolytically active structures (Figure 54A, lower panel, B).

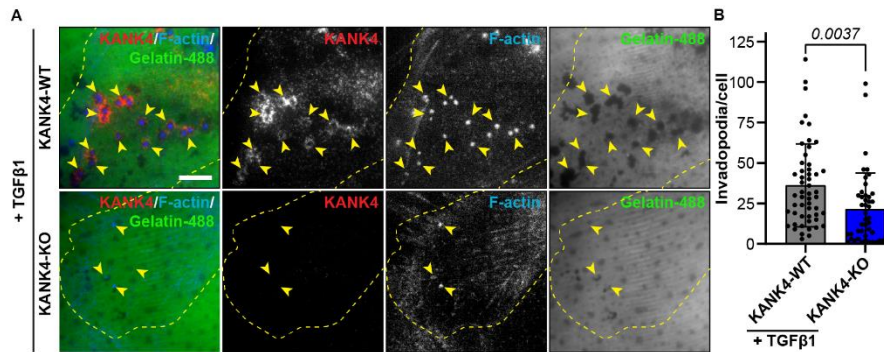


Figure 54: KANK4 promotes TGFβ1-induced invadopodia formation. (A) IF staining of TGFβ1-treated MCF10A^{KANK4-WT} and MCF10A^{KANK4-KO} cells seeded on gelatin-488 for KANK4 (red) and F-actin (blue). Arrowheads indicate invadopodia. Dotted lines mark the cell outline. Scale bar: 10 μm. (B) Quantification of the invadopodia formation shown in (A) (n=53 MCF10A^{KANK4-WT} and n=44 MCF10A^{KANK4-KO} cells analyzed, pooled from n=2 independent experiments). *P* value was calculated by unpaired Student's *t*-test. Mean ± SD is shown. In parts taken from a manuscript (Seiwert *et al.*) in consideration.

The data demonstrate that TGFβ1-induced KANK4 expression facilitates TGFβ1-mediated lamellipodia and invadopodia formation, which represents a crucial step in mesenchymal cell migration and invasion. Consequently, the depletion of KANK4 impairs this initial step, resulting in the inhibition of migration and 3D invasion.

4.3.6.5 KANK4 promotes TGFβ1-induced Rac1 activation

The formation of lamellipodia and invadopodia is driven by the small GTPases Rac1 (Pignatelli *et al.*, 2012; Moshfegh *et al.*, 2014; Ma *et al.*, 2023). To examine whether KANK4 affects Rac1 activity to promote TGFβ1-driven lamellipodia and invadopodia formation, the subcellular localization of KANK4 and Rac1 was determined. As a FA protein, KANK4 localized as anticipated in paxillin⁺ FAs (Figure 55, first panel). Furthermore, KANK4 localized to NAs at the leading edge of the cells. A comparable expression profile was discerned for Rac1. The co-localization of Rac1 and KANK4 suggests their potential crosstalk (Figure 55, second panel). The localization of the Rac1 complex at lamellipodia was confirmed by Arp3 (Figure 55, third panel). The td-tomato-WASp construct was used to indirectly visualize Rac1 localization, as WASp binds to

endogenous active Rac1 at its native cellular localization (Mahlandt *et al.*, 2023). Additionally, td-tomato-WASp was concentrated together with KANK4 at lamellipodia (Figure 55, fourth panel).

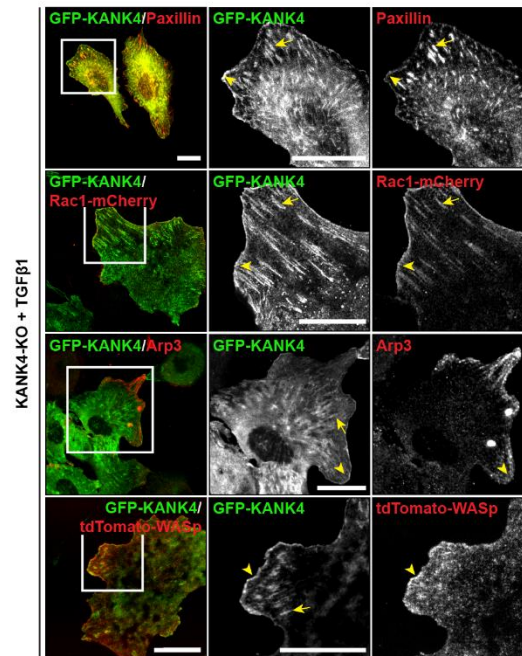


Figure 55: KANK4 and Rac1 localize to lamellipodia. IF staining of MCF10A^{KANK4-KO} cells treated with TGFβ1 for three days and transfected with GFP-KANK4 (green), Rac1-mCherry or tdTomato-WASp (both shown in red), or transfected with GFP-KANK4 (green) and IF-stained for Paxillin or Arp3 (both shown in red). Arrows indicate FAs and arrowheads indicate lamellipodia. Scale bars: 20 μm. In parts taken from a manuscript (Seiwert *et al.*) in consideration.

To assess whether there is a crosstalk between KANK4 and Rac1 signaling, Rac1 activity was determined in MCF10A^{KANK4-WT} and MCF10A^{KANK4-KO} cells in the absence or presence of TGFβ1 using an active-Rac1-IP kit. Here, beads are coupled to a GST-Pak1-PBD fusion protein, which specifically interacts with GTP-bound small GTPases. Interestingly, while TGFβ1 augmented active Rac1 levels in MCF10A^{KANK4-WT} cells, this was significantly diminished in MCF10A^{KANK4-KO} cells (Figure 56A, B). The activity of Cdc42, which is also implicated in invadopodia formation, remained unaltered in the absence of KANK4 (Figure 56C, D), suggesting a selective involvement of KANK4 in Rac1 activation.

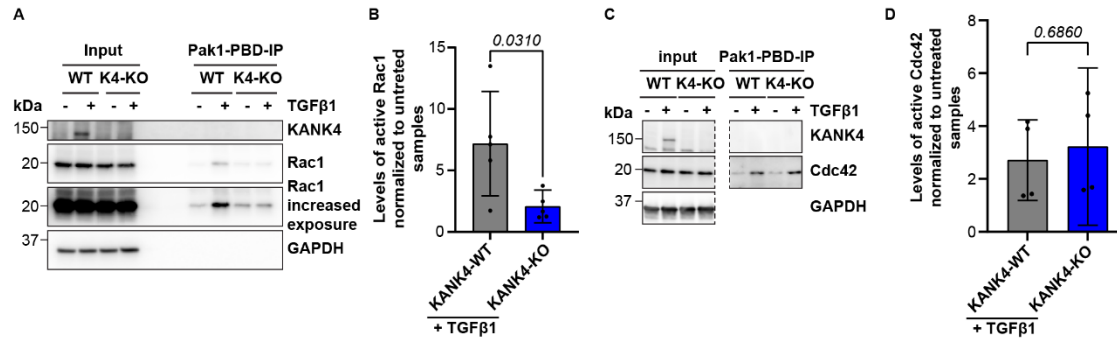


Figure 56: KANK4 promotes TGFβ1-induced Rac1 but not Cdc42 activation. (A, B) Lysates of MCF10A cells treated without or with TGFβ1 for three days were used for GST-Pak1-PBD pulldowns to detect levels of activated Rac1 and were analyzed by WB with indicated antibodies (A). GAPDH served as loading control. Quantification (B) shows abundance of active Rac1 protein levels normalized to input levels. Rac1 levels without TGFβ1 treatment were set to 1 (n=5 independent experiments). *P* value was calculated by unpaired Student's *t*-test. Mean ± SD is shown. (C, D) Lysates of MCF10A cells treated without or with TGFβ1 for three days were used for GST-Pak1-PBD pulldowns to detect levels of activated Cdc42 and were analyzed by WB with indicated antibodies (A). GAPDH served as loading control. Quantification (D) shows abundance of active Cdc42 protein levels normalized to input levels. Cdc42 levels without TGFβ1 treatment were set to 1 (n=4 independent experiments). *P* value was calculated by unpaired Student's *t*-test. Mean ± SD is shown. In parts taken from a manuscript (Seiwert *et al.*) in consideration.

The experiments demonstrate that KANK4 is essential for the promotion of TGFβ1-mediated Rac1 activation, which is implicated in the formation of 2D lamellipodia and 3D invadopodia. To assess the role of Rac1 in 3D invasion, a constitutively active Rac1 construct was introduced into MCF10A^{KANK4-WT} and MCF10A^{KANK4-KO} cells and invasion into the collagen/Matrigel matrix was evaluated. The expression of CA-Rac1 alone was insufficient to induce invasion (Figure 57A, upper two panels). However, treatment with TGFβ1 resulted in invasion of MCF10A^{KANK4-WT} cells, which exhibited a slight increase in invasion when CA-Rac1 was present (Figure 57A, B). More importantly, CA-Rac1 was able to rescue the impaired invasion phenotype observed in MCF10A^{KANK4-KO} cells (Figure 57A, B), whereas GFP alone was unable to do so (Figure 57A, lower two panels).

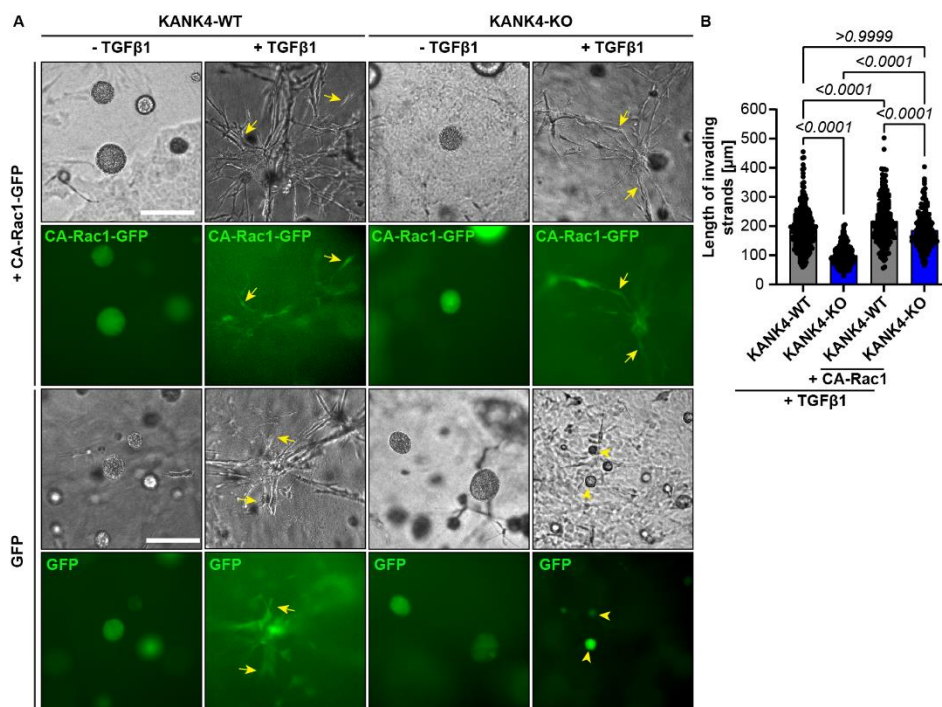


Figure 57: CA-Rac1 rescues 3D invasion in MCF10A^{KANK4-KO} cells. (A) MCF10A^{KANK4-WT} and MCF10A^{KANK4-KO} cells without or with ectopic CA-Rac1-GFP or GFP expression cultured in collagen/Matrigel matrix without or with TGFβ1 for 12 days. Arrows indicate invading strands and arrowheads indicate spheroids. Scale bar: 200 μm. (B) Quantification of the invading strands shown in (A) (n>20 spheroids measured per condition and experiment, pooled from n=3 independent experiments). *P* values (one-way ANOVA with multiple comparison and Šídák correction) are indicated on top of each comparison. Mean ± SD is shown. In parts taken from a manuscript (Seiwert *et al.*) in consideration.

In order to confirm the specificity of Rac1, the chemical inhibitors EHT1864 and NSC23766 were used to inhibit Rac1 in MCF10A^{KANK4-WT} cells. This resulted in a significant decrease in 3D invasion in the presence of TGFβ1 (Figure 58A, B). In contrast, inhibition of Cdc42 via ML141 did not interfere with invasion (Figure 58A, B). These findings confirm the importance of Rac1 activity in the invasion setup used in this study.

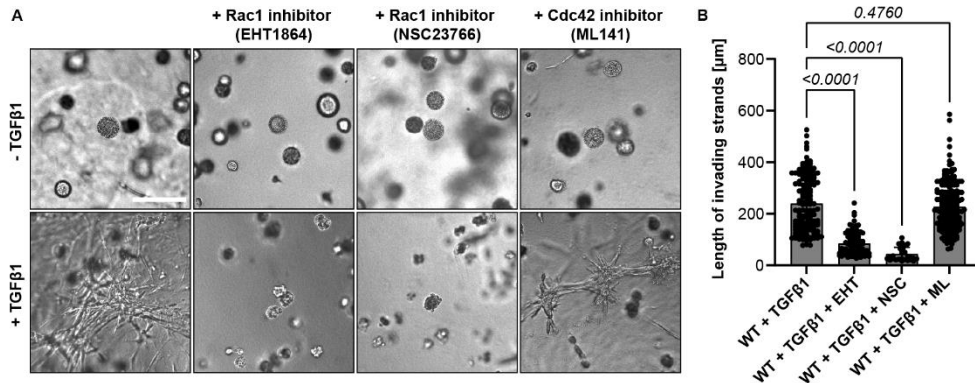


Figure 58: Inhibition of Rac1 impairs 3D invasion. (A) MCF10A^{KANK4-WT} cells cultured in collagen/Matrigel without or with TGFβ1 and with Rac1 inhibitors (EHT1864 and NSC23766) or Cdc42 inhibitor (ML141) for 12 days. Scale bar: 200 μm. (B) Quantification of the invading strands shown in (A) (n>20 spheroids measured per condition and experiment, pooled from n=2 independent experiments). *P* values (one-way ANOVA with multiple comparison and Šidák correction) are indicated on top of each comparison. Mean ± SD is shown. In parts taken from a manuscript (Seiwert *et al.*) in consideration.

In addition to Rac1 and Cdc42, RhoA represents the third member of the Rho family of small GTPases. RhoA plays a pivotal role in the contraction of actomyosin and is particularly crucial in amoeboid migration. An active RhoA-specific IP showed that RhoA levels remained unaltered without or with TGFβ1 treatment, as well as in the presence or absence of KANK4 (Figure 59A). The contractility of MCF10A^{KANK4-WT} and MCF10A^{KANK4-KO} cells was determined by culturing the cells in a collagen matrix in the absence or presence of TGFβ1 and assessing the gel area after the indicated timepoints. The results demonstrated that the two cell lines exhibited comparable cell contractility (Figure 59B), and that TGFβ1 further enhanced contractility, suggesting that RhoA activation and contraction were not affected by KANK4.

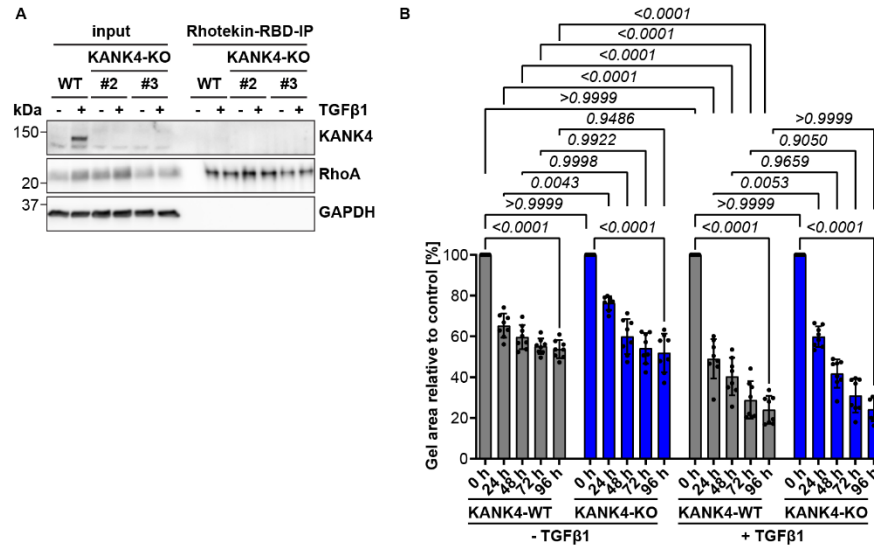


Figure 59: KANK4 does not affect RhoA activity. (A) Lysates of MCF10A^{KANK4-WT} and MCF10A^{KANK4-KO} cells treated without or with TGFβ1 for three days were used for Rhotekin-RBD-IP to detect levels of activated RhoA and were analyzed by WB with indicated antibodies. GAPDH served as loading control. (B) Quantification shows area of gel contraction normalized to timepoint 0 hour of MCF10A^{KANK4-WT} and MCF10A^{KANK4-KO} cells treated without or with TGFβ1 and embedded in 1 mg/mL collagen for indicated timepoints (quadruplicates measured per condition and experiment, pooled from n=2 independent experiments). *P* values (one-way ANOVA with multiple comparison and Šídák correction) are indicated on top of each comparison. Mean ± SD is shown.

The data show that KANK4 specifically promotes TGFβ1-dependent activation of Rac1, which is essential for effective 3D invasion.

4.3.6.6 KANK4 interacts with Coro1A/B to facilitate lamellipodia formation and 3D invasion

How does KANK4 promotes Rac1 activation? To address this question, an endogenous KANK4-IP/MS experiment was conducted, and TGFβ1-specific KANK4 interaction partners were identified. Interestingly, the identified interaction partners were predominantly actin-binding proteins (Figure 60A). Of particular interest were the Coro1A and Coro1B proteins, which have been previously reported to facilitate the translocation of Rac1, but not RhoA or Cdc42, to the plasma membrane and to activate Rac1 by releasing its inhibitor RhoGDIα (see chapter 1.6) (Castro-Castro *et al.*, 2011, 2016). The interactions between KANK4 and Coro1A and Coro1B were confirmed by performing a GFP-IP in

GFP- or GFP-KANK4-expressing cells and transiently expressing HA-tagged Coro1A, followed by analysis via WB (Figure 60B). The interactions between KANK4 and Coro1A and Coro1B were significantly stronger in comparison to the GFP control (Figure 60C).

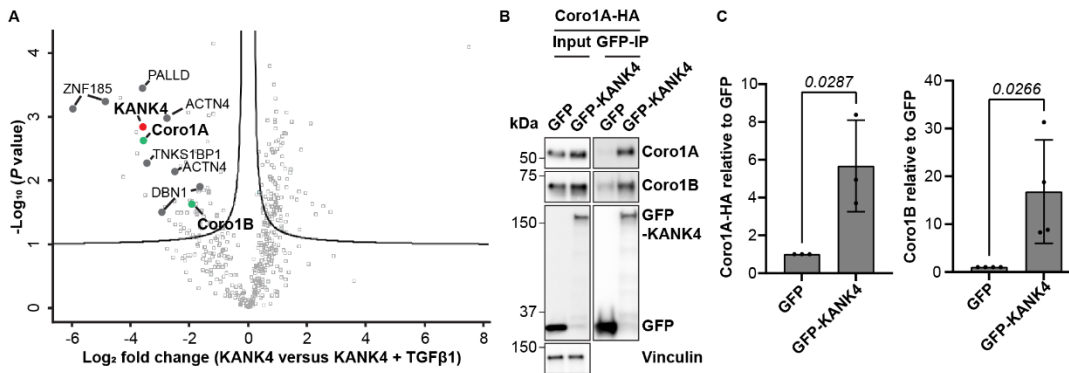


Figure 60: KANK4 interacts with Coro1A and Coro1B. (A) Volcano plot of KANK4 interacting proteins in MCF10A^{KANK4-WT} cells treated without versus with TGFβ1. KANK4 is highlighted in red. Coro1A and Coro1B are highlighted in green and other novel KANK4 interacting proteins are highlighted in grey. Black line indicates the significance cut-off (false discovery rate of 0.05, S0: 0.5) estimated with the Perseus software. (B, C) Lysates of MCF10A^{KANK4-WT} cells with ectopic GFP or GFP-KANK4 expression and transient HA-tagged Coro1A (Coro1A-HA) expression were used for GFP-IP and analyzed by WB with indicated antibodies (B). Vinculin served as loading control. Quantification (C) shows abundance of Coro1A and Coro1B protein levels normalized to input levels (n=3 independent experiments). P values (unpaired Student's *t*-test) are indicated on top of each comparison. Mean ± SD is shown. In parts taken from a manuscript (Seiwert *et al.*) in consideration.

To assess the impact of Coro1A and Coro1B on lamellipodia formation, siRNA-mediated single KDs and double KD were generated in MCF10A^{KANK4-WT} cells. It should be noted that while Coro1A siRNA was specific for Coro1A, Coro1B siRNA targeted both Coro1A and Coro1B, yet Coro1A was not completely depleted (Figure 61A). Additionally, Coro1A levels increased upon TGFβ1 treatment, indicating that it is a TGFβ1-dependent protein, whereas Coro1B levels remained unaffected by TGFβ1 (Figure 61A).

The formation of lamellipodia was moderately hindered by single KDs in the presence of TGFβ1. However, the number of cells forming lamellipodia was significantly reduced by double KD (Figure 61B, C). Similarly, cell circularity increased in double KD cells (Figure 61D). These findings are analogous to the phenotype observed in MCF10A^{KANK4-KO} cells

and indicate that Coro1A and Coro1B may serve as a compensatory mechanism for each other's loss.

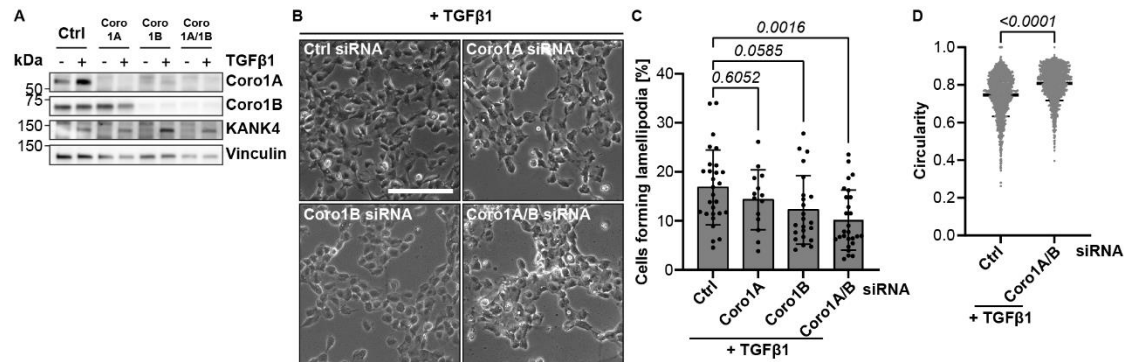


Figure 61: Depletion of Coro1A and Coro1B impairs lamellipodia formation. (A) Lysates of MCF10A^{KANK4-WT} cells treated without or with TGFβ1 and siRNA-depleted of Coro1A, Coro1B, or Coro1A/B, respectively, were analyzed by WB with indicated antibodies. Vinculin served as loading control. (B) Light microscopy images of MCF10A^{KANK4-WT} cells siRNA-depleted of Coro1A, Coro1B, or Coro1A/B, respectively, seeded on collagen I-coated 0.5 kPa hydrogel plates treated with TGFβ1 for 48 hours. Scale bar: 50 μm. (C, D) Quantification of lamellipodia (C) and cell circularity (D) are shown for n>100 cells analyzed per condition and experiment, pooled from n=3 independent experiments with three images analyzed, respectively. P values (one-way ANOVA with multiple comparison and Tukey correction) are indicated on top of each comparison. Mean ± SD is shown. In parts taken from a manuscript (Seiwert *et al.*) in consideration.

In accordance with the impeded lamellipodia formation observed in 2D, the 3D invasion was also inhibited upon Coro1A and Coro1B double KD (Figure 62A, B).

To investigate the relevance *in vivo*, adjacent sections of KANK4-WT^{PyMT} tumor tissues were stained for KANK4 and Coro1B, revealing regions of overlapping KANK4 and Coro1B expression (Figure 62C). This demonstrates that, *in vivo*, both proteins are expressed in the same cells, suggesting that an interaction is feasible.

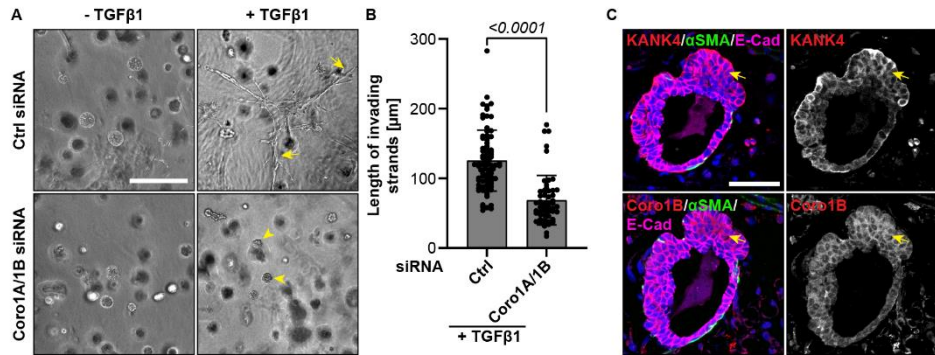


Figure 62: Depletion of Coro1A and Coro1B impairs 3D invasion. (A) MCF10A^{KANK4-WT} cells cultured in collagen/Matrigel matrix without or with TGFβ1 and siRNA-depleted of Coro1A/1B for 12 days. Arrows indicate invading strands and arrowheads spheroids. Scale bar: 200 μm. (B) Quantification of the invading strands shown in (A) (n>20 spheroids measured per condition and experiment, pooled from n=3 independent experiments). *P* value was calculated by unpaired Student's *t*-test (two tailed). Mean ± SD is shown. (C) IF staining of MG tumor tissues from KANK4-WT^{PyMT} mice for KANK4 and Coro1B (both shown in red), αSMA⁺ myoepithelial cells (green) and E-Cad⁺ transformed LECs (magenta). Nuclei were counterstained with DAPI (blue). Arrows show regions with KANK4 and Coro1B co-expression. Scale bar: 50 μm. In parts taken from a manuscript (Seiwert *et al.*) in consideration.

In conclusion, the presented data demonstrate that KANK4 interacts with Coro1A and Coro1B, which are essential for lamellipodia formation and three-dimensional invasion.

4.3.7 KANK4 acts as tumor promoter in several human cancers

To ascertain whether the findings in mice could be extrapolated to human, correlation analyses between KANK4 expression levels and survival probability in various human cancer types were performed. These revealed that high KANK4 levels are associated with reduced survival probability in ER-neg breast cancer, esophageal adenocarcinoma, bladder carcinoma, lungs squamous cell carcinoma, pancreatic ductal adenocarcinoma or sarcoma patients (Figure 63A-F).

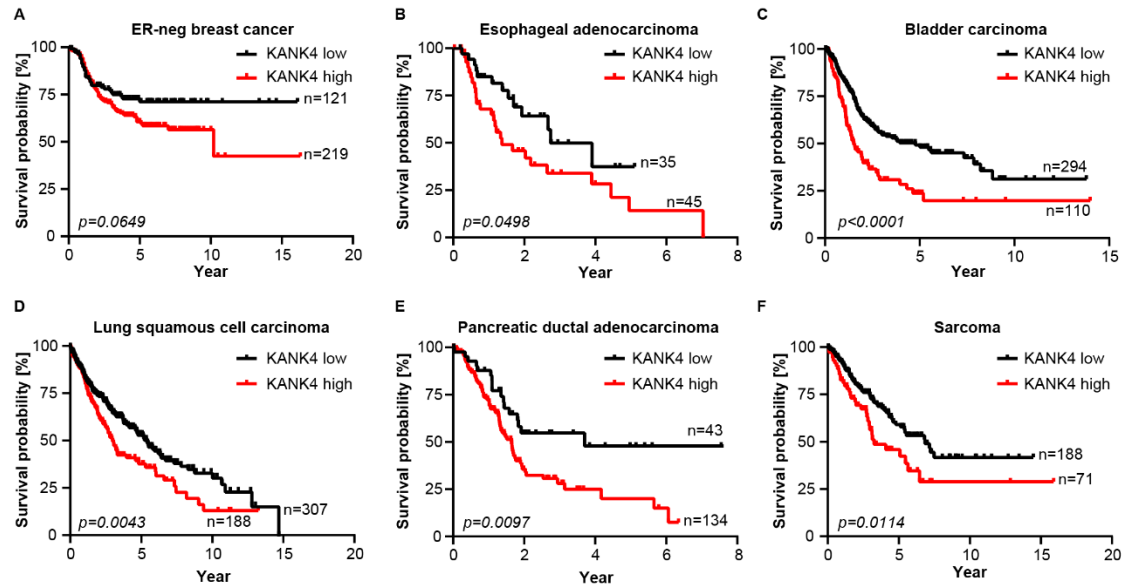


Figure 63: High KANK4 levels correlate with poor survival probability in human cancers. Kaplan-Meier survival analysis of patients from TCGA cohort of different cancer types with high (red line) versus low (black line) KANK4 expression. ER-neg breast cancer (A), esophageal adenocarcinoma (B), bladder carcinoma (C), lung squamous cell carcinoma (D), pancreatic ductal adenocarcinoma (E), and sarcoma (F). Patient numbers included in the analysis are indicated on each plot. *P* values (Log-rank test) are indicated in each graph. In parts taken from a manuscript (Seiwert *et al.*) in consideration.

This confirms the mouse data showing that KANK4 functions as a tumor promoter in these specific cancer types.

4.3.8 Human breast cancer patients show KANK4 expression in LECs

To further validate the mouse findings specifically in breast cancer, clinical samples of breast cancer patients obtained from the Institute of Pathology, University of Cologne, Cologne, Germany were stained for KANK4 (Figure 64A). KANK4 was observed in α SMA⁺ myoepithelial cells and also in E-Cad⁺ transformed LECs, indicating that KANK4 is expressed *de novo* in human cancer cells. Staining of KANK4 and pSmad3 in adjacent sections suggests that this *de novo* expression of KANK4 is also associated with TGF β 1 signaling, evidenced by overlapping expression of KANK4 and pSmad3 in LECs (Figure 64B).

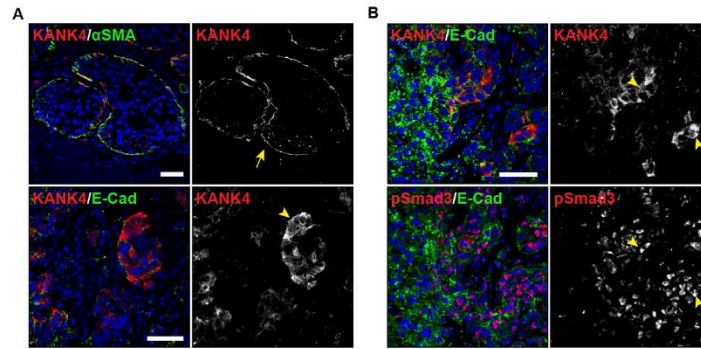


Figure 64: KANK4 is expressed in transformed LECs of human breast cancer patients. (A) IF staining of MG tumor tissues from female patients for KANK4 (red) and E-Cad⁺ transformed LECs (green). Nuclei were counterstained with DAPI (blue). Arrow indicates KANK4 expression in α SMA⁺ myoepithelial cells and arrowhead in E-Cad⁺ transformed LECs. Scale bars: 50 μ m. (B) IF staining of MG tumor tissues from female patients for KANK4 and pSmad3 (both shown in red) and E-Cad⁺ transformed LECs (green). Nuclei were counterstained with DAPI (blue). Arrowheads show regions with KANK4 and pSmad3 co-expression. Scale bar: 50 μ m. In parts taken from a manuscript (Seiwert *et al.*) in consideration.

This shows that the mouse findings also are relevant in human.

5 Discussion

KANKs are FA proteins that regulate FA turnover, migration, and MT targeting to FAs (Sun *et al.*, 2016; Noordstra and Akhmanova, 2017; Aureille *et al.*, 2024). Nevertheless, research on the *in vivo* functions of KANKs are limited. The objective of this study was to address this knowledge gap by utilizing KANK-KO mouse models.

We demonstrated that KANK2 and KANK4 are expressed in mesenchymal and contractile cells of murine tissues, with KANK4 exhibiting a more limited expression in tissues compared to the other KANKs (Guo *et al.*, 2021).

In C57BL/6 background, no developmental defects were observed in KANK2-KO, KANK4-KO, and KANK2/4-dKO mice. However, in FVB background, KANK2-KO embryos were lethal prior to E11.5. At E8.5, a failure in the fusion of chorion and allantois was detected, which inhibited further development.

In addition to the background-specific role of KANK2 in normal development, in a stress situation, namely MMTV-PyMT-driven breast cancer, my findings indicate that KANK4, but not KANK2, plays a tumor promoting role. I found that KANK4 is *de novo* expressed in transformed mammary LECs, which correlates with enhanced cancer development and increased incidence of lung metastasis. Mechanistically, TGF β 1 induces EMT in MCF10A and HMLE-Twist1-ER cells, and simultaneously induces KANK4 expression via the canonical Smad3/4 signaling pathway. KANK4 interacts with Coro1A and Coro1B to promote TGF β 1-dependent Rac1 activation, resulting in enhanced lamellipodia and invadopodia formation. This signaling cascade is required for efficient single-cell detachment from collectively migrating cells, 3D invasion *in vitro* and lung metastasis formation *in vivo* (Figure 65). Tumor correlation analyses of several human cancer patients

confirm that high expression of KANK4 correlates with poor patient survival and staining of tissues derived from human breast cancer patients confirm KANK4 expression in transformed LECs, suggesting that the mouse findings are applicable in human.

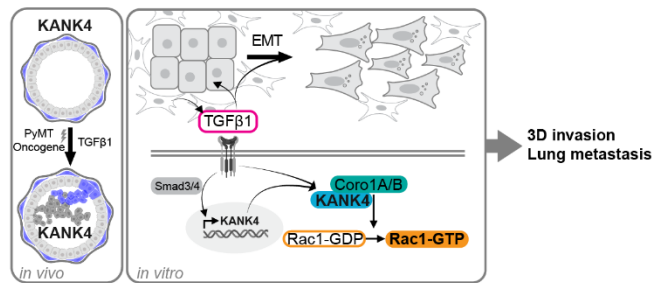


Figure 65: TGFβ1-induced *de novo* expression of KANK4 in breast cancer cells promotes invasion and metastasis. Model illustrating the mechanism underlying TGFβ1-induced KANK4-Rac1 signaling axis, which operates in parallel to TGFβ1-induced EMT to promote 3D invasion and lung metastasis. In parts taken from a manuscript (Seiwert *et al.*) in consideration.

5.1 KANK2 and KANK4 are non-essential in normal murine development (C57BL/6)

My results revealed that KANK2- and KANK4-deficient mice exhibited normal developmental and aging processes in C57BL/6 background, with no discernible defects. To investigate whether KANK2 and KANK4 are compensating each other functionally due to their overlapping expression patterns, the KANK2/4-dKO was generated and studied. Experiments revealed that KANK2/4-dKO mice also developed and aged normally, with no sign of obvious developmental defects. This suggests that KANK2 and KANK4 exhibit functions which are non-essential for normal development. An independent KANK4-KO mouse line was generated by Zhang *et al.*, in which the *KANK4* gene was disrupted by a 11-bp deletion in exon 3 (Zhang *et al.*, 2022). Consistent to my findings, the authors also report that KANK4-KO mice are viable and fertile.

In the MG, KANK4 is specifically expressed in α SMA⁺ myoepithelial cells that surround LECs. Myoepithelial cells are a specialized type of epithelial cell that are highly contractile

and serve to mediate the interaction between the basement membrane and LECs, facilitating milk secretion during lactation. These cells exhibit an elongated and spindle-shaped cell morphology and express CKs such as CK5 and CK14, which mediate cell-cell interaction and cell attachment to the basement membrane via desmosomes and hemidesmosomes. Additionally, myoepithelial cells display a high density of actin-myosin filaments and α SMA, which endow the cells with contractile ability (Deugnier *et al.*, 2002). Therefore, as myoepithelial cells and pericytes show analogous contractile capabilities, the expression of KANK4 in myoepithelial cells aligns with the findings of our expression study (Guo *et al.*, 2021). Similarly, KANK2 is also expressed in myoepithelial cells, but additionally in stromal fibroblast cells. Although KANK4 is specifically expressed in α SMA⁺ myoepithelial cells surrounding LECs, the MG development and its functions were not affected, evidenced by normal morphologies of MG trees and normal litter sizes at the weaning stages of KANK4-KO mice.

Additionally, KANKs have been identified in the context of nephrotic syndrome and proteinuria in zebrafish and drosophila (Sarkar *et al.*, 2002; Gee *et al.*, 2015). This could not be confirmed in the KANK-KO mouse models of the current C57BL/6 background, indicating that the function of KANKs may differ in distinct animal models. Oda *et al.* generated a podocyte-specific KANK1-KO mouse in C57BL/6 background and also did not observe altered urinary ACRs or blood urea nitrogen or serum creatinine levels in one-year old mutants, suggesting that KANK1 is dispensable for kidney function (Oda *et al.*, 2024). Genetic screening suggested that recessive point mutations in KANK1/2/4 are linked to nephrotic syndrome. Furthermore, Gee *et al.* used RNAi-mediated KD of the drosophila KANK homolog *dkank* and KANK2 in zebrafish and demonstrated impaired

podocyte functions *in vivo* (Gee *et al.*, 2015). Our expression data and public mRNA expression databases argue against such a simplified model in which KANKs function equally in the same cell type. Thus, at this stage, it can only be assumed that KANK dependency is different in distant model organisms. As a side note, we found KANK4 specifically expressed in mesangial cells (Guo *et al.*, 2021), whereas Gee *et al.* detected KANK4 in podocyte cell bodies, yet without clarifying antibody specificity. This suggests that the used KANK4 antibody might have shown high non-specific signal. In addition, the development of kidney disease is highly correlated with genetic backgrounds in which the C57BL/6 substrain is relatively resistant to kidney damage (Bufi and Korstanje, 2022). Further investigation of KANKs function in specific genetic backgrounds is needed to fully dissect the correlation between genetic findings and potential consequences.

To decipher whether KANKs play a role in normal development, the investigation of triple or quadruple KO mice of KANKs or talin-1-deficient KANK binding mutant mice (G1404L) (Bouchet *et al.*, 2016) could be useful tools.

5.2 Role of KANK2 in normal development is background-specific

FVB and C57BL/6 are two commonly used inbred mouse strains. Inbred strains are characterized by high degrees of genetic homogeneity, which are employed to minimize biological variability in research studies. This allows for the investigation of a specific parameter of interest while ensuring reproducibility (Casellas, 2011). The process of mating littermates results in the achievement of genomic homozygosity, which renders each individual more identical. Although FVB and C57BL/6 mice exhibit discernible distinctions, such as the coat color, they also demonstrate genomic and phenotypic variability (Chebib *et al.*, 2021). Accordingly, the selection of an appropriate mouse strain

can have a substantial impact on the outcomes of genetic research. This phenomenon is particularly evident in KANK2-KO mice. While the C57BL/6 background does not exhibit any obvious developmental abnormalities, I discovered that KANK2-KO mice in the FVB background are embryonically lethal. It is likely that the FVB background possesses a distinctive set of genes that are indispensable for embryonic development. When this genetic configuration is disrupted by the KANK2-KO, the result is a lethal outcome. In contrast, the C57BL/6 background may provide a more robust genetic environment that can withstand the loss of KANK2. This could include alternative pathways that compensate for the absence of KANK2 or a lower reliance on its functions during critical stages of development.

KANK2-KO embryos died from failure to form the chorioallantois at E8.5. The allantois had elongated into a balloon-shaped structure within exocoelom cavity, suggesting that the growth and development of the allantois itself was not affected. Given that the chorioallantois subsequently develops into the placenta and umbilical cord, which are responsible for transporting maternal nutrients and oxygen to the embryo (Arora and Papaioannou, 2012), KANK2-KO deficiency results in lethality due to a lack of nutrient supply caused by failed chorioallantoic fusion.

The fusion defect was also observed in VCAM-1-KO and α_4 integrin-KO embryos (Gurtner *et al.*, 1995; Kwee *et al.*, 1995; Yang, Rayburn and Hynes, 1995). The defects here were not only observed in the C57BL/6J background, but also in BALB/c and 129/Sv backgrounds. Given that KANK2 is a component of the FA complex and is involved in integrin activation and FA turnover, KANK2 deficiency may impact the ability of α_4 integrin to bind VCAM-1. This lack of interaction between α_4 integrin and VCAM-1

might not only affect the adhesion of the allantois and chorion but also impairs further integrin signaling in the chorion. The interaction of receptor and ligand upon KANK2 loss should be further investigated.

However, approximately 50% of VCAM-1-KO or α_4 integrin-KO embryos were still able to establish the chorioallantois. This was not observed in KANK2-KO embryos, where all KANK2-KO embryos exhibited impaired fusion. Therefore, while the function of VCAM-1 or α_4 integrin in the fusion event can be compensated by other mechanisms, it appears unlikely that other proteins, such as KANK1, 3, or 4 can compensate for the loss of KANK2. Further research is required to gain a detailed understanding of the expression patterns of KANK1, 3 and 4. It is possible that KANK2, in contrast to VCAM-1 or α_4 integrin, might play a role in more than just the initial contact between the chorion and allantois. It is also conceivable that KANK2 is essential for the fusion of the allantoic mesothelium and the chorionic mesoderm by enabling proper function of other integrins like α_v , α_2 , β_1 , β_3 , β_5 , β_6 , and β_8 , which are present in the placental development (Johnson *et al.*, 2023). This might facilitate the allantoic vascularization of the chorion and establishes a strong connection between maternal and embryonic circulation.

Embryos lacking VCAM-1 or α_4 integrin ultimately succumb to cardiac failure. It remains to be elucidated whether KANK2-KO embryos also exhibit additional anomalies, such as impaired heart development. However, cardiac abnormalities only manifested after E11.5, a stage at which KANK2-KO embryos already undergo resorption.

Preliminary staining results suggest that KANK2 is expressed in the VCAM-1⁺ allantois and the α_4 integrin⁺ chorion. Following fusion, the distinction between the allantois and chorion is challenging. In contrast, due to failed fusion, the allantois can clearly be outlined

in KANK2-KO tissue and exhibits a pronounced presence of VCAM-1 in the distal mesothelium, with no α_4 integrin being detected. This expression pattern of VCAM-1 and α_4 integrin aligns with the existing literature (Gurtner *et al.*, 1995; Kwee *et al.*, 1995; Yang, Rayburn and Hynes, 1995). Given the difficulty in dissecting the chorion in the KANK2-KO embryos due to the failed fusion with the allantois, IF staining of the chorion was not yet feasible. Therefore, the staining of α_4 integrin in the chorion of KANK2-KO tissue remains to be conducted and the specificity of the detected KANK2 signal in allantois and chorion requires further investigation. To examine the function of a protein that is expressed in both structures, microsurgical assays can be performed (Inman and Downs, 2007). In these assays, the mutant allantois is replaced with a WT allantois, and chorioallantoic fusion is monitored. This allows the identification of whether the protein of interest is essential in either chorion or allantois, depending on whether fusion is still impaired or not. Furthermore, staining of KANK2 in the heart needs to be performed, to assess a possible involvement of KANK2 in heart development.

Further investigations on the observed phenotype are required to elucidate the function of KANK2 in murine development. It would be worthwhile to identify novel KANK2 interactors as a yet unidentified interactor of KANK2 might exhibit a restricted expression pattern, either within the chorion or the allantois. Alternatively, the loss of KANK2 could result in the impairment of allantois expansion, encompassing proliferation and survival, as well as extension, thereby hindering movement towards the exocoelomic cavity, which is essential for the occurrence of the fusion event.

KANK4 was backcrossed to F6 in FVB background. In this mixed background, KANK4-

KO mice developed without obvious defects. It remains to be seen whether background-specific functions of KANK4 appear in pure FVB background.

5.3 KANK4 promotes cancer development and metastasis

Metastasis represents the leading cause of mortality among cancer patients (Seyfried and Huysentruyt, 2013). In the MMTV-PyMT-driven breast cancer model in C57BL/6 background, KANK4, in contrast to KANK2, exerted a tumor-promoting function, particularly by enhancing the formation of lung metastasis. Surprisingly, I found that KANK4 was *de novo* expressed in transformed LECs, which could be responsible for the enhanced tumor development and metastasis. Moreover, KANK4 expression was observed in transformed LECs that were breaking through the basement membrane, indicating that KANK4 enables cell evasion from the primary tumor and facilitates metastasis formation. The expression of KANK4 was not uniform in all transformed LECs, but rather restricted to certain areas. These cells presumably are exposed to specific ECM signaling, which subsequently induce KANK4 expression. I showed that KANK4 responds to TGF β 1 stimulation with significant upregulation at both the transcriptional and translational level. In contrast, KANK2 was not responding to TGF β 1. Staining of KANK2 in cancer tissue showed KANK2 expression restricted to stromal CAFs, but never extended its expression to transformed LECs (data not shown), making the *de novo* expression a unique feature of KANK4. Although we hypothesized that loss of KANK2 in CAFs would increase cell contractility and mechanotransduction based on the findings of Sun *et al.* (Sun *et al.*, 2016), thus enhancing matrix deposition, remodeling and stiffness, which would promote tumor development, I did not observe enhanced tumor development in absence of KANK2. Thus, KANK2 neither acts as tumor suppressor by decreasing tumor stiffness, nor as tumor

promoter by being *de novo* expressed in transformed LECs. As such, KANK2 was not further analyzed.

Although KANK1 was initially identified as a tumor suppressor, Guo *et al.* revealed that KANK1 functions as a tumor promotor in breast cancer (Guo *et al.*, 2024). Similar to KANK4, KANK1 is also expressed in transformed LECs. However, it seems that KANK1 and KANK4 promote tumor development via distinct mechanisms. KANK1 was shown to specifically localize to cell-cell contacts, where it interacts with NOS1APc to compromise the activation of the SCRIB-mediated Hippo pathway and thus facilitates the stabilization and nuclear translocation of TAZ. Ultimately, KANK1 promotes tumor cell proliferation and primary tumor growth. However, no interaction between KANK4 and NOS1APc was observed (Guo *et al.*, 2024).

The proliferation of cancer cells *in vivo* was found to be decreased in the absence of KANK4. It is conceivable that transformed LECs devoid of the *de novo* expression of KANK4 exhibit reduced mobility, thereby receiving diminished nutrients and consequently undergoing less proliferation. *In vitro* experiments did not reveal a proliferation discrepancy between MCF10A^{KANK4-WT} and MCF10A^{KANK4-KO} cells. This could be attributed to the absence of interactions with the TME, which may contribute to the proliferation defect *in vivo*.

The decrease in lung metastasis formation in KANK4-KO^{PyMT} mice was observed by counting superficial lung metastatic nodules. Here, the investigation of micrometastasis formation is required to address the question of whether KANK4 either promotes the extravasation and initial colonization of cancer cells in the lung, which would be reflected by an enhanced incidence of micrometastasis in KANK4-WT^{PyMT} compared to KANK4-

KO^{PyMT} mice, or promotes proliferation and outgrowth of the metastatic nodules. This would be reflected by a similar number of micrometastases, but an enhanced number of superficial macrometastases in KANK4-WT^{PyMT} mice.

TGF β 1 levels have been shown to be upregulated in invasive carcinoma compared to *in situ* carcinoma (Walker, Dearing and Gallacher, 1994). Additionally, the TGF β 1-activating $\alpha_v\beta_6$ integrin shows increased expression in transformed LECs (Breuss *et al.*, 1995). This may explain why TGF β 1 does not induce KANK4 expression in LECs of normal MG, as low levels of TGF β 1 and $\alpha_v\beta_6$ integrin may be insufficient for cells to respond with KANK4 expression. A feedback cycle of TGF β 1 inducing the secretion of MMP2 and MMP9 in cancer tissues, which in turn release and activate more TGF β 1 dimers, thus making more TGF β 1 available to interact with transformed LECs, is conceivable to cause KANK4 induction in breast cancer but not in normal MG tissue. Another possible feedback cycle could be that TGF β 1 induces KANK4 expression, which in turn leads to integrin activation and thus increased TGF β 1 release from its inhibitory latent complex. This could explain why KANK4-KO^{PyMT} mice develop fewer metastases, as the absence of KANK4 would reduce the levels of active TGF β 1. However, TGF β 1 activation requires force transduction via integrins to open up the straitjacket surrounding the TGF β 1 dimer (Shi *et al.*, 2011). Assuming that KANK4 functions similarly to KANK2 in releasing the molecular clutch (Sun *et al.*, 2016), integrins would receive less force coming from the retrograde flow of actin because KANK4 impairs actin-talin binding. Therefore, the force exerted by integrins may be insufficient to activate TGF β 1. According to this concept, the absence of KANK4 would result in elevated levels of TGF β 1 available for cells to respond to. Nevertheless,

given that KANK4-KO^{PyMT} mice show slower tumor development, KANK4 must have a role other than TGFβ1 activation to promote tumor and metastasis formation.

5.4 TGFβ1-induces *de novo* expression of KANK4 in parallel to EMT

During tumor development, the TME undergoes active remodeling, driven by the crosstalk between the cancer cells and the surrounding stroma. TME remodeling facilitates cancer progression by recruiting diverse cell types, including immune cells, CAFs, endothelial cells, and numerous other tissue-resident cells. These cells serve as a source for the secretion of growth factors and cytokines, such as TGFβs (Brabletz *et al.*, 2021). TGFβs are recognized as potent inducers of EMT, particularly during advanced stages when tumor cells attempt to evade their original site and disseminate to a distant organ. Interestingly, I show that KANK4 and EMT are induced in parallel by TGFβ1, as evidenced by the inability of EMT-TFs to induce KANK4 expression. Although out of the TFs Zeb1, Twist1 and Snail, only overexpression of Snail in MCF10A cells was successful, Twist1 and Zeb1 can be excluded by using the HMLE-Twist1-ER cell model. Tamoxifen-induced activation of Twist1 was unable to induce KANK4 expression. However, clear upregulation of Zeb1 was observed, indicating that, similar to Snail, neither Twist1 nor Zeb1 can induce KANK4 expression. This indicates that the core EMT-TFs alone are insufficient for KANK4 induction and that KANK4 is dependent on TGFβ1 signaling rather than on the TGFβ1-induced EMT process. Indeed, KD of Smad3 and particularly Smad4 impaired KANK4 induction. Promoter-wide ChIP experiments with Smad3 support these findings, as they demonstrate that Smad3 binds to the promoter of KANK4 upon TGFβ1 treatment (Sato *et al.*, 2014). Importantly, TGFβ1-induced gene expression profiles characteristic of EMT are not affected by KANK4 deficiency.

5.5 KANK4 facilitates 3D invasion

Cellular migration can occur in either an individual (mesenchymal or amoeboid) or collective manner. While individually migrating cells detach from cell clusters, collectively migrating cells rely on a leader-follower principle, whereby cells form robust cell-cell interactions and follow leader cells at the migrative front (Yamada and Sixt, 2019). TGF β 1 is known to induce EMT, which leads to single-cell detachment and increased cell motility and invasiveness (Kalluri and Weinberg, 2009; Flum *et al.*, 2022; Xin *et al.*, 2022). Cancer cell migration is highly dynamic, and the transition from single-cell exploration to collective strand migration is a well-documented phenomenon in cancer invasion. This process enables cells to retain some epithelial characteristics while acquiring invasive properties, a state often referred to as ‘partial EMT’ (Flum *et al.*, 2022).

In contrast to single-cells, which are highly mobile, collectively migrating cells exhibit a reduced metastatic burden in orthotopic mouse models. However, a mixture of both migration modes could potentially enhance metastasis formation, as single-cells guide cell clusters for invasion. This highlights the importance of the interaction between single and collectively migrating cells in promoting invasion (Hapach *et al.*, 2021, 2023). Similarly, the co-culture of cancer cells and CAFs showed that CAFs can assume the function of leader cells by interacting with and remodeling the ECM in an α_3/α_5 integrin and RhoA-dependent manner to direct cancer cells for invasion (Gaggioli, 2008). By sensing the local ECM stiffness and degrading the ECM via invadopodia formation, single or leader cells create migratory routes through ECM remodeling, which allow collectively migrating cells to follow (Friedl *et al.*, 2012).

In MCF10A^{KANK4-WT} cells, I observed that treatment with TGF β 1 resulted in the

detachment of single-cells from the cell layer or spheroid core, in both 2D and 3D culture. The detached cells were migrating ahead of the remaining cells, subsequently rejoining them as leader cells and eventually migrating and invading as collective strands. Hereby, TGF β 1 induced a mesenchymal cell shape, with broad lamellipodia and invadopodia formation, which aligns with the concept of TGF β 1-induced EMT and thus enhances migration capacity (Flum *et al.*, 2022; Xin *et al.*, 2022). Expressing GFP-KANK4 in untreated MCF10A cells did not induce 3D invasion, indicating that the cells additionally require the multiple signaling functions of TGF β 1 as a trigger, which is then re-enforced by KANK4.

The enhanced formation of invadopodia and elevated ECM degradation activity observed in TGF β 1-treated MCF10A^{KANK4-WT} cells align with the invasive characteristics exhibited by cancer cells undergoing (partial) EMT. Invadopodia are actin-rich protrusions that concentrate proteolytic activity, thereby enabling cells to degrade and navigate through the ECM (Weaver, 2006). This function is crucial for various biological processes, including cancer metastasis. Matrix degradation, which is mediated by MMPs, is crucial for collective invasion, as it creates paths through which follower cells can migrate (Friedl *et al.*, 2012). Therefore, it can be proposed that in our model, TGF β 1 initially induces mesenchymal single-cell migration in cells of the outer layer of epithelial sheets or spheroids, allowing them to probe the environment and degrade the ECM, thus initiating collective cell migration and invasion through provided paths. MCF10A^{KANK4-KO} cells, in which TGF β 1 failed to induce lamellipodia and invadopodia formation, lack this initial step of single-cell detachment and are unable to remodel the ECM. This results in the lack of track formation and impaired collective invasion ability.

The TGF β 1-induced 3D invasion was confirmed with HMLE-Twist1-ER cells. Using this cell line, it would have been interesting to study whether EMT itself, without TGF β 1 stimulation, can induce invasion, as EMT is induced by Tamoxifen-dependent Twist1 activation. However, Tamoxifen is widely used for treatment and prevention in breast cancer. As selective estrogen receptor modulator (SERM), it blocks the ER on breast cancer cells and therefore inhibits the growth and proliferation of cancer cells that rely on estrogen for survival and growth (Cuzick *et al.*, 2002; Howell and Howell, 2023). This anti-proliferative effect was observed by decreased spheroid growth of Tamoxifen-treated HMLE-Twist1-ER cells, which outweighed the effect of TGF β 1 inducing 3D invasion when both, Tamoxifen and TGF β 1 were added. Thus, this model cannot be used to answer whether EMT alone (TGF β 1-independent EMT) induces 3D invasion.

5.6 KANK4 does not play a significant role in CMSC recruitment or MMP secretion

Cell protrusions show high activity of matrix-degrading enzymes, such as MMPs, within the vicinity of FAs. These enzymes are recruited via the CMSC. It has been proposed that KANK1 and KANK2 interact with CMSC components liprin β 1 and KIF21A via the preceding sequence of the ankyrin repeats, thereby facilitating the recruitment of CMSC to FAs (Stehbens *et al.*, 2014; Bouchet *et al.*, 2016; Sun *et al.*, 2016). It has been demonstrated that this binding motif is not conserved in KANK4 (Guo *et al.*, 2018; Weng *et al.*, 2018), suggesting that KANK4 is incapable of binding liprin β 1 or KIF21A. KANK1 binds KIF21A via its ankyrin repeats. A comparative structural analysis of the four different KANK proteins revealed that KANK2 exhibits identical KIF21A-binding residues to those observed in KANK1. In contrast, KANK4 displays a slightly altered amino acid sequence,

characterized by the replacement of two negatively charged amino acids with two uncharged amino acids, which effectively abolishes KIF21A binding (Guo *et al.*, 2018; Pan *et al.*, 2018). These findings were recently corroborated by Zhang *et al.* performing KANK-IPs (Zhang *et al.*, 2022). Furthermore, my proteomic interaction studies of KANK4 in MCF10A cells did not reveal any interaction between KANK4 and members of the CMSC, and also excluded a possible indirect interaction via heterodimer formation of KANK4 and KANK1. Additionally, KANK4 depletion did not impact the MT targeting to FAs. Kumari *et al.* demonstrated that mislocalization of KANK2 resulted in disorganized MTs that bypassed FAs (Kumari *et al.*, 2024). Similarly, Aureille *et al.* showed that photoactivation of KANK1 recruits MT to FAs (Aureille *et al.*, 2024), indicating, in conjunction with my findings that both KANK1 and KANK2, but not KANK4, are involved in MT targeting to FAs. Furthermore, MMP localization and secretion were not affected in MCF10A^{KANK4-KO} cells upon TGFβ1 treatment. TGFβ1 has been shown to upregulate MMP2 and MMP9 secretion and that this is essential for 3D invasion (Kim, Kim and Moon, 2004; Wiercinska *et al.*, 2011). Note that MCF10A^{KANK4-WT} cells exhibited elevated secretion of MMP2 and MMP9 in the absence of TGFβ1 relative to MCF10A^{KANK4-KO} cells. While the underlying mechanism for this discrepancy remains unclear, TGFβ1 treatment led to comparable levels of MMP secretion in both cell lines, suggesting that MCF10A^{KANK4-KO} cells retained the capacity to secrete MMPs in response to TGFβ1. It is therefore unlikely that KANK4 plays a role in the recruitment of the CMSC to FAs or the directed transport of MMPs via the MT network. It is probable that MMP secretion is facilitated by KANK1, which localizes to FAs in LECs (Guo *et al.*, 2021) and guides the CMSC to the leading edge (Aureille *et al.*, 2024).

5.7 KANK4 promotes TGF β 1-mediated Rac1 activation

Given that MMP localization, secretion, and activity remained unaltered and the formation of lamellipodia and invadopodia was reduced in MCF10A^{KANK4-KO} cells, it is possible that KANK4 is relevant for Rac1-dependent lamellipodia or invadopodia formation and that KANK1, in parallel and independently of KANK4, orchestrates MMP secretion in the vicinity of FAs.

Mesenchymal cell migration requires Rac1-dependent protrusion formation (Yamada and Sixt, 2019). This process involves the activation of the Rac1-dependent WAVE regulatory complex (Mehidi *et al.*, 2019), as well as the regulation of invadopodia-mediated ECM degradation (Revach *et al.*, 2016). Rac1 plays a pivotal role in cancer development: The inhibition of Rac1 in MMTV-PyMT transgenic mice significantly decreases lung metastasis formation, thereby underscoring the role of Rac1 in invasion (Floerchinger *et al.*, 2021). Furthermore, Rac1 has been demonstrated to be hyperactive and overexpressed in breast cancer patients (Schnelzer *et al.*, 2000).

Cell staining revealed that KANK4, Rac1, and Arp3 co-localize at the leading front. Interestingly, upon KANK4 depletion, there was a notable decline in Rac1 activity. Depletion of KANK4 did not affect the activity of the other Rho GTPases, Cdc42 and RhoA. Although TGF β 1 has been previously reported to activate RhoA (Bhowmick *et al.*, 2001; Fleming *et al.*, 2009), this was not observed in the presented experiment, in which active RhoA levels were comparable in all conditions. However, a significant increase in cell contractility was observed upon TGF β 1 treatment. Cell contractility was comparable between MCF10A^{KANK4-WT} and MCF10A^{KANK4-KO} cells in all conditions. This suggests that neither filopodia formation (Cdc42), nor cell contractility (RhoA) are regulated by

KANK4.

To ascertain the mechanism by which KANK4 activates Rac1, I performed KANK4-IP experiments to identify novel KANK4 interaction partners in response to TGF β 1 stimulation. Interestingly, the interacting proteins were predominantly involved in actin cytoskeleton regulation. Coro1A and Coro1B were of particular interest, as they are type I coronins, which have been demonstrated to regulate Arp2/3-mediated actin filament branching (Chan, Creed and Bear, 2011). Moreover, they facilitate the translocation and activation of Rac1 at lamellipodia by releasing Rac1 from its inhibitor RhoGDI α (Castro-Castro *et al.*, 2011, 2016). In contrast to Coro1B, which is ubiquitously expressed in mammals, Coro1A expression is limited to hematopoietic cells (Chan, Creed and Bear, 2011). However, I observed that TGF β 1 upregulates Coro1A in MCF10A cells, while no change was noted in Coro1B levels. Therefore, Coro1A shows a comparable response to that of KANK4. It is also noteworthy that the single KDs of Coro1A or Coro1B exhibited only marginal effects on lamellipodia formation. This illustrates that Coro1A and Coro1B are analogous in function and can compensate, at least in part, for the loss of the respective other protein.

I showed that KANK4 localizes to NAs at the leading edge, additionally to FAs, presumably recruited by talin binding. KANK1 and KANK2 exclusively localize to FAs (Sun *et al.*, 2016). It is conceivable that interaction with the CMSC restricts KANK1 and KANK2 to FAs, thereby preventing their localization to NAs. KANK4, however, which does not interact with the CMSC, localizes to both FAs and NAs. This could be crucial for the direct or indirect localization of Coro1A and Coro1B to the leading edge, which in turn promotes TGF β 1-induced Rac1 activation. Active Rac1 can then activate the Arp2/3

complex to promote actin filament nucleation and branching and subsequent protrusion formation.

5.8 KANK4 findings can be applied in human

Importantly, expression of KANK4 in transformed LECs could also be observed in tumor sections from human breast cancer patients and high KANK4 expression correlates with poor survival probability of ER-neg breast cancer patients. Moreover, a positive correlation between high KANK4 expression and poor patient outcome was detected in several other cancer types, suggesting that the same mechanism might apply to these cancers. Altogether, these findings suggest a metastasis promoting role of KANK4 in breast cancer with relevance in human and thus making KANK4 an interesting target in cancer therapy.

In summary, I have shown that KANK2 and KANK4 exhibit background- and cancer-specific functions. How KANK2 contributes to embryonic development needs to be further investigated. It would be interesting to elucidate the reason for the background specificity and whether KANK1, KANK3, or KANK4 also show this phenomenon. The tumor promoting function of KANK4 is an interesting finding with potential application in cancer treatment due to KANK4's involvement in metastasis formation. The exact mechanism by which KANK4 activates Rac1 via Coro1A and Coro1B remains to be elucidated and it could be further investigated, in which step of the metastatic cascade KANK4 is relevant. That TGF β 1-induced KANK4 expression promotes cancer development is a general concept for other cancers as supported by human cancer database mining, however needs further confirmation. In summary, this thesis provides a more detailed understanding in the *in vivo* functions of KANK2 and KANK4.

6 Short summary of manuscripts

6.1 Paper I – Tissue distribution and subcellular localization of the family of Kidney Ankyrin Repeat Domain (KANK) proteins

Shiny Shengzhen Guo*, [Andrea Seiwert](#), Irene Y.Y. Szeto, Reinhard Fässler.
Experimental Cell Research 398 (2021). doi: 10.1016/j.yexcr.2020.112391

Aim and key results:

The KANK proteins have been widely studied in *in vitro* situations. In this study, we aimed to analyze distribution of the four different KANKs in several murine tissues, suggesting tissue- and cell-type-dependent altering functions of KANKs.

Analysis of mRNA levels revealed that *Kank2* mRNA was highly expressed in almost all of the analyzed tissues, with spleen being the only exception. Similarly, *Kank1* mRNA showed high expression in the majority of the investigated tissues, but was less expressed in bone marrow, intestine, spleen and thymus. *Kank3* and *Kank4* mRNAs were in general less expressed and were more restricted to certain tissues. All four *Kanks* showed high mRNA expression levels in lung, which was also confirmed on the protein level.

Via immunofluorescent staining of kidney, lung, skin, brain, aorta, retina, spleen and esophagus, we aimed to localize the KANK proteins to the respective cell types. Interestingly, we found that the KANKs showed cell-type-specific expression patterns. KANK1 was expressed in epithelial derived cells like podocytes, bronchial epithelial cells, keratinocytes, astrocytes, and stratified squamous epithelial cells. KANK2 was predominantly expressed in mesenchymal cells like mesangial cells, α SMA⁺ cells, pericytes, Type I and II cells and fibroblasts. The exception was found in the kidney, where

KANK2 is also expressed in epithelial podocytes. KANK3 was exclusively expressed in endothelial cells in all analyzed tissues. KANK4 shared the expression pattern with KANK2 in mesangial cells and pericytes, but was only detected in lung and kidney. Tissues from respective KANK-KO animals were used to assure specificity of our homemade antibodies.

This study serves as basis for following research on KANKs, as it provides detailed insight in the physiological distribution of KANKs, which is essential for putting *in vitro* findings into context.

Contribution:

A.S. conducted western blots of different tissues, performed immunofluorescent stainings, evaluated antibodies, helped and prepared mouse tissues, as well as helped writing and revising the manuscript.

6.2 Paper II – Lfc subcellular localization and activity is controlled by α_v -class integrin

Georgina Coló*, [Andrea Seiwert](#), Raquel B. Haga. **Journal of Cell Science** 136 (2023).
doi: 10.1242/jcs.260740.

Aim and key results:

Integrins are known transmembrane proteins to transmit signals from the ECM to intracellular responses by interacting with ECM proteins like fibronectin, vitronectin, collagen and laminin. Among the vast variety of integrins, $\alpha_v\beta_3$ and $\alpha_5\beta_1$ integrins are well-studied receptors both binding to fibronectin, but showing distinct cellular responses, namely increased RhoA activity resulting in enhanced stress fiber formation and increased FA size upon $\alpha_v\beta_3$ engagement.

In this study, we aimed to further elucidate the integrin-specific mechanisms induced intracellularly upon fibronectin binding. For this, we used murine fibroblasts lacking all integrins (pKO fibroblasts) and re-expressed either α_v -class integrins, β_1 -class integrins, or $\alpha_v\beta_3$ and $\alpha_5\beta_1$ integrins (pKO- α_v , pKO- β_1 , and pKO- $\alpha_v\beta_1$ fibroblasts respectively). We showed that pKO- α_v fibroblasts form increased ventral stress fibers in a RhoA-dependent manner. We identified Arhgef2/Lfc out of nine GEFs involved in RhoA activation in our used cell systems as being highly involved especially upon α_v -engagement.

Depletion of Lfc decreased the formation of ventral stress fibers and size of FAs in all three cell lines, confirming the role of Lfc in F-actin arrangement. In pKO- α_v fibroblasts, which show higher levels of active RhoA compared to pKO- β_1 and pKO- $\alpha_v\beta_1$ fibroblasts, KO of Lfc also lead to decreased RhoA activity, suggesting that Lfc-RhoA signaling is specific to $\alpha_v\beta_3$ integrin-expressing cells. Via immunofluorescent staining of Lfc, we found that Lfc

was predominantly localized in its active state in the cytoplasm of pKO- α_v fibroblasts, whereas Lfc was retained at MTs of pKO- β_1 fibroblasts, resembling its inactive state. Seeding WT mouse fibroblasts on $\alpha_v\beta_3$ -specific peptidomimetics was sufficient to release Lfc from MTs into the cytoplasm, resulting in Lfc activation and enhanced membrane protrusion formation.

Phospho-enrichment proteomic analyses revealed that Lfc showed distinct phosphorylation patterns upon different integrin engagement and that phosphorylation of S151 in pKO- α_v fibroblasts was specifically important for the cytoplasmic translocation of Lfc and the interaction with active RhoA. In contrast, inhibition of phosphorylation by the kinase inhibitor Staurosporine retained Lfc at MTs and decreased Lfc activity. We suggest a role of the kinases MARK2 and MARK3 as possible kinases to phosphorylate Lfc^{S151}, resulting in its cytoplasmic translocation, activation of RhoA, and formation of stress fibers in pKO- α_v fibroblasts.

Contribution:

A.S. conducted cell staining experiments, quantification and statistical analysis of cell images, and helped assembling and arranging the figures and revising the manuscript.

7 References

- Aashaq, S. *et al.* (2021) ‘TGF- β signaling: A recap of SMAD-independent and SMAD-dependent pathways’, *Journal of Cellular Physiology*, (June), pp. 1–27. doi: 10.1002/jcp.30529.
- Ahmad, W. *et al.* (2023) ‘Global Down-regulation of Gene Expression Induced by Mouse Mammary Tumor Virus (MMTV) in Normal Mammary Epithelial Cells’, *Viruses*, 15(5), p. 1110. doi: 10.3390/v15051110.
- Akiyoshi, S. *et al.* (1999) ‘c-Ski acts as a transcriptional co-repressor in transforming growth factor- β signaling through interaction with Smads’, *Journal of Biological Chemistry*, 274(49), pp. 35269–35277. doi: 10.1074/jbc.274.49.35269.
- Alexander, N. R. *et al.* (2008) ‘Extracellular Matrix Rigidity Promotes Invadopodia Activity’, *Current Biology*, 18(17), pp. 1295–1299. doi: 10.1016/j.cub.2008.07.090.
- Alvarez Juliá, A., Frasch, A. C. and Fuchsova, B. (2016) ‘Neuronal filopodium formation induced by the membrane glycoprotein M6a (Gpm6a) is facilitated by coronin-1a, Rac1, and p21-activated kinase 1 (Pak1).’, *Journal of neurochemistry*, 137(1), pp. 46–61. doi: 10.1111/jnc.13552.
- Anderson, N. M. and Simon, M. C. (2020) ‘The tumor microenvironment’, *Current Biology*. Elsevier, 30(16), pp. R921–R925. doi: 10.1016/j.cub.2020.06.081.
- Andrews, J. L., Kim, A. C. and Hens, J. R. (2012) ‘The role and function of cadherins in the mammary gland.’, *Breast cancer research : BCR*, 14(1), p. 203. doi: 10.1186/bcr3065.
- Appleton, B. A., Wu, P. and Wiesmann, C. (2006) ‘The crystal structure of murine coronin-1: A regulator of actin cytoskeletal dynamics in lymphocytes’, *Structure*, 14(1), pp. 87–96. doi: 10.1016/j.str.2005.09.013.
- Aragón, E. *et al.* (2019) ‘Structural basis for distinct roles of SMAD2 and SMAD3 in FOXH1 pioneer-directed TGF- β signaling’, *Genes & development*, 33(21–22), pp. 1506–1524. doi: 10.1101/gad.330837.119.
- Aretz, J. *et al.* (2023) ‘Talin and kindlin use integrin tail allostery and direct binding to activate integrins.’, *Nature structural & molecular biology*. Springer US, 30(12), pp. 1913–1924. doi: 10.1038/s41594-023-01139-9.
- Arora, R. and Papaioannou, V. E. (2012) ‘The murine allantois: A model system for the study of blood vessel formation’, *Blood*, 120(13), pp. 2562–2572. doi: 10.1182/blood-2012-03-390070.
- Attalla, S. *et al.* (2021) ‘Insights from transgenic mouse models of PyMT-induced breast cancer: recapitulating human breast cancer progression in vivo.’, *Oncogene*, 40(3), pp. 475–491. doi: 10.1038/s41388-020-01560-0.
- Aureille, J. *et al.* (2024) ‘Focal adhesions are controlled by microtubules through local contractility regulation’, *The EMBO Journal*. doi: 10.1038/s44318-024-00114-4.

- Baardsnes, J. *et al.* (2009) 'T β R-II Discriminates the High- and Low-Affinity TGF- β Isoforms via Two Hydrogen-Bonded Ion Pairs', *Biochemistry*, 48(10), pp. 2146–2155. doi: 10.1021/bi8019004.
- Bachmann, M. *et al.* (2019) 'Cell adhesion by integrins', *Physiological Reviews*, 99(4), pp. 1655–1699. doi: 10.1152/physrev.00036.2018.
- Bakin, A. V. *et al.* (2002) 'p38 mitogen-activated protein kinase is required for TGF β -mediated fibroblastic transdifferentiation and cell migration', *Journal of Cell Science*, 115(15), pp. 3193–3206. doi: 10.1242/jcs.115.15.3193.
- Battle, E. *et al.* (2000) 'The transcription factor Snail is a repressor of E-cadherin gene expression in epithelial tumour cells', *Nature Cell Biology*, 2(2), pp. 84–89. doi: 10.1038/35000034.
- Beningo, K. A. *et al.* (2001) 'Nascent focal adhesions are responsible for the generation of strong propulsive forces in migrating fibroblasts.', *The Journal of cell biology*, 153(4), pp. 881–8. doi: 10.1083/jcb.153.4.881.
- Bertrand-Chapel, A. *et al.* (2022) 'SMAD2/3 mediate oncogenic effects of TGF- β in the absence of SMAD4', *Communications Biology*, 5(1), p. 1068. doi: 10.1038/s42003-022-03994-6.
- Beunk, L. *et al.* (2022) 'Actomyosin contractility requirements and reciprocal cell–tissue mechanics for cancer cell invasion through collagen-based channels', *The European Physical Journal E*, 45(5), p. 48. doi: 10.1140/epje/s10189-022-00182-6.
- Bhowmick, N. A. *et al.* (2001) 'Transforming growth factor- β 1 mediates epithelial to mesenchymal transdifferentiation through a RhoA-dependent mechanism', *Molecular Biology of the Cell*, 12(1), pp. 27–36. doi: 10.1091/mbc.12.1.27.
- te Boekhorst, V. *et al.* (2021) 'Calpain-2 regulates hypoxia/HIF-induced plasticity toward amoeboid cancer cell migration and metastasis', *Current Biology*, pp. 412–427. doi: 10.1016/j.cub.2021.11.040.
- Bolós, V. *et al.* (2016) 'The transcription factor Slug represses E-cadherin expression and induces epithelial to mesenchymal transitions: a comparison with Snail and E47 repressors', *Journal of Cell Science*, 129(6), pp. 1283–1283. doi: 10.1242/jcs.188243.
- Böttcher, R. T., Sun, Z. and Fässler, R. (2017) 'A forceful connection: mechanoregulation of oncogenic YAP', *The EMBO Journal*, 36(17), pp. 2467 LP – 2469. doi: 10.15252/emboj.201797527.
- Bottinger, E. P., Letterio, J. J. and Roberts, A. B. (1997) 'Biology of TGF- β in knockout and transgenic mouse models', *Kidney International*, 51(5), pp. 1355–1360. doi: 10.1038/ki.1997.185.
- Bouchet, B. P. *et al.* (2016) 'Talin-KANK1 interaction controls the recruitment of cortical microtubule stabilizing complexes to focal adhesions.', *eLife*. eLife Sciences Publications, Ltd, 5, p. e18124. doi: 10.7554/eLife.18124.
- Brabletz, S. *et al.* (2021) 'Dynamic EMT: a multi-tool for tumor progression.', *The EMBO*

journal, 40(18), p. e108647. doi: 10.15252/embj.2021108647.

Brabletz, T. *et al.* (2018) 'EMT in cancer.', *Nature reviews. Cancer*, 18(2), pp. 128–134. doi: 10.1038/nrc.2017.118.

Branch, K. M., Hoshino, D. and Weaver, A. M. (2012) 'Adhesion rings surround invadopodia and promote maturation', *Biology Open*, 1(8), pp. 711–722. doi: 10.1242/bio.20121867.

Breuss, J. M. *et al.* (1995) 'Expression of the $\beta 6$ integrin subunit in development, neoplasia and tissue repair suggests a role in epithelial remodeling', *Journal of Cell Science*, 108(6), pp. 2241–2251. doi: 10.1242/jcs.108.6.2241.

Briskin, C. *et al.* (1999) 'Prolactin controls mammary gland development via direct and indirect mechanisms.', *Developmental biology*, 210(1), pp. 96–106. doi: 10.1006/dbio.1999.9271.

Bufl, R. and Korstanje, R. (2022) 'The impact of genetic background on mouse models of kidney disease.', *Kidney international*, 102(1), pp. 38–44. doi: 10.1016/j.kint.2022.03.020.

Busch, S. *et al.* (2014) 'TGF-beta receptor type-2 expression in cancer-associated fibroblasts regulates breast cancer cell growth and survival and is a prognostic marker in pre-menopausal breast cancer', *Oncogene*, 34, pp. 27–38. doi: 10.1038/onc.2013.527.

Buser, A. C. *et al.* (2007) 'Progesterone Receptor Repression of Prolactin/Signal Transducer and Activator of Transcription 5-Mediated Transcription of the β -Casein Gene in Mammary Epithelial Cells', *Molecular Endocrinology*, 21(1), pp. 106–125. doi: 10.1210/me.2006-0297.

Buwaneka, P. *et al.* (2021) 'Phosphoinositide-binding activity of Smad2 is essential for its function in TGF- β signaling', *Journal of Biological Chemistry*. American Society for Biochemistry and Molecular Biology, 297(5), p. 101303. doi: 10.1016/j.jbc.2021.101303.

Byron, A. *et al.* (2009) 'Anti-integrin monoclonal antibodies.', *Journal of cell science*, 122(Pt 22), pp. 4009–11. doi: 10.1242/jcs.056770.

Cai, L. *et al.* (2005) 'Phosphorylation of coronin 1B by protein kinase C regulates interaction with Arp2/3 and cell motility', *Journal of Biological Chemistry*, 280(36), pp. 31913–31923. doi: 10.1074/jbc.M504146200.

Cai, L. *et al.* (2007) 'Coronin 1B Coordinates Arp2/3 Complex and Cofilin Activities at the Leading Edge', *Cell*, 128(5), pp. 915–929. doi: 10.1016/j.cell.2007.01.031.

Calvo, F. *et al.* (2013) 'Mechanotransduction and YAP-dependent matrix remodelling is required for the generation and maintenance of cancer-associated fibroblasts', *Nature Cell Biology*, 15(6), pp. 637–646. doi: 10.1038/ncb2756.

Cano, A. *et al.* (2000) 'The transcription factor Snail controls epithelial–mesenchymal transitions by repressing E-cadherin expression', *Nature Cell Biology*, 2(2), pp. 76–83. doi: 10.1038/35000025.

Carver, E. A. *et al.* (2001) 'The Mouse Snail Gene Encodes a Key Regulator of the

Epithelial-Mesenchymal Transition', *Molecular and Cellular Biology*, 21(23), pp. 8184–8188. doi: 10.1128/MCB.21.23.8184-8188.2001.

Case, L. B. and Waterman, C. M. (2015) 'Integration of actin dynamics and cell adhesion by a three-dimensional, mechanosensitive molecular clutch', *Nature Cell Biology*. Nature Publishing Group, 17(8), pp. 955–963. doi: 10.1038/ncb3191.

Casellas, J. (2011) 'Inbred mouse strains and genetic stability: a review', *Animal*. Elsevier, 5(1), pp. 1–7. doi: 10.1017/S1751731110001667.

Castro-Castro, A. *et al.* (2011) 'Coronin 1A promotes a cytoskeletal-based feedback loop that facilitates Rac1 translocation and activation.', *The EMBO journal*, 30(19), pp. 3913–27. doi: 10.1038/emboj.2011.310.

Castro-Castro, A. *et al.* (2016) 'Characterization of Novel Molecular Mechanisms Favoring Rac1 Membrane Translocation.', *PloS one*. Edited by M. M. Zegers, 11(11), p. e0166715. doi: 10.1371/journal.pone.0166715.

Cavallaro, U. *et al.* (2001) 'N-CAM modulates tumour-cell adhesion to matrix by inducing FGF-receptor signalling', *Nature Cell Biology*, 3(7), pp. 650–657. doi: 10.1038/35083041.

Chacko, B. M. *et al.* (2001) 'The L3 loop and C-terminal phosphorylation jointly define Smad protein trimerization', *Nature Structural Biology*, 8(3), pp. 248–253. doi: 10.1038/84995.

Chacko, B. M. *et al.* (2004) 'Structural basis of heteromeric Smad protein assembly in TGF- β signaling', *Molecular Cell*, 15(5), pp. 813–823. doi: 10.1016/j.molcel.2004.07.016.

Chan, K. T., Creed, S. J. and Bear, J. E. (2011) 'Unraveling the enigma: Progress towards understanding the coronin family of actin regulators', *Trends in Cell Biology*. Elsevier Ltd, 21(8), pp. 481–488. doi: 10.1016/j.tcb.2011.04.004.

Chastney, M. R., Conway, J. R. W. and Ivaska, J. (2021) 'Integrin adhesion complexes', *Current Biology*, 31(10), pp. R536–R542. doi: 10.1016/j.cub.2021.01.038.

Chebib, J. *et al.* (2021) 'Inbred lab mice are not isogenic: genetic variation within inbred strains used to infer the mutation rate per nucleotide site', *Heredity*, 126(1), pp. 107–116. doi: 10.1038/s41437-020-00361-1.

Chen, B. *et al.* (2017) 'Rac1 GTPase activates the WAVE regulatory complex through two distinct binding sites', *eLife*, 6. doi: 10.7554/eLife.29795.

Chen, C.-R. *et al.* (2002) 'E2F4/5 and p107 as Smad cofactors linking the TGFbeta receptor to c-myc repression.', *Cell*, 110(1), pp. 19–32. doi: 10.1016/s0092-8674(02)00801-2.

Chen, F. *et al.* (2000) 'Cdc42 is required for PIP2-induced actin polymerization end early development but not for cell viability', *Current Biology*, 10(13), pp. 758–765. doi: 10.1016/S0960-9822(00)00571-6.

Chen, N.-P. P., Aretz, J. and Fässler, R. (2022) 'CDK1–cyclin-B1-induced kindlin degradation drives focal adhesion disassembly at mitotic entry', *Nature Cell Biology*. Springer US, 24(5), pp. 723–736. doi: 10.1038/s41556-022-00886-z.

- Cho, K.-W. *et al.* (2006) 'Molecular interactions between Tbx3 and Bmp4 and a model for dorsoventral positioning of mammary gland development.', *Proceedings of the National Academy of Sciences of the United States of America*, 103(45), pp. 16788–93. doi: 10.1073/pnas.0604645103.
- Chu, E. Y. *et al.* (2004) 'Canonical WNT signaling promotes mammary placode development and is essential for initiation of mammary gland morphogenesis', *Development*, 131(19), pp. 4819–4829. doi: 10.1242/dev.01347.
- Cichon, M. A. *et al.* (2010) 'Microenvironmental influences that drive progression from benign breast disease to invasive breast cancer', *Journal of Mammary Gland Biology and Neoplasia*, 15(4), pp. 389–397. doi: 10.1007/s10911-010-9195-8.
- Clohisey, S. M. R., Dzhindzhev, N. S. and Ohkura, H. (2014) 'Kank Is an EB1 Interacting Protein that Localises to Muscle-Tendon Attachment Sites in *Drosophila*', *PLoS ONE*. Edited by H. White-Cooper, 9(9), p. e106112. doi: 10.1371/journal.pone.0106112.
- Cowell, A. R. *et al.* (2021) 'Talin rod domain-containing protein 1 (TLNRD1) is a novel actin-bundling protein which promotes filopodia formation', *Journal of Cell Biology*, 220(9). doi: 10.1083/jcb.202005214.
- Cox, J. and Mann, M. (2008) 'MaxQuant enables high peptide identification rates, individualized p.p.b.-range mass accuracies and proteome-wide protein quantification.', *Nature biotechnology*, 26(12), pp. 1367–72. doi: 10.1038/nbt.1511.
- Curtis, M. *et al.* (2019) 'Fibroblasts Mobilize Tumor Cell Glycogen to Promote Proliferation and Metastasis', *Cell Metabolism*. Elsevier Inc., 29(1), pp. 141-155.e9. doi: 10.1016/j.cmet.2018.08.007.
- Cuzick, J. *et al.* (2002) 'First results from the International Breast Cancer Intervention Study (IBIS-I): a randomised prevention trial.', *Lancet (London, England)*, 360(9336), pp. 817–24. doi: 10.1016/s0140-6736(02)09962-2.
- Dalal, B. I., Keown, P. A. and Greenberg, A. H. (1993) 'Immunocytochemical localization of secreted transforming growth factor- β 1 to the advancing edges of primary tumors and to lymph node metastases of human mammary carcinoma', *American Journal of Pathology*, 143(2), pp. 381–389.
- David, C. J. and Massagué, J. (2018) 'Contextual determinants of TGF β action in development, immunity and cancer', *Nature Reviews Molecular Cell Biology*, 19, p. 419. doi: 10.1038/s41580-018-0007-0.
- Davie, S. A. *et al.* (2007) 'Effects of FVB/NJ and C57Bl/6J strain backgrounds on mammary tumor phenotype in inducible nitric oxide synthase deficient mice', *Transgenic research*. 2007/01/06. Kluwer Academic Publishers, 16(2), pp. 193–201. doi: 10.1007/s11248-006-9056-9.
- Debnath, J., Muthuswamy, S. K. and Brugge, J. S. (2003) 'Morphogenesis and oncogenesis of MCF-10A mammary epithelial acini grown in three-dimensional basement membrane cultures', *Methods*, 30(3), pp. 256–268. doi: 10.1016/S1046-2023(03)00032-X.
- Debnath, P. *et al.* (2021) 'Epithelial-mesenchymal transition and its transcription factors',

Bioscience Reports. doi: 10.1042/BSR20211754.

Deng, Z. *et al.* (2024) 'TGF- β signaling in health, disease, and therapeutics', *Signal Transduction and Targeted Therapy*. Springer US, 9(1), p. 61. doi: 10.1038/s41392-024-01764-w.

Deugnier, M.-A. *et al.* (2002) 'The importance of being a myoepithelial cell', *Breast Cancer Research*, 4(6), p. 224. doi: 10.1186/bcr459.

Díaz, B. (2013) 'Invadopodia Detection and Gelatin Degradation Assay.', *Bio-protocol*, 3(24). doi: 10.21769/BioProtoc.997.

Dickson, M. C. *et al.* (1995) 'Defective haematopoiesis and vasculogenesis in transforming growth factor-beta 1 knock out mice.', *Development (Cambridge, England)*, 121(6), pp. 1845–54. doi: 10.1242/dev.121.6.1845.

Ding, M. *et al.* (2003) 'C. elegans ankyrin repeat protein VAB-19 is a component of epidermal attachment structures and is essential for epidermal morphogenesis.', *Development (Cambridge, England)*, 130(23), pp. 5791–801. doi: 10.1242/dev.00791.

Djomehri, S. I. *et al.* (2019) 'A reproducible scaffold-free 3D organoid model to study neoplastic progression in breast cancer', *Journal of Cell Communication and Signaling*, 13(1), pp. 129–143. doi: 10.1007/s12079-018-0498-7.

Downs, K. M. (2002) 'Early placental ontogeny in the mouse.', *Placenta*, 23(2–3), pp. 116–31. doi: 10.1053/plac.2001.0763.

Du, L. *et al.* (2016) 'Transcriptome profiling reveals novel gene expression signatures and regulating transcription factors of TGF β -induced epithelial-to-mesenchymal transition.', *Cancer medicine*, 5(8), pp. 1962–72. doi: 10.1002/cam4.719.

Eichelberger, L. *et al.* (2020) 'Maintenance of epithelial traits and resistance to mesenchymal reprogramming promote proliferation in metastatic breast cancer', *bioRxiv*, p. 2020.03.19.998823. doi: 10.1101/2020.03.19.998823.

Elosegui-Artola, A. *et al.* (2016) 'Mechanical regulation of a molecular clutch defines force transmission and transduction in response to matrix rigidity', *Nature Cell Biology*. Nature Publishing Group, 18, p. 540. Available at: <https://doi.org/10.1038/ncb3336>.

Elosegui-Artola, A. *et al.* (2017) 'Force Triggers YAP Nuclear Entry by Regulating Transport across Nuclear Pores.', *Cell*. Elsevier, 171(6), pp. 1397–1410.e14. doi: 10.1016/j.cell.2017.10.008.

Engel, M. E. *et al.* (1999) 'Interdependent SMAD and JNK signaling in transforming growth factor- β - mediated transcription', *Journal of Biological Chemistry*, 274(52), pp. 37413–37420. doi: 10.1074/jbc.274.52.37413.

Fares, J. *et al.* (2020) 'Molecular principles of metastasis: a hallmark of cancer revisited.', *Signal transduction and targeted therapy*, 5(1), p. 28. doi: 10.1038/s41392-020-0134-x.

Fässler, R. and Meyer, M. (1995) 'Consequences of lack of β 1 integrin gene expression in mice', *Genes and Development*, 9(15), pp. 1896–1908. doi: 10.1101/gad.9.15.1896.

- Fata, J. E. *et al.* (2000) 'The Osteoclast Differentiation Factor Osteoprotegerin-Ligand Is Essential for Mammary Gland Development', *Cell*, 103(1), pp. 41–50. doi: 10.1016/S0092-8674(00)00103-3.
- Faustino-Rocha, A. *et al.* (2013) 'Estimation of rat mammary tumor volume using caliper and ultrasonography measurements', *Lab Animal*. Nature Publishing Group, 42(6), pp. 217–224. doi: 10.1038/labani.254.
- Feng, J. *et al.* (2019) 'Maternal exposure to cadmium impairs cognitive development of male offspring by targeting the Coronin-1a signaling pathway', *Chemosphere*. Elsevier Ltd, 225, pp. 765–774. doi: 10.1016/j.chemosphere.2019.03.094.
- Fischer, K. R. *et al.* (2015) 'Epithelial-to-mesenchymal transition is not required for lung metastasis but contributes to chemoresistance', *Nature*. Nature Publishing Group, 527(7579), pp. 472–476. doi: 10.1038/nature15748.
- Fischer, L. S. *et al.* (2021) 'Quantitative single-protein imaging reveals molecular complex formation of integrin, talin, and kindlin during cell adhesion', *Nature Communications*. Springer US, 12(1). doi: 10.1038/s41467-021-21142-2.
- Fleming, Y. M. *et al.* (2009) 'TGF- β -mediated activation of RhoA signalling is required for efficient V12HaRas and V600EBRAF transformation', *Oncogene*, 28(7), pp. 983–993. doi: 10.1038/onc.2008.449.
- Van der Flier, A. and Sonnenberg, A. (2001) 'Function and interactions of integrins', *Cell and Tissue Research*, 305(3), pp. 285–298. doi: 10.1007/s004410100417.
- Floerchinger, A. *et al.* (2021) 'Optimizing metastatic-cascade-dependent Rac1 targeting in breast cancer: Guidance using optical window intravital FRET imaging.', *Cell reports*, 36(11), p. 109689. doi: 10.1016/j.celrep.2021.109689.
- Fluck, M. M. and Schaffhausen, B. S. (2009) 'Lessons in Signaling and Tumorigenesis from Polyomavirus Middle T Antigen', *Microbiology and Molecular Biology Reviews*, 73(3), pp. 542 LP – 563. doi: 10.1128/MMBR.00009-09.
- Flum, M. *et al.* (2022) 'Canonical TGF β signaling induces collective invasion in colorectal carcinogenesis through a Snail1- and Zeb1-independent partial EMT.', *Oncogene*, 41(10), pp. 1492–1506. doi: 10.1038/s41388-022-02190-4.
- Francis, S. E. *et al.* (2002) 'Central roles of $\alpha 5 \beta 1$ integrin and fibronectin in vascular development in mouse embryos and embryoid bodies', *Arteriosclerosis, Thrombosis, and Vascular Biology*, 22(6), pp. 927–933. doi: 10.1161/01.ATV.0000016045.93313.F2.
- Friedl, P. *et al.* (2012) 'Classifying collective cancer cell invasion.', *Nature cell biology*, 14(8), pp. 777–83. doi: 10.1038/ncb2548.
- Friedl, P. and Alexander, S. (2011) 'Cancer invasion and the microenvironment: plasticity and reciprocity.', *Cell*. Elsevier Inc., 147(5), pp. 992–1009. doi: 10.1016/j.cell.2011.11.016.
- Friedl, P. and Zegers, M. (2024) 'A collective strategy to promote the dissemination of single cancer cells', *Journal of Cell Biology*, 223(6), pp. 9428–35. doi:

10.1083/jcb.202405014.

Fu, R. *et al.* (2019) 'A ZEB1/p53 signaling axis in stromal fibroblasts promotes mammary epithelial tumours', *Nature Communications*. Springer US, 10(1). doi: 10.1038/s41467-019-11278-7.

Gaggioli, C. (2008) 'Collective invasion of carcinoma cells: when the fibroblasts take the lead.', *Cell adhesion & migration*, 2(1), pp. 45–7. doi: 10.4161/cam.2.1.5705.

Gandhi, M. *et al.* (2009) 'Coronin Switches Roles in Actin Disassembly Depending on the Nucleotide State of Actin', *Molecular Cell*, 34(3), pp. 364–374. doi: 10.1016/j.molcel.2009.02.029.

Gatfield, J. *et al.* (2005) 'Association of the leukocyte plasma membrane with the actin cytoskeleton through coiled coil-mediated trimeric coronin 1 molecules.', *Molecular biology of the cell*, 16(6), pp. 2786–98. doi: 10.1091/mbc.e05-01-0042.

Gee, H. Y. *et al.* (2015) 'KANK deficiency leads to podocyte dysfunction and nephrotic syndrome.', *The Journal of clinical investigation*. 2015/05/11. American Society for Clinical Investigation, 125(6), pp. 2375–84. doi: 10.1172/JCI79504.

Gemmill, R. M. *et al.* (2011) 'ZEB1-responsive genes in non-small cell lung cancer', *Cancer Letters*, 300(1), pp. 66–78. doi: 10.1016/j.canlet.2010.09.007.

Giampieri, S. *et al.* (2009) 'Localized and reversible TGF β signalling switches breast cancer cells from cohesive to single cell motility', *Nature Cell Biology*, 11(11), pp. 1287–1296. doi: 10.1038/ncb1973.

Gilbert, R., Vickaryous, M. and Vitoria-Petit, A. (2016) 'Signalling by Transforming Growth Factor Beta Isoforms in Wound Healing and Tissue Regeneration', *Journal of Developmental Biology*, 4(2), p. 21. doi: 10.3390/jdb4020021.

Ginsberg, M. H. (2014) 'Integrin activation', *BMB Reports*, 47(12), pp. 655–659. doi: 10.5483/BMBRep.2014.47.12.241.

Goley, E. D. and Welch, M. D. (2006) 'The ARP2/3 complex: an actin nucleator comes of age', *Nature Reviews Molecular Cell Biology*, 7(10), pp. 713–726. doi: 10.1038/nrm2026.

Grimm, S. L. and Nordeen, S. K. (1998) 'Mouse mammary tumor virus sequences responsible for activating cellular oncogenes.', *Journal of virology*, 72(12), pp. 9428–35. doi: 10.1128/JVI.72.12.9428-9435.1998.

Grooteclaes, M. L. and Frisch, S. M. (2000) 'Evidence for a function of CtBP in epithelial gene regulation and anoikis', *Oncogene*, 19(33), pp. 3823–3828. doi: 10.1038/sj.onc.1203721.

Gross, S. M. *et al.* (2022) 'A multi-omic analysis of MCF10A cells provides a resource for integrative assessment of ligand-mediated molecular and phenotypic responses.', *Communications biology*. Springer US, 5(1), p. 1066. doi: 10.1038/s42003-022-03975-9.

Gui, T. *et al.* (2012) 'The Roles of Mitogen-Activated Protein Kinase Pathways in TGF- β -Induced Epithelial-Mesenchymal Transition ', *Journal of Signal Transduction*,

2012(type I), pp. 1–10. doi: 10.1155/2012/289243.

Guillou, H. *et al.* (2008) ‘Lamellipodia nucleation by filopodia depends on integrin occupancy and downstream Rac1 signaling’, *Experimental Cell Research*, 314(3), pp. 478–488. doi: 10.1016/j.yexcr.2007.10.026.

Guo, K. *et al.* (2023) ‘KANK1 shapes focal adhesions by orchestrating protein binding, mechanical force sensing, and phase separation’, *Cell Reports*. The Author(s), 42(11), p. 113321. doi: 10.1016/j.celrep.2023.113321.

Guo, Q. *et al.* (2018) ‘Structural basis for the recognition of kinesin family member 21A (KIF21A) by the ankyrin domains of KANK1 and KANK2 proteins.’, *The Journal of biological chemistry*. © 2018 by The American Society for Biochemistry and Molecular Biology, Inc., 293(2), pp. 557–566. doi: 10.1074/jbc.M117.817494.

Guo, S. S. *et al.* (2021) ‘Tissue distribution and subcellular localization of the family of Kidney Ankyrin Repeat Domain (KANK) proteins’, *Experimental Cell Research*, 398(1), p. 112391. doi: 10.1016/j.yexcr.2020.112391.

Guo, S. S. *et al.* (2024) ‘KANK1 promotes breast cancer development by compromising Scribble-mediated Hippo activation’, *Nature Communications*, 15(1), p. 10381. doi: 10.1038/s41467-024-54645-9.

Guo, S. S. and Fässler, R. (2022) ‘KANK proteins’, *Current Biology*. Elsevier, 32(19), pp. R990–R992. doi: 10.1016/j.cub.2022.08.073.

Guo, W. *et al.* (2012) ‘Slug and Sox9 cooperatively determine the mammary stem cell state’, *Cell*, 148(5), pp. 1015–1028. doi: 10.1016/j.cell.2012.02.008.

Gurtner, G. C. *et al.* (1995) ‘Targeted disruption of the murine VCAM1 gene: Essential role of VCAM-1 in chorioallantoic fusion and placentation’, *Genes and Development*, 9(1), pp. 1–14. doi: 10.1101/gad.9.1.1.

Guy, C. T., Cardiff, R. D. and Muller, W. J. (1992) ‘Induction of mammary tumors by expression of polyomavirus middle T oncogene: a transgenic mouse model for metastatic disease.’, *Molecular and Cellular Biology*, 12(3), pp. 954 LP – 961. doi: 10.1128/MCB.12.3.954.

Györfy, B. (2021) ‘Survival analysis across the entire transcriptome identifies biomarkers with the highest prognostic power in breast cancer.’, *Computational and structural biotechnology journal*, 19, pp. 4101–4109. doi: 10.1016/j.csbj.2021.07.014.

Györfy, B. (2023) ‘Discovery and ranking of the most robust prognostic biomarkers in serous ovarian cancer.’, *GeroScience*. Springer International Publishing, 45(3), pp. 1889–1898. doi: 10.1007/s11357-023-00742-4.

Györfy, B. (2024) ‘Integrated analysis of public datasets for the discovery and validation of survival-associated genes in solid tumors.’, *Innovation (Cambridge (Mass.))*, 5(3), p. 100625. doi: 10.1016/j.xinn.2024.100625.

Hachim, M. Y. *et al.* (2018) ‘Differential expression of TGFβ isoforms in breast cancer highlights different roles during breast cancer progression’, *Tumor Biology*, 40(1), p.

101042831774825. doi: 10.1177/1010428317748254.

Haeger, A. *et al.* (2020) 'Collective cancer invasion forms an integrin-dependent radioresistant niche', *Journal of Experimental Medicine*, 217(1), pp. 1–18. doi: 10.1084/jem_20181184.

Hage, B. *et al.* (2009) 'Rac1 activation inhibits E-cadherin-mediated adherens junctions via binding to IQGAP1 in pancreatic carcinoma cells.', *Cell communication and signaling: CCS*, 7, p. 23. doi: 10.1186/1478-811X-7-23.

Halper, J., Burt, D. W. and Romanov, M. N. (2004) 'On Reassessment of the Chicken TGFB4 Gene as TGFB1', *Growth Factors*, 22(2), pp. 121–122. doi: 10.1080/08977190410001712878.

Hamidi, A. *et al.* (2017) 'TGF- β promotes PI3K-AKT signaling and prostate cancer cell migration through the TRAF6-mediated ubiquitylation of p85 α ', *Science Signaling*, 10(486), pp. 1–15. doi: 10.1126/scisignal.aal4186.

Hannan, F. M. *et al.* (2023) 'Hormonal regulation of mammary gland development and lactation', *Nature Reviews Endocrinology*, 19(1), pp. 46–61. doi: 10.1038/s41574-022-00742-y.

Hapach, L. A. *et al.* (2021) 'Phenotypic heterogeneity and metastasis of breast cancer cells', *Cancer Research*, 81(13), pp. 3649–3663. doi: 10.1158/0008-5472.CAN-20-1799.

Hapach, L. A. *et al.* (2023) 'Phenotypically sorted highly and weakly migratory triple negative breast cancer cells exhibit migratory and metastatic commensalism', *Breast Cancer Research*. BioMed Central, 25(1), pp. 1–12. doi: 10.1186/s13058-023-01696-3.

Hata, A. *et al.* (1997) 'Mutations increasing autoinhibition inactivate tumour suppressors Smad2 and Smad4', *Nature*, 388(6637), pp. 82–87. doi: 10.1038/40424.

Hattori, N. *et al.* (2011) 'Methylation silencing of angiopoietin-like 4 in rat and human mammary carcinomas.', *Cancer science*, 102(7), pp. 1337–43. doi: 10.1111/j.1349-7006.2011.01955.x.

Hay, E. D. (1968) 'Organization and fine structure of epithelium and mesenchyme in the developing chick embryo'. In *Epithelial-Mesenchymal Interactions*; 18th Hahemann Symposium: Baltimore: Williams & Wilkins.

Hay, E. D. (1995) 'An Overview of Epithelio-Mesenchymal Transformation', *Cells Tissues Organs*, 154(1), pp. 8–20. doi: 10.1159/000147748.

Haydont, V. *et al.* (2019) 'Genome-wide profiling of adult human papillary and reticular fibroblasts identifies ACAN, Col XI α 1, and PSG1 as general biomarkers of dermis ageing, and KANK4 as an exemplary effector of papillary fibroblast ageing, related to contractility', *Mechanisms of Ageing and Development*, 177, pp. 157–181. doi: <https://doi.org/10.1016/j.mad.2018.06.003>.

Hazan, R. B. *et al.* (2000) 'Exogenous Expression of N-Cadherin in Breast Cancer Cells Induces Cell Migration, Invasion, and Metastasis', *The Journal of Cell Biology*, 148(4), pp. 779–790. doi: 10.1083/jcb.148.4.779.

- Heasman, S. J. and Ridley, A. J. (2008) 'Mammalian Rho GTPases: new insights into their functions from in vivo studies', *Nature Reviews Molecular Cell Biology*, 9(9), pp. 690–701. doi: 10.1038/nrm2476.
- Heino, J. *et al.* (1989) 'Regulation of cell adhesion receptors by transforming growth factor-beta. Concomitant regulation of integrins that share a common beta 1 subunit.', *The Journal of biological chemistry*, 264(1), pp. 380–8. doi: 10.1016/s0021-9258(17)31269-3.
- Heldin, C. H., Miyazono, K. and Ten Dijke, P. (1997) 'TGF- β signalling from cell membrane to nucleus through SMAD proteins', *Nature*, 390(6659), pp. 465–471. doi: 10.1038/37284.
- Hendrickx, D. A. E. *et al.* (2017) 'Gene Expression Profiling of Multiple Sclerosis Pathology Identifies Early Patterns of Demyelination Surrounding Chronic Active Lesions', *Frontiers in Immunology*, p. 1810. Available at: <https://www.frontiersin.org/article/10.3389/fimmu.2017.01810>.
- Hensley, M. R. *et al.* (2016) 'Evolutionary and developmental analysis reveals KANK genes were co-opted for vertebrate vascular development', *Scientific Reports*. Nature Publishing Group, 6(April), pp. 1–10. doi: 10.1038/srep27816.
- Herschkowitz, J. I. *et al.* (2007) 'Identification of conserved gene expression features between murine mammary carcinoma models and human breast tumors', *Genome Biology*, 8(5), pp. 1–17. doi: 10.1186/gb-2007-8-5-r76.
- Herzog, D. *et al.* (2011) 'The small GTPase RhoA is required to maintain spinal cord neuroepithelium organization and the neural stem cell pool', *Journal of Neuroscience*, 31(13), pp. 5120–5130. doi: 10.1523/JNEUROSCI.4807-10.2011.
- Hill, C. S. (2016) 'Transcriptional Control by the SMADs', *Cold Spring Harbor perspectives in biology*. Cold Spring Harbor Laboratory Press, 8(10), p. a022079. doi: 10.1101/cshperspect.a022079.
- Hinck, L. M. H. (1978) 'Wandering epithelial cells in the rabbit embryo milk line', *Developmental Biology*, 67(1), pp. 225–231. doi: 10.1016/0012-1606(78)90311-1.
- Hino, N. *et al.* (2022) 'A feedback loop between lamellipodial extension and HGF-ERK signaling specifies leader cells during collective cell migration', *Developmental Cell*. Elsevier Inc., 57(19), pp. 2290-2304.e7. doi: 10.1016/j.devcel.2022.09.003.
- Hodge, R. G. and Ridley, A. J. (2016) 'Regulating Rho GTPases and their regulators', *Nature Publishing Group*. doi: 10.1038/nrm.2016.67.
- Horev, G. *et al.* (2011) 'Dosage-dependent phenotypes in models of 16p11.2 lesions found in autism', *Proceedings of the National Academy of Sciences of the United States of America*, 108(41), pp. 17076–17081. doi: 10.1073/pnas.1114042108.
- Hoshino, K. (1965) 'Development and Function of Mammary Glands of Mice Prenatally Exposed to Testosterone Propionate¹', *Endocrinology*, 76(4), pp. 789–794. doi: 10.1210/endo-76-4-789.
- de Hostos, E. L. *et al.* (1991) 'Coronin, an actin binding protein of Dictyostelium

discoideum localized to cell surface projections, has sequence similarities to G protein beta subunits.’, *The EMBO Journal*, 10(13), pp. 4097–4104. doi: 10.1002/j.1460-2075.1991.tb04986.x.

Howell, A. and Howell, S. J. (2023) ‘Tamoxifen evolution.’, *British journal of cancer*. https, 128(3), pp. 421–425. doi: 10.1038/s41416-023-02158-5.

Huang, T., Schor, S. L. and Hinck, A. P. (2014) ‘Biological Activity Differences between TGF- β 1 and TGF- β 3 Correlate with Differences in the Rigidity and Arrangement of Their Component Monomers’, *Biochemistry*, 53(36), pp. 5737–5749. doi: 10.1021/bi500647d.

Huang, W. *et al.* (2020) ‘Pattern of invasion in human pancreatic cancer organoids is associated with loss of SMAD4 and clinical outcome’, *Cancer Research*, 80(13), pp. 2804–2817. doi: 10.1158/0008-5472.CAN-19-1523.

Hudson, C. A., McArdle, C. A. and Bernal, A. L. (2016) ‘Steroid receptor co-activator interacting protein (SIP) mediates EGF-stimulated expression of the prostaglandin synthase COX2 and prostaglandin release in human myometrium’, *Molecular Human Reproduction*, 22(7), pp. 512–525. doi: 10.1093/molehr/gaw031.

Humphries, C. L. *et al.* (2002) ‘Direct regulation of Arp2/3 complex activity and function by the actin binding protein coronin’, *Journal of Cell Biology*, 159(6), pp. 993–1004. doi: 10.1083/jcb.200206113.

Huynh, L. K., Hipolito, C. J. and Dijke, P. Ten (2019) ‘A perspective on the development of TGF- β inhibitors for cancer treatment’, *Biomolecules*, 9(11). doi: 10.3390/biom9110743.

Hynes, R. (1987) ‘Integrins: A family of cell surface receptors’, *Cell*, 48(4), pp. 549–554. doi: 10.1016/0092-8674(87)90233-9.

Irina, O. *et al.* (2020) ‘Cell-cell adhesion and 3D matrix confinement determine jamming transitions in breast cancer invasion.’, *Nature cell biology*, 22(9), pp. 1103–1115. doi: 10.1038/s41556-020-0552-6.

Inman, G. J. and Hill, C. S. (2002) ‘Stoichiometry of active Smad-transcription factor complexes on DNA’, *Journal of Biological Chemistry*. © 2002 ASBMB. Currently published by Elsevier Inc; originally published by American Society for Biochemistry and Molecular Biology., 277(52), pp. 51008–51016. doi: 10.1074/jbc.M208532200.

Inman, K. E. and Downs, K. M. (2007) ‘The murine allantois: emerging paradigms in development of the mammalian umbilical cord and its relation to the fetus’, *genesis*, 45(5), pp. 237–258. doi: 10.1002/dvg.20281.

Jain, S. *et al.* (2020) ‘The role of single-cell mechanical behaviour and polarity in driving collective cell migration’, *Nature Physics*, 16(7), pp. 802–809. doi: 10.1038/s41567-020-0875-z.

Jerrell, R. J. and Parekh, A. (2014) ‘Cellular traction stresses mediate extracellular matrix degradation by invadopodia’, *Acta Biomaterialia*. Acta Materialia Inc., 10(5), pp. 1886–1896. doi: 10.1016/j.actbio.2013.12.058.

- Johnson, G. A. *et al.* (2023) 'Integrins and their potential roles in mammalian pregnancy.', *Journal of animal science and biotechnology*, 14(1), p. 115. doi: 10.1186/s40104-023-00918-0.
- Kadry, Y. A. and Calderwood, D. A. (2020) 'Chapter 22: Structural and signaling functions of integrins', *Biochimica et Biophysica Acta (BBA) - Biomembranes*. Elsevier, 1862(5), p. 183206. doi: 10.1016/j.bbamem.2020.183206.
- Kafer, G. R. and Cesare, A. J. (2020) 'A Survey of Essential Genome Stability Genes Reveals That Replication Stress Mitigation Is Critical for Peri-Implantation Embryogenesis', *Frontiers in Cell and Developmental Biology*, 8. doi: 10.3389/fcell.2020.00416.
- Kajita, M., McClinic, K. N. and Wade, P. A. (2004) 'Aberrant expression of the transcription factors snail and slug alters the response to genotoxic stress.', *Molecular and cellular biology*, 24(17), pp. 7559–7566. doi: 10.1128/MCB.24.17.7559-7566.2004.
- Kakinuma, N. *et al.* (2008) 'Kank regulates RhoA-dependent formation of actin stress fibers and cell migration via 14-3-3 in PI3K-Akt signaling.', *The Journal of cell biology*, 181(3), pp. 537–49. doi: 10.1083/jcb.200707022.
- Kakinuma, N. and Kiyama, R. (2009) 'A major mutation of KIF21A associated with congenital fibrosis of the extraocular muscles type 1 (CFEOM1) enhances translocation of Kank1 to the membrane', *Biochemical and Biophysical Research Communications*. Elsevier Inc., 386(4), pp. 639–644. doi: 10.1016/j.bbrc.2009.06.109.
- Kalluri, R. and Weinberg, R. A. (2009) 'The basics of epithelial-mesenchymal transition.', *The Journal of clinical investigation*. The American Society for Clinical Investigation, 119(6), pp. 1420–8. doi: 10.1172/JCI39104.
- Kaminski, S. *et al.* (2011) 'Coronin 1A is an essential regulator of the TGF β receptor/SMAD3 signaling pathway in Th17 CD4(+) T cells.', *Journal of autoimmunity*, 37(3), pp. 198–208. doi: 10.1016/j.jaut.2011.05.018.
- Kammerer, P., Aretz, J. and Fässler, R. (2017) 'Lucky kindlin: A cloverleaf at the integrin tail', *Proceedings of the National Academy of Sciences of the United States of America*. 2017/08/22. National Academy of Sciences, 114(35), pp. 9234–9236. doi: 10.1073/pnas.1712471114.
- Kanchanawong, P. *et al.* (2010) 'Nanoscale architecture of integrin-based cell adhesions', *Nature*. Nature Publishing Group, 468(7323), pp. 580–584. doi: 10.1038/nature09621.
- Katsuno, Y. and Derynck, R. (2021) 'Epithelial plasticity, epithelial-mesenchymal transition, and the TGF- β family', *Developmental Cell*. Elsevier Inc., 56(6), pp. 726–746. doi: 10.1016/j.devcel.2021.02.028.
- Kechagia, J. Z., Ivaska, J. and Roca-Cusachs, P. (2019) 'Integrins as biomechanical sensors of the microenvironment', *Nature Reviews Molecular Cell Biology*. Springer US, 20(8), pp. 457–473. doi: 10.1038/s41580-019-0134-2.
- Kim, E. S., Kim, M. S. and Moon, A. (2004) 'TGF-beta-induced upregulation of MMP-2 and MMP-9 depends on p38 MAPK, but not ERK signaling in MCF10A human breast

- epithelial cells.', *International journal of oncology*, 25(5), pp. 1375–1382. doi: 10.3892/ijo.25.5.1375.
- Kim, I. *et al.* (2018) 'A novel HIF1AN substrate KANK3 plays a tumor-suppressive role in hepatocellular carcinoma', *Cell Biology International*, 42(3), pp. 303–312. doi: 10.1002/cbin.10895.
- Kim, J.-Y. *et al.* (2017) 'The value of phosphohistone H3 as a proliferation marker for evaluating invasive breast cancers: A comparative study with Ki67', *Oncotarget*, 8(39), pp. 65064–65076. doi: 10.18632/oncotarget.17775.
- King, Z. T. *et al.* (2022) 'Coro1B and Coro1C regulate lamellipodia dynamics and cell motility by tuning branched actin turnover', *Journal of Cell Biology*, 221(8). doi: 10.1083/jcb.202111126.
- Kojima, Y. *et al.* (2010) 'Autocrine TGF- β and stromal cell-derived factor-1 (SDF-1) signaling drives the evolution of tumor-promoting mammary stromal myofibroblasts', *Proceedings of the National Academy of Sciences*, 107(46), pp. 20009–20014. doi: 10.1073/pnas.1013805107.
- Kondaiah, P. *et al.* (1990) 'Identification of a novel transforming growth factor- β (TGF- β 5) mRNA in *Xenopus laevis*', *Journal of Biological Chemistry*, 265(2), pp. 1089–1093. doi: 10.1016/s0021-9258(19)40162-2.
- Koo, S.-H. *et al.* (2001) 'The Transforming Growth Factor- β 3 Knock-Out Mouse: An Animal Model for Cleft Palate.', *Plastic and Reconstructive Surgery*, 108(4), pp. 938–947.
- Kratochwil, K. (1971) 'In vitro analysis of the hormonal basis for the sexual dimorphism in the embryonic development of the mouse mammary gland', *Journal of Embryology and Experimental Morphology*, 25(1). Available at: <http://dev.biologists.org/content/25/1/141.abstract>.
- Kratochwil, K. (1977) 'Development and loss of androgen responsiveness in the embryonic rudiment of the mouse mammary gland', *Developmental Biology*, 61(2), pp. 358–365. doi: 10.1016/0012-1606(77)90305-0.
- Kratochwil, K. and Schwartz, P. (1976) 'Tissue interaction in androgen response of embryonic mammary rudiment of mouse: identification of target tissue for testosterone.', *Proceedings of the National Academy of Sciences*, 73(11), pp. 4041–4044. doi: 10.1073/pnas.73.11.4041.
- Krause, M. and Gautreau, A. (2014) 'Steering cell migration: lamellipodium dynamics and the regulation of directional persistence', *Nature Reviews Molecular Cell Biology*, 15(9), pp. 577–590. doi: 10.1038/nrm3861.
- Kretschmar, M. *et al.* (1999) 'A mechanism of repression of TGF β / Smad signaling by oncogenic Ras', *Genes & Development*, 13(7), pp. 804–816. doi: 10.1101/gad.13.7.804.
- Kulkarni, A. B. *et al.* (1993) 'Transforming growth factor β 1 null mutation in mice causes excessive inflammatory response and early death', *Proceedings of the National Academy of Sciences of the United States of America*, 90(2), pp. 770–774. doi: 10.1073/pnas.90.2.770.

- Kumari, R. *et al.* (2024) 'Focal adhesions contain three specialized actin nanoscale layers', *Nature Communications*, 15(1), p. 2547. doi: 10.1038/s41467-024-46868-7.
- Kwee, L. *et al.* (1995) 'Defective development of the embryonic and extraembryonic circulatory systems in vascular cell adhesion molecule (VCAM-1) deficient mice.', *Development (Cambridge, England)*, 121(2), pp. 489–503. doi: 10.1242/dev.121.2.489.
- L. Attisano, S. T. L.-H. (2001) 'The Smads', *Genome Biology*, 10, pp. 235.1–7.
- Lau, T.-L. *et al.* (2009) 'The structure of the integrin α IIb β 3 transmembrane complex explains integrin transmembrane signalling', *The EMBO Journal*, 28(9), pp. 1351–1361. doi: 10.1038/emboj.2009.63.
- Law, R. A. *et al.* (2023) 'Cytokinesis machinery promotes cell dissociation from collectively migrating strands in confinement.', *Science advances*, 9(2), p. eabq6480. doi: 10.1126/sciadv.abq6480.
- Le, V. Q. *et al.* (2023) 'A specialized integrin-binding motif enables proTGF- β 2 activation by integrin α V β 6 but not α V β 8', *Proceedings of the National Academy of Sciences*, 120(24), p. 2017. doi: 10.1073/pnas.2304874120.
- Lee, J. Y. *et al.* (2019) 'YAP-independent mechanotransduction drives breast cancer progression', *Nature Communications*. Springer US, 10(1), pp. 1–9. doi: 10.1038/s41467-019-09755-0.
- Lee, P. S. W. *et al.* (2003) 'Sumoylation of Smad4, the common Smad mediator of transforming growth factor- β family signaling', *Journal of Biological Chemistry*. © 2003 ASBMB. Currently published by Elsevier Inc; originally published by American Society for Biochemistry and Molecular Biology., 278(30), pp. 27853–27863. doi: 10.1074/jbc.M301755200.
- Legerstee, K. and Houtsmuller, A. B. (2021) 'A layered view on focal adhesions', *Biology*, 10(11). doi: 10.3390/biology10111189.
- Lehmann, S. *et al.* (2017) 'Hypoxia Induces a HIF-1-Dependent Transition from Collective-to-Amoeboid Dissemination in Epithelial Cancer Cells', *Current Biology*. Elsevier Ltd., 27(3), pp. 392–400. doi: 10.1016/j.cub.2016.11.057.
- Lerer, I. *et al.* (2005) 'Deletion of the ANKRD15 gene at 9p24.3 causes parent-of-origin-dependent inheritance of familial cerebral palsy.', *Human molecular genetics*. England, 14(24), pp. 3911–3920. doi: 10.1093/hmg/ddi415.
- Li, J. *et al.* (2017) 'Conformational equilibria and intrinsic affinities define integrin activation', *The EMBO Journal*, 36(5), pp. 629–645. doi: 10.15252/emboj.201695803.
- Li, J. *et al.* (2024) 'Ligand binding initiates single-molecule integrin conformational activation', *Cell*. Cell Press, 187(12), pp. 2990–3005.e17. doi: 10.1016/J.CELL.2024.04.049.
- Li, J., Yan, J. and Springer, T. A. (2021) 'Low-affinity integrin states have faster ligand-binding kinetics than the high-affinity state', *eLife*, 10, pp. 1–22. doi: 10.7554/eLife.73359.

- Li, Y. *et al.* (2020) ‘Genetic Fate Mapping of Transient Cell Fate Reveals N-Cadherin Activity and Function in Tumor Metastasis’, *Developmental Cell*. Elsevier Inc., 54(5), pp. 593–607.e5. doi: 10.1016/j.devcel.2020.06.021.
- Li, Z.-X. *et al.* (2022) ‘TGF- β 1 promotes human breast cancer angiogenesis and malignant behavior by regulating endothelial-mesenchymal transition.’, *Frontiers in oncology*, 12(November), p. 1051148. doi: 10.3389/fonc.2022.1051148.
- Liao, J. *et al.* (2024) ‘Cross-Talk between the TGF- β and Cell Adhesion Signaling Pathways in Cancer’, *International Journal of Medical Sciences*, 2024(7), pp. 1307–1320. doi: 10.7150/ijms.96274.
- Lin, E. Y. *et al.* (2003) ‘Progression to malignancy in the polyoma middle T oncoprotein mouse breast cancer model provides a reliable model for human diseases.’, *The American journal of pathology*, 163(5), pp. 2113–26. doi: 10.1016/S0002-9440(10)63568-7.
- Linder, S. *et al.* (2023) ‘Mechanisms and roles of podosomes and invadopodia’, *Nature Reviews Molecular Cell Biology*, 24(2), pp. 86–106. doi: 10.1038/s41580-022-00530-6.
- Liu, F. *et al.* (2023) ‘Integrins in cancer: Emerging mechanisms and therapeutic opportunities’, *Pharmacology & Therapeutics*. Pergamon, 247, p. 108458. doi: 10.1016/J.PHARMTHERA.2023.108458.
- Liu, J. *et al.* (2011) ‘Structural Basis of Phosphoinositide Binding to Kindlin-2 Protein Pleckstrin Homology Domain in Regulating Integrin Activation’, *Journal of Biological Chemistry*, 286(50), pp. 43334–43342. doi: 10.1074/jbc.M111.295352.
- Liu, L. *et al.* (2016) ‘Smad2 and Smad3 have differential sensitivity in relaying TGF β signaling and inversely regulate early lineage specification’, *Scientific Reports*. Nature Publishing Group, 6(September 2015), pp. 1–14. doi: 10.1038/srep21602.
- Liu, M. *et al.* (2020) ‘TGF- β suppresses type 2 immunity to cancer’, *Nature*, 587. doi: 10.1038/s41586-020-2836-1.
- Liu, Q. *et al.* (2019) ‘Identification of novel TGF- β regulated genes with pro-migratory roles’, *Biochimica et Biophysica Acta - Molecular Basis of Disease*. Elsevier, 1865(12). doi: 10.1016/j.bbadis.2019.165537.
- Liu, S.-L. *et al.* (2011) ‘Mechanism of a concentration-dependent switch between activation and inhibition of Arp2/3 complex by coronin.’, *The Journal of biological chemistry*. © 2011 ASBMB. Currently published by Elsevier Inc; originally published by American Society for Biochemistry and Molecular Biology., 286(19), pp. 17039–46. doi: 10.1074/jbc.M111.219964.
- Lockhart-Cairns, M. P. *et al.* (2022) ‘Latent TGF β complexes are transglutaminase cross-linked to fibrillin to facilitate TGF β activation’, *Matrix Biology*, pp. 24–39. doi: 10.1016/j.matbio.2022.01.005.
- Lönn, P. *et al.* (2010) ‘PARP-1 attenuates smad-mediated transcription’, *Molecular Cell*, 40(4), pp. 521–532. doi: 10.1016/j.molcel.2010.10.029.
- Lopez, J. I. *et al.* (2011) ‘In situ force mapping of mammary gland transformation.’,

Integrative biology : quantitative biosciences from nano to macro, 3(9), pp. 910–21. doi: 10.1039/c1ib00043h.

Lu, F. *et al.* (2022) ‘Mechanism of integrin activation by talin and its cooperation with kindlin’, *Nature Communications*. Springer US, 13(1), p. 2362. doi: 10.1038/s41467-022-30117-w.

Luo, B. H. and Springer, T. A. (2006) ‘Integrin structures and conformational signaling’, *Current Opinion in Cell Biology*, 18(5), pp. 579–586. doi: 10.1016/j.ceb.2006.08.005.

Lüönd, F. *et al.* (2021) ‘Distinct contributions of partial and full EMT to breast cancer malignancy’, *Developmental Cell*, 56(23), pp. 3203–3221.e11. doi: 10.1016/j.devcel.2021.11.006.

Lüönd, F. *et al.* (2022) ‘Tracking and characterization of partial and full epithelial-mesenchymal transition cells in a mouse model of metastatic breast cancer’, *STAR Protocols*, 3(2), p. 101438. doi: 10.1016/j.xpro.2022.101438.

Ma, N. *et al.* (2023) ‘Rac1: A Regulator of Cell Migration and a Potential Target for Cancer Therapy.’, *Molecules (Basel, Switzerland)*, 28(7), p. 2976. doi: 10.3390/molecules28072976.

Macias, H. and Hinck, L. (2012) ‘Mammary gland development’, *WIREs Developmental Biology*, 1(4), pp. 533–557. doi: 10.1002/wdev.35.

Mahlandt, E. K. *et al.* (2023) ‘Cell-based optimization and characterization of genetically encoded location-based biosensors for Cdc42 or Rac activity.’, *Journal of cell science*, 136(10). doi: 10.1242/jcs.260802.

Mani, S. A. *et al.* (2008) ‘The Epithelial-Mesenchymal Transition Generates Cells with Properties of Stem Cells’, *Cell*, 133(4), pp. 704–715. doi: 10.1016/j.cell.2008.03.027.

Martin, S. K. *et al.* (2011) ‘The emerging role of hypoxia, HIF-1 and HIF-2 in multiple myeloma’, *Leukemia*, 25, pp. 1533–1542. doi: 10.1038/leu.2011.122.

Massagué, J. (2008) ‘TGF β in Cancer’, *Cell*, 134(2), pp. 215–230. doi: 10.1016/j.cell.2008.07.001.

Massagué, J. (2012) ‘TGF β signalling in context.’, *Nature reviews. Molecular cell biology*, 13(10), pp. 616–30. doi: 10.1038/nrm3434.

Mattila, P. K. and Lappalainen, P. (2008) ‘Filopodia: Molecular architecture and cellular functions’, *Nature Reviews Molecular Cell Biology*, 9(6), pp. 446–454. doi: 10.1038/nrm2406.

Mazars, P. *et al.* (1995) ‘Effects of TGF- β 1 (transforming growth factor- β 1) on the cell cycle regulation of human breast adenocarcinoma (MCF-7) cells’, *FEBS Letters*, 362(3), pp. 295–300. doi: 10.1016/0014-5793(95)00247-7.

Mehidi, A. *et al.* (2019) ‘Transient Activations of Rac1 at the Lamellipodium Tip Trigger Membrane Protrusion’, *Current Biology*, 29(17), pp. 2852–2866.e5. doi: 10.1016/j.cub.2019.07.035.

- Míguez, D. G. *et al.* (2013) ‘Smad2 and Smad3 cooperate and antagonize simultaneously in vertebrate neurogenesis’, *Journal of Cell Science*, 126, pp. 5335–5343. doi: 10.1242/jcs.130435.
- Mikati, M. A. *et al.* (2015) ‘Coronin Enhances Actin Filament Severing by Recruiting Cofilin to Filament Sides and Altering F-Actin Conformation.’, *Journal of molecular biology*. Elsevier B.V., 427(19), pp. 3137–47. doi: 10.1016/j.jmb.2015.08.011.
- Miller, D. S. J. and Hill, C. S. (2023) ‘TGF- β Family Signaling’, *Encyclopedia of Cell Biology: Volume 1-6, Second Edition*. Academic Press, 4, pp. 46–61. doi: 10.1016/B978-0-12-821618-7.00242-X.
- Miyazono, K., Kamiya, Y. and Morikawa, M. (2010) ‘Bone morphogenetic protein receptors and signal transduction’, *Journal of Biochemistry*, 147(1), pp. 35–51. doi: 10.1093/jb/mvp148.
- Mori, S. *et al.* (2015) ‘Enhanced Expression of Integrin $\alpha\beta 3$ Induced by TGF- β Is Required for the Enhancing Effect of Fibroblast Growth Factor 1 (FGF1) in TGF- β -Induced Epithelial-Mesenchymal Transition (EMT) in Mammary Epithelial Cells.’, *PloS one*, 10(9), p. e0137486. doi: 10.1371/journal.pone.0137486.
- Moser, M. *et al.* (2009) ‘The Tail of Integrins, Talin, and Kindlins’, *Science*, 324(5929), pp. 895 LP – 899. doi: 10.1126/science.1163865.
- Moshfegh, Y. *et al.* (2014) ‘A Trio–Rac1–Pak1 signalling axis drives invadopodia disassembly’, *Nature Cell Biology*, 16(6), pp. 571–583. doi: 10.1038/ncb2972.
- Nagy, Á. *et al.* (2018) ‘Validation of miRNA prognostic power in hepatocellular carcinoma using expression data of independent datasets’, *Scientific Reports*, 8(1), pp. 1–9. doi: 10.1038/s41598-018-27521-y.
- Nieman, M. T. *et al.* (1999) ‘N-Cadherin Promotes Motility in Human Breast Cancer Cells Regardless of their E-Cadherin Expression’, *The Journal of Cell Biology*, 147(3), pp. 631–643. doi: 10.1083/jcb.147.3.631.
- Nieto, M. A. *et al.* (1994) ‘Control of cell behavior during vertebrate development by Slug, a zinc finger gene.’, *Science (New York, N.Y.)*, 264(5160), pp. 835–9. doi: 10.1126/science.7513443.
- Nobes, C. D. and Hall, A. (1995) ‘Rho, Rac, and Cdc42 GTPases regulate the assembly of multimolecular focal complexes associated with actin stress fibers, lamellipodia, and filopodia’, *Cell*, 81(1), pp. 53–62. doi: 10.1016/0092-8674(95)90370-4.
- Nomura, M. and Li, E. (1998) ‘Smad2 role in mesoderm formation, left-right patterning and craniofacial development’, *Nature*, 393(6687), pp. 786–790. doi: 10.1038/31693.
- Noordstra, I. and Akhmanova, A. (2017) ‘Linking cortical microtubule attachment and exocytosis’, *F1000Research*. F1000Research, 6, p. 469. doi: 10.12688/f1000research.10729.1.
- Oakes, S. R., Hilton, H. N. and Ormandy, C. J. (2006) ‘Key stages in mammary gland development - The alveolar switch: coordinating the proliferative cues and cell fate

- decisions that drive the formation of lobuloalveoli from ductal epithelium', *Breast Cancer Research*, 8(2), p. 207. doi: 10.1186/bcr1411.
- Oda, K. *et al.* (2024) 'The Protective Role of KANK1 in Podocyte Injury', *International Journal of Molecular Sciences*, 25(11), p. 5808. doi: 10.3390/ijms25115808.
- Oishi, M. *et al.* (2024) 'Exclusive expression of KANK4 promotes myofibroblast mobility in keloid tissues', *Scientific Reports*, 14(1), p. 8725. doi: 10.1038/s41598-024-59293-z.
- Orrantia-Borunda, E. *et al.* (2022) 'Subtypes of Breast Cancer', in *Breast Cancer*. Exon Publications, pp. 31–42. doi: 10.36255/exon-publications-breast-cancer-subtypes.
- Özdemir, B. C. *et al.* (2014) 'Depletion of carcinoma-associated fibroblasts and fibrosis induces immunosuppression and accelerates pancreas cancer with reduced survival', *Cancer Cell*, 25(6), pp. 719–734. doi: 10.1016/j.ccr.2014.04.005.
- Pagani, G. and Gohlke, H. (2018) 'On the contributing role of the transmembrane domain for subunit-specific sensitivity of integrin activation', *Scientific Reports*, 8(1), p. 5733. doi: 10.1038/s41598-018-23778-5.
- Paine, I. S. and Lewis, M. T. (2017) 'The Terminal End Bud: the Little Engine that Could', *Journal of Mammary Gland Biology and Neoplasia*. Journal of Mammary Gland Biology and Neoplasia, 22(2), pp. 93–108. doi: 10.1007/s10911-017-9372-0.
- Pan, W. *et al.* (2018) 'Structural insights into ankyrin repeat-mediated recognition of the kinesin motor protein KIF21A by KANK1, a scaffold protein in focal adhesion.', *The Journal of biological chemistry*, 293(6), pp. 1944–1956. doi: 10.1074/jbc.M117.815779.
- Paňková, K. *et al.* (2010) 'The molecular mechanisms of transition between mesenchymal and amoeboid invasiveness in tumor cells', *Cellular and Molecular Life Sciences*, 67(1), pp. 63–71. doi: 10.1007/s00018-009-0132-1.
- Paszek, M. J. *et al.* (2005) 'Tensional homeostasis and the malignant phenotype', *Cancer Cell*, 8(3), pp. 241–254. doi: 10.1016/j.ccr.2005.08.010.
- Patel, S. *et al.* (2019) 'Wnt Signaling and Its Significance Within the Tumor Microenvironment: Novel Therapeutic Insights', *Frontiers in Immunology*, 10, p. 2872. doi: 10.3389/fimmu.2019.02872.
- Phanish, M. K. *et al.* (2006) 'The differential role of Smad2 and Smad3 in the regulation of pro-fibrotic TGFβ1 responses in human proximal-tubule epithelial cells', *Biochemical Journal*, 393(2), pp. 601–607. doi: 10.1042/BJ20051106.
- Pick, R. *et al.* (2017) 'Coronin 1A, a novel player in integrin biology, controls neutrophil trafficking in innate immunity', *Blood*, 130(7), pp. 847–858. doi: 10.1182/blood-2016-11-749622.
- Pierce, D. F. *et al.* (1995) 'Mammary tumor suppression by transforming growth factor beta 1 transgene expression.', *Proceedings of the National Academy of Sciences*, 92(10), pp. 4254–4258. doi: 10.1073/pnas.92.10.4254.
- Pignatelli, J. *et al.* (2012) 'Hic-5 promotes invadopodia formation and invasion during

TGF- β -induced epithelial-mesenchymal transition', *Journal of Cell Biology*, 197(3), pp. 421–437. doi: 10.1083/jcb.201108143.

Pollard, T. D. and Borisy, G. G. (2003) 'Cellular Motility Driven by Assembly and Disassembly of Actin Filaments', *Cell*, 113(4), p. 549. doi: 10.1016/S0092-8674(03)00357-X.

Pratt, S. J. P., Lee, R. M. and Martin, S. S. (2020) 'The Mechanical Microenvironment in Breast Cancer.', *Cancers*, 12(6), p. 1452. doi: 10.3390/cancers12061452.

Priya, R. *et al.* (2016) 'Coronin 1B supports RhoA signaling at cell-cell junctions through Myosin II', *Cell Cycle*. Taylor & Francis, 15(22), pp. 3033–3041. doi: 10.1080/15384101.2016.1234549.

Proetzel, G. *et al.* (1995) 'Transforming growth factor- β 3 is required for secondary palate fusion', *Nature Genetics*, 11(4), pp. 409–414. doi: 10.1038/ng1295-409.

Propper, A. Y. (1978) 'Wandering epithelial cells in the rabbit embryo milk line: A preliminary scanning electron microscope study', *Developmental Biology*. Academic Press, 67(1), pp. 225–231. doi: 10.1016/0012-1606(78)90311-1.

Puisieux, A., Brabletz, T. and Caramel, J. (2014) 'Oncogenic roles of EMT-inducing transcription factors', *Nature Cell Biology*. Nature Publishing Group, 16(6), pp. 488–494. doi: 10.1038/ncb2976.

Pylayeva, Y. *et al.* (2009) 'Ras- and PI3K-dependent breast tumorigenesis in mice and humans requires focal adhesion kinase signaling', *Journal of Clinical Investigation*, (C). doi: 10.1172/JCI37160.

Quinn, J. J. *et al.* (2021) 'Single-cell lineages reveal the rates, routes, and drivers of metastasis in cancer xenografts', *Science*, 371(6532). doi: 10.1126/science.abc1944.

Rafiq, N. B. M. *et al.* (2019) 'A mechano-signalling network linking microtubules, myosin IIA filaments and integrin-based adhesions.', *Nature materials*. Springer US, 18(6), pp. 638–649. doi: 10.1038/s41563-019-0371-y.

Ramesh, S., Wildey, G. M. and Howe, P. H. (2009) 'Transforming growth factor β (TGF β)-induced apoptosis: The rise and fall of Bim', *Cell Cycle*, 8(1), pp. 11–17. doi: 10.4161/cc.8.1.7291.

Ramot, Y. *et al.* (2014) 'Mutation in KANK2, encoding a sequestering protein for steroid receptor coactivators, causes keratoderma and woolly hair', *Journal of Medical Genetics*, 51(6), pp. 388–394. doi: 10.1136/jmedgenet-2014-102346.

Revach, O.-Y. *et al.* (2015) 'Mechanical interplay between invadopodia and the nucleus in cultured cancer cells', *Scientific Reports*, 5(1), p. 9466. doi: 10.1038/srep09466.

Revach, O.-Y. *et al.* (2016) 'The involvement of mutant Rac1 in the formation of invadopodia in cultured melanoma cells', *Experimental Cell Research*. Elsevier, 343(1), pp. 82–88. doi: 10.1016/j.yexcr.2016.02.003.

Ripamonti, M., Wehrle-Haller, B. and de Curtis, I. (2022) 'Paxillin: A Hub for Mechano-

Transduction from the $\beta 3$ Integrin-Talin-Kindlin Axis', *Frontiers in Cell and Developmental Biology*, 10(April), pp. 1–10. doi: 10.3389/fcell.2022.852016.

Rival-Gervier, S. *et al.* (2013) 'Kinetics and epigenetics of retroviral silencing in mouse embryonic stem cells defined by deletion of the D4Z4 element.', *Molecular therapy : the journal of the American Society of Gene Therapy*. The American Society of Gene & Cell Therapy, 21(8), pp. 1536–50. doi: 10.1038/mt.2013.131.

Rivina, L., Davoren, M. J. and Schiestl, R. H. (2016) 'Mouse models for radiation-induced cancers', *Mutagenesis*, 31(5), pp. 491–509. doi: 10.1093/mutage/gew019.

Robertson, I. B. *et al.* (2015) 'Latent TGF- β -binding proteins', *Matrix Biology*. Elsevier, 47, pp. 44–53. doi: 10.1016/J.MATBIO.2015.05.005.

Rodal, A. A. *et al.* (2005) 'Conformational changes in the Arp2/3 complex leading to actin nucleation', *Nature Structural & Molecular Biology*, 12(1), pp. 26–31. doi: 10.1038/nsmb870.

Ross, S. R. (2008) 'MMTV Infectious Cycle and the Contribution of Virus-encoded Proteins to Transformation of Mammary Tissue', *Journal of Mammary Gland Biology and Neoplasia*, 13(3), pp. 299–307. doi: 10.1007/s10911-008-9090-8.

Ross, S. R. (2010) 'Mouse Mammary Tumor Virus Molecular Biology and Oncogenesis', *Viruses*, 2(9), pp. 2000–2012. doi: 10.3390/v2092000.

Roth, H. *et al.* (2017) 'Filamin A promotes efficient migration and phagocytosis of neutrophil-like HL-60 cells.', *European journal of cell biology*, 96(6), pp. 553–566. doi: 10.1016/j.ejcb.2017.05.004.

Roy, B. C., Kakinuma, N. and Kiyama, R. (2009) 'Kank attenuates actin remodeling by preventing interaction between IRSp53 and Rac1.', *The Journal of cell biology*. The Rockefeller University Press, 184(2), pp. 253–67. doi: 10.1083/jcb.200805147.

Sakamoto, K., Schmidt, J. W. and Wagner, K.-U. (2015) 'Mouse Models of Breast Cancer', in *Methods in Molecular Biology*, pp. 47–71. doi: 10.1007/978-1-4939-2297-0_3.

Sanford, L. P. *et al.* (1997) 'TGF β 2 knockout mice have multiple developmental defects that are non-overlapping with other TGF β knockout phenotypes', *Development*, 124(13), pp. 2659–2670. doi: 10.1242/dev.124.13.2659.

Santibáñez, J. F. *et al.* (2010) 'Rac1 modulates TGF-beta1-mediated epithelial cell plasticity and MMP9 production in transformed keratinocytes.', *FEBS letters*, 584(11), pp. 2305–10. doi: 10.1016/j.febslet.2010.03.042.

Santner, S. J. *et al.* (2001) 'Malignant MCF10CA1 Cell Lines Derived from Premalignant Human Breast Epithelial MCF10AT Cells', *Breast Cancer Research and Treatment*, 65(2), pp. 101–110. doi: 10.1023/A:1006461422273.

Sanz-Moreno, V. *et al.* (2008) 'Rac activation and inactivation control plasticity of tumor cell movement.', *Cell*, 135(3), pp. 510–23. doi: 10.1016/j.cell.2008.09.043.

Sanz, A. L. and Míguez, D. G. (2014) 'Dual R-Smads interplay in the regulation of

- vertebrate neurogenesis', *Neurogenesis*, 1(1). doi: 10.4161/neur.29529.
- Sarkar, S. *et al.* (2002) 'A Novel Ankyrin Repeat-containing Gene (Kank) Located at 9p24 Is a Growth Suppressor of Renal Cell Carcinoma', *Journal of Biological Chemistry*, 277(39), pp. 36585–36591. doi: 10.1074/jbc.M204244200.
- Sato, M. *et al.* (2014) 'An integrated genomic approach identifies persistent tumor suppressive effects of transforming growth factor- β in human breast cancer.', *Breast cancer research : BCR*, 16(3), p. R57. doi: 10.1186/bcr3668.
- Savagner, P., Yamada, K. M. and Thiery, J. P. (1997) 'The Zinc-Finger Protein Slug Causes Desmosome Dissociation, an Initial and Necessary Step for Growth Factor-induced Epithelial–Mesenchymal Transition', *The Journal of Cell Biology*, 137(6), pp. 1403–1419. doi: 10.1083/jcb.137.6.1403.
- Scheel, C. and Weinberg, R. A. (2012) 'Cancer stem cells and epithelial-mesenchymal transition: Concepts and molecular links', *Seminars in Cancer Biology*. Elsevier Ltd, 22(5–6), pp. 396–403. doi: 10.1016/j.semcancer.2012.04.001.
- Schiller, H. B. *et al.* (2011) 'Quantitative proteomics of the integrin adhesome show a myosin II-dependent recruitment of LIM domain proteins', *EMBO Reports*, 12(3), pp. 259–266. doi: 10.1038/embor.2011.5.
- Schnelzer, A. *et al.* (2000) 'Rac1 in human breast cancer: overexpression, mutation analysis, and characterization of a new isoform, Rac1b.', *Oncogene*, 19(26), pp. 3013–20. doi: 10.1038/sj.onc.1203621.
- Seyfried, T. N. and Huysentruyt, L. C. (2013) 'On the origin of cancer metastasis.', *Critical reviews in oncogenesis*, 18(1–2), pp. 43–73. doi: 10.1615/critrevoncog.v18.i1-2.40.
- Sheppard, A. M. *et al.* (1994) 'Expanding Roles for $\alpha 4$ Integrin and its Ligands in Development', *Cell Adhesion and Communication*, 2(1), pp. 27–43. doi: 10.3109/15419069409014200.
- Shi, M. *et al.* (2011) 'Latent TGF- β structure and activation', *Nature*, 474. doi: 10.1038/nature10152.
- Shi, Y. *et al.* (1998) 'Crystal structure of a Smad MH1 domain bound to DNA: Insights on DNA binding in TGF- β signaling', *Cell*, 94(5), pp. 585–594. doi: 10.1016/S0092-8674(00)81600-1.
- Shull, M. M. *et al.* (1992) 'Targeted disruption of the mouse transforming growth factor-beta 1 gene results in multifocal inflammatory disease.', *Nature*, 359(6397), pp. 693–9. doi: 10.1038/359693a0.
- Sonnenberg, A. *et al.* (1987) 'Oncogene expression during progression of mouse mammary tumor cells; activity of a proviral enhancer and the resulting expression of int-2 is influenced by the state of differentiation.', *The EMBO journal*, 6(1), pp. 121–125. doi: 10.1002/j.1460-2075.1987.tb04728.x.
- van Steenhoven, J. E. C. *et al.* (2020) 'Assessment of tumour proliferation by use of the mitotic activity index, and Ki67 and phosphohistone H3 expression, in early-stage luminal

- breast cancer.’, *Histopathology*. Exon Publications, 77(4), pp. 579–587. doi: 10.1111/his.14185.
- Stehbens, S. J. *et al.* (2014) ‘CLASPs link focal-adhesion-associated microtubule capture to localized exocytosis and adhesion site turnover’, *Nature Cell Biology*, 16(6), pp. 558–570. doi: 10.1038/ncb2975.
- Stemmler, M. P. *et al.* (2019) ‘Non-redundant functions of EMT transcription factors’, *Nature Cell Biology*, 21(1), pp. 102–112. doi: 10.1038/s41556-018-0196-y.
- Strickland, L. B. *et al.* (2000) ‘Progression of Premalignant MCF10AT Generates Heterogeneous Malignant Variants with Characteristic Histologic Types and Immunohistochemical Markers’, *Breast Cancer Research and Treatment*, 64(3), pp. 235–240. doi: 10.1023/A:1026562720218.
- Su, Y. *et al.* (2016) ‘Relating conformation to function in integrin $\alpha 5 \beta 1$.’, *Proceedings of the National Academy of Sciences of the United States of America*, 113(27), pp. E3872–81. doi: 10.1073/pnas.1605074113.
- Subik, K. *et al.* (2010) ‘The Expression Patterns of ER, PR, HER2, CK5/6, EGFR, Ki-67 and AR by Immunohistochemical Analysis in Breast Cancer Cell Lines.’, *Breast cancer: basic and clinical research*, 4(1), pp. 35–41. doi: 10.1177/117822341000400004.
- Sugihara, K. *et al.* (1998) ‘Rac1 is required for the formation of three germ layers during gastrulation’, *Oncogene*, 17(26), pp. 3427–3433. doi: 10.1038/sj.onc.1202595.
- Sun, Z. (2015) *Kank family proteins comprise a novel type of talin activator*. Ludwig-Maximilian Universität München. doi: 10.5282/edoc.20215.
- Sun, Z. *et al.* (2016) ‘Kank2 activates talin, reduces force transduction across integrins and induces central adhesion formation’, *Nature Cell Biology*, 18(9), pp. 941–953. doi: 10.1038/ncb3402.
- Sun, Z., Costell, M. and Fässler, R. (2019) ‘Integrin activation by talin, kindlin and mechanical forces’, *Nature Cell Biology*. Springer US, 21(1), pp. 25–31. doi: 10.1038/s41556-018-0234-9.
- Sun, Z., Guo, S. S. and Fässler, R. (2016) ‘Integrin-mediated mechanotransduction’, *The Journal of Cell Biology*, 215(4), pp. 445 LP – 456. doi: 10.1083/jcb.201609037.
- Swaminathan, V. and Waterman, C. M. (2016) ‘The molecular clutch model for mechanotransduction evolves’, *Nature Cell Biology*. Nature Publishing Group, a division of Macmillan Publishers Limited. All Rights Reserved., 18, p. 459. Available at: <https://doi.org/10.1038/ncb3350>.
- Symons, M. (2011) ‘Rac1 activation comes full circle’, *EMBO Journal*, 30, pp. 3875–3877. doi: 10.1038/emboj.2011.330.
- Tadijan, A. *et al.* (2021) ‘KANK family proteins in cancer’, *The International Journal of Biochemistry & Cell Biology*, 131(November 2020), p. 105903. doi: <https://doi.org/10.1016/j.biocel.2020.105903>.

- Tang, B. *et al.* (2003) 'TGF- β switches from tumor suppressor to prometastatic factor in a model of breast cancer progression', *Journal of Clinical Investigation*, 112(7), pp. 1116–1124. doi: 10.1172/JCI200318899.
- Tanzer, M. L. (1973) 'Cross-Linking of Collagen', *Science*, 180(4086), pp. 561–566. doi: 10.1126/science.180.4086.561.
- Tatarano, S. *et al.* (2012) 'Novel oncogenic function of mesoderm development candidate 1 and its regulation by MiR-574-3p in bladder cancer cell lines', *International Journal of Oncology*, 40(4), pp. 951–959. doi: 10.3892/ijo.2011.1294.
- Theodosiou, M. *et al.* (2016) 'Kindlin-2 cooperates with talin to activate integrins and induces cell spreading by directly binding paxillin', *eLife*, 5. doi: 10.7554/eLife.10130.
- Theriot, J. A. and Mitchison, T. J. (1991) 'Actin microfilament dynamics in locomoting cells', *Nature*, 352(6331), pp. 126–131. doi: 10.1038/352126a0.
- Théry, M. and Blanchoin, L. (2024) 'Reconstituting the dynamic steady states of actin networks in vitro', *Nature Cell Biology*, 26(4), pp. 494–497. doi: 10.1038/s41556-024-01379-x.
- Thiery, J. P. *et al.* (2009) 'Epithelial-Mesenchymal Transitions in Development and Disease', *Cell*, 139(5), pp. 871–890. doi: 10.1016/j.cell.2009.11.007.
- Thome, S. *et al.* (2018) 'Intracellular $\beta 2$ integrin (CD11/CD18) interacting partners in neutrophil trafficking.', *European journal of clinical investigation*, 48 Suppl 2, p. e12966. doi: 10.1111/eci.12966.
- Trelford, C. B., Dagnino, L. and Di Guglielmo, G. M. (2022) 'Transforming growth factor- β in tumour development', *Frontiers in Molecular Biosciences*, 9(October), pp. 1–29. doi: 10.3389/fmolb.2022.991612.
- Tsujita, K. *et al.* (2010) 'Proteome of acidic phospholipid-binding proteins: spatial and temporal regulation of Coronin 1A by phosphoinositides.', *The Journal of biological chemistry*, 285(9), pp. 6781–9. doi: 10.1074/jbc.M109.057018.
- Ungefroren, H., Witte, D. and Lehnert, H. (2018) 'The role of small GTPases of the Rho/Rac family in TGF- β -induced EMT and cell motility in cancer', *Developmental Dynamics*, 247(3), pp. 451–461. doi: 10.1002/dvdy.24505.
- van der Vaart, B. *et al.* (2013) 'CFEOM1-associated kinesin KIF21A is a cortical microtubule growth inhibitor', *Developmental Cell*. United States: Elsevier Inc., 27(2), pp. 145–160. doi: 10.1016/j.devcel.2013.09.010.
- Vicente-Manzanares, M. and Horwitz, A. R. (2011) 'Adhesion dynamics at a glance', *Journal of Cell Science*, 124(23), pp. 3923–3927. doi: 10.1242/jcs.095653.
- Walker, R. A., Dearing, S. J. and Gallacher, B. (1994) 'Relationship of transforming growth factor beta 1 to extracellular matrix and stromal infiltrates in invasive breast carcinoma.', *British journal of cancer*, 69(6), pp. 1160–5. doi: 10.1038/bjc.1994.228.
- Wang, D. *et al.* (2012) 'Steroid receptor coactivator-interacting protein (SIP) inhibits

- caspase-independent apoptosis by preventing apoptosis-inducing factor (AIF) from being released from mitochondria', *The Journal of biological chemistry*, 2012/02/27. American Society for Biochemistry and Molecular Biology, 287(16), pp. 12612–12621. doi: 10.1074/jbc.M111.334151.
- Wang, Q. A. and Scherer, P. E. (2019) 'Remodeling of Murine Mammary Adipose Tissue during Pregnancy, Lactation, and Involution', *Journal of Mammary Gland Biology and Neoplasia*, 24(3), pp. 207–212. doi: 10.1007/s10911-019-09434-2.
- Wang, Y. *et al.* (2005) 'Alternative splicing of the human Kank gene produces two types of Kank protein', *Biochemical and Biophysical Research Communications*, 330(4), pp. 1247–1253. doi: 10.1016/j.bbrc.2005.03.106.
- Wang, Y. *et al.* (2006) 'Nucleo-cytoplasmic shuttling of human Kank protein accompanies intracellular translocation of β -catenin', *Journal of Cell Science*, 119(19), pp. 4002–4010. doi: 10.1242/jcs.03169.
- Watson, C. J. and Khaled, W. T. (2008) 'Mammary development in the embryo and adult: A journey of morphogenesis and commitment', *Development*, 135(6), pp. 995–1003. doi: 10.1242/dev.005439.
- Watson, E. D. and Cross, J. C. (2005) 'Development of structures and transport functions in the mouse placenta.', *Physiology (Bethesda, Md.)*, 20(3), pp. 180–93. doi: 10.1152/physiol.00001.2005.
- Weaver, A. M. (2006) 'Invadopodia: specialized cell structures for cancer invasion.', *Clinical & experimental metastasis*, 23(2), pp. 97–105. doi: 10.1007/s10585-006-9014-1.
- Wei, S. C. *et al.* (2015) 'Matrix stiffness drives epithelial–mesenchymal transition and tumour metastasis through a TWIST1–G3BP2 mechanotransduction pathway', *Nature Cell Biology*, 17(5), pp. 678–688. doi: 10.1038/ncb3157.
- Weinberg, R. A. (2013) 'The Biology of Cancer', in. New York: W.W. Norton & Company, p. 960. doi: 10.1201/9780429258794.
- Weiss, A. and Attisano, L. (2013) 'The TGF β superfamily signaling pathway', *Wiley Interdisciplinary Reviews: Developmental Biology*, 2(1), pp. 47–63. doi: 10.1002/wdev.86.
- Weng, Z. *et al.* (2018) 'Structural analyses of key features in the KANK1·KIF21A complex yield mechanistic insights into the cross-talk between microtubules and the cell cortex.', *The Journal of biological chemistry*, 293(1), pp. 215–225. doi: 10.1074/jbc.M117.816017.
- Werner, A.-C. *et al.* (2020) 'Coronin 1B Controls Endothelial Actin Dynamics at Cell-Cell Junctions and Is Required for Endothelial Network Assembly.', *Frontiers in cell and developmental biology*, 8, p. 708. doi: 10.3389/fcell.2020.00708.
- Wiercinska, E. *et al.* (2011) 'The TGF- β /Smad pathway induces breast cancer cell invasion through the up-regulation of matrix metalloproteinase 2 and 9 in a spheroid invasion model system', *Breast Cancer Research and Treatment*, 128(3), pp. 657–666. doi: 10.1007/s10549-010-1147-x.
- Wiseman, B. S. and Werb, Z. (2002) 'Stromal effects on mammary gland development and

- breast cancer.’, *Science (New York, N.Y.)*, 296(5570), pp. 1046–9. doi: 10.1126/science.1067431.
- Wrana, J. L. *et al.* (1994) ‘Mechanism of activation of the TGF- β receptor’, *Nature*, 370(6488), pp. 341–347. doi: 10.1038/370341a0.
- Wrans, J. and Pawson, T. (1997) ‘Mad about SMADs’, *Nature*, 388(6637), pp. 28–29. doi: 10.1038/40290.
- Wu, J. *et al.* (2021) ‘Plasticity of cancer cell invasion: Patterns and mechanisms’, *Translational Oncology*. Elsevier Inc., 14(1), p. 100899. doi: 10.1016/j.tranon.2020.100899.
- Wu, S. G. *et al.* (2017) ‘miR-508-5p acts as an anti-oncogene by targeting MESDC1 in hepatocellular carcinoma.’, *Neoplasma*, 64(1), pp. 40–47. doi: 10.4149/neo_2017_105.
- Xin, Z. *et al.* (2022) ‘Quantitative Analysis of Collective Migration by Single-Cell Tracking Aimed at Understanding Cancer Metastasis.’, *International journal of molecular sciences*, 23(20), p. 12372. doi: 10.3390/ijms232012372.
- Xu, J., Lamouille, S. and Derynck, R. (2009) ‘TGF-B-induced epithelial to mesenchymal transition’, *Cell Research*, 19(2), pp. 156–172. doi: 10.1038/cr.2009.5.
- Yamada, K. M. and Sixt, M. (2019) ‘Mechanisms of 3D cell migration.’, *Nature reviews. Molecular cell biology*. Springer US, 20(12), pp. 738–752. doi: 10.1038/s41580-019-0172-9.
- Yamaguchi, H. *et al.* (2005) ‘Molecular mechanisms of invadopodium formation’, *The Journal of Cell Biology*, 168(3), pp. 441–452. doi: 10.1083/jcb.200407076.
- Yamaguchi, H. (2012) ‘Pathological roles of invadopodia in cancer invasion and metastasis’, *European Journal of Cell Biology*. Elsevier GmbH., 91(11–12), pp. 902–907. doi: 10.1016/j.ejcb.2012.04.005.
- Yamashiro, S. *et al.* (2023) ‘Force transmission by retrograde actin flow-induced dynamic molecular stretching of Talin’, *Nature Communications*, 14(1), p. 8468. doi: 10.1038/s41467-023-44018-z.
- Yamashita, H. *et al.* (1994) ‘Formation of hetero-oligomeric complexes of type I and type II receptors for transforming growth factor-beta.’, *Journal of Biological Chemistry*, 269(31), pp. 20172–20178. doi: 10.1016/S0021-9258(17)32142-7.
- Yang, J. *et al.* (2004) ‘Twist, a master regulator of morphogenesis, plays an essential role in tumor metastasis’, *Cell*, 117(7), pp. 927–939. doi: 10.1016/j.cell.2004.06.006.
- Yang, J. *et al.* (2020) ‘Guidelines and definitions for research on epithelial–mesenchymal transition’, *Nature Reviews Molecular Cell Biology*. Springer US, 21(6), pp. 341–352. doi: 10.1038/s41580-020-0237-9.
- Yang, J. T., Rayburn, H. and Hynes, R. O. (1995) ‘Cell adhesion events mediated by alpha 4 integrins are essential in placental and cardiac development.’, *Development (Cambridge, England)*, 121(2), pp. 549–60. doi: 10.1242/dev.121.2.549.

- Yang, X. *et al.* (1998) 'The tumor suppressor SMAD4/DPC4 is essential for epiblast proliferation and mesoderm induction in mice', *Proceedings of the National Academy of Sciences of the United States of America*, 95(7), pp. 3667–3672. doi: 10.1073/pnas.95.7.3667.
- Ye, X. *et al.* (2017) 'Upholding a role for EMT in breast cancer metastasis', *Nature*, 547(7661), pp. E1–E6. doi: 10.1038/nature22816.
- Yoon, S. B. *et al.* (2024) 'Subpopulation commensalism promotes Rac1-dependent invasion of single cells via laminin-332', *Journal of Cell Biology*. United States, 223(6). doi: 10.1083/jcb.202308080.
- Yoshinaga, K. *et al.* (2008) 'Perturbation of transforming growth factor (TGF)- β 1 association with latent TGF- β binding protein yields inflammation and tumors', *Proceedings of the National Academy of Sciences*, 105(48), pp. 18758–18763. doi: 10.1073/pnas.0805411105.
- Yu, M. *et al.* (2019) 'Force-Dependent Regulation of Talin–KANK1 Complex at Focal Adhesions', *Nano Letters*. American Chemical Society, 19(9), pp. 5982–5990. doi: 10.1021/acs.nanolett.9b01732.
- Yu, Y. *et al.* (2014) 'Cancer-associated fibroblasts induce epithelial-mesenchymal transition of breast cancer cells through paracrine TGF- β signalling', *British Journal of Cancer*, 110(3), pp. 724–732. doi: 10.1038/bjc.2013.768.
- Ben Zablah, Y., Merovitch, N. and Jia, Z. (2020) 'The Role of ADF/Cofilin in Synaptic Physiology and Alzheimer's Disease', *Frontiers in Cell and Developmental Biology*, 8. doi: 10.3389/fcell.2020.594998.
- Zhang, C. *et al.* (2022) 'KANK4 Promotes Arteriogenesis by Potentiating VEGFR2 Signaling in a TALIN-1–Dependent Manner', *Arteriosclerosis, Thrombosis, and Vascular Biology*. American Heart Association, 42(6), pp. 772–788. doi: 10.1161/ATVBAHA.122.317711.
- Zhang, J. *et al.* (2014) 'TGF- β -induced epithelial-to-mesenchymal transition proceeds through stepwise activation of multiple feedback loops', *Science Signaling*, 7(345), p. ra91. doi: 10.1126/scisignal.2005304.
- Zhang, J. *et al.* (2019) 'Energetic regulation of coordinated leader–follower dynamics during collective invasion of breast cancer cells', *Proceedings of the National Academy of Sciences of the United States of America*, 116(16), pp. 7867–7872. doi: 10.1073/pnas.1809964116.
- Zhang, Y. *et al.* (2001) 'Regulation of Smad degradation and activity by Smurf2, an E3 ubiquitin ligase', *Proceedings of the National Academy of Sciences of the United States of America*, 98(3), pp. 974–979. doi: 10.1073/pnas.98.3.974.
- Zhang, Y. *et al.* (2007) 'SIP, a novel ankyrin repeat containing protein, sequesters steroid receptor coactivators in the cytoplasm', *EMBO Journal*, 26(11), pp. 2645–2657. doi: 10.1038/sj.emboj.7601710.
- Zhang, Y. E. (2009) 'Non-Smad pathways in TGF- β signaling', *Cell Research*, 19(1), pp.

128–139. doi: 10.1038/cr.2008.328.

Zhao, Y. *et al.* (2021) ‘Identification of predictors based on drug targets highlights accurate treatment of goserelin in breast and prostate cancer.’, *Cell & bioscience*, 11(1), p. 5. doi: 10.1186/s13578-020-00517-w.

Zhu, J. *et al.* (2008) ‘Structure of a Complete Integrin Ectodomain in a Physiologic Resting State and Activation and Deactivation by Applied Forces’, *Molecular Cell*. Elsevier Ltd, 32(6), pp. 849–861. doi: 10.1016/j.molcel.2008.11.018.

Zhu, Y. *et al.* (2008) ‘Kank proteins: a new family of ankyrin-repeat domain-containing proteins.’, *Biochimica et biophysica acta*. Elsevier, 1780(2), pp. 128–33. doi: 10.1016/j.bbagen.2007.09.017.

8 Appendix

The appendix contains supplementary mouse data (Table 14, Table 15, Table 16, and Table 17), the generation of the human KANK4 antibody and MCF10A^{KANK4-KO} cells, and reprints of the paper I and II.

8.1 Mouse Data

Table 14: KANK2 mice analyzed for tumor growth, burden, and metastasis formation at 60 days after tumor onset

KANK2-WT ^{PyMT}							KANK2-KO ^{PyMT}					
	Mouse -ID	total tumor weight	size of largest tumor			N (metastasis)	Mouse -ID	total tumor weight	size of largest tumor			N (metastasis)
			b	w	volume				b	w	volume	
1	59430	2.6	10.5	8.9	415.9	0	55295	2.4	6	5.5	90.8	0
2	59433	1.9	6.7	6.3	133.0	0	55304	2.1	10	8.7	378.5	0
3	61038	2.6	7.5	7.0	183.8	0	61034	2.8	5.1	4.9	61.2	0
4	61037	2.4	11.4	10.0	570.0	0	61114	2.9	9.3	7.2	241.1	0
5	61356	2.6	6.7	5.6	105.1	0	61116	3.0	7.7	7.5	216.6	0
6	62539	3.2	10.6	8.4	374.0	0	61180	2.4	8.7	6.3	172.7	0
7	62933	2.5	11	8.8	425.9	0	61173	3.3	7.4	6	133.2	0
8	62972	2.3	6.0	5.2	81.1	2	61369	2.3	7.6	6.8	175.7	1
9	26725	1.8	10.6	6.4	217.1	0	61425	1.8	7.4	6.8	171.1	0
10	26857	1.7	6.0	5.5	90.8	0	61426	1.8	11.4	5.9	198.4	1
11	26986	2.4	10.0	9.6	460.8	7	61428	2.0	8.9	8.3	306.6	2
12	15317	1.9	8.3	6.4	170.0	0	62511	3.2	7.6	6.8	175.7	0
13	15409	2.8	7.7	6.8	178.0	0	62793	2.9	7.9	7.8	240.3	0
14	15410	1.7	5.1	4.0	40.8	0	62794	2.5	10.3	8.7	389.8	0
15	55266	2.2	9.0	8.6	332.8	0	62811	3.2	7.8	4.8	89.9	0
16	55369	3.9	7.7	7.5	216.6	0	62970	1.9	8.1	5.9	141.0	0
17							26990	2.8	6.2	5	77.5	0
% of mice developing metastasis							12.5					
							17.6					

Table 15: KANK4 mice analyzed for tumor growth, burden, and metastasis formation at 60 days after tumor onset

	KANK4-WT ^{PyMT}						KANK4-KO ^{PyMT}					
	Mouse-ID	total tumor weight	size of largest tumor			N (metastasis)	Mouse-ID	total tumor weight	size of largest tumor			N (metastasis)
			b	w	volume				b	w	volume	
1	62671	1.2	8.5	5.9	147.9	0	26713	0.7	4.5	4.5	45.6	0
2	62578	1.4	8.3	8.2	279.0	0	61473	0.8	4.1	4	32.8	0
3	61494	1.7	9.9	9.2	419.0	3	55264	0.9	6.2	5.5	93.8	0
4	62758	1.7	5.2	5.1	67.6	0	61490	0.98	7.7	4.8	88.7	0
5	62782	1.7	8.2	7.2	212.5	0	55343	0.99	8.5	8	272.0	0
6	26857	1.7	11.9	10.7	681.2	1	55345	1	5	3.3	27.2	0
7	26725	1.8	10.6	6.4	217.1	0	26854	1.1	5.7	3.7	39.0	0
8	62886	1.8	7	5.1	91.0	0	61491	1.25	6.9	4.8	79.5	0
9	62593	1.95	6.2	4.4	60.0	0	61448	1.3	6.5	5.5	98.3	0
10	62595	2	7.5	7.1	189.0	0	62674	1.37	5.7	5.3	80.1	0
11	62669	2	8.2	5.8	137.9	3	61243	1.4	5.5	4.8	63.4	0
12	26696	2	8.5	6.1	158.1	0	62784	1.4	3.6	3.6	23.3	1
13	55266	2.2	9	8.6	332.8	0	61156	1.45	6	5	75.0	0
14	61405	2.2	5.9	5.4	86.0	13	61154	1.5	5.6	5.3	78.7	0
15	62885	2.2	7	5.8	117.7	0	61349	1.56	6.1	5.8	102.6	0
16	59846	2.2	10	9	405.0	0	55366	1.58	7.4	7	181.3	0
17	62972	2.25	12	10	600.0	2	55355	1.6	5.7	5.6	89.4	0
18	62756	2.3	8.6	7.2	222.9	0	61153	1.6	5.2	4.3	48.1	1
19	26986	2.4	10	9.6	460.8	7	55265	1.75	5.9	5.9	102.7	0
20	61037	2.4	11.4	10	570.0	0	61249	1.8	8	6.2	153.8	0
21	62505	2.4	7	6.7	157.1	0	61350	1.8	9.5	5.8	159.8	0
22	62560	2.4	8.6	6.8	198.8	0	62956	1.8	7.2	5.3	101.1	0
23	62576	2.4	10.6	8.5	382.9	0	61455	1.87	7.4	5.5	111.9	0
24	62708	2.4	11.8	7.4	323.1	0	26818	1.9	7.3	6.3	144.9	0
25	62933	2.5	11	8.8	425.9	0	61240	2	8.6	5.4	125.4	0
26	26814	2.5	9.8	8.6	362.4	0	61346	2	6.6	6	118.8	0
27	62667	2.5	8.4	6.8	194.2	3	61492	2	6.8	5.6	106.6	0
28	62781	2.5	12.6	8.6	465.9	2	62918	2	9.7	8	310.4	0
29	59430	2.58	10.5	8.9	415.9	0	61217	2.16	8.7	7.9	271.5	0
30	61038	2.6	7.5	7	183.8	0	61406	2.2	7	6.2	134.5	0
31	61356	2.6	6.7	5.6	105.1	0	61447	2.3	10.6	6.9	252.3	0
32	61410	2.7	12.7	8.6	469.6	0	62954	2.3	4.2	4.2	37.0	0
33	62829	2.9	7	6.7	157.1	1	26820	2.3	12.5	10.9	742.6	0
34	26661	2.9	12.5	7.6	361.0	0	55351	2.78	10.3	8.3	354.8	0
35	26810	3.1	12.4	11.1	763.9	0	61456	2.8	9.9	6.8	228.9	0
36	26812	3.2	7.9	6.7	177.3	0	55268	3.1	12	10.2	624.2	0
37	62539	3.2	10.6	8.4	374.0	0	61246	3.5	10.8	9	437.4	0
38	62504	3.6	10.3	8.6	380.9	0						
39	55369	3.9	7.7	7.5	216.6	0						

% of mice developing metastasis

23.1

5.4

Table 16: Mouse pairs selected for lung histology

KANK4-WT ^{PyMT}						KANK4-KO ^{PyMT}					
Mouse-ID	total tumor weight	size of largest tumor			N (metastasis)	Mouse-ID	total tumor weight	size of largest tumor			N (metastasis)
		b	w	volume				b	w	volume	
62886	1.8	7	5.1	91.0	0	62956	1.8	7.2	5.3	101.1	0
62595	2	7.5	7.1	189.0	0	62918	2	9.7	8	310.4	0
62885	2.2	7	5.8	117.7	0	61406	2.2	7	6.2	134.5	0
62505	2.4	7	6.7	157.1	0	61447	2.3	10.6	6.9	252.3	0
61410	2.7	12.7	8.6	469.6	0	62562	2.5	18.4	12.1	1347.0	0
62504	3.6	10.3	8.6	380.9	0	61246	3.5	10.8	9	437.4	0
61494	1.7	9.9	9.2	419.0	3	62784	1.4	3.6	3.6	23.3	1
61405	2.2	5.9	5.4	86.0	13						

Table 17: Calculation of average number of metastatic nodules per mouse

KANK4-WT ^{PyMT}			KANK4-KO ^{PyMT}		
N (animals)	N (metastases)	Product	N (animals)	N (metastases)	Product
2	1	2	2	1	2
2	2	4			
3	3	9			
1	7	7			
1	13	13			
Sum	9	26	2	1	2
Average number of metastatic nodules per mouse					
3.9			1.0		

8.2 Generation of human KANK4 antibody

To generate a human-specific KANK4 antibody, two distinct peptide sequences, designated sequence 1 (P2811) and sequence 2 (P2812), were designed to target human KANK4. Both peptides target the KANK4 protein between the coiled-coil domain and ankyrin repeats (Figure 66A). A total of four rabbits were immunized, with two rabbits immunized per peptide. The final sera were tested for KANK4 specificity by overexpressing human KANK4 in MKF cells, which are stromal cells and normally do not

express KANK4 (Figure 66B). Only peptide sequence 1 (P2811) was able to recognize human KANK4, with no discernable difference between the two rabbits. Peptide sequence 2 (P2812) was unable to bind to human KANK4 and was thus discarded. Therefore, a human KANK4-specific antibody was successfully generated in rabbits.

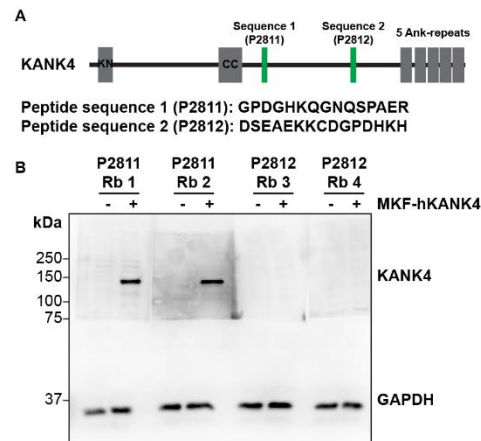


Figure 66: Generation of human KANK4 antibody. (A) Scheme of KANK4 aa sequence. The two peptide sequences designed for antibody generation are highlighted in green. (B) Lysates of MKF cells transfected with human KANK4 were analyzed by WB with indicated sera obtained from two rabbit pairs injected with peptide sequence 1 or 2, respectively. GAPDH served as loading control. In parts taken from a manuscript (Seiwert *et al.*) in consideration.

8.3 Generation of MCF10A^{KANK4-KO} cells

To analyze its function, KANK4 was depleted using CRISPR/Cas9 in MCF10A cells. The specific human KANK4 gRNA targets exon 4. Clones were established and checked for efficient KANK4-KO via WB and sequencing analysis (Figure 67A). In addition to the parental MCF10A cells, three single-cell clones were selected for further experimentation (Figure 67B): Clone #1 served as a positive WT control, stably expressing Cas9 to verify that constant Cas9 expression does not interfere with the observed results. Clone #2 and #3 were sequencing-confirmed KO of KANK4, and all experiments were conducted with both clones to avoid clonal effects.

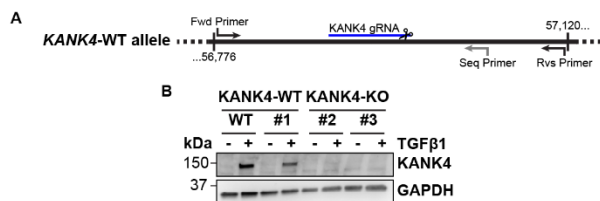


Figure 67: Generation of MCF10A^{KANK4-KO} cells. (A) Scheme of *KANK4* cDNA allele, highlighting binding of *KANK4* gRNA so generate *KANK4*-KO. For sequencing, the indicated part of *KANK4* cDNA was amplified (fwd primer & rvs primer) and sent for sequencing using the sequencing primer (Seq primer). (B) Lysates of MCF10A cells with ectopic eSPCas9PlusT2A-TagBFP2 expression transfected with human *KANK4* targeting gRNA treated without or with TGFβ1 for three days were analyzed by WB with indicated antibodies. GAPDH served as loading control. In parts taken from a manuscript (Seiwert *et al.*) in consideration.

8.4 Paper I – Tissue distribution and subcellular localization of the family of Kidney Ankyrin Repeat Domain (KANK) proteins

Published in Experimental Cell Research, Volume 398, Issue 1 (2021).

doi: 10.1016/j.yexcr.2020.112391.

Shiny Shengzhen Guo^{*}, Andrea Seiwert, Irene Y.Y. Szeto, and Reinhard Fässler

Max Planck Institute of Biochemistry, Department of Molecular Medicine, Martinsried, Germany



Tissue distribution and subcellular localization of the family of Kidney Ankyrin Repeat Domain (KANK) proteins

Shiny Shengzhen Guo^{*}, Andrea Seiwert, Irene Y.Y. Szeto, Reinhard Fässler

Department of Molecular Medicine, Max Planck Institute of Biochemistry, Martinsried, Germany

ARTICLE INFO

Keywords:

KANK
Expression
Mouse
Human
Western blot
Immunostaining

ABSTRACT

Kidney Ankyrin Repeat-containing Proteins (KANKs) comprise a family of four evolutionary conserved proteins (KANK1 to 4) that localize to the belt of mature focal adhesions (FAs) where they regulate integrin-mediated adhesion, actomyosin contractility, and link FAs to the cortical microtubule stabilization complex (CMSC). The human KANK proteins were first identified in kidney and have been associated with kidney cancer and nephrotic syndrome. Here, we report the distributions and subcellular localizations of the four *Kank* mRNAs and proteins in mouse tissues. We found that the KANK family members display distinct and rarely overlapping expression patterns. Whereas KANK1 is expressed at the basal side of epithelial cells of all tissues tested, KANK2 expression is mainly observed at the plasma membrane and/or cytoplasm of mesenchymal cells and KANK3 exclusively in vascular and lymphatic endothelial cells. KANK4 shows the least widespread expression pattern and when present, overlaps with KANK2 in contractile cells, such as smooth muscle cells and pericytes. Our findings show that KANKs are widely expressed in a cell type-specific manner, which suggests that they have cell- and tissue-specific functions.

1. Introduction

Kidney Ankyrin Repeat-containing protein (KANK1 or ANKRD15) was originally identified as a growth suppressor in human renal cell carcinoma (RCC) [1]. *In silico* analyses subsequently identified three additional KANK proteins (KANK2-4) in vertebrates [2] and one ortholog in *Drosophila melanogaster* (dKank) and *Caenorhabditis elegans* (VAB-19), respectively [3,4]. The KANK proteins consist of a unique and conserved KANK-N-terminal (KN) motif, variable numbers of central coiled-coil domains and five C-terminal ankyrin repeats (ANKs) [3].

Genetic studies of the KANK family members have re-enforced the notion that they play prominent roles in kidney physiology and disease. Besides mutations in human *KANK1* promoting growth in RCC [1,5,6], recessive mutations in human *KANK1*, *KANK2* and *KANK4* were linked to nephrotic syndrome (NS) [7]. Furthermore, *KANK1* has been associated with neurodegenerative disease, such as cerebral palsy and spastic quadriplegic 2 (CPSQ2) [8]. Disruption of the *Kank2* gene in zebrafish leads to NS-like defects [7] and *in vivo* depletion of *dKank* in nephrocytes of *Drosophila melanogaster* results in the disruption of a highly specialized filtration structure that share notable similarities with the slit diaphragm of mammalian glomerular podocytes [7,9]. In *Caenorhabditis*

elegans, loss of the *Kank* ortholog *VAB-19* causes multiple abnormalities including epidermal detachment, defective axon outgrowth and the formation of gaps in basement membrane during vulva development [10–12]. Altogether, these observations point to a broad involvement of KANKs in development.

Studies with cultured cell lines revealed that KANK1-4 bind to and activate the integrin-binding and activating adaptor protein Talin, diminish actin stress fiber formation by inhibiting GEF-H1 release from microtubules (MTs), and curb integrin mechanotransduction by blocking actomyosin attachment to Talin [13–15]. Interestingly, fibroblasts and HeLa cells do not recruit KANK1-4 to nascent adhesions (NAs) but to the outer border or belt of focal adhesions (FAs) as well as to central fibrillar adhesions (FBs) [13,15]. The FA belt-localized KANK proteins directly bind to Liprin- β and KIF21 α and thereby link FAs to the cortical microtubule stabilization complex (CMSC), which regulates exocytosis of cargo such as MT1-MMP in the vicinity of FAs [13,15–18]. It was also reported that KANK1 binds to the insulin receptor substrate (IRS) p53, which in turn prevents association of IRSp53 with GTP-loaded Rac, activation of Arp2/3, and lamellipodia formation [19,20]. The human KANK2 was also shown to regulate steroid receptor-mediated gene transcription by binding and sequestering steroid receptor coactivators

^{*} Corresponding author.

E-mail address: shguo@biochem.mpg.de (S.S. Guo).

<https://doi.org/10.1016/j.yexcr.2020.112391>

Received 9 October 2020; Received in revised form 16 November 2020; Accepted 19 November 2020

Available online 28 November 2020

0014-4827/© 2020 Elsevier Inc. All rights reserved.

in the cytoplasm [21]. Mutation that disrupts this function affects skin and hair morphogenesis, hinting at *KANK2* as a candidate gene for palmoplantar keratoderma and wooly hair in humans [22].

The pleiotropic effects of KANK family members indicate intricate expression patterns. The aim of the present paper was to generate specific anti-KANK antibodies and to determine the expression patterns of KANK proteins in mouse tissues at the protein and mRNA levels. The specificity of the antibodies was controlled with tissue sections from KANK-null mice whose phenotypes will be reported elsewhere. The results of our experiments revealed that KANK1 is expressed in epithelial cells, while KANK2 is mainly found in mesenchymal cells. KANK3 is exclusively expressed in endothelial cells of blood and lymphatic vessels, and KANK4 only in few tissues, often co-expressed with KANK2.

2. Results

2.1. mRNA and protein expression of the KANK family in mouse tissues

The tissue distributions of the murine *Kank* mRNA expression was analyzed by qRT-PCR in indicated tissues of 8-week old mice (Fig. 1A). Primer pairs for each *Kank* gene flanking short introns were designed to ensure amplification of mRNA. The experiments revealed that *Kank1* is highly expressed in lung, skin and testis, slightly lower in adipose tissue, heart, kidney, ovary and stomach, and weakly in brain, liver and pancreas. *Kank2* was also expressed in most tissues examined, with the highest levels in lung, intermediate levels in adipose tissue, heart and testis, and lower levels in brain, kidney, liver, ovary, pancreas, skin and stomach. *Kank3* and *Kank4* displayed a restricted expression pattern with strong signals in lung, pancreas and testis.

To investigate protein expression, we synthesized peptides specific for each KANK protein, coupled them to a carrier protein and immunized rabbits. The specificity of the polyclonal antiserum was confirmed by Western blot experiments using a recently established mouse kidney fibroblast (MKF) cell line that exclusively expresses KANK2 [15]. As shown in Fig. 1B, the anti-KANK2 antibodies detected a protein of around 120 kDa in lysates of scrambled shRNA treated MKF cells, which was absent upon stable expression of a specific *Kank2* shRNA. To confirm the specificities of the other anti-KANK antibodies, a cDNA encoding the respective mouse *Kank* was expressed in *Kank2*-depleted MKF cells followed by Western blot analyses. The experiments revealed that our homemade antibodies recognized specific protein bands produced by each *Kank* cDNAs in the corresponding lysates with molecular weights of ~200 kDa for KANK1, ~100 kDa for KANK3, and ~150 kDa for KANK4.

Next, we determined the protein expression in lysates from different mouse tissues (Fig. 1C). In line with the qRT-PCR results, we found that all four KANK family members are highly expressed in lung. KANK2 protein is more widely expressed when compared to KANK1, 3 and 4. Interestingly, KANK1 and KANK3 are produced in at least two different molecular weights in pancreas, heart and muscle. Despite the high protein level in lung, KANK4 expression is low in most other tissues. Altogether these findings indicate that the four KANK family members are found in all tissues tested, albeit with variable levels. Since whole tissue lysates were analyzed in both qRT-PCR and Western blot studies, we next perform immunofluorescence on representative tissues to pinpoint in which cell-types the KANK family members can be found.

2.2. Expression of KANK proteins in mouse kidney

In humans, *KANK1* mutations have been linked to RCC [1] and missense mutations in *KANK1*, *KANK2* and *KANK4* with nephrotic syndrome [7]. In line with a potential role in kidney, we found that KANK1-4 are expressed in kidney glomeruli (Fig. 2). KANK1 and KANK2 co-localize with Synaptopodin (SYNPO) in podocyte foot processes and are absent in PECAM⁺ endothelial cells (Fig. 2A-B, and Fig. S1B). KANK1 is additionally produced by the surrounding tubular epithelial cells

where the protein is located at the plasma membrane (Fig. S1A). KANK2 and KANK4 are co-expressed throughout the cytoplasm of PDGFRβ⁺ mesangial cells and along the plasma membrane as well as in the cytoplasm of PDGFRβ⁺ pericytes surrounding the blood vessels, respectively (Fig. 2B1–B2, 2D, and Fig. S1C). Interestingly, KANK4 is absent in podocytes (data not shown), which express both KANK1 and KANK2 in their foot processes. KANK3 is expressed in PECAM⁺ endothelial cells at the membrane and is absent in both podocytes and mesangial cells (Fig. 2C, and data not shown). The specificity of the signals was corroborated by staining tissue sections of kidneys from nullizygous mice (Fig. S2).

Altogether these expression data demonstrate that the KANK family members show distinct as well as partly overlapping expression patterns in kidney, indicating that mutations of the different KANK genes can indeed lead to kidney pathology.

2.3. Localization of KANKs in podocyte-like cells cultured in vitro

Since KANK1 and KANK2 are highly expressed in podocyte foot processes and are associated with nephrotic syndrome in humans, we decided to investigate the subcellular distributions of KANKs in mouse podocyte-like cells [23]. Laminin (LN) expression changes dynamically from LN111 to LN511 and finally to LN521 during glomerulogenesis in the glomerular basement membrane [24]. Podocytes are one of the major cell types secreting these LNs into the basement membrane. Interestingly, when the podocyte-like cells were seeded on LN511-coated surface, they assembled Paxillin⁺ ring-shaped podosomes in the cell center and FAs in their periphery. KANK1 was readily detected in the podosome rings and weakly in peripheral FAs (Fig. 3A). However, when the podocyte-like cells were seeded on LN111-coated surface, they fail to form podosomes, and instead only assemble FAs. Interestingly, podocytes seeded on LN111 distribute KANK1 in close vicinity of FAs, which likely represents CMSCs (Fig. 3C). Since LN521 was not available to us neither adhesion site formation nor KANK1 distribution on LN521 could be investigated.

KANK2, on the other hand, is weakly present in some podosomes of LN511-seeded cells (Fig. 3B) and accumulates, similarly like in fibroblasts seeded on FN [15], in the belt of peripheral FAs and in central adhesion of LN111-seeded podocytes (Fig. 3D). Consistent with the immunostaining of kidney sections (Fig. 2), neither KANK3 nor KANK4 are expressed in the podocyte-like cells. The specificities of the immunosignals were confirmed by blocking the antibodies with peptides used to generate the KANK antisera (data not shown).

2.4. KANK distributions in mouse lung and skin

In the lung we also observed expression of all KANK family members in a cell type-specific manner. KANK1 is expressed at the basal side of bronchial epithelial cells and is absent in type I (T1α⁺) and type II (TTF1⁺) alveolar epithelial cells (Fig. 4A), which express KANK2 at the plasma membrane (Fig. 4B and C; white arrowheads for T1α and yellow arrowheads for TTF1 positivity, respectively). KANK2 is also enriched at the plasma membrane of smooth muscle cells that line PECAM⁺ endothelial cells of large and small vessels (Fig. 4D; arrow and asterisk). PECAM⁺ endothelial cells only express KANK3, which is absent from all other cell types in lung (Fig. 4E, arrowheads). KANK4 is not expressed in epithelial cells but shares the expression with KANK2 at the plasma membrane of pericytes in capillaries (Fig. 4F).

In the epidermis of the mouse skin, KANK1 is enriched at the plasma membrane of basal and present throughout the cytoplasm of suprabasal keratinocytes (Fig. 5A; arrowhead and arrow). A similar expression pattern is observed in the hair follicles (Fig. 5A, asterisk). Epidermal and hair follicle keratinocytes lack expression of the other KANK family members (Fig. 5B and C, and data not shown). KANK2 is expressed along the plasma membrane of dermal fibroblasts (Fig. 5B1, arrowhead), pericytes surrounding the capillaries (Fig. 5B1, arrow), and Vimentin⁺

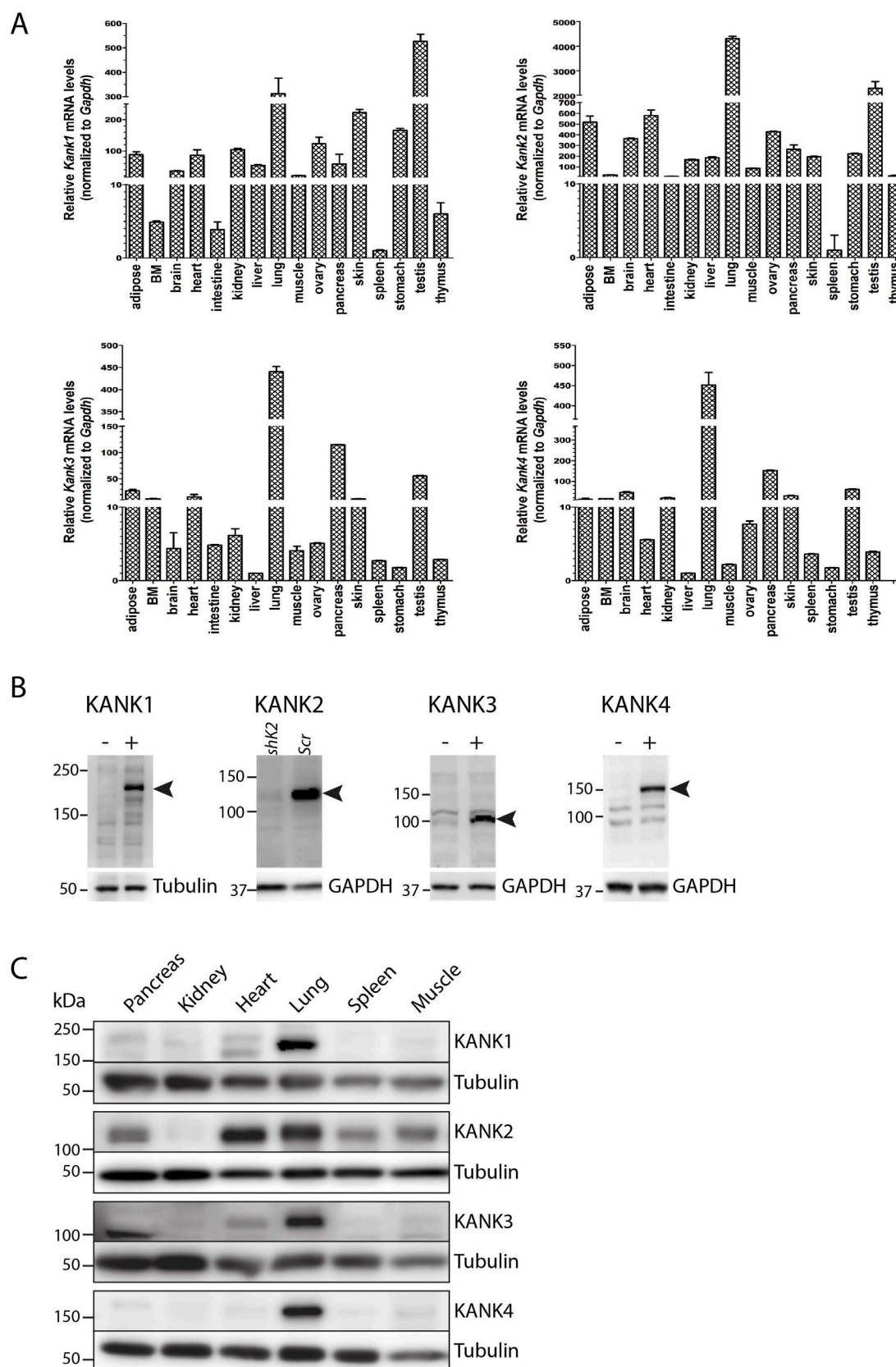


Fig. 1. Tissue distributions of *Kank1-4* mRNAs and proteins. (A) Total RNA from 8-week-old C57/BL6 mice examined by qRT-PCR. Expression levels were first normalized to *Gapdh* levels and then plotted relative to the expression level of tissue with the lowest expression level, which was spleen in the *Kank1* and *Kank2* analyses, and liver in the *Kank3* and *Kank4* analyses. BM: bone marrow. (B) Characterization of homemade rabbit anti-mouse KANK1-4 antibody specificities using mouse kidney fibroblasts expressing *Kank2*. Stable shRNA-mediated *Kank2* depletion (*shK2*) served as negative control for the KANK2 antibody. *Scr*: scramble shRNA control. Transient transfections of *Kank1*, *Kank3* and *Kank4* cDNAs (+) were used to probe antibody specificities for KANK1, 3 and 4. Arrowheads indicate the specific bands. (C) Western blot of mouse tissue lysates from adult C57/BL6 mice probed with homemade rabbit anti-mouse KANK1, 2, 3 and 4 antibodies.

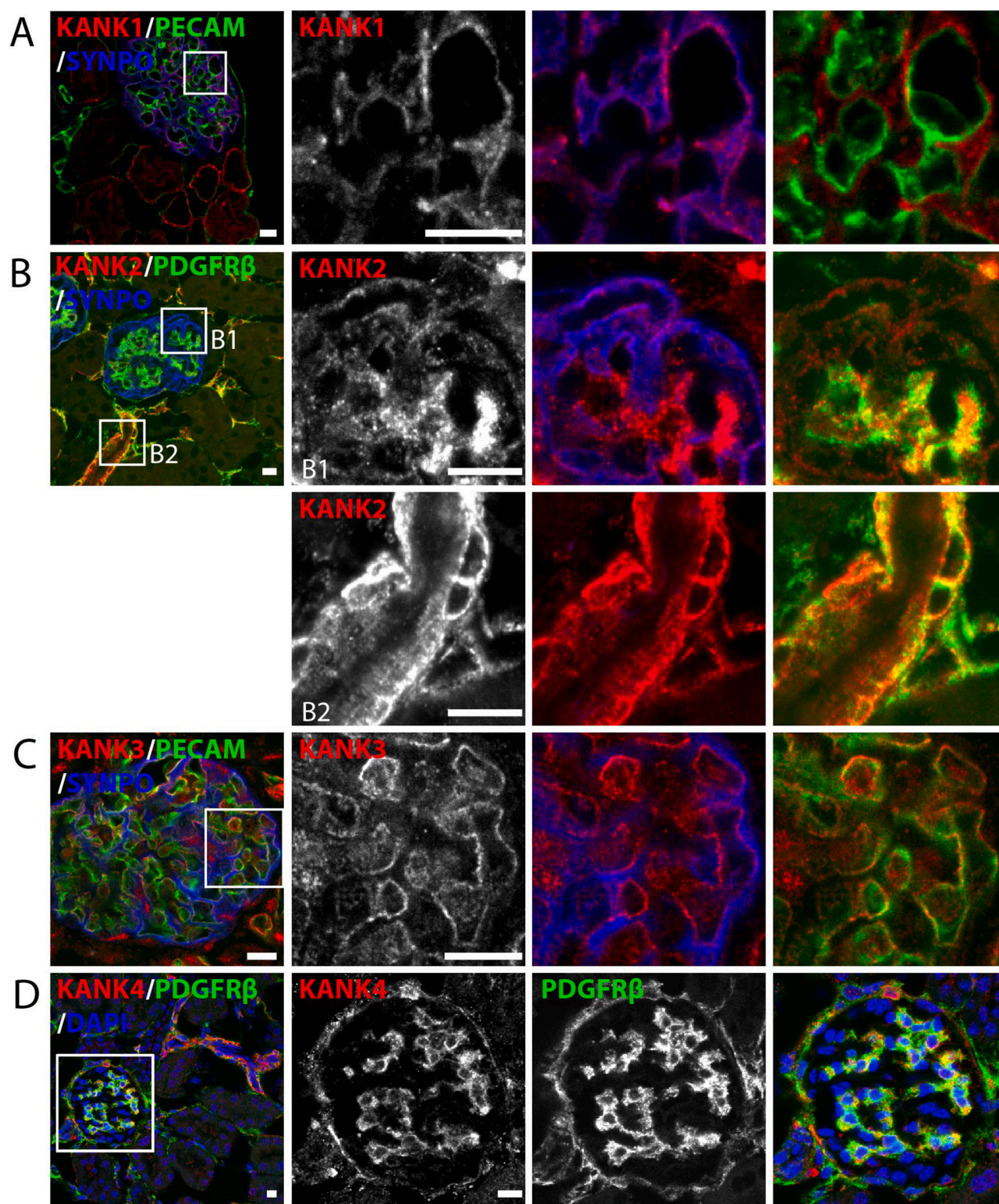


Fig. 2. KANK1-4 expression in mouse kidney. KANKs are shown in red, Synaptopodin (SYNPO)⁺ podocytes in blue, PDGFRβ⁺ mesangial cells and PECAM⁺ endothelial cells in green. Nuclei are counterstained with DAPI. (A) KANK1 is expressed in SYNPO⁺ glomerular podocytes. (B) KANK2 is expressed in SYNPO⁺ podocytes and PDGFRβ⁺ mesangial cells of glomeruli (B1) and in PDGFRβ⁺ pericytes surrounding arteries (B2). (C) KANK3 is exclusively present in PECAM⁺ endothelial cells of glomeruli. (D) KANK4 is expressed in PDGFRβ⁺ glomerular mesangial cells. Scale bars: 10 μm. (For interpretation of the references to colour in this figure legend, the reader is referred to the Web version of this article.)

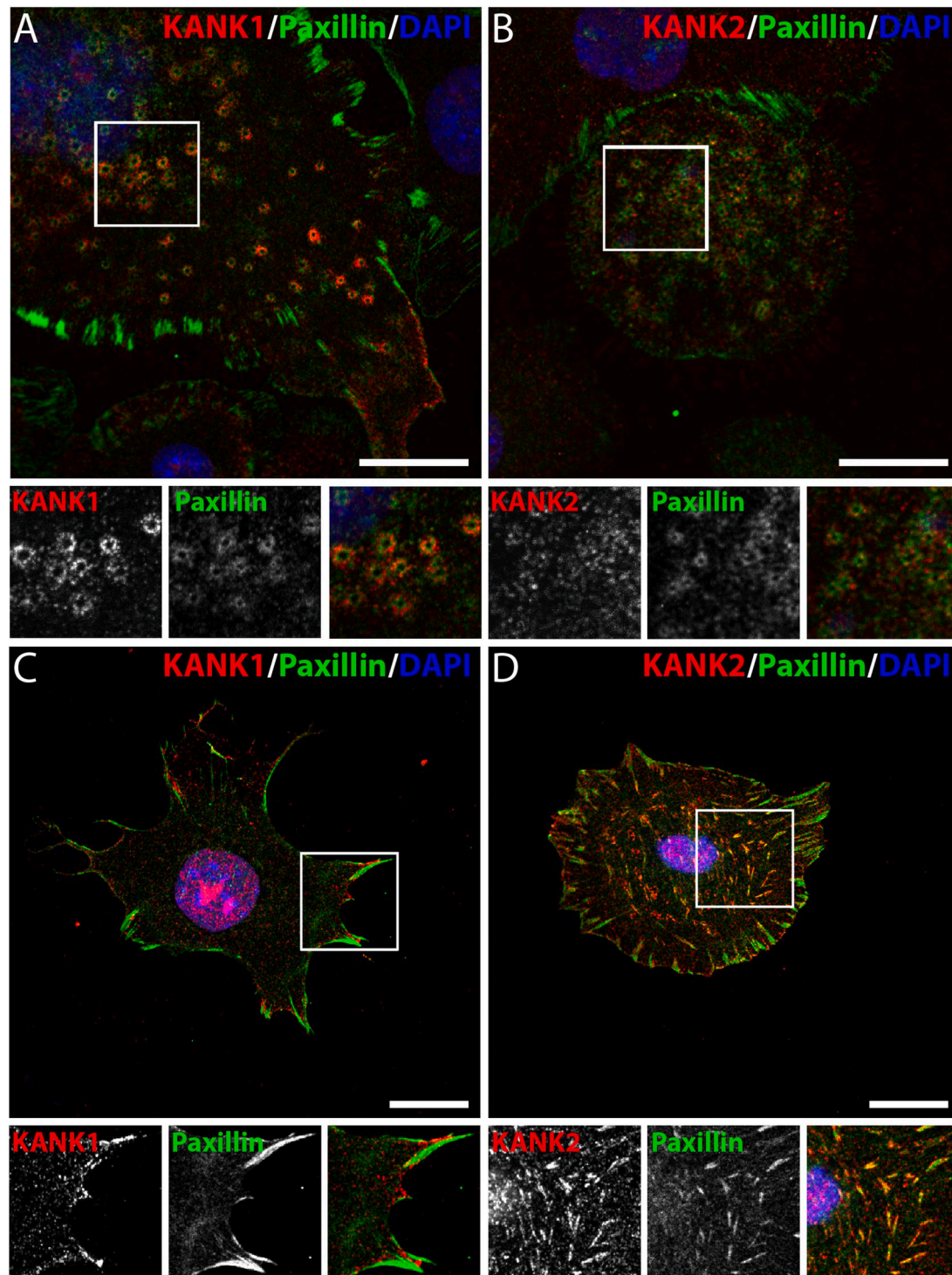


Fig. 3. Subcellular localization of KANK1 and 2 in mouse podocyte-like cells. KANK1 and 2 are shown in red and Paxillin⁺ podosomes and focal adhesions in green. Nuclei are counterstained with DAPI. (A, B) Podocytes cultured on LN511 show strong KANK1 (A) and weak KANK2 (B) expression in the outer ring of Paxillin⁺ podosomes. (C, D) Podocytes cultured on LN111 display KANK1 in the vicinity of Paxillin⁺ FAs (C) and KANK2 in the belt of FAs and fibrillar adhesions (D). Scale bars: 20 μ m. (For interpretation of the references to colour in this figure legend, the reader is referred to the Web version of this article.)

cells surrounding the hair follicles (Fig. 5B2). KANK3 is exclusively expressed at the plasma membrane of PECAM⁺ endothelial cells of dermal vessels (Fig. 5C), and KANK4 expression is barely detectable in mouse skin (data not shown).

2.5. KANK expression in mouse brain

In the brain parenchyma of adult mice, we only observed expression of KANK1 in GFAP⁺ astrocytes within the medulla oblongata (Fig. 6A), while no specific signals for KANK1 could be found in the cortex, midbrain and cerebellum. KANKs are absent in the foot process of astrocytes adjacent to the brain capillaries, whereas KANK2 is found in

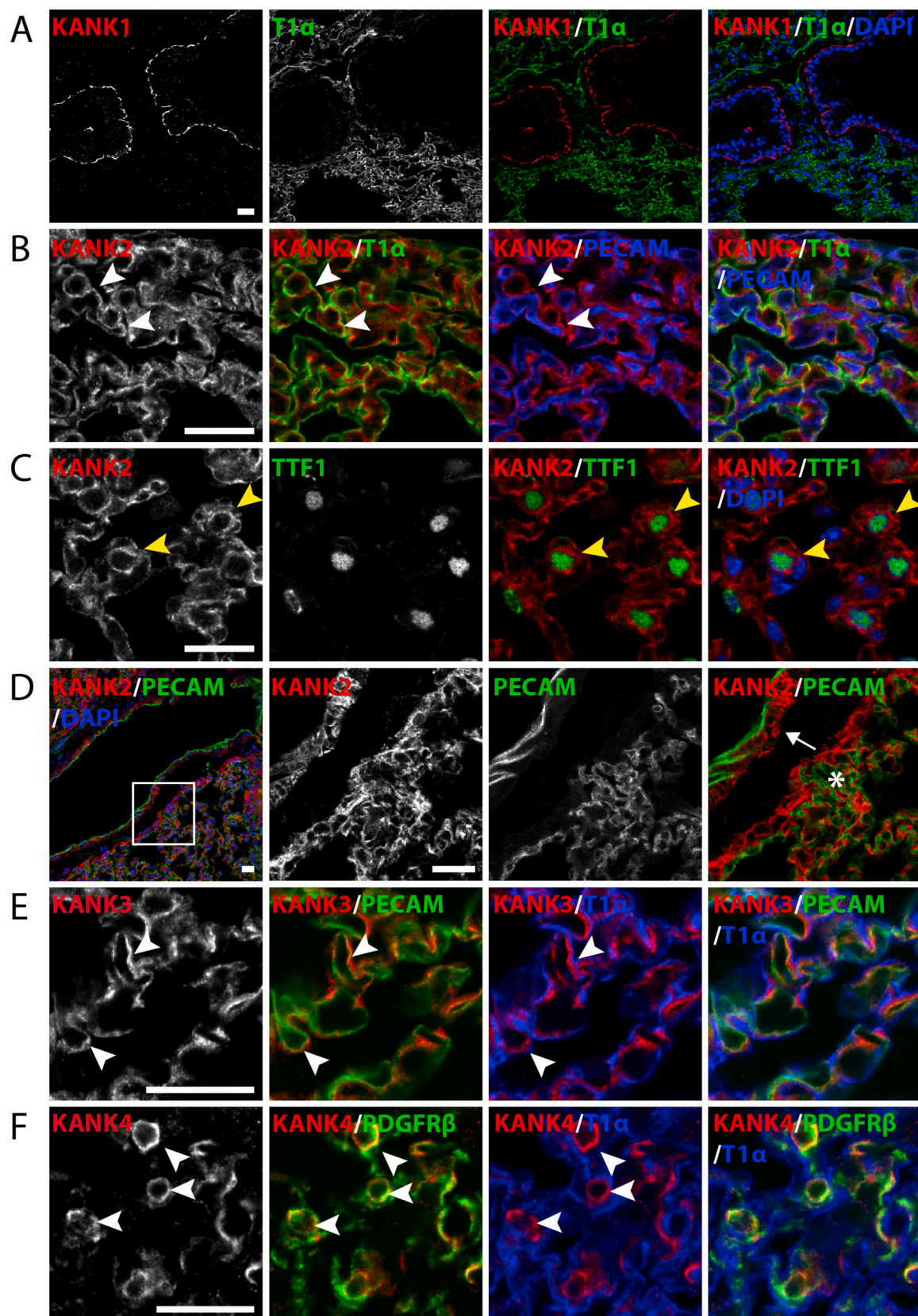


Fig. 4. KANK1-4 expression in mouse lung. KANKs are shown in red, T1 α ⁺ type I alveolar cells in green or blue, TTF1⁺ type II alveolar cells in green, PECAM⁺ endothelial cells in green or blue, and PDGFR β ⁺ pericytes in green. Nuclei are counterstained with DAPI. (A) KANK1 is present at the basal side of bronchial epithelial cells and is absent in alveolar cells. (B–D) KANK2 is found in type I alveolar cells (B; white arrowheads), type II alveolar cells (C; yellow arrowheads) and smooth muscle cells surrounding PECAM⁺ endothelial blood vessels (D; arrow). The asterisk (D) indicates capillaries decorated by KANK2 expressing pericytes. (E) KANK3 is only expressed in PECAM⁺ endothelial cells (arrowheads). (F) KANK4 staining is overlapping with PDGFR β signals, but absent in T1 α ⁺ cells (arrowheads). Scale bars: 20 μ m. (For interpretation of the references to colour in this figure legend, the reader is referred to the Web version of this article.)

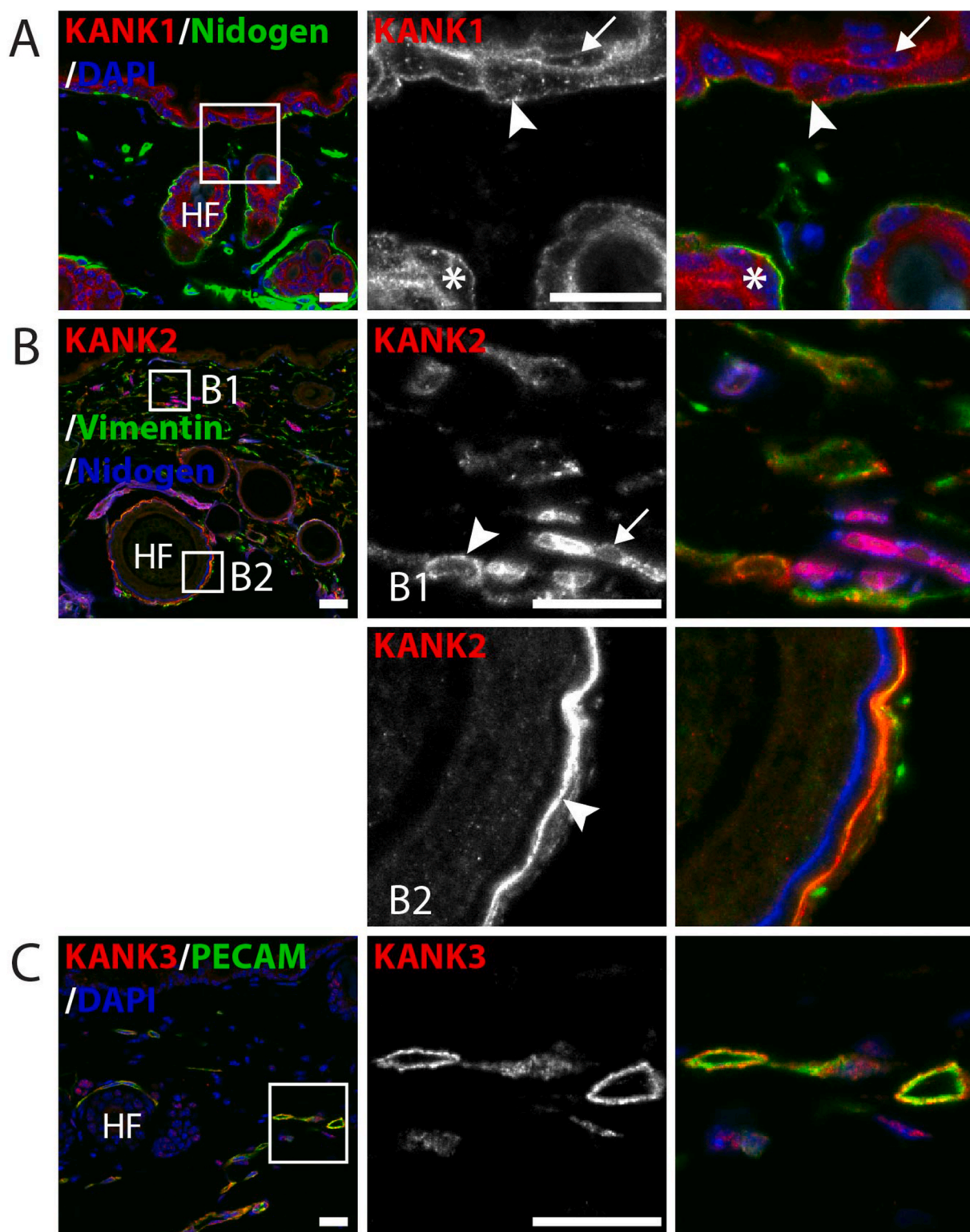


Fig. 5. KANK1-3 expression in mouse skin. KANKs are shown in red, PECAM⁺ endothelial cells and Vimentin⁺ fibroblasts in green, and Nidogen⁺ basement membranes in green or blue. Nuclei are counterstained with DAPI. (A) KANK1 is expressed in basal (arrowhead) and suprabasal keratinocytes (arrow). The asterisk indicates KANK1 expression in hair follicles. (B) KANK2 is present in Vimentin⁺ dermal fibroblasts (B1, arrowhead), pericytes surrounding capillaries (B1, arrow), and Vimentin⁺ fibroblasts surrounding hair follicles (B2, arrowhead). (C) KANK3 is restricted to PECAM⁺ endothelial cells. HF, hair follicle. Scale bars: 20 μ m. (For interpretation of the references to colour in this figure legend, the reader is referred to the Web version of this article.)

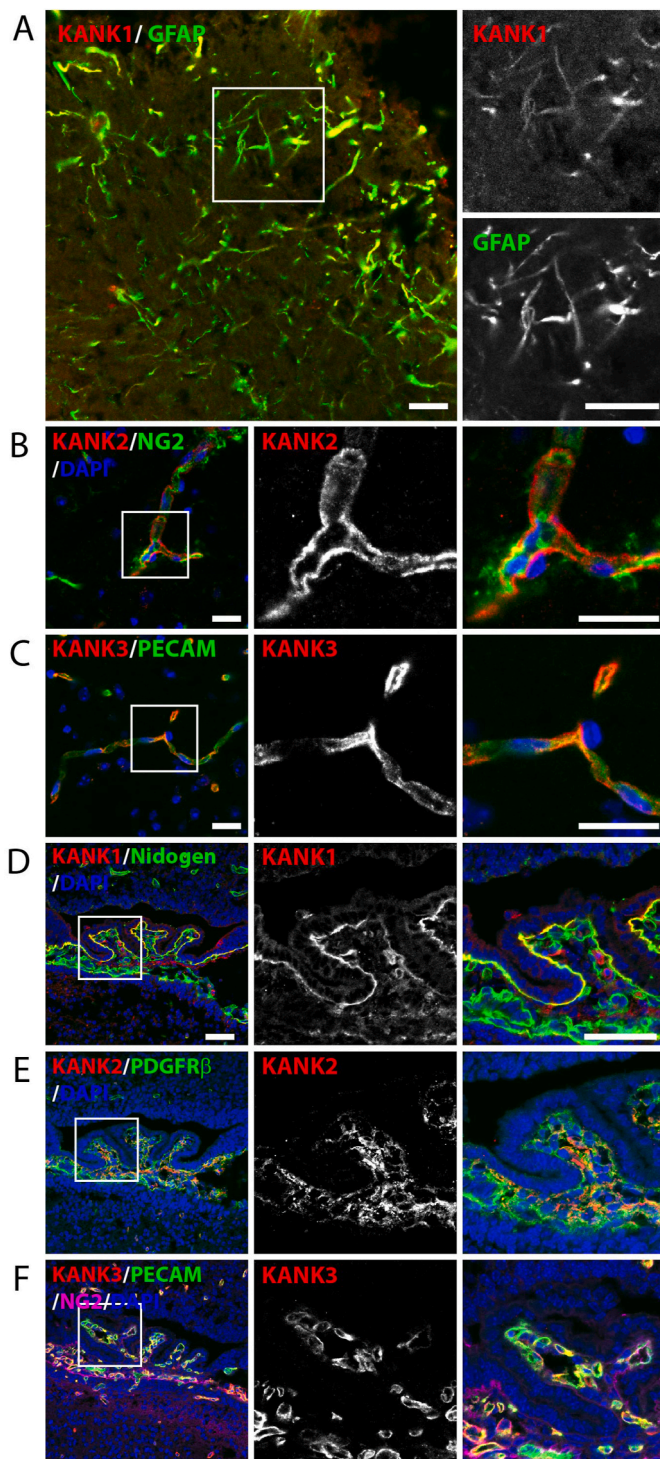


Fig. 6. KANK1-3 expression in murine brain. KANKs are shown in red and GFAP⁺ astrocytes, NG2⁺ pericytes, PECAM⁺ endothelial cells, Nidogen⁺ basement membrane and PDGFRβ⁺ stromal cells in green. Nuclei are counterstained with DAPI. (A) KANK1 is detected in GFAP⁺ astrocytes of the medulla oblongata. (B) KANK2 is expressed in pericytes surrounding PECAM⁺ endothelial cells. (C) KANK3 expression is restricted to PECAM⁺ endothelial cells. (D) KANK1 is detected at the basal side of ependymal cells of ED14.5 telencephalic choroid plexus. (E) KANK2 is detected in PDGFRβ⁺ stromal cells, and (F) KANK3 in PECAM⁺ endothelial cells of the ED14.5 choroid plexus. Scale bars: 20 μm. (For interpretation of the references to colour in this figure legend, the reader is referred to the Web version of this article.)

NG2⁺ pericytes (Fig. 6B) and KANK3 in PECAM⁺ endothelial cells of these capillaries (Fig. 6C). KANK4 was not detected in the brain (data not shown).

KANK1 has been linked to cerebral palsy and spastic quadriplegic 2 (CPSQ2) where brain atrophy and ventriculomegaly had been observed by neuroimaging [8]. Ventriculomegaly can result from abnormal absorption and/or production of cerebrospinal fluid by the choroid plexus (ChP). Interestingly, in the brain harvested at embryonic day (ED) 14.5, KANK1 localizes to the basal side of ependymal cells (epithelial cells) of the ChP, while KANK2 and KANK3 are present in the stromal and endothelial cells of the ChP core, respectively (Fig. 6D–F). KANK4 was not detected. In the telencephalic ChP of the adult brain, KANK1 is absent from ependymal cells, while KANK2 and KANK3 remain expressed in NG2⁺ pericytes and PECAM⁺ endothelial cells, respectively (data not shown).

2.6. Expression of KANKs in the mouse vasculature

Similarly like in kidney, lung, brain and all other organs analyzed so far, in the aorta, KANK2 is also strongly expressed throughout the cytoplasm of αSMA⁺ muscle cells of the tunica media layer (Fig. 7A) and KANK3 in PECAM⁺ endothelial cells (Fig. 7B). KANK1 as well as KANK4 are absent in cells of the aorta (data not shown).

In the mouse retina, KANK2 is expressed in the PDGFRβ⁺ pericytes (Fig. 7C, arrows) but not in the endothelial cells (Fig. S3A, arrowheads). KANK3, in contrast, is present in PECAM⁺ endothelial cells of the vascular tube as well as in sprouting tip cells (Fig. 7D, arrowheads indicating sprouting cells) and absent from PDGFRβ⁺ pericytes (Fig. S3B, arrows).

Finally, we stained tissue sections of spleen to test whether KANK3 is expressed in lymphatic in addition to blood endothelial cells. KANK3 is found at the plasma membrane of VEGFR3⁺ lymphatic endothelial cells (Fig. 7E).

2.7. KANK protein distributions in mouse esophagus

Since KANK4 is found in contractile mesangial cells (kidney) but absent from vascular NG2⁺ pericytes (brain) and αSMA⁺ muscle cells (aorta), we decided to investigate the distribution of KANK proteins in the esophagus which consist of a stratified layer of epithelial cells that is surrounded by a thick layer of smooth muscle cells. Cross-sections revealed that KANK1 is enriched at the basal side and in the cytoplasm of the stratified squamous epithelial cell layers (Fig. 8A, arrowhead indicating the basal side). KANK1 is absent in αSMA⁺ smooth muscle cells, which strongly express KANK2 in the cytoplasm and along the entire plasma membrane (Fig. 8B). KANK3 was found in PECAM⁺ endothelial cells (Fig. 8C, arrowheads) and KANK4 was not expressed in the smooth muscle cells of the esophagus (Fig. 8D, asterisk indicating non-specific signals), indicating that KANK4 expression is restricted to a very limited population of contractile cells.

3. Discussion

The KANK protein family consists of 4 members and was initially linked to nephrotic syndrome and kidney cancer [1,6]. In the present paper, we report the generation of specific, polyclonal peptide antisera against mouse KANK1, 2, 3 and 4, which we used to determine their expression pattern in mouse tissues. The antibodies produced KANK isoform-specific signals on Western blots, and moreover, revealed a cell type-specific expression pattern in PFA-fixed mouse tissue sections.

Our immunostaining demonstrated KANK1 expression in epithelial cells of all organs that were tested in this study. KANK1 localized to the basal side of basal keratinocytes, bronchial and esophageal epithelial cells, and around the entire plasma membrane and in the cytoplasm of suprabasal cells of the epidermis and esophagus. This staining pattern indicates that in some tissues KANK1 localizes to integrin adhesion sites

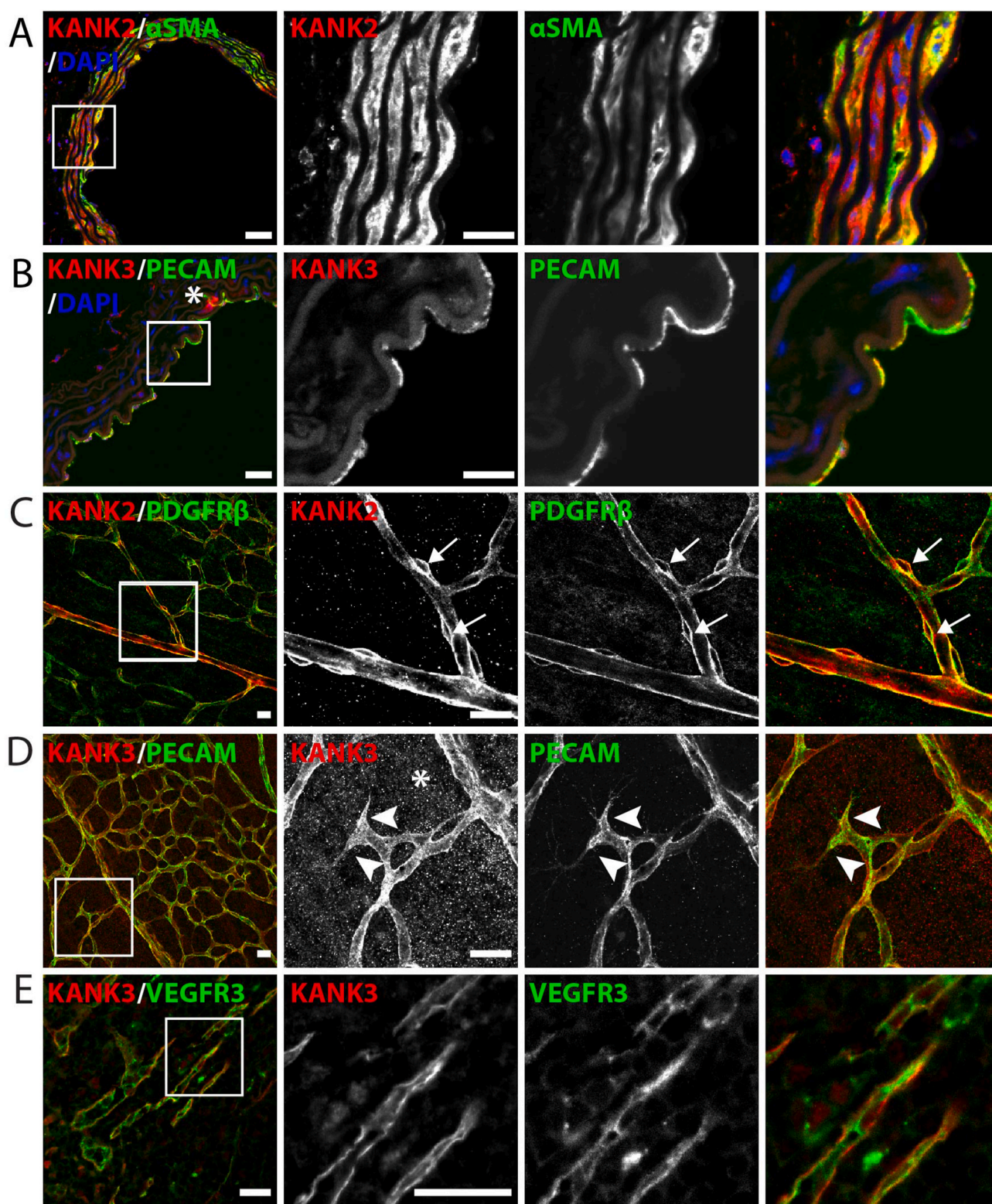


Fig. 7. KANK2 and 3 expression in murine vasculature. KANKs signals are shown in red, α SMA⁺ smooth muscle cells, PECAM⁺ endothelial cells, PDGFR β ⁺ pericytes, and VEGFR3⁺ lymphatic endothelial cells in green. Nuclei are counterstained with DAPI. (A–B) KANKs expression in aorta. KANK2 is highly expressed in α SMA⁺ smooth muscle cells (A) and KANK3 expression is restricted to PECAM⁺ endothelial cells (B). (C–E) KANKs expression in retina and spleen. (C) showing KANK2 expression in adjacent PDGFR β ⁺ pericytes, (D) showing KANK3 staining in PECAM⁺ endothelial cells of the vascular tube and in tip cells indicated with arrowheads, and (E) showing KANK3 is also expressed in VEGFR3⁺ lymphatic endothelial cells of the spleen. Asterisks in (B) and (D) indicate non-specific antibody signals. Scale bars: 20 μ m. (For interpretation of the references to colour in this figure legend, the reader is referred to the Web version of this article.)

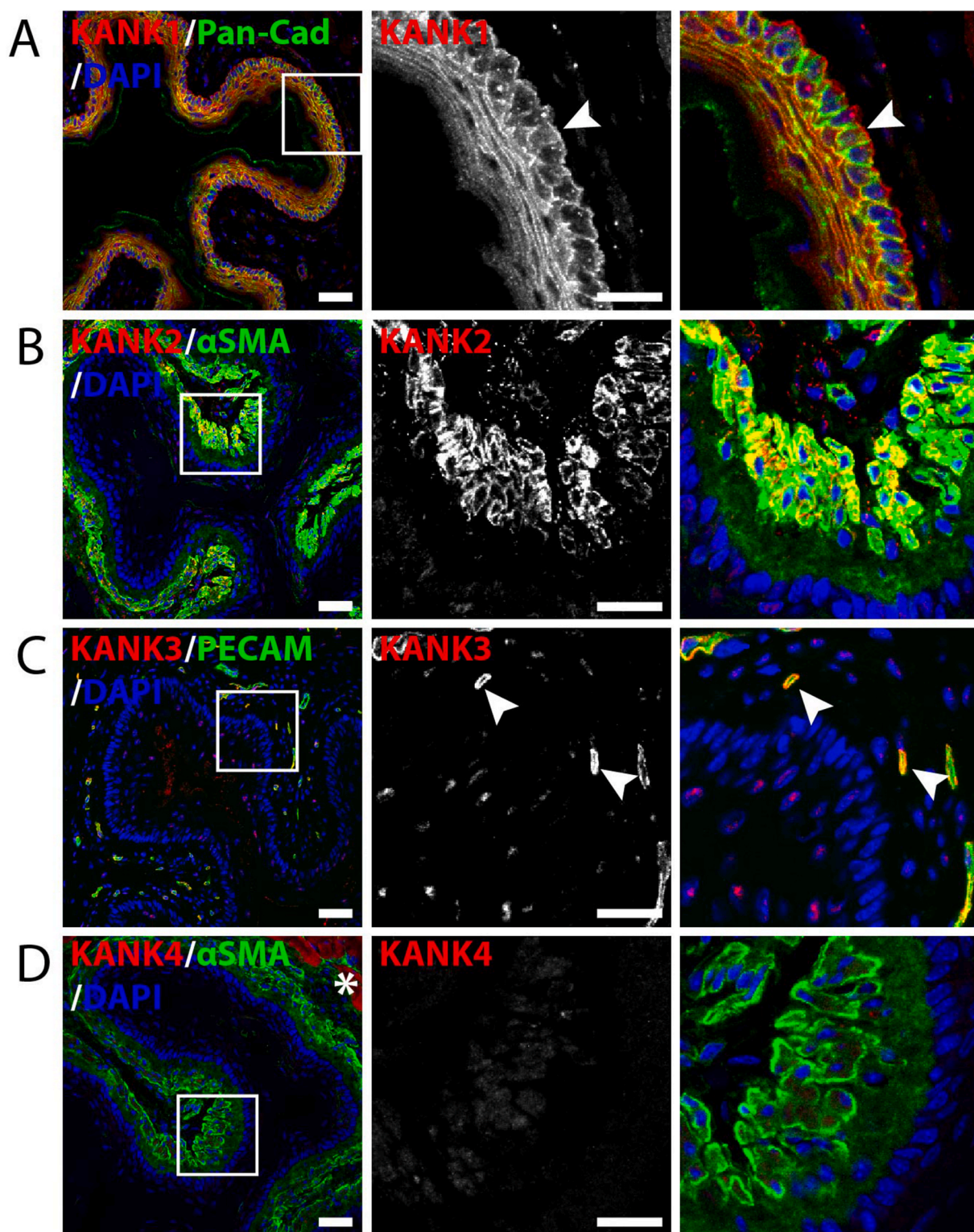


Fig. 8. KANK1-4 expression in mouse esophagus. KANKs are shown in red and α SMA⁺ smooth muscle cells, pan-Cadherin (pan-Cad)⁺ epithelial cells and PECAM⁺ endothelial cells in green. Nuclei are counterstained with DAPI. (A) KANK1 expression is restricted to the stratified squamous epithelial cell layers. KANK1 is enriched at the basal side of the basal epithelial cell layer (arrowhead) and diffusely distributed in the cytoplasm of suprabasal cells. (B) KANK2 is strongly expressed in α SMA⁺ smooth muscle cells. (C) KANK3 is exclusively expressed in PECAM⁺ endothelial cells (arrowheads), and (D) KANK4 is not expressed in esophagus tissue. The asterisk marks non-specific antibody signals. Scale bars: 20 μ m. (For interpretation of the references to colour in this figure legend, the reader is referred to the Web version of this article.)

at basal plasma membrane domains and in other tissues KANK1 expression extends to basolateral and apical plasma membrane domains. KANK2 was mainly found in mesenchymal cells including mesangial cells in kidney glomeruli (throughout the cytoplasm), pericytes, tissue fibroblasts (at the plasma membrane) and vascular smooth muscle cells (at the plasma membrane and in the cytoplasm). Notable exceptions were alveolar cells of the lung and podocytes of kidney glomeruli, in which KANK2 is strongly expressed along the plasma membrane. KANK3 is expressed in all tissues analyzed where it was exclusively found in endothelial cells of blood and lymphatic vessels. KANK4 expression is restricted to mesenchymal cells of few tissues including lung and kidney. In kidney, KANK4 co-localizes with KANK2 in the cytoplasm of mesangial cells and vascular pericytes. Mutations in KANK1, KANK2 and KANK4 were shown to cause nephrotic syndrome in humans [1]. Although our immunostaining supports this notion, the cell type-specific expression of the KANKs hints at specific functions that, when lost, may lead to distinct kidney pathologies.

Our experiments also revealed a substrate-dependent distribution of KANK1 and KANK2 in podocyte-like cells. This is of interest, as podocytes express and deposit different laminins in a highly dynamic manner during glomerulogenesis: the first LN deposited into glomerular basement membranes is LN111, which is then replaced by LN511, which in turn is finally substituted by LN521 [24]. Mouse podocyte cells (established by Nicolaou et al., 2012 [23]) seeded on LN111 assembled numerous peripheral and central FAs, which accumulated KANK2 along the FA belt [15] and KANK1 in CMSCs that are in close vicinity of FAs [13,15]. Interestingly, podocyte cells cultured on LN511 assembled Paxillin-positive ring-shaped podosomes in the cell center and FAs in the cell periphery. KANK1 and KANK2 are expressed in the podosomal rings, and adjacent to the peripheral FAs. Unfortunately, adhesion site assembly as well as KANK1 and KANK2 distributions in podocytes seeded on LN521 could not be analyzed, as LN521 was not available to us. Nevertheless, our observations strongly indicate that mutations in KANK1 and KANK2, although expressed in the same cell type, probably affect the kidney filtration unit differently and hence, may cause specific subtypes of nephrotic syndromes.

Interestingly, we found no KANKs expressed in neurons. A reason for the absence of KANKs in neurons may be due to the molecular composition of the MT attachment complex at plasma membranes of epithelial cells versus presynaptic membranes of neurons. At sites of exocytosis in epithelial cells, KANK1 is recruited to the CMSC through direct binding to Liprin- β 1. In neurons, exocytosis of neurotransmitters occurs at the active zone (CAZ) of the presynaptic membrane. CAZs share components of CMSC such as ELKS and Liprin- α , however, neither LL5 nor the KANK-binding Liprin- β are found in CAZs [25,26]. The absence of Liprin- β , which recruits KANK1 to the CMSC in epithelial cells, is probably the reason why KANK1 is not required to co-ordinate MT attachment and hence, not needed in neurons. Interestingly, we observed KANK1 expression in GFAP⁺ astrocytes in the medulla oblongata, but not in astrocytes of other brain regions. The reason for this region-specific astrocyte expression of KANK1 is unclear. We also found that KANK proteins are expressed in the ChP: in embryonic ChP, KANK1 is expressed in ependymal cells developed from the neuroepithelium, KANK2 in stromal cells that are derived from the head mesenchyme and KANK3 in endothelial cells. KANK1 expression vanishes in the ChP of adult mice pointing to a specific role of KANK1 in ChP during fetal period.

In summary, KANK proteins show a cell type-specific expression pattern, which rarely overlaps, suggesting their potential specific function(s) during mammalian development, postnatal homeostasis and diseases. To address the *in vivo* function of the KANK proteins, we generated KANK1-4-null mouse strains that are currently analyzed for their loss-of-function phenotypes. These studies will certainly shed light on the functional properties of this new and interesting family of adaptor proteins.

4. Materials and methods

4.1. Tissue sampling

Wild-type (WT) C57BL/6 N mice were obtained from the animal facility at the Max-Planck Institute of Biochemistry, Martinsried, Germany. Mice were bred in a special pathogen-free mouse facility and all animal experiments were conducted in accordance with the protocol approved by the government of Upper Bavaria.

Female KANK1-, KANK2-, KANK3-, KANK4-null and WT littermate mice were euthanized at 4–12 months of age to isolate desired organs. For immunostaining, tissues were fixed in 4% paraformaldehyde (PFA) for 4 h at 4 °C, equilibrated in 30% sucrose overnight at 4 °C, embedded in Cryomatrix (Thermo Scientific, 6769006) and cryosectioned at 7–10 μ m.

4.2. Cell culture

Stable depletion of *Kank2* in the SV40 large T-immortalized mouse kidney-derived fibroblasts (MKF) [15] and the generation of the mouse podocyte-like epithelial cells [23] have been previously described and were used to analyze the specificity of the homemade KANK antibodies and the subcellular localization of KANKs. MKFs were cultured in DMEM (Gibco, 31966–021) supplemented with 10% FBS, Penicillin/Streptomycin (Gibco, 15140–122) and MEM NEAA (Gibco, 11140–35). Mouse podocyte-like cells were cultured in Keratinocyte-SFM medium (Gibco, 10725–018).

4.3. Plasmids and transient transfection

The expression plasmid for each mouse *Kank* was subcloned from pEGFP-N1-KANKs (Sun et al., 2016) into the pcDNA3.1(–) vector. *Kank1* was cloned with restriction sites *Xho*I and *Eco*RI, *Kank3* with *Xba*I and *Eco*RI, and *Kank4* with *Nhe*I and *Xho*I into the pcDNA3.1(–) vector. The plasmids were transfected using LipofectamineTM 2000 Transfection Reagent according to the manufacturer's instructions (Invitrogen, 11668–019).

4.4. Quantitative real time-PCR (qRT-PCR)

Indicated mouse organs were isolated from 8-week old WT mice. Total RNA was extracted with RNeasy Mini extraction kit (Qiagen, 74104) and transcribed into cDNA with the iScript cDNA Synthesis Kit (Biorad, 170–8891). Real time PCR was performed with the Light-Cycler[®]480 Instrument II (Roche). PCR protocol: 5 min. 95 °C; 40 x (15 s 95 °C, 15 s 68 °C (*Kank1*, 2, 4)/15 s 65 °C (*Kank3*)); 15 s 95 °C; 15 s 60 °C; 15 s 95 °C; ∞ 4 °C. Samples were measured in triplicates. *Kank* levels in different tissues were first normalized to *Gapdh* levels and then plotted relative to the expression level of the tissue with the lowest level, which was set to 1. In the *Kank1* and *Kank2* analyses, expression levels of spleen were set to 1, and in the *Kank3* and *Kank4* analyses, expression levels of liver were set to 1. PCR primers are listed in Table S1.

4.5. Antibody production and affinity purification

Specific and unique peptides were synthesized for each KANK protein. Sequences are listed in Table S2. The peptides carried either an N- or C-terminal cysteine residue for coupling with the carrier protein. TiterMax Gold Adjuvant (Sigma, T2684) was used for the first and incomplete Freund's Adjuvant (Sigma, F5506) was used for the subsequent three immunizations of rabbits. Final serum was tested by Western blot and purified with the MelonTM Gel IgG purification Kit (Thermo-fisher, 45212) following manufacturer's instructions.

4.6. Protein isolation and Western blot

Cells were washed once with PBS, lysed with RIPA buffer supplemented with protease inhibitors (Roche, 04693159001) and incubated for 20 min on ice followed by centrifugation for 20 min at maximum speed at 4 °C.

Tissue organs from mice were snap-frozen in liquid nitrogen, homogenized using the Ultra-Turrax T8 disperser (IKA) and lysed with RIPA buffer and further processed as described above.

The cell and tissue lysates were then separated by 10% SDS gel, transferred onto pre-activated PVDF membranes (Immobilon-P, Merck KGaA, IPVH00010). After blocking with 3% BSA in PBST for 1 h at RT, membranes were incubated with the indicated primary antibodies overnight at 4 °C. Anti-mouse or anti-rabbit-HRP secondary antibodies were applied for 1 h at RT and the membranes were developed with Chemiluminescent HRP substrate (Millipore, P90720). The antibody dilutions are listed in Table S3.

4.7. Immunofluorescence

Cryosections were washed with PBS three times and antigen retrieval was performed if necessary. The sections were permeabilized in 0.1% Triton X-100 for 15 min and blocked in PBS supplemented with 3–5% BSA for 2 h at RT. Sections were incubated with primary antibody overnight at 4 °C, washed five times with PBS, incubated with secondary antibody for 2 h at RT, washed five times with PBS and stained with DAPI for 10 min at RT. Finally, sections were mounted with Elvanol. Images were taken on a Zeiss (Jena) LSM780 confocal laser scanning microscope. The antibody dilutions are listed in Table S3.

WT podocyte-like cells were cultured on 4-well chamber slides (ibidi, 80427) coated with either 0.5 µg/cm² laminin iMatrix-511 (LN5111) (Matrixome, 892 012) or 2 µg/cm² mouse laminin LN111 (Invitrogen, 23017–015) for 1 h at 37 °C. The immunofluorescent staining was performed as described above. Staining for KANKs on these cells was controlled by blocking the primary KANK antibody with the peptides used to generate the antiserum (Table S2). Both, the KANK antibodies and the blocking peptides were incubated in a 1:30 ratio for 1 h at RT before applying to the cells.

4.8. Whole mount staining of postnatal retinas

Eyes were isolated from WT mice at postnatal day 7 (P7), fixed in 4% PFA for 2 h on ice. Retinas were dissected, flattened on drops of cold methanol, incubated in blocking solution (PBS supplemented with 0.3% Triton-X-100, 0.2% BSA, 5% goat serum) overnight at 4 °C, incubated with primary antibodies overnight at 4 °C, washed five times with PBS supplemented with 0.3% Triton-X-100 at RT, incubated with secondary antibodies at 4 °C overnight, washed five times with PBS supplemented with 0.3% Triton-X-100 and mounted with Elvanol under the microscope.

CRedit authorship contribution statement

Shiny Shengzhen Guo: Conceptualization, Methodology, Data curation, Investigation, Supervision, Writing - original draft, Writing - review & editing. **Andrea Seiwert:** Methodology, Data curation, Investigation, Writing - review & editing. **Irene Y.Y. Szeto:** Methodology, Data curation, Investigation, Writing - review & editing. **Reinhard Fässler:** Conceptualization, Methodology, Data curation, Investigation, Supervision, Resources, Writing - review & editing, Project administration, Funding acquisition.

Declaration of competing interest

The authors have no affiliation with any organization with a direct or indirect financial interest in the subject matter discussed in the

manuscript.

Acknowledgements

We are grateful to the employees of our animal house. The work was supported by the ERC and Max Planck Society.

Appendix A. Supplementary data

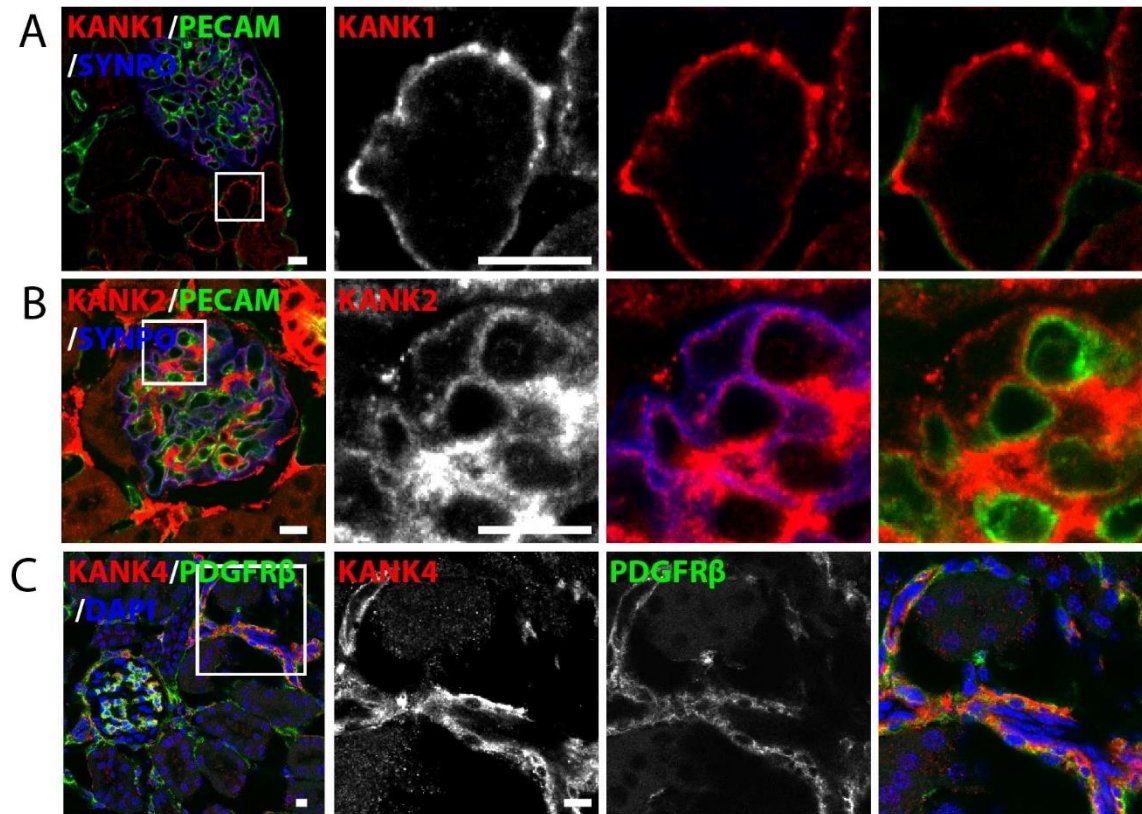
Supplementary data to this article can be found online at <https://doi.org/10.1016/j.yexcr.2020.112391>.

References

- [1] S. Sarkar, B.C. Roy, N. Hatano, T. Aoyagi, K. Gohji, R. Kiyama, A novel ankyrin repeat-containing gene (Kank) located at 9p24 is a growth suppressor of renal cell carcinoma, *J. Biol. Chem.* 277 (2002) 36585–36591.
- [2] Y. Zhu, N. Kakinuma, Y. Wang, R. Kiyama, Kank proteins: a new family of ankyrin-repeat domain-containing proteins, *Biochim. Biophys. Acta* 1780 (2008) 128–133.
- [3] N.P. Chen, Z. Sun, R. Fassler, The Kank family proteins in adhesion dynamics, *Curr. Opin. Cell Biol.* 54 (2018) 130–136.
- [4] M.R. Hensley, Z. Cui, R.F. Chua, S. Simpson, N.L. Shammas, J.Y. Yang, Y.F. Leung, G. Zhang, Evolutionary and developmental analysis reveals KANK genes were co-opted for vertebrate vascular development, *Sci. Rep.* 6 (2016) 27816.
- [5] B.C. Roy, T. Aoyagi, S. Sarkar, K. Nomura, H. Kanda, K. Iwaya, M. Tachibana, R. Kiyama, Pathological characterization of Kank in renal cell carcinoma, *Exp. Mol. Pathol.* 78 (2005) 41–48.
- [6] N. Kakinuma, Y. Zhu, Y. Wang, B.C. Roy, R. Kiyama, Kank proteins: structure, functions and diseases, *Cell. Mol. Life Sci.* 66 (2009) 2651–2659.
- [7] H.Y. Gee, F. Zhang, S. Ashraf, S. Kohl, C.E. Sadowski, V. Vega-Warner, W. Zhou, S. Lovric, H. Fang, M. Nettleton, J.Y. Zhu, J. Hoefele, L.T. Weber, L. Podracka, A. Boor, H. Fehrenbach, J.W. Innis, J. Washburn, S. Levy, R.P. Lifton, E.A. Otto, Z. Han, F. Hildebrandt, KANK deficiency leads to podocyte dysfunction and nephrotic syndrome, *J. Clin. Invest.* 125 (2015) 2375–2384.
- [8] I. Lerer, M. Sagi, V. Meiner, T. Cohen, J. Zlotogora, D. Abeliovich, Deletion of the ANKRD15 gene at 9p24.3 causes parent-of-origin-dependent inheritance of familial cerebral palsy, *Hum. Mol. Genet.* 14 (2005) 3911–3920.
- [9] H. Weavers, S. Prieto-Sanchez, F. Grawe, A. Garcia-Lopez, R. Artero, M. Wilsch-Brauninger, M. Ruiz-Gomez, H. Skaer, B. Denholm, The insect nephrocyte is a podocyte-like cell with a filtration slit diaphragm, *Nature* 457 (2009) 322–326.
- [10] M. Ding, A. Goncharov, Y. Jin, A.D. Chisholm, C. elegans ankyrin repeat protein VAB-19 is a component of epidermal attachment structures and is essential for epidermal morphogenesis, *Development* 130 (2003) 5791–5801.
- [11] S. Ihara, E.J. Hagedorn, M.A. Morrissey, Q. Chi, F. Motegi, J.M. Kramer, D. R. Sherwood, Basement membrane sliding and targeted adhesion remodels tissue boundaries during uterine-vulval attachment in *Caenorhabditis elegans*, *Nat. Cell Biol.* 13 (2011) 641–651.
- [12] Y. Yang, W.S. Lee, X. Tang, W.G. Wadsworth, Extracellular matrix regulates UNC-6 (netrin) axon guidance by controlling the direction of intracellular UNC-40 (DCC) outgrowth activity, *PLoS One* 9 (2014), e97258.
- [13] B.P. Bouchet, R.E. Gough, Y.C. Ammon, D. van de Willige, H. Post, G. Jacquemet, A.M. Altaalar, A.J. Heck, B.T. Goult, A. Akhmanova, Talin-KANK1 interaction controls the recruitment of cortical microtubule stabilizing complexes to focal adhesions, *Elife* 5 (2016).
- [14] N.B.M. Rafiq, Y. Nishimura, S.V. Plotnikov, V. Thiagarajan, Z. Zhang, S. Shi, M. Natarajan, V. Viasnoff, P. Kanchanawong, G.E. Jones, A.D. Bershadsky, A mechano-signalling network linking microtubules, myosin IIA filaments and integrin-based adhesions, *Nat. Mater.* 18 (2019) 638–649.
- [15] Z. Sun, H.Y. Tseng, S. Tan, F. Senger, L. Kurazawa, D. Dedden, N. Mizuno, A. Wasik, M. Thery, A.R. Dunn, R. Fassler, Kank2 activates talin, reduces force transduction across integrins and induces central adhesion formation, *Nat. Cell Biol.* 18 (2016) 941–953.
- [16] N. Kakinuma, R. Kiyama, A major mutation of KIF21A associated with congenital fibrosis of the extraocular muscles type 1 (CFEOM1) enhances translocation of Kank1 to the membrane, *Biochem. Biophys. Res. Commun.* 386 (2009) 639–644.
- [17] S. Stehbens, T. Wittmann, Targeting and transport: how microtubules control focal adhesion dynamics, *J. Cell Biol.* 198 (2012) 481–489.
- [18] B. van der Vaart, W.E. van Riel, H. Doodhi, J.T. Kevenaar, E.A. Katrukha, L. Gummy, B.P. Bouchet, I. Grigoriev, S.A. Spangler, K.L. Yu, P.S. Wulf, J. Wu, G. Lansbergen, E.Y. van Battum, R.J. Pasterkamp, Y. Mimori-Kiyosue, J. Demmers, N. Olieric, I. V. Maly, C.C. Hoogenraad, A. Akhmanova, CFEOM1-associated kinesin KIF21A is a cortical microtubule growth inhibitor, *Dev. Cell* 27 (2013) 145–160.
- [19] N. Kakinuma, B.C. Roy, Y. Zhu, Y. Wang, R. Kiyama, Kank regulates RhoA-dependent formation of actin stress fibers and cell migration via 14-3-3 in PI3K-Akt signaling, *J. Cell Biol.* 181 (2008) 537–549.
- [20] B.C. Roy, N. Kakinuma, R. Kiyama, Kank attenuates actin remodeling by preventing interaction between IRSp53 and Rac1, *J. Cell Biol.* 184 (2009) 253–267.
- [21] Y. Zhang, H. Zhang, J. Liang, W. Yu, Y. Shang, SIP, a novel ankyrin repeat containing protein, sequesters steroid receptor coactivators in the cytoplasm, *EMBO J.* 26 (2007) 2645–2657.

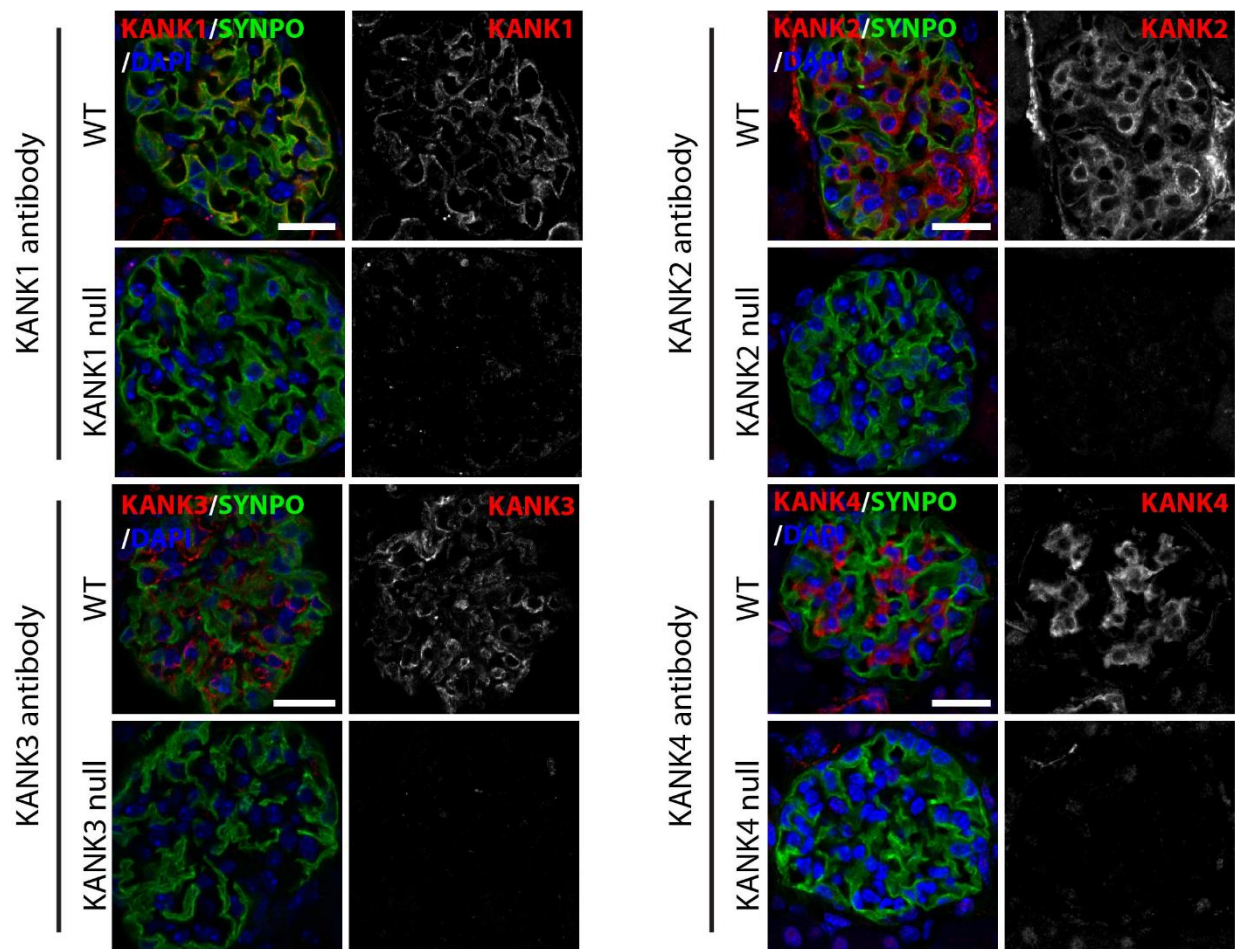
- [22] Y. Ramot, V. Molho-Pessach, T. Meir, R. Alper-Pinus, I. Siam, S. Tams, S. Babay, A. Zlotogorski, Mutation in KANK2, encoding a sequestering protein for steroid receptor coactivators, causes keratoderma and woolly hair, *J. Med. Genet.* 51 (2014) 388–394.
- [23] N. Nicolaou, C. Margadant, S.H. Kevelam, M.R. Lilien, M.J. Oosterveld, M. Kreft, A. M. van Eerde, R. Pfundt, P.A. Terhal, B. van der Zwaag, P.G. Nikkels, N. Sachs, R. Goldschmeding, N.V. Knoers, K.Y. Renkema, A. Sonnenberg, Gain of glycosylation in integrin alpha3 causes lung disease and nephrotic syndrome, *J. Clin. Invest.* 122 (2012) 4375–4387.
- [24] J.H. Miner, Developmental biology of glomerular basement membrane components, *Curr. Opin. Nephrol. Hypertens.* 7 (1998) 13–19.
- [25] R.G. Held, P.S. Kaeser, ELKS active zone proteins as multitasking scaffolds for secretion, *Open Biol* 8 (2018).
- [26] I. Noordstra, A. Akhmanova, Linking cortical microtubule attachment and exocytosis, *F1000Res* 6 (2017) 469.

Supplementary Data



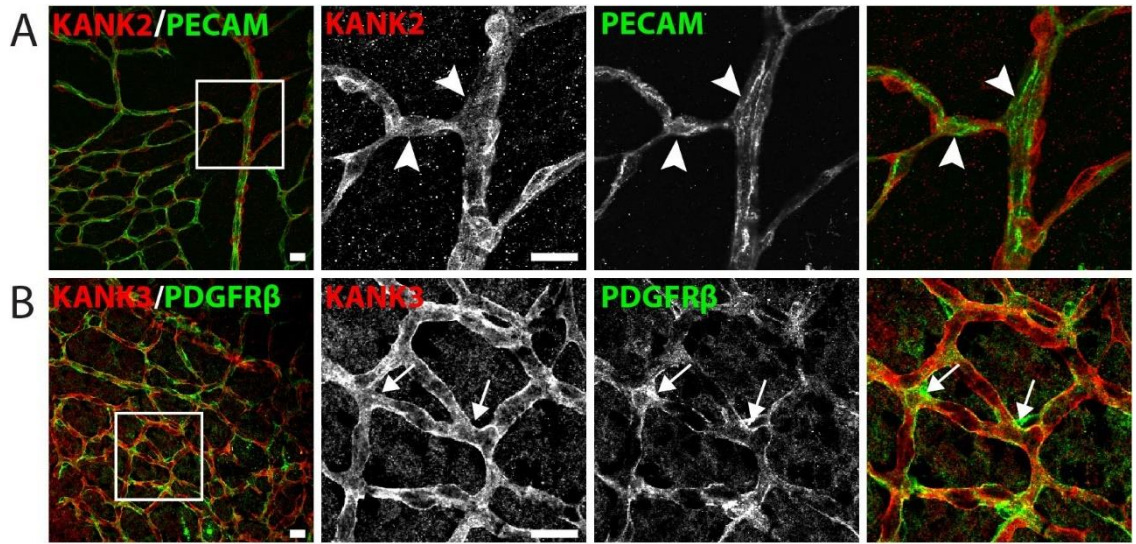
Guo et al., Supp Figure 1A-C

Supplementary Fig. 1. KANK1, 2 and 4 expression in murine kidney. KANKs are shown in red, Synaptopodin (SYNPO)⁺ podocytes in blue, and PECAM⁺ endothelial cells and PDGFR⁺ pericytes in green. Nuclei are counterstained with DAPI. (A) KANK1 is also expressed in epithelial cells of kidney tubules. (B) KANK2 is expressed in SYNPO⁺ podocytes of glomeruli but absent in PECAM⁺ endothelial cells. (C) KANK4 is expressed in PDGFR⁺ pericytes of blood vessels. Scale bars: 10 μm.



Guo et al., Supp Figure 2

Supplementary Fig. 2. KANK1-4 antibodies on kidney sections from KANK1-, 2-, 3-, 4-null mice. KANK1-4 are shown in red, and Synaptopodin (SYNPO)⁺ podocytes in green. Nuclei are counterstained with DAPI. No obvious signals are detected in respective KANK-null tissues, confirming the antibody specificity. Scale bars: 20 μ m.



Guo et al., Supp Figure 3A-B

Supplementary Fig. 3. KANK2 and 3 expression in murine retina. KANKs signals are shown in red, PECAM⁺ endothelial cells and PDGFR⁺ pericytes in green. (A) No KANK2 expression in PECAM⁺ endothelial cells (arrowheads). (B) No KANK3 expression in PDGFR⁺ pericytes (arrows). Scale bars: 20 μ m.

Supplementary Tables

Table S1: Primers used for quantitative RT-PCR

Gene	Primer	Sequence
Gapdh	Forward	5'-AAGGTCATCCCAGAGCTGAACG-3'
	Reverse	5'-CCTCAGATGCCTGCTTCACCA-3'
Kank1	Forward	5'-GAACTCTGACTTCCAGAAAGCCA-3'
	Reverse	5'-TACATTTAACAGTCCTCCTGACCG-3'
Kank2	Forward	5'-GCATGAACATCAAGTGCTCGTT-3'
	Reverse	5'-TTTGATGCGTGGCTTGTGG-3'
Kank3	Forward	5'-ACCACACAGACAGAGCTGCCAGT-3'
	Reverse	5'-CTGACTGGATTGTGCACCTGGA-3'
Kank4	Forward	5'-GACTTGCATCCCAGCTGTGAGG-3'
	Reverse	5'-TGGCACGCGTTAAGAAATTCCT-3'

Table S2: Mouse peptide sequence used to generate rabbit antisera

Antibody	Sequence
KANK1	CPRLGRKTSPGP ^{THRG}
KANK2	CKRKEDPADPEVNQ ^{RN}
KANK3	GTPGPHNDKDAGD ^C
KANK4	QGDEEKEPPKSY ^{PYS} C

Table S3: Antibody dilutions

1 st Antibody	Source	Concentration
KANK1	Homemade	1:1000 (WB), 1:2000 (IF)
KANK1	Sigma, HPA056090	1:1000 (WB, IF)
KANK2	Homemade	1:1000 (WB), 1:4000 (IF)
KANK2	Sigma, HPA015643	1:2000 (WB, IF)
KANK3	Homemade	1:1000 (WB), 1:6000 (IF)
KANK3	Sigma, HPA051153	1:1000 (WB, IF)
KANK4	Homemade	1:1000 (WB), 1:4000 (IF)
KANK4	Sigma, HPA014030	1:1000 (WB, IF)
Tubulin	Milipore MAB1864	1:1000 (WB)
PECAM-1	PharMingen 553370	1:600 (IF)
TTF1*	NSJ Bioreagents V7084	1:200 (IF)
T1 α	R&D systems AF3244	1:400 (IF)
Synaptopodin	Santa Cruz, sc-21537	1:200 (IF)

PDGFR β	Abcam, ab91066	1:400 (IF)
Nidogen	Millipore, MAB1946-I	1:2000 (IF)
α SMA	Sigma, A2547	1:400 (IF)
Paxillin	Transduction Laboratories, 610051	1:400 (IF)
GFAP	Abcam, ab4674	1:5000 (IF)
NG2	Millipore, MAB5384	1:200 (IF)
Pan-cadherin	Santa Cruz, sc-1499	1:600 (IF)
Vimentin	Abcam, ab24525	1:2000 (IF)
VEGFR3/FH-4	R+D Systems, AF743	1:200 (IF)

2 nd Antibody	Source	Concentration
Donkey α -rabbit ^{Cy3}	Jackson Lab, 711-165-152	1:800 (IF)
Donkey α -rat ^{Alexa488}	Life technologies, A21208	1:800 (IF)
Goat α -rat ^{Alexa647}	Invitrogen, A21247	1:500 (IF)
Donkey mouse ^{Alexa488}	α - Invitrogen, A21202	1:800 (IF)
Donkey mouse ^{Alexa647}	α - Invitrogen, A31571	1:500
Donkey α -goat ^{Alexa647}	Invitrogen A21447	1:500 (IF)

*Antigen retrieval is required (Citric buffer, pH 6.0, boil for 15 min)

8.5 Paper II – Lfc subcellular localization and activity is controlled by α v-class integrin

Published in Journal of Cell Science, Volume 136, Issue 9 (2023).

doi: 10.1242/jcs.260740.

Georgina Coló^{1*}, Andrea Seiwert, and Raquel B. Haga

Max Planck Institute of Biochemistry, Department of Molecular Medicine, Martinsried, Germany

¹Present address: Instituto de Investigaciones Bioquímicas de Bahía Blanca (CONICET), Departamento de Biología, Bioquímica y Farmacia, Universidad Nacional del Sur.

This paper was summarized in the research highlights of Journal of Cell Science, Volume 136, Issue 9 (2023):

Downstream of integrin-fibronectin binding: Lfc has a front Rho seat

Integrins are transmembrane proteins that interact with the extracellular matrix (ECM) to transduce mechanical signals to the cell cytoskeleton. Integrin dimers α v β 3 and α 5 β 1 are known to bind to the ECM component fibronectin, which induces the formation of stress fibres and clustering of integrins into focal adhesions (FAs). Although formation of these structures is known to require RhoA GTPase signalling, the guanine nucleotide exchange factor (GEF) that couples integrin-fibronectin binding to RhoA activation is not known. In this study (Coló et al., 2023), Raquel Haga and colleagues use a nucleotide-free mutant of RhoA to trap and identify active GEFs in genetically modified mouse fibroblasts expressing only α v β 3 and/or α 5 β 1 integrins. Here, the authors find that the RhoA GEF Lfc binds more abundantly to RhoA in α v β 3- than in α 5 β 1-expressing cells. Mechanistically, α v β 3-fibronectin binding promotes dissociation of Lfc from microtubules, and the authors show that this is mediated by phosphorylation of Lfc at Ser151 by the MARK2/3 kinases.

Subsequent activation of RhoA by Lfc results in increased stress fibre formation and maturation of FAs. Consistent with this, CRISPR-mediated knockout of Lfc in fibroblasts expressing only $\alpha v \beta 3$ resulted in reduced RhoA activity, stress fibre formation and FA size. Together, these findings suggest that Lfc is the GEF required for RhoA activation downstream of $\alpha v \beta 3$ -fibronectin binding, and that this occurs in an integrin-specific manner.

RESEARCH ARTICLE

Lfc subcellular localization and activity is controlled by α v-class integrin

Georgina P. Coló^{*,†}, Andrea Seiwert and Raquel B. Haga

ABSTRACT

Fibronectin (FN)-binding integrins control a variety of cellular responses through Rho GTPases. The FN-binding integrins, α v β 3 and α 5 β 1, are known to induce different effects on cell morphology and motility. Here, we report that FN-bound α v β 3 integrin, but not FN-bound α 5 β 1 integrin, triggers the dissociation of the RhoA GEF Lfc (also known as GEF-H1 and ARHGEF2 in humans) from microtubules (MTs), leading to the activation of RhoA, formation of stress fibres and maturation of focal adhesions (FAs). Conversely, loss of Lfc expression decreases RhoA activity, stress fibre formation and FA size, suggesting that Lfc is the major GEF downstream of FN-bound α v β 3 that controls RhoA activity. Mechanistically, FN-engaged α v β 3 integrin activates a kinase cascade involving MARK2 and MARK3, which in turn leads to phosphorylation of several phospho-sites on Lfc. In particular, S151 was identified as the main site involved in the regulation of Lfc localization and activity. Our findings indicate that activation of Lfc and RhoA is orchestrated in FN-adherent cells in an integrin-specific manner.

KEY WORDS: Integrin, Fibronectin, Signalling, Lfc, GEF-H1, Rho GTPase, Actin dynamics, MARK2, MARK3

INTRODUCTION

Integrins connect cells to a wide range of extracellular matrix (ECM) proteins, including fibronectin (FN), vitronectin (VN), collagens and laminins, as well as to other cell surface receptors such as VCAMs and ICAMs. Mammals express 18 α -integrin and eight β -integrin subunits, which assemble into 24 functionally distinct integrin receptors, binding to different ECM proteins and resulting in the transduction of several intracellular signals (Hynes, 2002). Most cell types simultaneously express a number of integrin subtypes, which can synergize to amplify signals and transmit information via a large signalling hub called the adhesome (Hynes, 2002; Schiller and Fässler, 2013; Schiller et al., 2013; Roca-Cusachs et al., 2009; Kuo et al., 2011). Integrin specificity plays a major role in signalling from ECM proteins into cells. The individual role of integrin receptors that bind to the same ECM ligand is still not completely understood.

Genetically manipulated cells are valuable tools to elucidate integrin-specific functions (Danen et al., 2002). For example, pan-

integrin knockout (pKO) murine fibroblasts (Schiller et al., 2013) expressing either α v β 3 (pKO- α v fibroblasts) and/or α 5 β 1 integrin (pKO- β 1 and pKO- α v, β 1 fibroblasts), and Chinese hamster ovary (CHO) cells overexpressing either β 1 or β 3 integrin (Miao et al., 2002) have been used to reveal that an increase of RhoA activity and formation of stress fibres and focal adhesions (FAs) is more pronounced upon α v β 3 integrin than α 5 β 1 integrin binding to FN. Nonetheless, the role of β 1 integrins in RhoA activation should not be neglected, as other cell systems have shown more pronounced RhoA signalling in the presence of β 1 integrins compared with α v β 3 integrins (Costa et al., 2013; Danen et al., 2002; Vial et al., 2003). RhoA is a classic member of the Rho GTPase family that cycles between an active GTP-bound and an inactive GDP-bound form, as controlled by guanine nucleotide exchange factors (GEFs) and GTPase-activating proteins (GAPs), respectively (Haga and Ridley, 2016; Marjoram et al., 2014). However, how α v β 3 integrin activates RhoA in a more pronounced way than α 5 β 1 in fibroblasts and CHO cells is not clear.

One of the major GEFs that activates RhoA is Lfc (also known as GEF-H1 and ARHGEF2 in humans). Lfc activity is tightly controlled, with inactive Lfc sequestered on polymerized microtubules (MTs) (Ren et al., 1998; Birkenfeld et al., 2008), whereas activation of Lfc requires its release from MTs (Krendel et al., 2002). The MT release can be mediated by phosphorylation of Lfc on specific threonine and/or serine residues, MT depolymerization or dissociation of Lfc from the MT-associated Tctex-1 (DYNLT1)-dynein intermediate chain (DIC) complex in response to lysophosphatidic acid (LPA) or thrombin stimulation, mediated by the G-protein G α 13 (GNA13) (Krendel et al., 2002; Meiri et al., 2014; Chang et al., 2008). Once Lfc is released and activated, it promotes the GDP to GTP exchange of RhoA, which results in RhoA activation, the recruitment of RhoA effector proteins such as mDia1 (DIAPH1), and actin polymerization (Narumiya et al., 2009).

Here, we investigated how Lfc is activated by α v β 3 integrin. We show that FN-mediated α v β 3 integrin engagement induces Lfc-activation via phosphorylation, which results in Lfc translocation from MTs to the cytoplasm, inducing stress fibre and FA formation.

RESULTS

GEF activation in pKO cells

It has previously been shown that FN-seeded pKO mouse fibroblasts expressing FN-binding α v-class integrins (pKO- α v fibroblasts) display higher RhoA activity, thicker stress fibres and larger FAs than pKO mouse fibroblasts expressing α 5 β 1 integrin (pKO- β 1 fibroblasts) or pKO mouse fibroblasts expressing both α v β 3 and α 5 β 1 integrins (pKO- α v, β 1) (Schiller et al., 2013). The three cell lines have different actin filament distribution (Fig. 1A; Fig. S1A). Quantification showed that pKO- β 1 cells had less fluorescence intensity of actin staining than pKO- α v and pKO- α v,

Department of Molecular Medicine, Max Planck Institute of Biochemistry, Am Klopferspitz 18, 82152, Martinsried, Germany.

^{*}Present address: Instituto de Investigaciones Bioquímicas de Bahía Blanca (CONICET), Departamento de Biología, Bioquímica y Farmacia, Universidad Nacional del Sur, 8000 Bahía Blanca, Argentina

[†]Author for correspondence (gcolo@inibibb-conicet.gob.ar)

DOI: G.P.C., 0000-0003-3476-8387; R.B.H., 0000-0001-5930-3311

Handling Editor: Arnoud Sonnenberg

Received 21 October 2022; Accepted 31 March 2023



2

Fig. 1. Differential GEF activation in pKO cells. (A) Immunostaining of indicated cell types plated on FN for 4 h in serum-free medium with either vehicle control or the C3 transferase rho inhibitor. The merged images show an overlay of F-actin (red), paxillin (green) and nuclei (DAPI, blue). Images are representative of two independent experiments. Scale bar: 10 μ m. (B) Quantification of F-actin fluorescence intensity and the percentage of cells with ventral stress fibres. Graphs show quantification of three independent experiments. * P <0.05; ** P <0.01; *** P <0.001; **** P <0.0001; ns, not significant (unpaired two-tailed t -test between pKO- α v, pKO- β 1 and pKO- α v, β 1 and pKO cells and the respective pKO cells+C3 inhibitor). A.U., arbitrary units. Results are mean \pm s.d. (C) Bar graph showing MS intensity of nine GEFs in the indicated cell types from three independent experiments. There were significant MS intensity changes among the cell types * P <0.05; ** P <0.01; *** P <0.001; **** P <0.0001; ns, not significant (one-way ANOVA followed by Dunnett's test). Results are mean \pm s.e.m. (D) Immunostaining of pKO- α v cells after transfection with indicated GEF-targeting siRNA pool. The merged images show an overlay of paxillin (green), F-actin (red) and nuclei (DAPI, blue). White arrowheads indicate cells that lost ventral stress fibres. Images are representative of three independent experiments. Scale bar: 20 μ m. (E) Quantification of cells with no ventral stress fibres in relation to total cells after siRNA transfection targeting indicated GEFs. Graph shows the quantification of 50–100 cells per condition from three independent experiments. ** P <0.01, *** P <0.001 and **** P <0.0001 (ordinary one-way ANOVA followed by Dunnett's test between control and siRNA pools). Results are mean \pm s.d.

β 1 cells (Fig. 1B) and that pKO- β 1 and pKO- α v, β 1 cells exhibited fewer ventral stress fibres compared to that seen in pKO- α v cells (Fig. 1B). To confirm the importance of Rho activity in the formation of FA and stress fibre assembly in the pKO cell lines, we treated FN-seeded pKO- α v, pKO- β 1 and pKO- α v, β 1 fibroblasts with C3 transferase, a well-known Rho inhibitor (Barbieri et al., 2002), which inhibits RhoA and its close relatives RhoB and RhoC. All three cell lines had reduced stress fibres and FAs following C3 transferase treatment (Fig. 1A,B), indicating that activated Rho promotes stress fibre formation downstream of FN-engaged α - as well as β 1-class integrins.

RhoA activity is controlled by many different GEFs and GAPs (Hodge and Ridley, 2016). To identify the GEFs that are activated by specific FN-binding integrin receptors, we performed pulldown assays with cell lysates from all three pKO cell lines using recombinantly expressed and purified GST-tagged RhoA G17A (a nucleotide-free mutant), which binds active GEFs (García-Mata et al., 2006; Guilly et al., 2011). Interacting GEFs were identified using mass spectrometry (MS; Fig. S1B). We identified nine different Rho GEFs that interacted with GST-RhoA G17A. Five out of the nine RhoA GEFs showed significantly higher activity in α -class integrin-expressing fibroblasts (Fig. 1C), and Lfc/Arhgef2 was the GEF that bound to RhoA G17A with the highest abundance. Total proteome analysis revealed equal expression levels of the different GEFs in all three cell lines (Fig. S1C). Although we could detect low levels of active Arhgef5, enriched via the pulldown assay, the total protein in our MS assays was not detectable in any of the cell lines. To identify which of the five GEFs are responsible for the pronounced stress fibre levels in pKO- α v fibroblasts, we transiently and individually depleted the GEFs and investigated their impact on ventral stress fibre formation (Fig. 1D). The experiments revealed that out of the five RhoA GEFs tested, depletion of Lfc/Arhgef2, Arhgef5 and Arhgef11 decreased ventral F-actin stress fibres (Fig. 1D,E), with Lfc depletion showing the most consistent and highest effect compared to that seen on Arhgef5 and Arhgef11 depletion (Fig. 1E). Based on these results, we decided to investigate the role of Lfc in RhoA activation, stress fibre formation and FA maturation in pKO cells.

α v-class integrins induce Lfc- and RhoA-mediated stress fibre formation

To determine how Lfc affects integrin class-specific stress fibre and FA formation, we deleted the Lfc-encoding *Arhgef2* genes (Lfc KO) in pKO- α v, pKO- β 1 and pKO- α v, β 1 fibroblasts using the Crispr/Cas9 gene editing technology and confirmed the successful KOs via western blotting (Fig. S2A). The different cell lines were seeded on FN-coated circular micropatterns to analyse F-actin organization (Fig. 2A). Loss of Lfc expression in pKO- α v and pKO- α v, β 1 fibroblasts reduced the number of organized stress fibres and the length of ventral stress fibres, increased the amount of circular actin filaments in the cell periphery, with an increase in number of junctions, and resulted in a decrease in the number of large FAs (>3 μ m) (Fig. 2A,B; Fig. S2B). Loss of Lfc in pKO- β 1 fibroblasts also led to reduced number of organized stress fibres and length of ventral stress fibres, with loss of central adhesions and a decrease in number of small adhesions (<3 μ m) (Fig. 2A,B; Fig. S2B). Re-expression of Lfc in the pKO cells rescued the phenotype of stress fibre formation in all three cell lines (Fig. S2C).

Next, we tested how loss of Lfc expression affects RhoA activity in the pKO cell system. In line with the previous report of Schiller et al. (2013), the levels of RhoA activity were higher in pKO- α v fibroblasts than in pKO- β 1 and pKO- α v, β 1 fibroblasts cultured for 45 min on FN (Fig. 2C). Deletion of *Arhgef2* genes decreased RhoA activity in pKO- α v fibroblasts compared to that in pKO- α v WT cells. Given that RhoA activity remained unaffected by *Arhgef2* loss in pKO- β 1 fibroblasts (Fig. 2C), we conclude that Lfc plays an important role on RhoA activation downstream of FN-engaged α v β 3 integrins. Western blots of Lfc after pulldown with GST-tagged RhoA G17A demonstrated that pKO- α v fibroblasts contained more active Lfc than pKO- β 1 and pKO- α v, β 1 fibroblasts (Fig. 2D), confirming that α v-class integrin engagement increases Lfc activity, which in turn leads to RhoA activation and the formation of thick, ventral F-actin fibres connected to large FAs.

α v β 3 integrin engagement induces the release of Lfc from MTs

Inactive Lfc is sequestered on MTs, whereas active Lfc is released into the cytoplasm (Krendel et al., 2002). Immunostaining revealed that Lfc was predominantly localized in the cytoplasm of FN-seeded pKO- α v fibroblasts, whereas the majority of Lfc colocalized with the MTs in pKO- β 1 fibroblasts (Fig. 3A,B). pKO- α v, β 1 fibroblasts exhibited an intermediate Lfc distribution between the MTs and cytosol (Fig. 3A,B). Note that no clear difference in MT distribution was observed between the three cell lines (Fig. 3A).

To confirm that FN engagement of α v-class integrins suffices to release Lfc from MTs, we seeded wild-type (WT) mouse fibroblasts on glass coverslips coated with either an α 5 β 1- or cRGD- α v β 3-specific peptidomimetic (Rechenmacher et al., 2013) and determined Lfc localization. WT fibroblasts cultured on α v β 3 peptidomimetic had substantial amounts of Lfc in the cytoplasm and adopted a polygonal shape with few lamellipodium-like membrane protrusions (Fig. 3C,D), whereas the WT fibroblasts seeded on α 5 β 1 peptidomimetic predominantly showed Lfc colocalized with MTs and developed multiple membrane protrusions (Fig. 3C,D). The actin cytoskeleton phenotype is similar to that of pKO- α v cells and pKO- β 1, respectively, when cultured on fibronectin (Fig. S1A; Schiller et al., 2013). To corroborate the findings, we seeded EGFP-tagged Lfc-expressing WT fibroblasts on either FN- or VN-coated glass coverslips and blocked α v-class or α 5 β 1-class integrins with cilengitide or β 1 integrin-blocking antibody (Hermann et al., 2016), respectively.

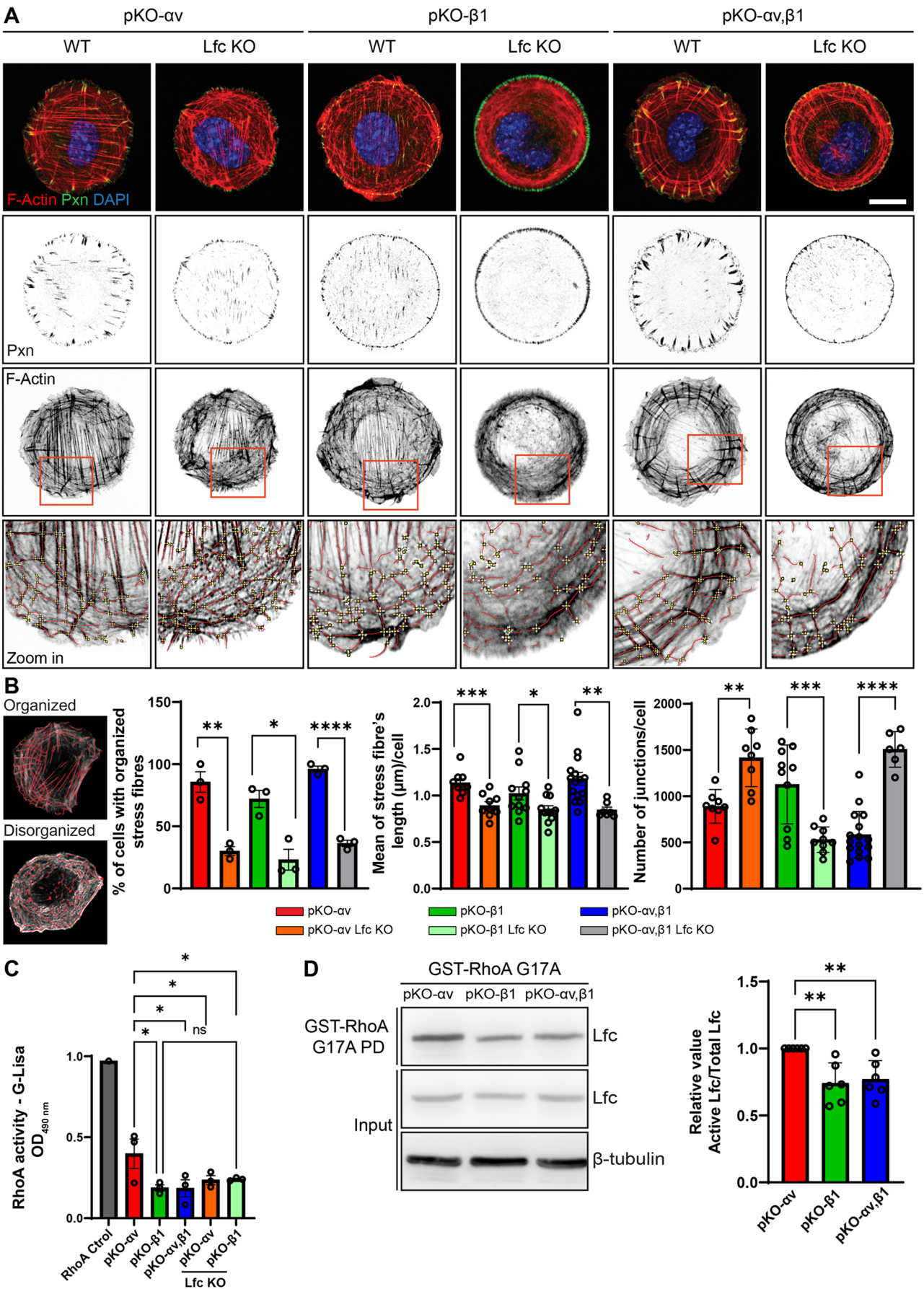


Fig. 2. See next page for legend.

Fig. 2. α v-class integrins induce Lfc and RhoA activation and stress fibre formation. (A) Cells plated on circular FN-coated micropatterns and stained for paxillin (green), F-actin (red) and nuclei (DAPI, blue). Scale bar: 10 μ m. The lower panel shows examples of the quantification of stress fibre length (red lines) and junctions (white crosses). (B) Quantification of the percentage of cells with organized stress fibres to total cells, mean of stress fibre length per cell and number of junctions per cell. The two images show examples of organized and disorganized stress fibres. Graphs show the quantification of 5–20 cells per condition. * P <0.05; ** P <0.01; *** P <0.001; **** P <0.0001 (unpaired two-tailed t -test between WT pKO cells and Lfc KO pKO cells). Quantitative results are mean \pm s.e.m. for the percentage of organized stress fibres and stress fibre length and mean \pm s.d. for number of junctions/cell. (C) RhoA activity of indicated cells determined by G-Lisa. Graph shows quantification of three independent experiments. * P <0.05; ns, not significant (ordinary one-way ANOVA between pKO- α v and other conditions, and pKO- β 1 and pKO- β 1 Lfc KO). Results are mean \pm s.e.m. (D) Lfc activity of indicated cells determined by western blotting after GST–RhoA-G17A pulldown. Graph shows quantification of five independent experiments. ** P <0.01 (one-sample t -test to theoretical mean 1 between pKO- α v and pKO- β 1, pKO- α v and pKO- α v, β 1). Quantitative results are mean \pm s.d.

These results confirmed that WT fibroblasts cultured on FN (bound by α 5 β 1 and α v-class integrins) harboured EGFP–Lfc in the cytoplasm and on MTs, whereas antibody-mediated blockade of β 1 integrins released EGFP–Lfc into the cytoplasm and α v-class integrin blockade with soluble cilengitide caused EGFP–Lfc to become associated with the MT network (Fig. S3A). Moreover, WT fibroblasts seeded on the α v-class integrin ligand VN, or β 1-null deficient fibroblasts seeded on FN, also displayed a diffuse cytoplasmic distribution of EGFP–Lfc (Fig. S3A). Levels of active Lfc were also decreased after treatment with cilengitide, whereas blocking α 5 β 1 integrins was without effect (Fig. S3B,C). Altogether, these findings strongly indicate that α v-class integrin engagement triggers Lfc release from MTs.

The release of Lfc from MTs can occur in cells by depolymerizing MTs, dissociating Lfc from the MT-associated Tctex-1–DIC complex after LPA or thrombin stimulation and/or direct phosphorylation of Lfc (Krendel et al., 2002; Meiri et al., 2012; Meiri et al., 2014; Fujishiro et al., 2008; von Thun et al., 2013; Patel and Karginov, 2014; Sandí et al., 2017; Yoshimura and Miki, 2011). Given that we performed our experiments under serum-free conditions, we can exclude a major involvement of LPA- and thrombin-mediated GPCR signalling in the α v-class integrin-induced Lfc release from MTs. MT dynamics of the three cell lines were similar after nocodazole washout, MT fractionation, and stability assays were performed (Fig. S4), indicating that the marked Lfc release from MTs in pKO- α v is not caused by unstable or depolymerized MTs. Therefore, release of Lfc from MTs in pKO- α v could be associated with differential phosphorylation of Lfc in these cells.

Lfc is differentially phosphorylated in pKO- α v and pKO- β 1 fibroblasts

To investigate whether Lfc is differentially phosphorylated in pKO- α v, pKO- β 1 and pKO- α v, β 1 fibroblasts, we performed an unbiased phospho-enrichment proteomic analysis. We found that phosphopeptides carrying the five serine residues (S129, S151, S174, S931 and S959; see asterisks in Fig. S5A) in Lfc were significantly more enriched in pKO- α v than in pKO- β 1 fibroblasts.

To determine whether these phospho-sites are involved in the release of Lfc from MTs, we replaced all five serine residues with alanine and expressed the resulting GFP-tagged Lfc-S5A in FN-seeded pKO- α v fibroblasts carrying a Crispr/Cas9-mediated deletion of the *Arhgef2* gene. Remarkably, replacements of the

five phospho-sites shifted the localization of the mutant Lfc from the cytoplasm to MTs (Fig. 4A,B). To further define the phosphoserine residue(s) promoting Lfc release from MTs in pKO- α v fibroblasts, we generated and transiently expressed Lfc mutants carrying individual serine replacements (GFP–Lfc S129A, GFP–Lfc-S151A, GFP–Lfc-S174A, GFP–Lfc-S931A and GFP–Lfc-S959A) in pKO- α v Lfc KO fibroblasts seeded on FN. GFP–Lfc-S151A was sequestered on MTs and GFP–Lfc-S174A showed a slight colocalization with MTs, whereas the remaining mutants were predominantly located in the cytoplasm (Fig. 4A,B), indicating that Lfc-S151 represents a major site for which phosphorylation triggers the dissociation of Lfc from MTs upon α v-class integrin engagement.

To test whether α v-class integrin-mediated phosphorylation of Lfc-S151 triggers the Lfc release from MTs and Lfc activation, we stably expressed WT GFP–Lfc, GFP–Lfc-S151A or GFP–Lfc-S151D in pKO- α v Lfc KO fibroblasts (Fig. S5B) and performed GST-tagged RhoA-G17A pulldown experiments. We found that binding of GFP–Lfc-S151A to RhoA-G17A was decreased, whereas binding increased when Lfc-S151 was substituted for the phospho-mimetic amino acid GFP–Lfc-S151D (Fig. 4C; Fig. S5C), indicating that Lfc-S151 phosphorylation affects localization and activity of Lfc.

Staurosporine affects Lfc localization and activity in pKO- α v fibroblasts

Given that Lfc localization is controlled by increased phosphorylation in pKO- α v fibroblasts, we treated these cells with the broad-range kinase inhibitor staurosporine or the broad-range phosphatase inhibitors sodium fluoride (NaF) and sodium orthovanadate (Na_3VO_4). Staining of endogenous Lfc revealed that the treatment of pKO- α v fibroblasts with a low dose (1 and 2 nM) of staurosporine changed localization of Lfc from the cytoplasm to MTs (Fig. 5A; Movie 1). In line with the Lfc translocation to MTs, staurosporine treatment also decreased formation of stress fibres and Lfc activity (Fig. 5B,C). The treatment of pKO- α v fibroblasts with NaF, to inhibit serine/threonine phosphatases, or with Na_3VO_4 , to inhibit tyrosine phosphatases, had no apparent effect on Lfc distribution (Fig. S6A), suggesting that kinases rather than phosphatases are the main players in signalling downstream of α v-class integrins.

The involvement of S151 in Lfc localization was further confirmed by stably overexpressing WT GFP–Lfc and the phospho-mimetic GFP–Lfc-S151D in pKO- α v Lfc KO fibroblasts. The experiments revealed that staurosporine treatment induced the translocation of WT GFP–Lfc from the cytoplasm to MTs. In contrast, phospho-mimicking GFP–Lfc-S151D remained cytoplasmic both before and after staurosporine treatment (Fig. 5D,E), underscoring the role of Lfc-S151 phosphorylation for MT translocation in pKO- α v cells. Treatment of pKO- α v with staurosporine decreased overall Lfc phosphorylation, including phosphorylation of S151 as observed by unbiased phospho-enrichment proteomic analysis (Fig. S6B,C).

MARK2 and MARK3 kinases are involved in Lfc release from MTs

MARK2 and MARK3 are members of the evolutionarily conserved MT-affinity regulating kinases (PAR-1) serine/threonine kinase family shown to bind and phosphorylate Lfc/GEF-H1 at several serine residues. MARK2 has been reported to phosphorylate Lfc-S143, -S885 and -S959, and MARK3 Lfc-S151 (Yamahashi et al., 2011; Yoshimura and Miki, 2011; Sandí et al., 2017). Nevertheless,

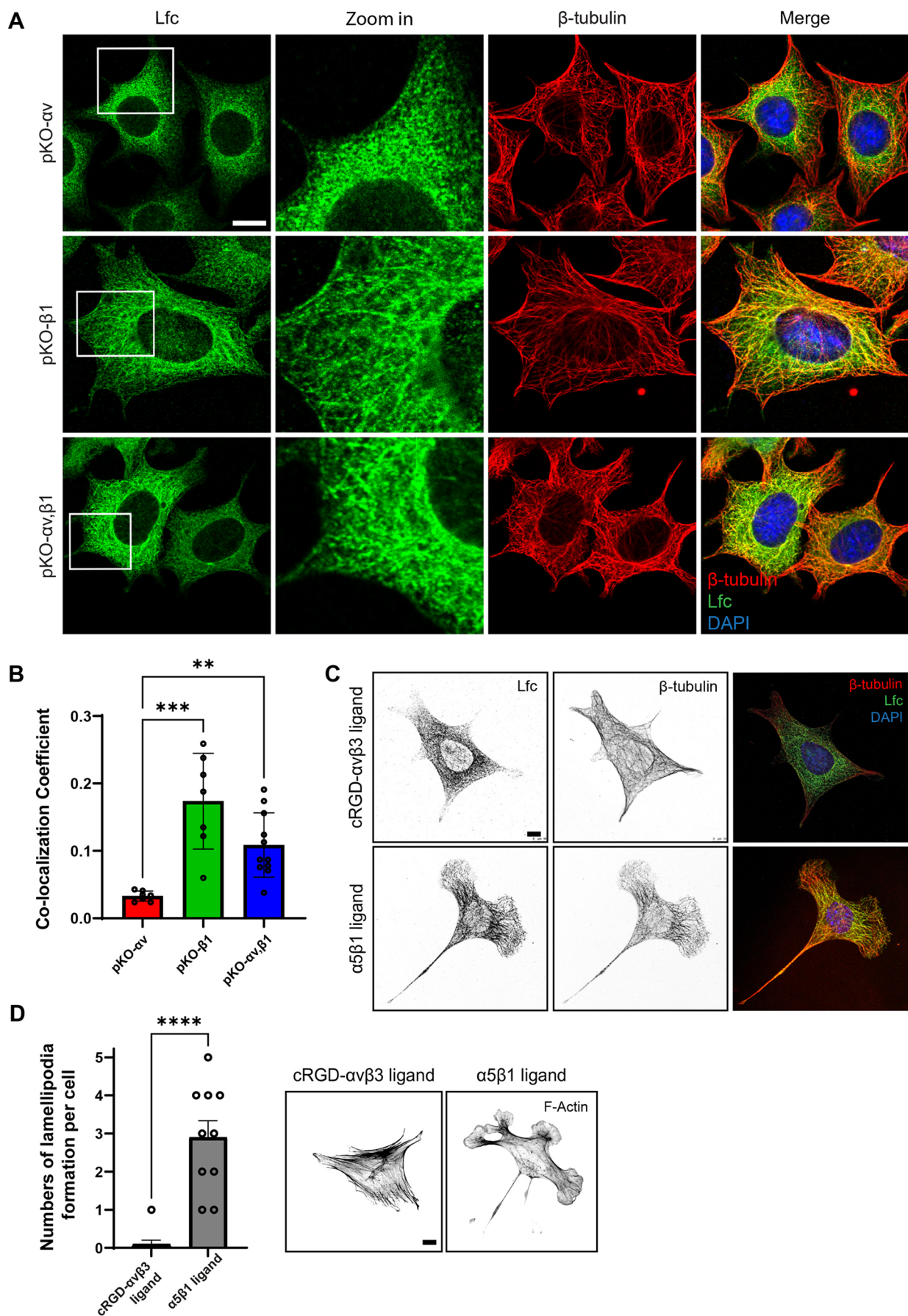


Fig. 3. See next page for legend.

Fig. 3. Integrin-mediated control of subcellular Lfc localization. (A) The indicated cells were plated for 45 min on FN in serum-free medium and stained for Lfc (green), β -tubulin (red) and nuclei (DAPI, blue). Scale bar: 10 μ m. (B) Quantification of colocalization between Lfc and β -tubulin. Graph shows the quantification of 7–11 cells per condition from two independent experiments. ** $P < 0.01$; *** $P < 0.001$ (Kruskal–Wallis test between pKO- α v, pKO- β 1 and pKO- α v, β 1). (C) Immunostaining of WT mouse fibroblasts cultured for 60 min on glass coverslips coated with either c-RGD- α v β 3- or α 5 β 1 specific peptidomimeticum in serum-free medium and then stained for Lfc (green), β -tubulin (red) and nuclei (DAPI, blue). Scale bar: 10 μ m. (D) Quantification of number of protrusions per cell. Graph shows the quantification of 10 cells per condition. **** $P < 0.0001$ (unpaired two-tailed t -test between cRGD- α v β 3 ligand and α 5 β 1 ligand). Grey scale images show F-actin. Scale bar: 10 μ m. Quantitative results are means \pm s.d.

MARK2 and MARK3 show high similarity in the N-terminal kinase domain and phosphorylate substrates at LXXRXXXXL and KXGS motifs (Sonntag et al., 2019; Shackelford and Shaw, 2009; Trinczek et al., 2004; Drewes et al., 1997). Based on these similarities, we depleted MARK2 and/or MARK3 by siRNA and disrupted *MARK2* and *MARK3* genes by Crispr/Cas9 in pKO- α v fibroblasts (Fig. S6D,E). We observed an increased association of Lfc with MTs in MARK2 and MARK3-depleted cells, with a slightly more pronounced effect when both MARK2 and MARK3 expression were lost (Fig. 6A,B; Fig. S6F). This suggests that MARK2 and MARK3 operate downstream of α v-class integrins in mouse fibroblasts to regulate Lfc association with MTs.

In summary, these results indicate that α v-class integrin engagement with FN activates a signalling cascade resulting in the activation of MARK2 and MARK3 kinases, which trigger phosphorylation of Lfc at S151, leading to the release from MTs, activation of RhoA, induction of stress fibres and FA maturation.

DISCUSSION

Little is known about how different integrins differentially control Rho GTPase activity through the regulation of GEFs and we therefore aimed to identify and characterize GEFs involved in integrin signalling. We demonstrate that FN-binding α v-class integrins stimulate activation and alter subcellular localization of the RhoA-specific GEF Lfc (GEF-H1 in humans). We found that α v-class, but not β 1, integrins induce high phosphorylation of Lfc and its translocation from MTs to the cytoplasm, followed by Lfc and RhoA activation and stress fibre formation. This does not exclude the role of β 1 integrin in activating RhoA in a normal cell setting. However, in our system, activation of RhoA by Lfc was more pronounced in cells expressing only α v β 3 compared to that in β 1 integrin-expressing cells, and expression of α 5 β 1 seemed to have a counter-balancing effect to the α v β 3 signalling on RhoA activation as evidenced by the pKO- α v, β 1 phenotype. pKO- α v, β 1 cells, which show similarity with the WT phenotype, had almost as much activation of Lfc as pKO- α v cells, but similar RhoA activation to that in pKO- β 1 cells. This indicates that although α v β 3 stimulates the activation of Lfc, if α 5 β 1 is present, levels of RhoA activation will remain at WT levels.

Lfc was first described as an oncogene in NIH 3T3 fibroblasts (Whitehead et al., 1995), exhibiting the particularly interesting feature of localizing to MTs, which serves as an important link for actin-microtubule crosstalk (Krendel et al., 2002; Azoitei et al., 2019). We suggest that neither MT depolymerization/unstable MTs (Krendel et al., 2002) nor G α -mediated dissociation of Lfc from the MT-resident Tctex-1–DIC complex (Meiri et al., 2014) play significant roles in the Lfc release from MTs in pKO- α v cells.

Instead, we identified phosphorylation as the major Lfc regulator in response to α v integrins.

Several kinases have been shown to phosphorylate Lfc at various serine and threonine residues (Meiri et al., 2012; Meiri et al., 2014; Fujishiro et al., 2008; Patel and Karginov, 2014; Sandi et al., 2017; Meiri et al., 2009; Yamahashi et al., 2011), often resulting in Lfc activation. Our unbiased phospho-enrichment proteomic analysis revealed that Lfc was highly phosphorylated in pKO- α v cells when compared to in pKO- β 1 cells, supporting a model in which increased Lfc phosphorylation upon α v-class integrin engagement leads to increased Lfc and RhoA activity. Interestingly, not only do pKO- α v, β 1 cells show high activation of the same phospho-sites as pKO- α v cells but also of S885 and S959 (Fig. S5A), which have been linked to Lfc inhibition (Yamahashi et al., 2011). This might hint to a balanced Lfc regulation in these cells, where both α v β 3 and α 5 β 1 integrins are expressed, leading to an even higher activation of the phospho-sites observed for the pKO- α v cells to balance the activation of the inhibitory sites S885 and S959 by α 5 β 1 integrins. Given that activation of Lfc and RhoA and formation of thick stress fibres connected to large FAs were less pronounced in pKO- α v, β 1 cells compared to pKO- α v cells, this further supports our hypothesis that α v β 3 and α 5 β 1 integrins counter balance each other in regulating Lfc and RhoA signalling in WT mouse fibroblasts.

We found that S151 has a critical role in the subcellular localization and activation of Lfc in pKO- α v cells. However, we cannot discard that other phospho-sites identified in our unbiased phospho-enrichment proteomic analysis could contribute to Lfc activity in pKO- α v cells, since regulation of Lfc is a highly complex and multi-step process (Joo and Olson, 2021). Furthermore, low dose treatment with the broad kinase inhibitor staurosporine was able to efficiently induce the translocation of Lfc from the cytoplasm to MTs in pKO- α v fibroblasts. In addition, staurosporine treatment decreased RhoA activity and reduced stress fibre formation in pKO- α v cells, which is similar to the phenotype observed in Lfc-depleted pKO- α v cells. Hence, this suggests that kinases are involved in FN-engaged α v β 3 integrin-mediated Lfc and RhoA activation, stress fibre formation and FA maturation.

The importance of MARK3-mediated Lfc phosphorylation on S151 and its release from MTs was previously described by Sandi et al. (2017). As expected, depletion of MARK3 in pKO- α v cells led to Lfc association with MTs. Interestingly, depletion of MARK2 also led to the same phenotype, suggesting that both kinases can regulate Lfc in our system. MARK2 has been shown to phosphorylate different phospho-sites, which mostly lead to Lfc activation and translocation to the cytoplasm (Yoshimura and Miki, 2011). Inhibition of the phosphorylation of these sites due to MARK2 depletion in combination with the inhibition of S151 by MARK3 depletion could lead to a more pronounced effect in comparison to depletion of MARK2 or MARK3 alone. The same was observed when five serine residues (S5A) were mutated in comparison to S151A alone (Fig. 4A). Pasapera et al. (2022) has shown that MARK2 can associate with FAs via its membrane-binding domain, which suggests that MARKs could be activated by integrins at the FAs. In addition, Zuidema et al. (2022) has shown that β 5 integrin can be regulated by MARK2, which shows a link of this kinase to the integrin signalling. Indeed, our pKO- α v cells express α v β 5 integrins. However, given that our experiments were performed on FN, α v β 5 might not play a role in MARK2 signalling in our system. Therefore, the association of MARK2 signalling with α v β 3 integrin could happen at the integrin level by a still unknown mechanism or through an unidentified kinase that might operate downstream of α v-class integrins and upstream of MARK2 and

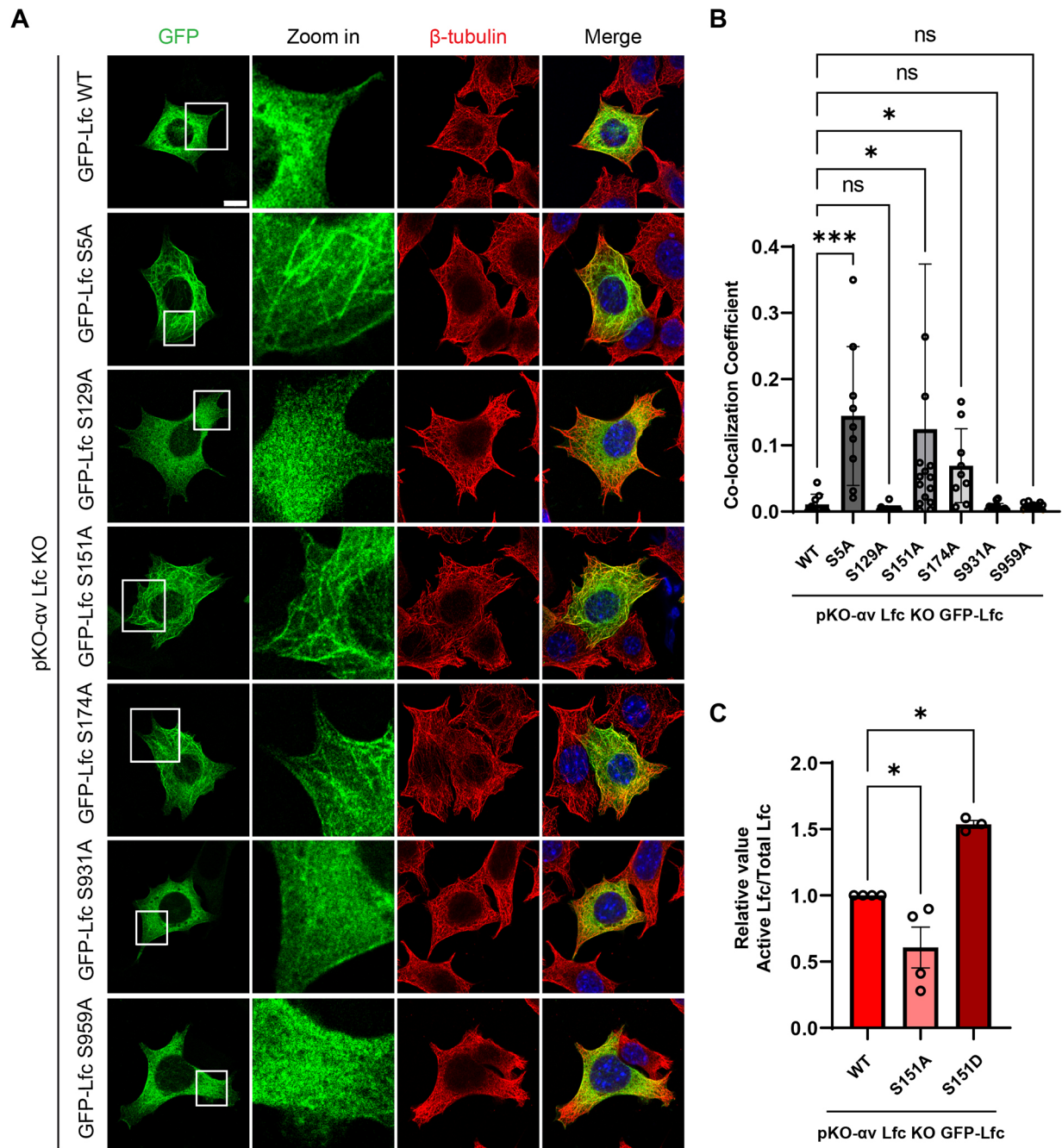


Fig. 4. Impact of Lfc phosphorylation on subcellular localization and activity. (A) pKO- α v Lfc KO cells overexpressing the indicated GFP-Lfc constructs cultured for 45 min on FN in serum-free medium and then visualized or stained for GFP-Lfc (green), β -tubulin (red) and nuclei (DAPI, blue). Scale bar: 10 μ m. (B) Quantification of colocalization between GFP-Lfc and β -tubulin. Graph shows the quantification of 9–15 cells from three independent experiments. * P <0.05; *** P <0.001; ns, not significant (Kruskal–Wallis test between pKO- α v Lfc KO GFP WT and other mutants). Results are mean \pm s.d. (C) Lfc activity in pKO- α v Lfc KO cells stably expressing GFP-Lfc-WT, GFP-Lfc-S151A or GFP-Lfc-S151D determined by western blotting after GST-RhoA-G17A pull-down. Graph shows quantification of four independent experiments. * P <0.05 (ordinary one-way ANOVA followed by Dunnett's test between GFP-Lfc-WT, GFP-Lfc-S151A and GFP-Lfc-S151D). Results are mean \pm s.e.m.

MARK3 in this pathway. A potential candidate is LKB1 (STK11), which has been shown to positively regulate MARKs (Lizcano et al., 2004; Timm et al., 2008) and to be involved in the translation of integrin signalling into cell polarity response (Chan et al., 2014).

Over the past decade, there has been a big emphasis on identifying key molecules and signalling pathways relevant to cellular mechanobiology. This study has shown that Lfc (GEF-H1) is an important link between specific integrin-ECM-sensing and

RhoA activation, inducing changes in the cytoskeleton and cell contractility.

MATERIALS AND METHODS

Cell lines and reagents

Reconstituted pKO- α v, pKO- β 1 and pKO- α v, β 1 mouse fibroblast cell lines were generated as described by Schiller et al. (2013). Cells were grown in Dulbecco's modified Eagle's medium (DMEM) supplemented

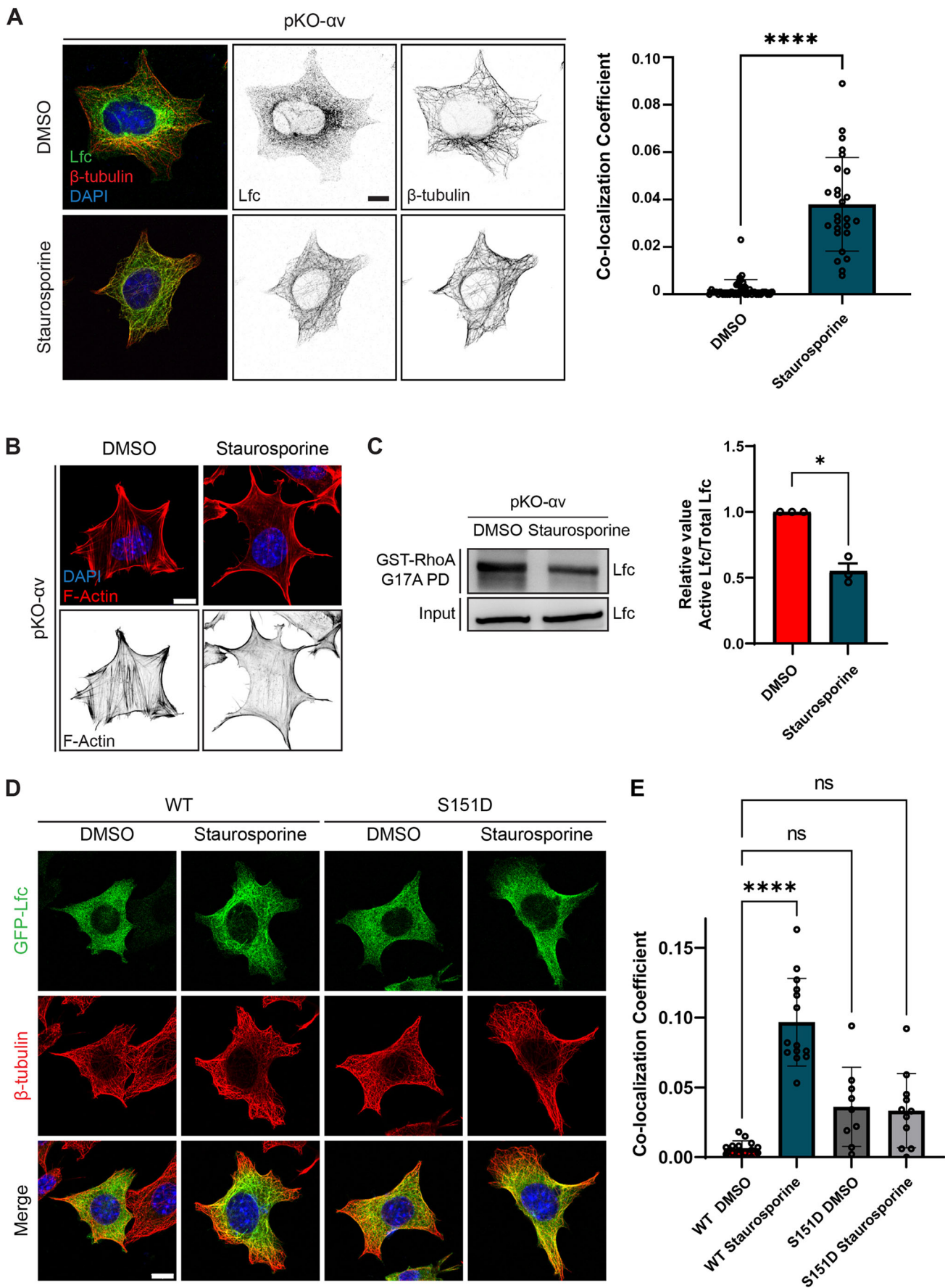


Fig. 5. See next page for legend.

Fig. 5. Staurosporine affects Lfc localization and activity in pKO- α v cells. (A) Immunostaining of pKO- α v cells plated on FN in serum-free medium and treated with staurosporine (2 nM). Graph shows the colocalization coefficient between Lfc and β -tubulin for 15 cells per condition. **** $P < 0.0001$ (unpaired two-tailed *t*-test between DMSO and staurosporine). Scale bar: 10 μ m. Quantitative results are mean \pm s.d. (B) pKO- α v cells plated on FN for 90 min in serum-free medium and treated with staurosporine, followed by F-actin (red) and nuclear staining (DAPI, blue). Images representative of three repeats. Scale bar: 10 μ m. (C) Lfc activity was determined by western blotting after GST-RhoA-G17A pulldown of DMSO- and staurosporine-treated pKO- α v cells cultured for 4 h on FN in serum-free medium. Graph shows quantification of three independent experiments. * $P < 0.05$; ns, not significant (one sample *t*-test to theoretical mean 1). Quantitative results are mean \pm s.e.m. (D) DMSO- and staurosporine-treated pKO- α v Lfc KO cells reconstituted with GFP-Lfc-WT or GFP-Lfc-S151D cultured for 90 min on FN in serum-free medium and then visualized or stained for GFP-Lfc (green), β -tubulin (red) and nuclei (DAPI, blue). Scale bar: 10 μ m. (E) Quantification of colocalization between GFP-Lfc and β -tubulin. Graph shows the quantification of 10–14 cells from two independent experiments. **** $P < 0.0001$; ns, not significant (Kruskal–Wallis test between pKO- α v Lfc KO GFP-WT DMSO and other conditions). Results are mean \pm s.d.

with 10% fetal bovine serum (FBS), 100 μ g/ml streptomycin, and 100 U/ml penicillin (10270106 and 15140122, Gibco™; complete medium). The following antibodies and other reagents were used: anti-GEF-H1/Lfc [1:2000 (western blotting, WB) and 1:500 (immunofluorescence, IF), ab155785, Abcam], anti- β -tubulin (1:5000, T5201, Sigma, WB), anti- β -tubulin (1:50, E7-s, DSHB by Michael Klymkowsky, IF), anti-GAPDH (1:10,000, CB1001, Calbiochem®, Millipore, WB), anti-paxillin (1:300, 610051 clone 349, BD Transduction Laboratories, IF), anti-MARK2 (1:1000, #9118, Cell Signaling, WB), anti-MARK3 (1:1000, #9311, Cell Signaling), Rhodamine-phalloidin (1:300, R415, Molecular Probes, Invitrogen, IF), Alexa Fluor 488 anti-rabbit-IgG (1:500, A11008, Invitrogen), Alexa Fluor 488 anti-mouse-IgG (1:400, A11029, Invitrogen), Alexa Fluor 546 anti-mouse-IgG (1:400, A11003, Invitrogen), DAPI (1:1000, Sigma-Aldrich), nocodazole (M1404, Sigma-Aldrich), bovine plasma FN (34163, Sigma-Aldrich), staurosporine (S1421, Selleckchem), NaF (Sigma-Aldrich), Na₃VO₄ (Sigma-Aldrich), anti-mouse integrin α 5 β 1 monoclonal antibody (MAB2575, clone BMC5, Merck), cilengitide (Hözlzel), cRGD- α v β 3 and α 5 β 1 selective peptidomimetic ligand (Rechenmacher et al., 2013).

Expression vectors and site-directed mutagenesis

Mouse full-length pCDNA3.1-EGFP-Lfc (transient expression) was kindly provided by Dr Michael Sixt (IST Austria, Klosterneuburg, Austria) and pRetroQ-AcGFP1-C1 (stable expression) was purchased from Clontech. Site-directed mutations were performed using the QuikChange site-directed mutagenesis kit (Agilent Technologies). Lfc was subcloned into pUC19 vector (Addgene #50005) for the mutation reactions and then subcloned again into pCDNA3.1-EGFP vector or pRetroQ-AcGFP1-C1. The nucleotide changes were verified by DNA sequencing (MWG-Eurofins). The correctness of the construct was verified by DNA sequencing (MWG-Eurofins). pGEX-GST-RhoA G17A was kindly provided by Rafael García-Mata (University of Toledo, Spain).

Generation of stable cell lines

pKO- α v Lfc KO were retrovirally transduced with mouse Lfc WT or Lfc mutant cDNA (pRetroQ-AcGFP1-C1-Lfc WT or pRetroQ-AcGFP1-C1-Lfc mutant). Cells were FACS sorted and GFP-Lfc levels were adjusted to endogenous Lfc expression.

DNA and siRNA transfection

Cells were transfected with different plasmids using 1:2 ratio of Lipofectamine® 2000 (Invitrogen) in medium without serum and antibiotics. Medium was changed to complete medium 6 h after transfection. After 48 h of transfection, cells were lysed or fixed for immunostaining.

Cells were transfected with different siRNAs using Viromer® Blue (0.5 μ l to every 25 nM siRNA, Lipocalix), following the manufacturer's

instructions. siRNAs were from Dharmacon: D-001810-10-05 (control, non-targeting SMART pool), L-040137-00-0005 (mouse MARK2 SMART pool), L040138-00-0005 (mouse MARK3 SMART pool), L-047092-00-0005 (mouse Arhgef1 SMART pool), L-040120-00-0005 (mouse Arhgef2 SMART pool), L-055988-01-0005 (mouse Arhgef5 SMART pool), L-049560-00-0005 (mouse Arhgef11 SMART pool), L-160106-00-0005 (mouse Akap13 SMART pool), L-045026-01-0005 (mouse Ect2 SMART pool) and L-051060-01-0005 (mouse Plekhg5 SMART pool). After 48 h of transfection, cells were lysed or fixed for immunostaining.

Active GEF pulldown assays

The protocol was performed as described by García-Mata et al. (2006) and Guilluy et al. (2011). Briefly, cells were seeded on FN 2 days before experiments. Cells were serum-starved for at least 3 h, detached with trypsin-EDTA and kept in suspension in serum-free medium for 1 h. Cells were re-seeded on FN in serum-free medium for the desired time points at 37°C, 5% CO₂. Lysis was performed on ice using lysis buffer (20 mM HEPES pH 7.5, 150 mM NaCl, 5 mM MgCl₂, 1% Triton X-100, protease inhibitor and phosphatase inhibitor). After clarification, lysates were incubated with GST-RhoA-G17A coupled to glutathione beads for 45 min at 4°C in an end-over-end mixer. A small aliquot was kept as loading control. Beads were washed with lysis buffer, resuspended in 2 \times Laemmli buffer and boiled for 5 min. Samples were either used for mass spectrometry analysis or western blotting.

G-Lisa RhoA activation assay

Cells were serum-starved overnight, detached with trypsin-EDTA and kept in suspension in serum-free medium for 1 h. Cells were then plated on FN-coated dishes (blocked with 1% BSA) in serum-free medium for 45 min. RhoA activity was measured by G-Lisa RhoA activation assay kit (Cytoskeleton, Inc.), following the manufacturer's instructions. Briefly, cells were lysed on ice with cell lysis buffer supplemented with protease inhibitor cocktail. Lysates were clarified by centrifugation at 10,000 *g* at 4°C for 1 min. The protein concentration of all samples was equalized after concentration was determined using Precision Red™ Advanced Protein Assay Reagent. Cell lysis buffer mixed with binding buffer was used as a blank and Rho control protein mixed with binding buffer was used as a positive control. Equalized lysates were mixed with binding buffer and added to the wells containing Rho GTP binding protein as well as the blank and positive control. After 30 min incubation under orbital shaking at 4°C, wells were washed twice with wash buffer and antigen presenting buffer was added to each well for 2 min at room temperature. Wells were washed again three times and anti-RhoA primary antibody was added to each well for 45 min at room temperature. After three washes, secondary antibody was added to each well for 45 min at room temperature. Signal was detected at absorbance 490 nm after HRP detection reagent incubation for 15 min at 37°C.

Western blotting

Lysates were resolved in SDS-polyacrylamide gels and transferred to PVDF membranes. Membranes were blocked in 5% (w/v) dried milk powder dissolved in Tris-buffered saline with 0.1% Tween 20 (TBS-T) and incubated with primary antibody overnight at 4°C. Membranes were washed three times with TBS-T and incubated for 1 h at room temperature with appropriated HRP-labelled secondary antibody. Enhanced chemiluminescence (Millipore) was used as a detection reagent. The original western blot images are shown in Figs S7 and S8.

Immunostaining

Cells were fixed with either 4% paraformaldehyde (PFA) for 15 min at room temperature or in methanol for 5 min at –20°C (anti-GEF-H1/Lfc and anti- β -tubulin). Cells were then permeabilized with 0.1% Triton X-100 in PBS for 5 min and blocked with 3% BSA with 0.1% Triton X-100 in PBS for 30 min. Cells were incubated with the required antibody in 1% BSA with 0.1% Triton X-100 in PBS overnight at 4°C followed by the incubation with the secondary antibody and phalloidin probe for 45 min. DAPI was used for nuclear staining. Confocal images were acquired with an inverted confocal microscope (Leica SP5 and Carl Zeiss LSM510).

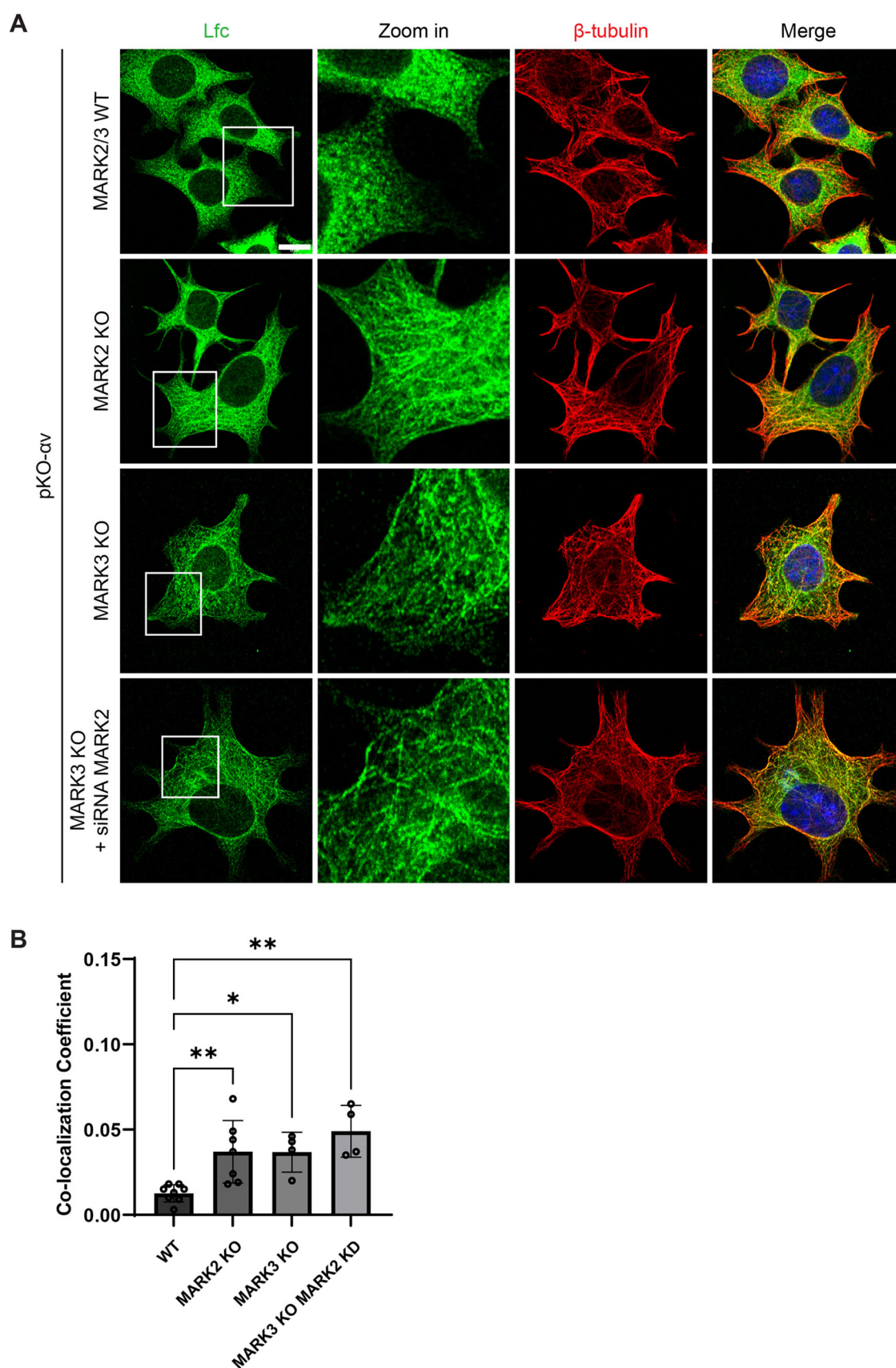


Fig. 6. MARK2 and MARK3 kinases mediate the Lfc release from MTs. (A) Indicated cells cultured for 45 min on FN in serum-free medium stained for Lfc (green), β -tubulin (red) and nuclei (DAPI, blue). Scale bar: 10 μ m. (B) Quantification of colocalization between Lfc and β -tubulin. Graph shows the quantification of 4–8 cells from two independent experiments. * $P < 0.05$ and ** $P < 0.01$ (Kruskal–Wallis test between pKO- α v Lfc KO GFP-WT DMSO and other conditions). Results are mean \pm s.d.

Microtubule fractionation

MT fractionation was performed using a Microtubules/Tubulin In Vivo assay kit (Cytoskeleton), following the manufacturer's instructions. Briefly, cells were seeded on 10 cm FN-coated dishes 2 days before experiments. Cells were serum-starved for at least 3 h, detached with trypsin-EDTA and kept in suspension in serum-free medium for 1 h. Cells were re-seeded on FN in serum-free medium for 45 min at 37°C, 5% CO₂. Cells were washed with 37°C PBS and an appropriate volume of 37°C lysis buffer was added to the plate. Cells were harvested and homogenized using a 200 µl pipet tip. Cells were centrifuged at 2000 *g* for 5 min at 37°C. Supernatants were transferred to a new microcentrifuge tube and the concentration of samples was normalized before the next step. A small aliquot was kept as a loading control. Samples were centrifuged at 100,000 *g* for 60 min at 37°C. After centrifugation, supernatants (soluble tubulin) were transferred to new microcentrifuge tubes and the pellets (MTs) were resuspended in MT depolymerization buffer. Samples were analysed by western blotting.

Microtubule cold stability

MT cold stability assays were carried out as described in Atkinson et al. (2018). Briefly, cells were seeded on a six-well plate coated with FN (blocked with 1% BSA). Cells were left to adhere for 90 min at 37°C, 5% CO₂. The plate was then placed on ice for 15 min to induce MT depolymerization. Cells were washed with PBS and 100 µl of PEM buffer [80 µM PIPES pH 6.8, 1 mM EGTA, 1 mM MgCl₂, 0.5% Triton X-100 and 25% (w/v) glycerol] was added for 3 min. The whole volume was collected into a new microcentrifuge tube and cells were briefly washed with additional 50 µl of PEM buffer. The volume was collected and 150 µl of PEM was mixed with 150 µl of 2× EB buffer (3% SDS, 60 mM sucrose, 65 mM Tris-HCl pH 6.8). This fraction contained the cold unstable MTs. The cells remaining on the plate were lysed using 300 µl of 1× EB buffer. This fraction contained the cold stable MTs. Laemmli buffer (5×) was added to the samples, and they were boiled for 5 min prior to analysis by western blotting.

Peptidomimetic binding assay

Nanopatterned gold surfaces were generated as described in Rechenmacher et al. (2013). Briefly, glass coverslips were passivated with polyethylene glycol (PEG), to prevent nonspecific protein adsorption or cell binding to the substrate area surrounding or in between the gold nanoparticles. Gold nanoparticles presenting integrin αvβ3 (cRGD) or α5β1 peptidomimetics were fixed on glass coverslips.

Mouse fibroblasts were serum-starved for 3 h, detached with trypsin-EDTA and blocked with trypsin inhibitor. Cells were resuspended in DMEM containing 0.5% BSA and seeded (~2×10³ cells) on nanopatterned gold surfaces. After 60 min, cells were fixed with methanol for 5 min at −20°C and permeabilized with 0.1% Triton X-100 in PBS for 5 min. Cells were blocked with 3% BSA in PBS for 30 min and then incubated with the required antibodies. Confocal images were acquired with an inverted confocal microscope (Leica SP5).

Micropatterning

Micropatterns were generated as described by Schiller et al. (2013). For immunofluorescence microscopy, cells were serum-starved for 3 h, detached with trypsin-EDTA and kept in suspension in serum-free medium for 1 h. Cells were then seeded on FN-coated circular micropatterns in 0.5% FBS medium for 90 min. Cells were fixed with 3% PFA in PBS for 5 min at room temperature, washed with PBS, blocked with 1% BSA in PBS for 1 h at room temperature and then incubated with antibodies. The fluorescence images were collected with a laser scanning confocal microscope (Leica SP5).

Fibroblast attachment to FN and VN

WT fibroblasts were serum-starved for 3 h and transfected with 1 µg of DNA (GFP-Lfc or GFP control). After 24 h, cells were detached with trypsin-EDTA and treated with cilengitide or α5β1 blocking antibody for 1 h in suspension in serum-free medium. Cells were seeded for 45 min either on FN-coated (10 µg/ml) or VN-coated (2.5 µg/ml) glass coverslips. β1 null fibroblast were seeded on FN-coated glass coverslips as

a control. Cells were fixed with 3% PFA in PBS for 5 min at room temperature, washed with PBS, blocked with 1% BSA in PBS for 1 h at room temperature and then incubated with antibodies. The fluorescent images were collected with a laser scanning confocal microscope (Leica SP5).

Treatment with inhibitors

Nocodazole (M1404, Sigma-Aldrich): cells were treated for 2 h with 0.5 µM nocodazole (dissolved in DMSO) diluted in serum-free medium. In control experiments, cells were treated with the same volume of DMSO. Images were acquired 15 min after washout.

Staurosporine (S1421, Selleckchem): cells were treated for 90 min (immunofluorescence) or 4 h (GST-RhoA-G17A pulldown) with 2 nM staurosporine (dissolved in DMSO) diluted in serum-free medium. For MS-phosphoenrichment and timelapse movie, cells were treated with 1 nM staurosporine. In control experiments, cells were treated with the same volume of DMSO.

Phosphatase inhibitor (Sigma-Aldrich): cells were treated with 0.1 mM Na₃VO₄ or 1 mM NaF for 30 min in serum-free medium.

Cilengitide (Hözlzel): cells were treated for 1 h with 2 µM of cilengitide diluted in serum-free medium.

α5β1 integrin-blocking antibody (MAB2575, clone BMC5, Merck/Millipore): cells were treated for 1 h with 10 µg/ml of α5β1-blocking antibody diluted in serum-free medium.

C3 transferase-based Rho inhibitor treatment (Cytoskeleton, Denver, USA): cells were treated for 4 h with 2.0 µg/ml (dissolved in water) diluted in serum-free medium.

Mass spectrometry

Active GEF sample preparation

Samples from active GEF pulldown assays were separated by SDS-polyacrylamide gel electrophoresis on a 4–15% gradient gel. Gel was stained with Coomassie using the GelCode™ Blue Safe Protein Stain reagent (Thermo Fisher Scientific).

Gel lanes of interest were excised, chopped and washed twice with 150 µl of de-staining buffer (25 mM ammonium bicarbonate and 50% ethanol). Gel pieces were dehydrated twice in 150 µl of 100% ethanol and dried by vacuum centrifugation. Then, 50 µl of digestion buffer (25 mM Tris-HCl, 10% acetonitrile, 10 ng/µl of trypsin) was added. After incubation for 20 min on ice, 50 µl of ammonium bicarbonate buffer (25 mM) was added and the gel pieces were incubated at 37°C overnight.

Peptides in the supernatant were collected and additional peptides were extracted from the gel pieces by repeated incubation at 25°C in 100 µl of extraction buffer [3% trifluoroacetic acid (TFA), 30% acetonitrile], with a subsequent centrifugation and collection of the supernatants. Finally, the gel pieces were dehydrated by incubation at 25°C in 100 µl of 100% acetonitrile and the supernatant was unified with the supernatants from previous extraction steps. Acetonitrile was removed by vacuum centrifugation and 70 µl of 2 M Tris-HCl as well as 10 mM tris(2-carboxyethyl) phosphine and 40 mM 2-chloroacetamide was added. After incubation for 30 min at 37°C, peptides were acidified to 1% TFA and desalted using Stage Tips.

Phospho-proteome sample preparation

For phospho-proteome analysis, cells were serum-starved for 3 h, detached with trypsin-EDTA and kept in suspension in serum-free medium for 1 h. Cells were washed twice with PBS, detached using a cell scraper and pelleted by centrifugation. Cell pellets were lysed in 700 µl lysis buffer [8 M Urea, 30 mM 2-Chloroacetamide (Sigma-Aldrich), 5 mM Tris (2-carboxyethyl) phosphine (TCEP; Pierce™, Thermo Fisher Scientific), 1% Benzoinase, 1 mM MgCl₂ in 100 mM Tris, pH 8.0] by incubation at 37°C for 10 min and subsequent sonication using a Sonoplus Ultrasonic homogenizer (Bandelin). Samples were incubated once more at 37°C for 10 min and sonicated in a Bioruptor Plus sonication system (Diogenode) for 10×30 s at high intensity. Before digestion, the samples were diluted 1:4 with MS grade water (VWR). Samples were digested for 2 h at 37°C with

1 µg of LysC and overnight at 37°C with 3 µg trypsin (Promega). The solution of peptides was then acidified with Trifluoroacetic acid (Merck) to a final concentration of 1%, followed by desalting via Sep-Pak C18 1cc vacuum cartridges (Waters). The cartridge was washed twice with 1 ml of 100% acetonitrile (ACN) and twice with 1 ml of 0.1 M acetic acid prior to sample loading. Subsequently, the cartridge was washed twice with 1 ml of 0.1 M acetic acid. Elution was done with 0.5 ml of 80% (v/v) acetonitrile (ACN) and 0.1 M acetic acid in Milli-Q water. Samples were vacuum dried. Phosphorylated peptides were enriched with Fe(III)-NTA cartridges (Agilent Technologies; Santa Clara, Ca) using the AssayMAP Bravo Platform (Agilent Technologies; Santa Clara, Ca) in an automated fashion. Cartridges were primed at a flow rate of 100 µl/min with 250 µl of priming buffer (0.1% TFA, 99.9% ACN) and equilibrated at a flow-rate of 50 µl/min with 250 µl of loading buffer (0.1% TFA, 80% ACN). The flow-through was collected into a separate plate. Dried samples were dissolved in 200 µl of loading buffer and loaded at a flow-rate of 5 µl/min onto the cartridge. Cartridges were washed with 250 µl of loading buffer at a flow-rate of 20 µl/min and cross-linked peptides were eluted with 35 µl of 10% ammonia directly into 35 µl of 10% formic acid. Samples were dried down and stored at -20°C prior to further use. Before to LC-MS/MS analysis, the samples were resuspended in 10% formic acid.

LC-MS/MS data acquisition

Purified and desalted peptides were loaded onto a 30 cm column (inner diameter: 75 microns; packed in-house with ReproSil-Pur C18-AQ 1.9-micron beads, Dr. Maisch GmbH) via the autosampler of the Thermo Easy-nLC 1000 (Thermo Fisher Scientific) at 60°C. Using the nanoelectrospray interface, eluting peptides were directly sprayed onto the benchtop Orbitrap mass spectrometer Q Exactive HF (Thermo Fisher Scientific). Peptides were loaded in buffer A (0.1% formic acid) at 250 nl/min and percentage of buffer B (80% acetonitrile, 0.1% formic acid) increased from 2% to 30% over 120 min, followed by an increase to 60% over 10 min and then 95% over the next 5 min. Percentage of buffer B was maintained at 95% for another 5 min. The mass spectrometer was operated in a data-dependent mode with survey scans from 300 to 1650 *m/z* (resolution of 60,000 at *m/z*=200), and up to 10 of the top precursors were selected and fragmented using higher energy collisional dissociation (HCD with a normalised collision energy of value of 28). The MS2 spectra were recorded at a resolution of 15,000 (at *m/z*=200). AGC target for MS and MS2 scans were set to 3E6 and 1E5, respectively. For active GEFs, data acquisition was set within a maximum injection time of 100 and 60 min for MS and MS2 scans, respectively. Dynamic exclusion was set to 30 ms. For the phospho-proteome, data acquisition was used a maximum injection time of 20 ms for MS1 and 50 ms for MS2 scans. Dynamic exclusion was set to 16 ms.

Data analysis

Raw data were processed using the MaxQuant computational platform (version 1.6.5.0; Cox and Mann, 2008) with standard settings applied. Shortly, the peak list was searched against the Uniprot database of *Mus musculus* (55,466 entries) with an allowed precursor mass deviation of 4.5 ppm and an allowed fragment mass deviation of 20 ppm. MaxQuant, by default, enables individual peptide mass tolerances, which was used in the search. Cysteine carbamidomethylation, methionine oxidation and N-terminal acetylation, deamidation and phosphorylation were set as variable modifications. Proteins were quantified across samples using the label-free quantification algorithm in MaxQuant as label-free quantification (LFQ) intensities.

Bioinformatic analysis and heatmaps generation were made with the free access program Perseus, developed at Max Planck Biochemistry institute by Dr Jürgen Cox (<https://maxquant.net/perseus/>; Tyanova et al., 2016). The data corresponding to the biological replicates were filtered, based on valid values. Multiple testing corrections were performed. The mass spectrometry proteomics data have been deposited to the ProteomeXchange Consortium via the PRIDE partner repository (<http://www.ebi.ac.uk/pride/archive/>) with the dataset identifier PXD037596 (Active GEFs) and PXD037633 (Lfc phospho-proteome).

Crispr/Cas9 gene editing

For Lfc, guide RNAs were designed using the online tool (<http://crispr.mit.edu/>). Two Crispr gRNAs were selected, targeting the first translated exons (exons 2, common in all the splicing forms) of *Arhgef2* gene (Guide #1: score 85: 5'-GAGGTGGCCGTTGGTATAGC-3'; Guide #2: score 83: 5'-GCACATGGTCATGCCGAGA-3'). A BbsI cut site was added and inserted into pX459 plasmid (Feng Zhang Lab - Addgene #62988). pKO-cells were transfected with 1 µg of pX459-gRNA1 or gRNA2, and pX459 alone as a control. Cells were treated for 3 days with puromycin (4 µg/ml), different clones were isolated and further characterized by western blotting, and the null mutation was confirmed by DNA sequencing of the targeted region using specific primers (MWG-Eurofins).

For MARK2 and MARK3, guide RNAs were designed following instructions on GeneArt™ Precision gRNA Synthesis Kit (Invitrogen). Two target sequences were selected for each gene (*MARK2*, 5'-CCCTACCCACGCTGAACGAA-3' and 5'-GCTGACGAGCAGCCCCA-TAT-3'; *MARK3*, 5'-GAACTTTGCAAAAGTGAAAT-3' and 5'-TACAGACTGTTGAAAACAAT-3'). Sequences were checked using Blast (<https://blast.ncbi.nlm.nih.gov/Blast.cgi>). GeneArt™ Precision gRNA Synthesis Kit (Invitrogen) was used to synthesize gRNA targeting mouse *MARK2* and mouse *MARK3* genes, following the manufacturer's instructions. Cells were transfected with gRNA and GFP-Cas9 (Invitrogen) using Viromer® Crispr (Lipocalix). Single cells were FACs sorted by GFP expression and grown in a 96-well plate. Clones were tested by western blotting and knockout was confirmed by DNA sequencing using specific primers for the targeted region (MWG-Eurofins).

Colocalization quantification

The colocalization of Lfc and β-tubulin was quantified using the colocalization tool in Zeiss Zen software version 2.3. The colocalization fraction was determined individually for each cell and individual thresholds were set accordingly. The colocalization coefficients were plotted as bar graphs and the appropriate statistical analysis was applied.

Stress fibre quantification

Stress fibre fluorescence intensity was quantified using ImageJ. The same threshold adjustments were used for all the images, followed by cell selection and measurement of the total fluorescent intensity.

The number of cells with ventral stress fibres was manually counted. Relative percentage of cells to total number of cells was calculated and plotted as bar graphs.

Organized and disorganized stress fibres, stress fibre length and junction number per cell were determined using the Ridge detection plugin from ImageJ. The parameters used for detection and fibres/junction quantification were line width 20.0, high contrast 230, low contrast 100, sigma 5, low threshold 0.0, and upper threshold 0.34.

FA quantification

Paxillin was used to mark FAs in pKO-cells adhered on FN-coated circular micropatterns. ImageJ was used to quantified FA sizes. The same threshold was applied for all the images and analysis was performed using the 'Analyze Particles' command. The parameters were set as size=0.06–10 and circularity=0.00–1.00. FA number was corrected on cell area.

Timelapse movies

Experiments were performed on pKO-αv cells attached on FN-coated glass without serum followed by treatment with 1 nM of staurosporine. Timelapse movie was acquired using a Leica SP8 confocal microscope.

Bioinformatics and statistics

Raw data were processed using the MaxQuant computational platform (Cox and Mann, 2008) with standard settings applied. Perseus was used to analyse the MS data and generate the heatmaps (Tyanova et al., 2016). Bar graphs and statistical analyses were generated in GraphPad Prism version 8.0.0 for Windows. The applied statistical methods are specified in the figure legends.

Acknowledgements

We thank Peter Krenn, Guan Wang, the Max Planck Institute of Biochemistry Imaging Facility and Max Planck Proteomic Facility for technical support, Reinhard Fässler for funding the project and editing the manuscript, and Anne Ridley for comments on the manuscript.

Competing interests

The authors declare no competing or financial interests.

Author contributions

Conceptualization: G.C., R.B.H.; Methodology: G.C., A.S., R.B.H.; Software: G.C., A.S., R.B.H.; Validation: G.C., R.B.H.; Formal analysis: G.C., A.S., R.B.H.; Investigation: G.C., A.S., R.B.H.; Data curation: G.C., R.B.H.; Writing - original draft: G.C., R.B.H.; Writing - review & editing: G.C., A.S., R.B.H.; Visualization: R.B.H., G.C.; Supervision: G.C., R.B.H.; Funding acquisition: G.C.

Funding

The work was funded by the Bundesministerium für Bildung und Forschung and Ministerio de Ciencia, Tecnología e Innovación Productiva (German-Argentinian Collaboration grant), Agencia Nacional de Promoción Científica y Tecnológica (PICT-Max Planck 2017-4685) and the Max Planck Society.

Data availability

The mass spectrometry proteomics data have been deposited to the ProteomeXchange Consortium via the PRIDE partner repository (<http://www.ebi.ac.uk/pride/archive/>) with the dataset identifier PXD037596 and PXD037633.

Peer review history

The peer review history is available online at <https://journals.biologists.com/jcs/lookup/doi/10.1242/jcs.260740.reviewer-comments.pdf>

References

- Atkinson, S. J., Gontarczyk, A. M., Alghamdi, A. A., Ellison, T. S., Johnson, R. T., Fowler, W. J., Kirkup, B. M., Silva, B. C., Harry, B. E., Schneider, J. G. et al. (2018). The $\beta 3$ -integrin endothelial adhesome regulates microtubule-dependent cell migration. *EMBO Rep.* **19**, e44578. doi:10.15252/embr.201744578
- Azoitei, M. L., Noh, J., Marston, D. J., Roudot, P., Marshall, C. B., Daugird, T. A., Lisanza, S. L., Sandí, M. J., Ikura, M., Sondek, J. et al. (2019). Spatiotemporal dynamics of GEF-H1 activation controlled by microtubule- and Src-mediated pathways. *J. Cell Biol.* **218**, 3077-3097. doi:10.1083/jcb.201812073
- Barbieri, J. T., Riese, M. J. and Aktories, K. (2002). Bacterial toxins that modify the actin cytoskeleton. *Annu. Rev. Cell Dev. Biol.* **18**, 315-344. doi:10.1146/annurev.cellbio.18.012502.134748
- Birkenfeld, J., Nalbant, P., Yoon, S. H. and Bokoch, G. M. (2008). Cellular functions of GEF-H1, a microtubule-regulated Rho-GEF: is altered GEF-H1 activity a crucial determinant of disease pathogenesis? *Trends Cell Biol.* **18**, 210-219. doi:10.1016/j.tcb.2008.02.006
- Chan, K. T., Asokan, S. B., King, S. J., Bo, T., Dubose, E. S., Liu, W., Berginski, M. E., Simon, J. M., Davis, I. J., Gomez, S. M. et al. (2014). LKB1 loss in melanoma disrupts directional migration toward extracellular matrix cues. *J. Cell Biol.* **207**, 299-315. doi:10.1083/jcb.201404067
- Chang, Y.-C., Nalbant, P., Birkenfeld, J., Chang, Z.-F. and Bokoch, G. M. (2008). GEF-H1 couples nocodazole-induced microtubule disassembly to cell contractility via RhoA. *Mol. Biol. Cell* **19**, 2147-2153. doi:10.1091/mbc.e07-12-1269
- Costa, P., Scales, T. M., Ivaska, J. and Parsons, M. (2013). Integrin-specific control of focal adhesion kinase and RhoA regulates membrane protrusion and invasion. *PLoS One* **8**, e74659. doi:10.1371/journal.pone.0074659
- Cox, J. and Mann, M. (2008). MaxQuant enables high peptide identification rates, individualized p.p.b.-range mass accuracies and proteome-wide protein quantification. *Nat. Biotechnol.* **26**, 1367-1372. doi:10.1038/nbt.1511
- Danen, E. H. J., Sonneveld, P., Brakebusch, C., Fässler, R. and Sonnenberg, A. (2002). The fibronectin-binding integrins $\alpha 5 \beta 1$ and $\alpha v \beta 3$ differentially modulate RhoA-GTP loading, organization of cell matrix adhesions, and fibronectin fibrillogenesis. *J. Cell Biol.* **159**, 1071-1086. doi:10.1083/jcb.200205014
- Drewes, G., Ebnet, A., Preuss, U., Mandelkow, E.-M. and Mandelkow, E. (1997). MARK, a novel family of protein kinases that phosphorylate microtubule-associated proteins and trigger microtubule disruption. *Cell* **89**, 297-308. doi:10.1016/S0092-8674(00)80208-1
- Fujishiro, S. H., Tanimura, S., Mure, S., Kashimoto, Y., Watanabe, K. and Kohno, M. (2008). ERK1/2 phosphorylate GEF-H1 to enhance its guanine nucleotide exchange activity toward RhoA. *Biochem. Biophys. Res. Commun.* **368**, 162-167. doi:10.1016/j.bbrc.2008.01.066
- García-Mata, R., Wennerberg, K., Arthur, W. T., Noren, N. K., Ellerbroek, S. M. and Burridge, K. (2006). Analysis of activated GAPs and GEFs in cell lysates. *Methods Enzymol.* **406**, 425-437. doi:10.1016/S0076-6879(06)06031-9
- Guilluy, C., Dubash, A. D. and García-Mata, R. (2011). Analysis of RhoA and Rho GEF activity in whole cells and the cell nucleus. *Nat. Protoc.* **6**, 2050-2060. doi:10.1038/nprot.2011.411
- Haga, R. B. and Ridley, A. J. (2016). Rho GTPases: regulation and roles in cancer cell biology. *Small GTPases* **7**, 207-221. doi:10.1080/21541248.2016.1232583
- Hermann, M. R., Jakobson, M., Colo, G. P., Rognoni, E., Jakobson, M., Kupatt, C., Posern, G. and Fässler, R. (2016). Integrins synergise to induce expression of the MRTF-A-SRF target gene ISG15 for promoting cancer cell invasion. *J. Cell Sci.* **129**, 1391-1403. doi:10.1242/jcs.177592
- Hodge, R. G. and Ridley, A. J. (2016). Regulating Rho GTPases and their regulators. *Nat. Rev. Mol. Cell Biol.* **17**, 496-510. doi:10.1038/nrm.2016.67
- Hynes, R. O. (2002). Integrins: bidirectional, allosteric signaling machines. *Cell* **110**, 673-687. doi:10.1016/S0092-8674(02)00971-6
- Joo, E. and Olson, M. F. (2021). Regulation and functions of the RhoA regulatory guanine nucleotide exchange factor GEF-H1. *Small GTPases* **12**, 358-371. doi:10.1080/21541248.2020.1840889
- Krendel, M., Zenke, F. T. and Bokoch, G. M. (2002). Nucleotide exchange factor GEF-H1 mediates cross-talk between microtubules and the actin cytoskeleton. *Nat. Cell Biol.* **4**, 294-301. doi:10.1038/ncb773
- Kuo, J.-C., Han, X., Hsiao, C.-T., Yates, J. R., 3RD and Waterman, C. M. (2011). Analysis of the myosin-II-responsive focal adhesion proteome reveals a role for β -Pix in negative regulation of focal adhesion maturation. *Nat. Cell Biol.* **13**, 383-393. doi:10.1038/ncb2216
- Lizcano, J. M., Göransson, O., Toth, R., Deak, M., Morrice, N. A., Boudeau, J., Hawley, S. A., Udd, L., Mäkelä, T. P., Hardie, D. G. et al. (2004). LKB1 is a master kinase that activates 13 kinases of the AMPK subfamily, including MARK/PAR-1. *EMBO J.* **23**, 833-843. doi:10.1038/sj.emboj.7600110
- Marjoram, R. J., Lessey, E. C. and Burridge, K. (2014). Regulation of RhoA activity by adhesion molecules and mechanotransduction. *Curr. Mol. Med.* **14**, 199-208. doi:10.2174/1566524014666140128104541
- Meiri, D., Greeve, M. A., Brunet, A., Finan, D., Wells, C. D., Larose, J. and Rottapel, R. (2009). Modulation of Rho guanine exchange factor Lfc activity by protein kinase A-mediated phosphorylation. *Mol. Cell Biol.* **29**, 5963-5973. doi:10.1128/MCB.01268-08
- Meiri, D., Marshall, C. B., Greeve, M. A., Kim, B., Balan, M., Suarez, F., Bakal, C., Wu, C., Larose, J., Fine, N. et al. (2012). Mechanistic insight into the microtubule and actin cytoskeleton coupling through dynein-dependent RhoGEF inhibition. *Mol. Cell* **45**, 642-655. doi:10.1016/j.molcel.2012.01.027
- Meiri, D., Marshall, C. B., Mokady, D., Larose, J., Mullin, M., Gingras, A. C., Ikura, M. and Rottapel, R. (2014). Mechanistic insight into GPCR-mediated activation of the microtubule-associated RhoA exchange factor GEF-H1. *Nat. Commun.* **5**, 4857. doi:10.1038/ncomms5857
- Miao, H., Li, S., Hu, Y.-L., Yuan, S., Zhao, Y., Chen, B. P. C., Puzon-McLaughlin, W., Tarui, T., Shyy, J. Y.-J., Takada, Y. et al. (2002). Differential regulation of Rho GTPases by $\beta 1$ and $\beta 3$ integrins: the role of an extracellular domain of integrin in intracellular signaling. *J. Cell Sci.* **115**, 2199-2206. doi:10.1242/jcs.115.10.2199
- Narumiya, S., Tanji, M. and Ishizaki, T. (2009). Rho signaling, ROCK and mDia1, in transformation, metastasis and invasion. *Cancer Metastasis Rev.* **28**, 65-76. doi:10.1007/s10555-008-9170-7
- Pasapera, A. M., Heissler, S. M., Eto, M., Nishimura, Y., Fischer, R. S., Thiam, H. R. and Waterman, C. M. (2022). MARK2 regulates directed cell migration through modulation of myosin II contractility and focal adhesion organization. *Curr. Biol.* **32**, 2704-2718.e6. doi:10.1016/j.cub.2022.04.088
- Patel, M. and Karginov, A. V. (2014). Phosphorylation-mediated regulation of GEFs for RhoA. *Cell Adh. Migr.* **8**, 11-18. doi:10.4161/cam.28058
- Rechenmacher, F., Neubauer, S., Polleux, J., Mas-Moruno, C., De, Simone, M., Cavalcanti-Adam, E. A., Spatz, J. P., Fässler, R. and Kessler, H. (2013). Functionalizing $\alpha v \beta 3$ - or $\alpha 5 \beta 1$ -selective integrin antagonists for surface coating: a method to discriminate integrin subtypes in vitro. *Angew. Chem. Int. Ed. Engl.* **52**, 1572-1575. doi:10.1002/anie.201206370
- Ren, Y., Li, R., Zheng, Y. and Busch, H. (1998). Cloning and characterization of GEF-H1, a microtubule-associated guanine nucleotide exchange factor for Rac and Rho GTPases. *J. Biol. Chem.* **273**, 34954-34960. doi:10.1074/jbc.273.52.34954
- Roca-Cusachs, P., Gauthier, N. C., Del Rio, A. and Sheetz, M. P. (2009). Clustering of $\alpha 5 \beta 1$ integrins determines adhesion strength whereas $\alpha v \beta 3$ and talin enable mechanotransduction. *Proc. Natl. Acad. Sci. USA* **106**, 16245-16250. doi:10.1073/pnas.0902818106
- Sandí, M. J., Marshall, C. B., Balan, M., Coyaude, É., Zhou, M., Monson, D. M., Ishiyama, N., Chandrakumar, A. A., La Rose, J., Couzens, A. L. et al. (2017). MARK3-mediated phosphorylation of ARHGEF2 couples microtubules to the actin cytoskeleton to establish cell polarity. *Sci. Signal.* **10**, eaan3286. doi:10.1126/scisignal.aan3286
- Schiller, H. B. and Fässler, R. (2013). Mechanosensitivity and compositional dynamics of cell-matrix adhesions. *EMBO Rep.* **14**, 509-519. doi:10.1038/embror.2013.49
- Schiller, H. B., Hermann, M. R., Polleux, J., Vignaud, T., Zanivan, S., Friedel, C. C., Sun, Z., Raducanu, A., Gottschalk, K. E., Thery, M. et al. (2013). β 1- and α 5-class integrins cooperate to regulate myosin II during rigidity sensing

- of fibronectin-based microenvironments. *Nat. Cell Biol.* **15**, 625-636. doi:10.1038/ncb2747
- Shackelford, D. B. and Shaw, R. J.** (2009). The LKB1-AMPK pathway: metabolism and growth control in tumour suppression. *Nat. Rev. Cancer* **9**, 563-575. doi:10.1038/nrc2676
- Sonntag, T., Moresco, J. J., Yates, J. R., III and Montminy, M.** (2019). The KLDpT activation loop motif is critical for MARK kinase activity. *PLoS One* **14**, e0225727. doi:10.1371/journal.pone.0225727
- Timm, T., Marx, A., Panneerselvam, S., Mandelkow, E. and Mandelkow, E.-M.** (2008). Structure and regulation of MARK, a kinase involved in abnormal phosphorylation of Tau protein. *BMC Neurosci.* **9**, S9. doi:10.1186/1471-2202-9-S2-S9
- Trinczek, B., Brajenovic, M., Ebner, A. and Drewes, G.** (2004). MARK4 is a novel microtubule-associated proteins/microtubule affinity-regulating kinase that binds to the cellular microtubule network and to centrosomes. *J. Biol. Chem.* **279**, 5915-5923. doi:10.1074/jbc.M304528200
- Tyanova, S., Temu, T., Sinitcyn, P., Carlson, A., Hein, M. Y., Geiger, T., Mann, M. and Cox, J.** (2016). The Perseus computational platform for comprehensive analysis of (prote)omics data. *Nat. Methods* **13**, 731-740. doi:10.1038/nmeth.3901
- Vial, E., Sahai, E. and Marshall, C. J.** (2003). ERK-MAPK signaling coordinately regulates activity of Rac1 and RhoA for tumor cell motility. *Cancer Cell* **4**, 67-79. doi:10.1016/S1535-6108(03)00162-4
- Von Thun, A., Preisinger, C., Rath, O., Schwarz, J. P., Ward, C., Monsefi, N., Rodríguez, J., Garcia-Munoz, A., Birtwistle, M., Bienvenut, W. et al.** (2013). Extracellular signal-regulated kinase regulates RhoA activation and tumor cell plasticity by inhibiting guanine exchange factor H1 activity. *Mol. Cell. Biol.* **33**, 4526-4537. doi:10.1128/MCB.00585-13
- Whitehead, I., Kirk, H., Tognon, C., Trigo-Gonzalez, G. and Kay, R.** (1995). Expression cloning of lfc, a novel oncogene with structural similarities to guanine nucleotide exchange factors and to the regulatory region of protein kinase C. *J. Biol. Chem.* **270**, 18388-18395. doi:10.1074/jbc.270.31.18388
- Yamashita, Y., Saito, Y., Murata-Kamiya, N. and Hatakeyama, M.** (2011). Polarity-regulating kinase partitioning-defective 1b (PAR1b) phosphorylates guanine nucleotide exchange factor H1 (GEF-H1) to regulate RhoA-dependent actin cytoskeletal reorganization. *J. Biol. Chem.* **286**, 44576-44584. doi:10.1074/jbc.M111.267021
- Yoshimura, Y. and Miki, H.** (2011). Dynamic regulation of GEF-H1 localization at microtubules by Par1b/MARK2. *Biochem. Biophys. Res. Commun.* **408**, 322-328. doi:10.1016/j.bbrc.2011.04.032
- Zuidema, A., Wang, W., Kreft, M., Bleijerveld, O. B., Hoekman, L., Aretz, J., Böttcher, R. T., Fässler, R. and Sonnenberg, A.** (2022). Molecular determinants of α V β 5 localization in flat clathrin lattices - role of α V β 5 in cell adhesion and proliferation. *J. Cell Sci.* **135**, jcs259465. doi:10.1242/jcs.259465

Supplementary Figure 1

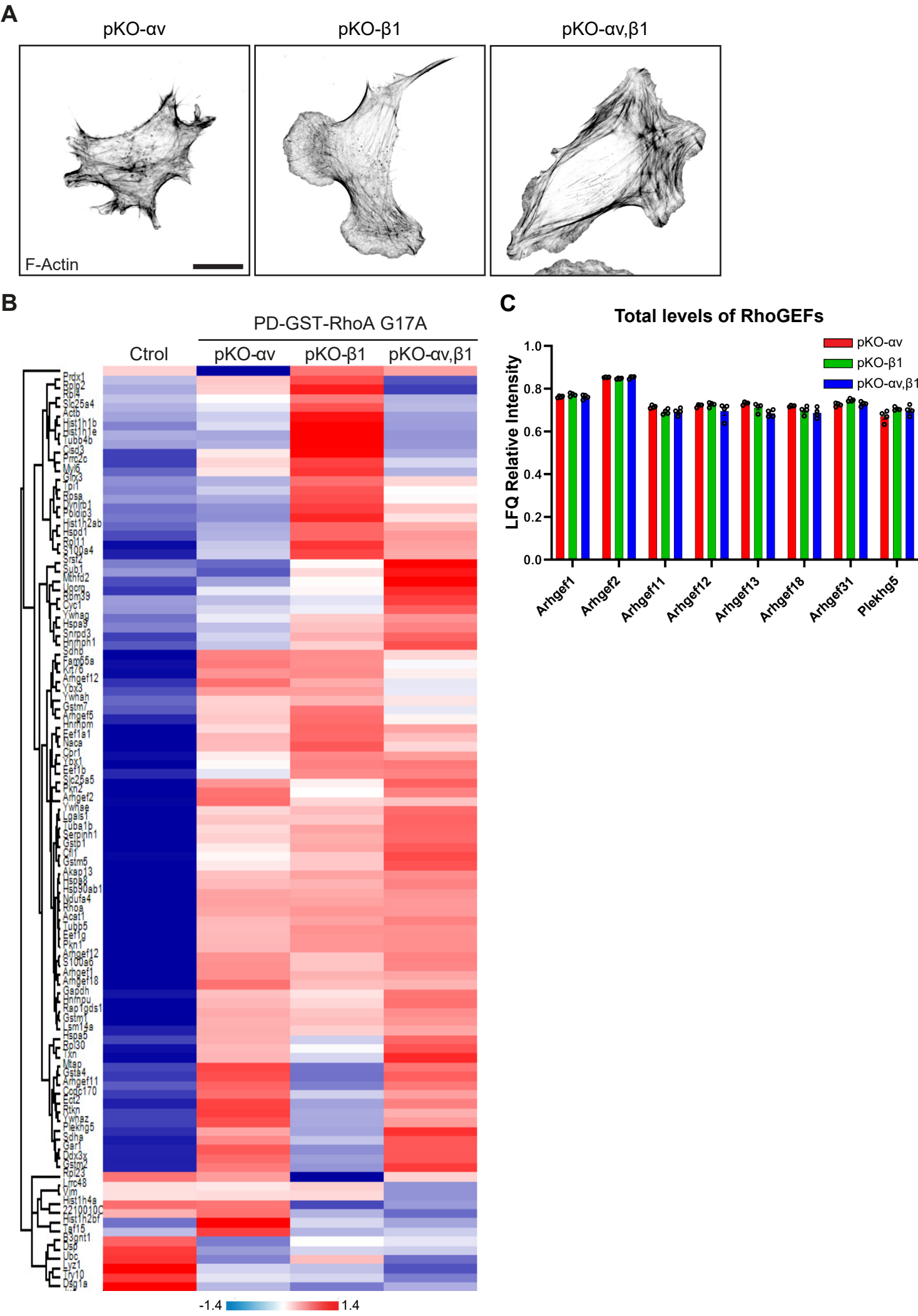


Fig. S1. A) Immunostaining of indicated cell types plated on FN for 4 h in serum-free medium. Images show F-actin. Scale bar, 10 μ m. B) Pulled-down proteins by GST-RhoA G17A were subject to hierarchical cluster analysis. PDs were performed with cells plated on FN for 45 min in serum-free medium. Heat map shows the Z-score and is representative of three independent experiments. C) Bar graph showing MS intensity of total levels of eight GEFs in the indicated cell types.

Supplementary Figure 2

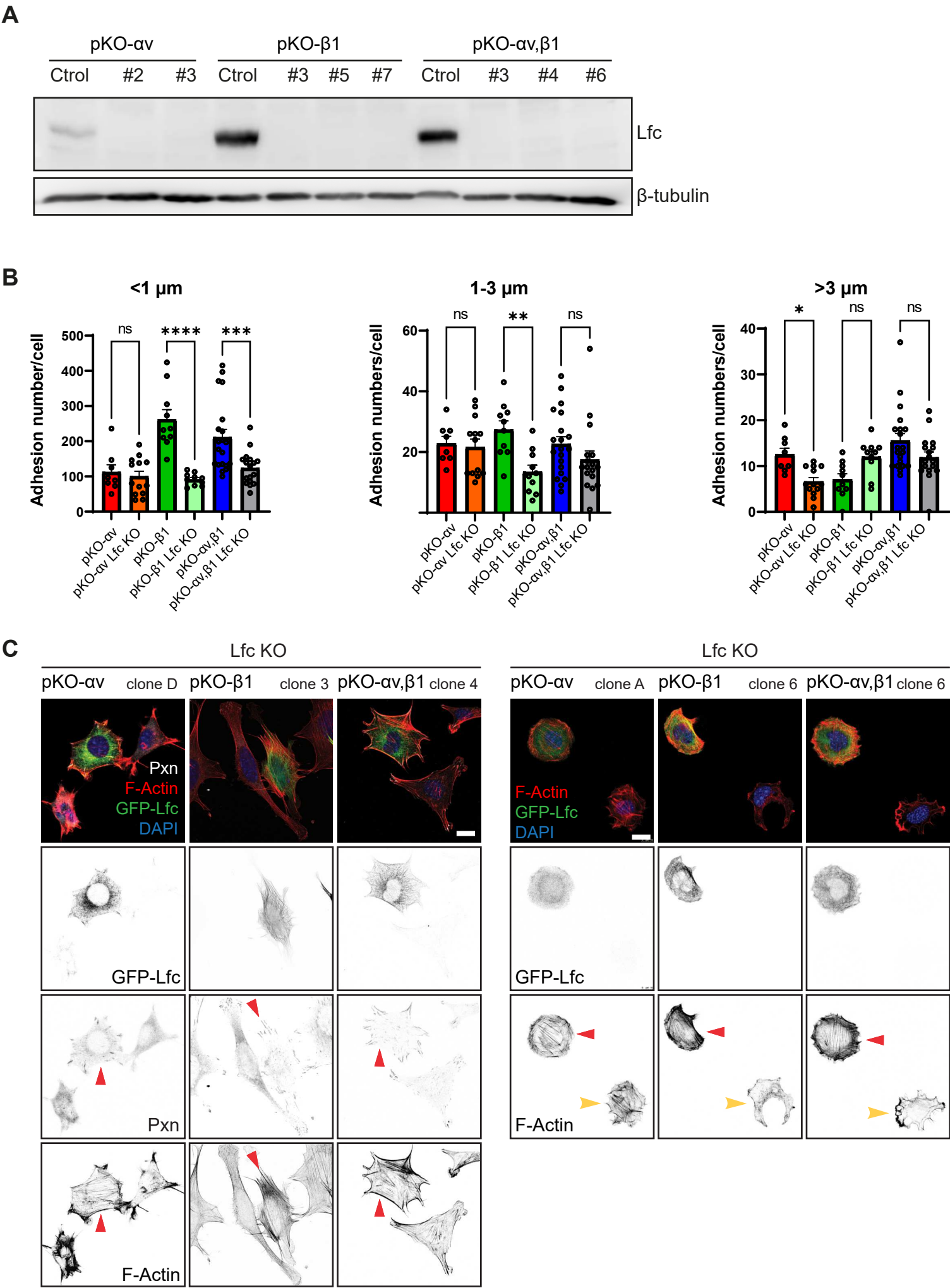


Fig. S2. A) Confirmation of Lfc KO in clones of indicated cells by western blotting. B) Quantification of adhesion number per cell in the indicated conditions. Adhesion size was divided into <1 μm , 1-3 μm and >3 μm . Graphs show the quantification of 8-20 cells per condition. Unpaired t-test between pKO- αv and pKO- αv Lfc KO, pKO- β1 and pKO- β1 Lfc KO, and pKO- $\alpha\text{v},\beta\text{1}$ and pKO- $\alpha\text{v},\beta\text{1}$ Lfc KO, * $p<0.05$, ** $p<0.01$, *** $p<0.001$ and **** $p<0.0001$. C) Indicated pKO cells overexpressing GFP-Lfc cultured for 45 min on FN-coated glass or on circular FN-coated micropatterns serum-free medium and then visualized or stained GFP-Lfc (green), F-actin (red), paxillin (white) and nuclei (DAPI, blue). Scale bar, 10 μm . Red arrows indicate GFP-Lfc expressing cells, and yellow arrows indicate GFP-Lfc non-expressing cells.

Supplementary Figure 3

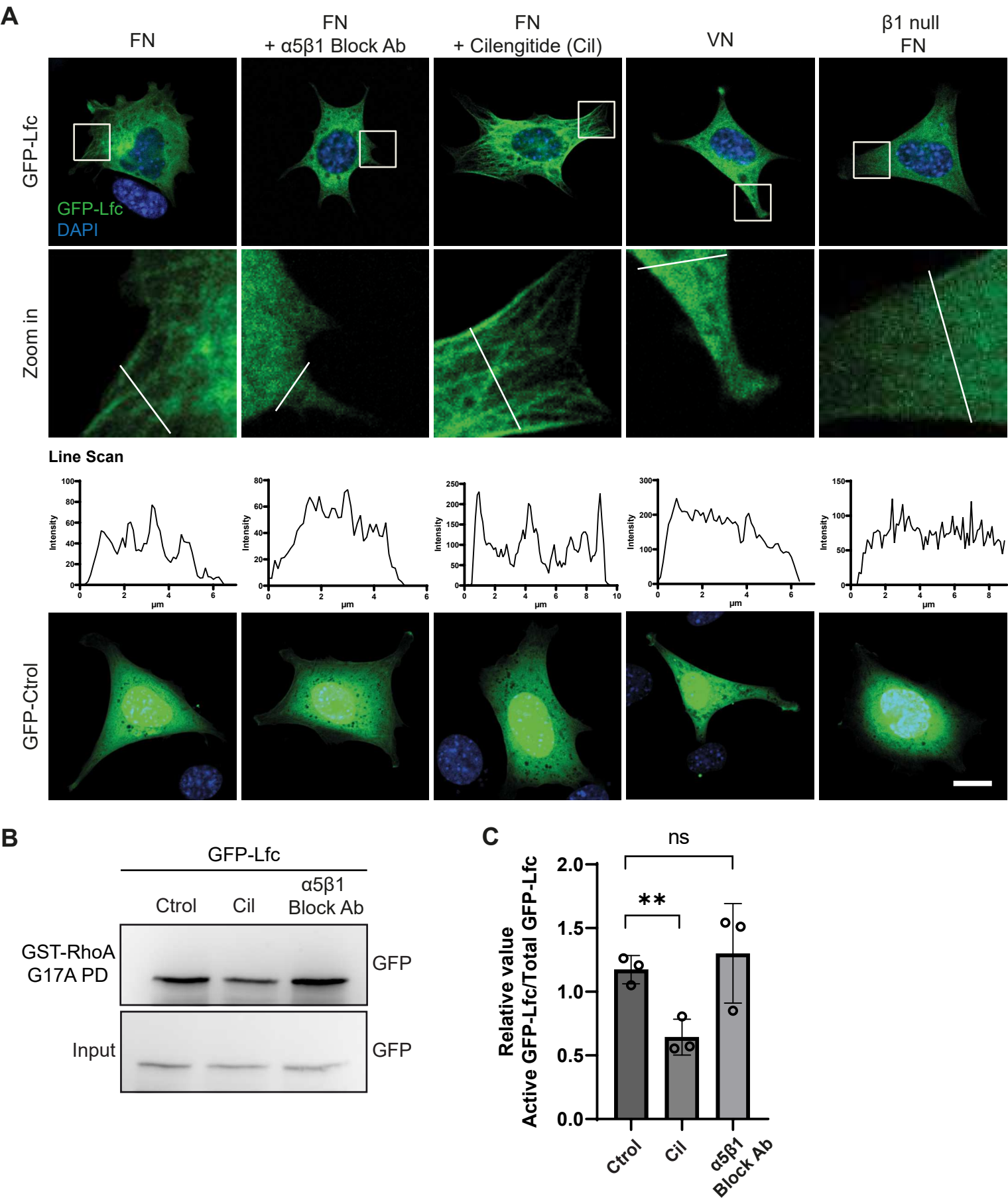


Fig. S3. A) Visualization of GFP-Lfc (green) or GFP alone as a control, in transfected WT mouse fibroblasts seeded on indicated ligand in the presence or absence of indicated compound. $\beta 1$ integrin-null fibroblasts served as a control. Nuclei were stained with DAPI (blue). Scale bar, 10 μ m. The line scan shows the intensity of the GFP-Lfc staining. B) Lfc activity in GFP-Lfc-transfected normal mouse kidney fibroblasts plated on fibronectin for 45 min and treated with either cilengitide (Cil) or $\alpha 5\beta 1$ blocking antibody was shown by western blotting after GST-RhoA G17A PD. C) Graph shows quantification of three independent experiments. Unpaired t-test between Ctrl and Cil, and Ctrl and $\alpha 5\beta 1$ Block Ab, ** $p < 0.01$.

Supplementary Figure 4

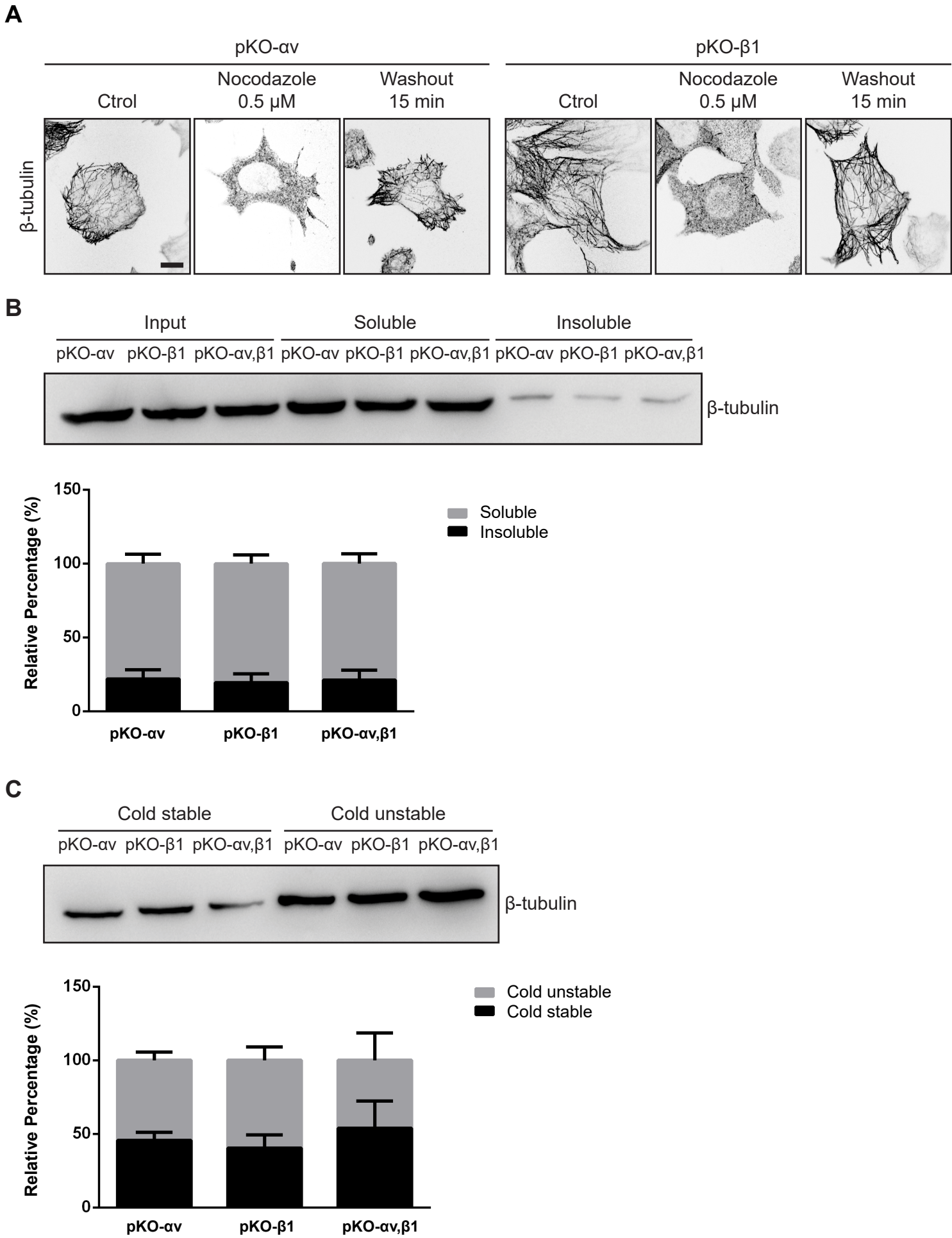


Fig. S4. A) Indicated cell types cultured on FN in serum-free medium and treated either with nocodazole or DMSO (Ctrol) for 2 h followed by 15 min washout and then staining for β -tubulin. Scale bar, 10 μ m. B) Microtubule fractionation of indicated cells followed by western blotting. Soluble fraction represents free and insoluble fraction polymerized tubulin. Graph below western blot shows the relative percentage of band densities of each fraction in relation to the sum of densities (density soluble + density insoluble = 100%). Quantification of four independent experiments. C) Cold stability assay followed by western blotting. Cold stable indicates tubulin that remained polymerized after 30 min incubation on ice. Graph below western blot shows the relative percentage of the band density of each fraction in relation to the sum of the densities (density cold stable + density cold unstable = 100%). Quantification of two independent experiments.

Supplementary Figure 5

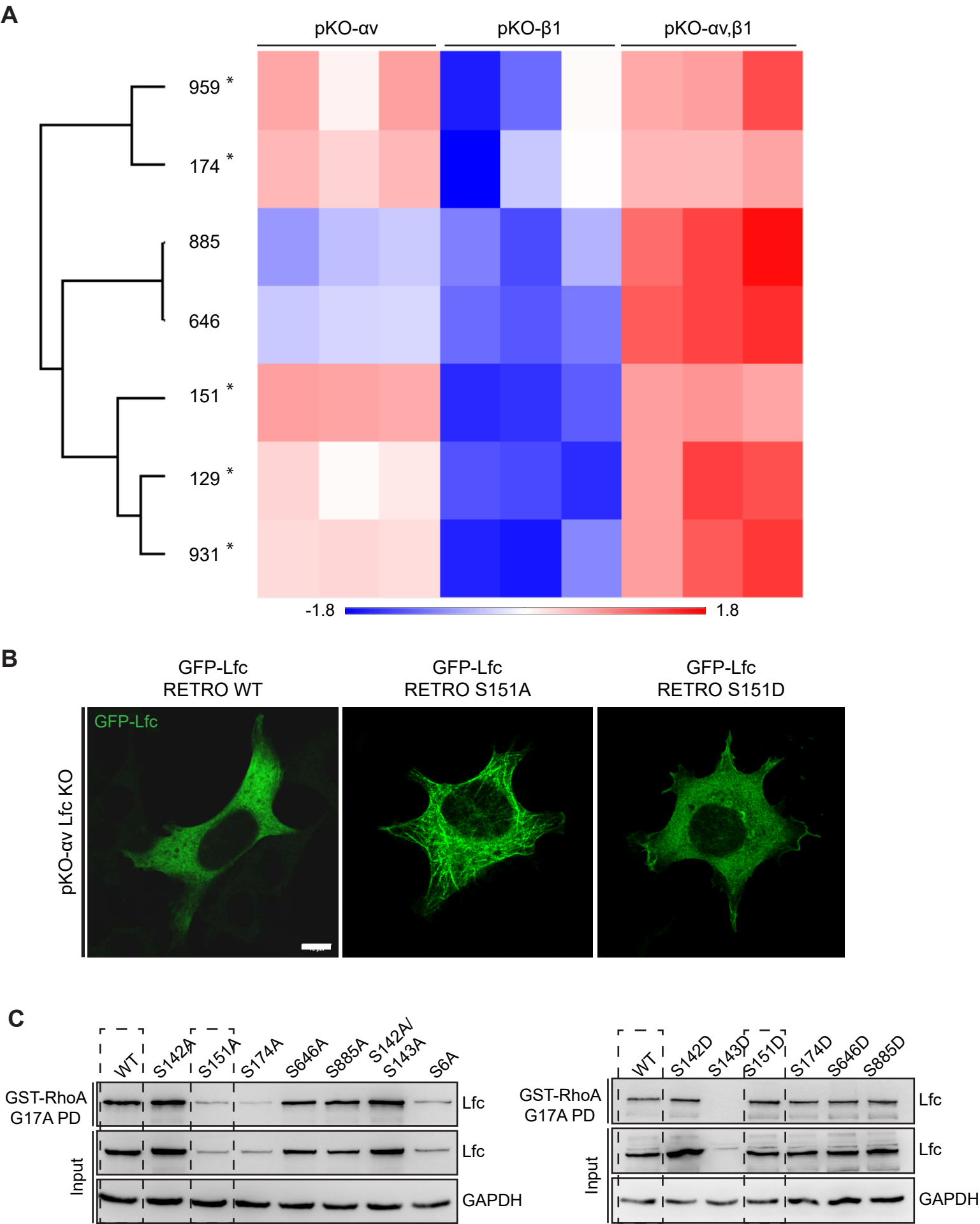


Fig. S5. A) Phospho-enrichment MS analysis of Lfc phosphorylation. Heatmap shows the Z-score of Lfc phosphorylation sites of pKO cells cultured on FN for 45 min in serum-free medium. Phosphorylation sites marked with asterisks are highly phosphorylated in pKO- α v cells when compared to pKO- β 1 cells. B) Stably-expressing GFP-Lfc-WT, GFP-Lfc-S151A or GFP-Lfc-S151D in pKO- α v Lfc KO cells showing GFP signals (green). Scale bar, 10 μ m. C) Lfc activity of pKO- α v Lfc KO cells overexpressing indicated GFP-Lfc constructs determined by western blotting after GST-RhoA-G17A pull-down. WT, S151A and S151D are highlighted.

Supplementary Figure 6

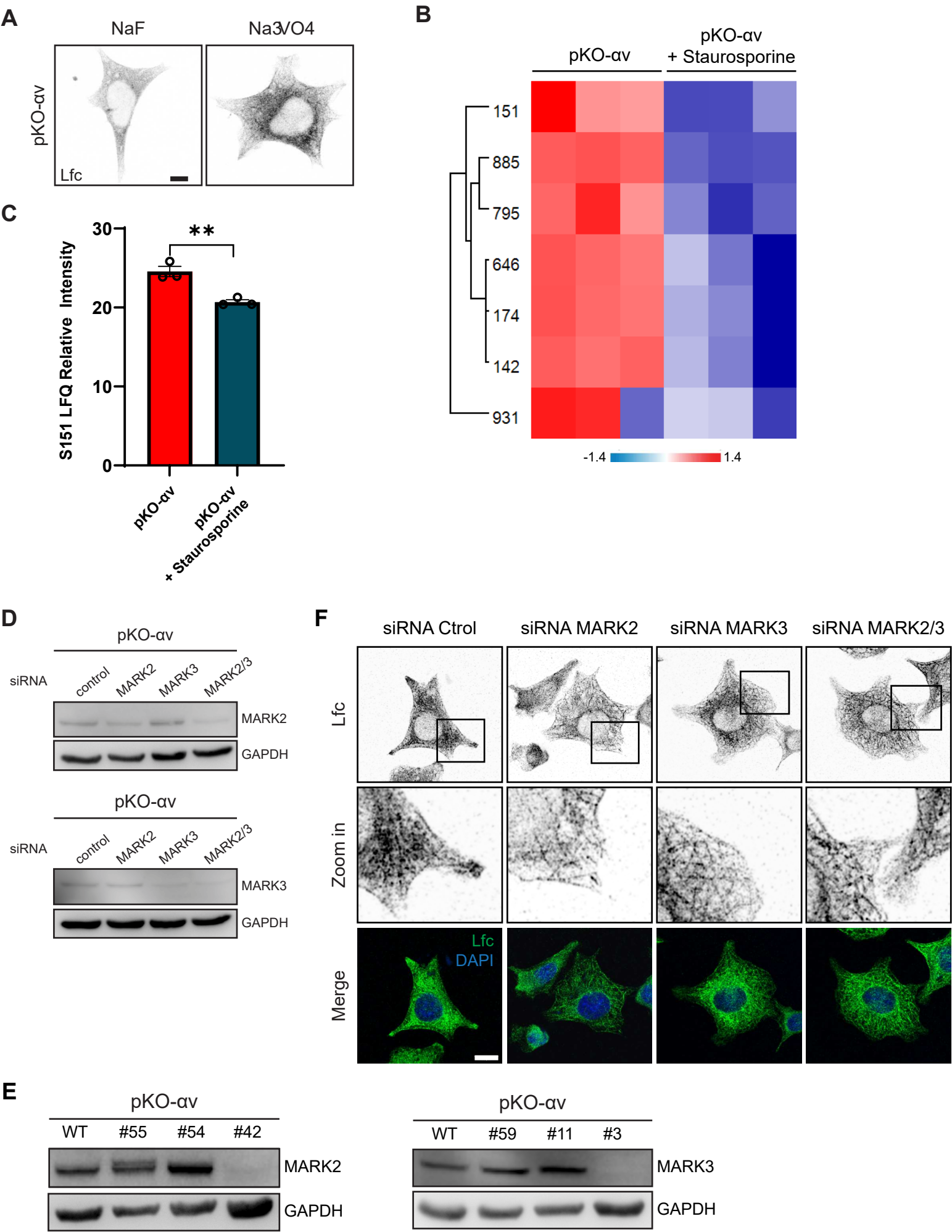


Fig. S6. A) Immunostaining of pKO- α v cells plated on FN in serum-free medium and treated with NaF (1 mM) and Na₃VO₄ (0,1 mM). Scale bar, 10 μ m. B) Phospho-enrichment MS analysis of Lfc phosphorylation in pKO- α v cells with or without 1 nM Staurosporine treatment. Heatmap shows the Z-score of Lfc phosphorylation sites of pKO cells cultured on FN for 45 min in serum-free medium. C) Bar graph showing MS intensity of S151 phospho-site for pKO- α v and pKO- α v with Staurosporine cells from three independent experiments. Unpaired t-test between pKO- α v and pKO- α v with Staurosporine, **p<0.01. D) Confirmation of siRNA-mediated depletion of MARK2 and/or MARK3 by western blotting. Blots are representative examples of two independent experiments. E) Confirmation of Crispr/Cas9-mediated MARK2 and MARK3 KO in pKO- α v cells by western blotting. F) Staining of pKO- α v cells cultured on FN for 45 min in serum-free medium and transfected with indicated siRNA for Lfc (green) and nuclei (DAPI, blue). Scale bar, 10 μ m.

Supplementary Figure 7

Figure 2D

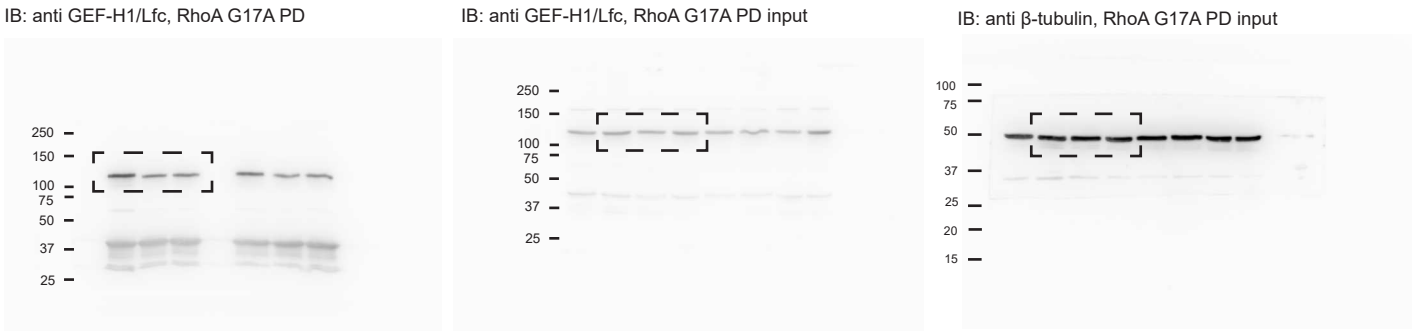
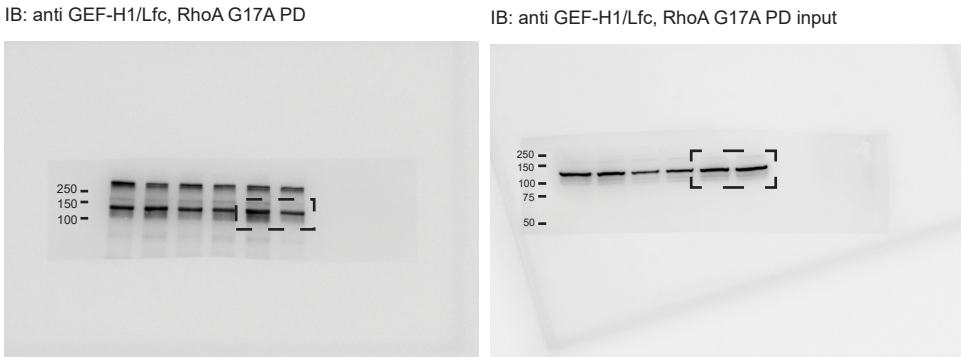
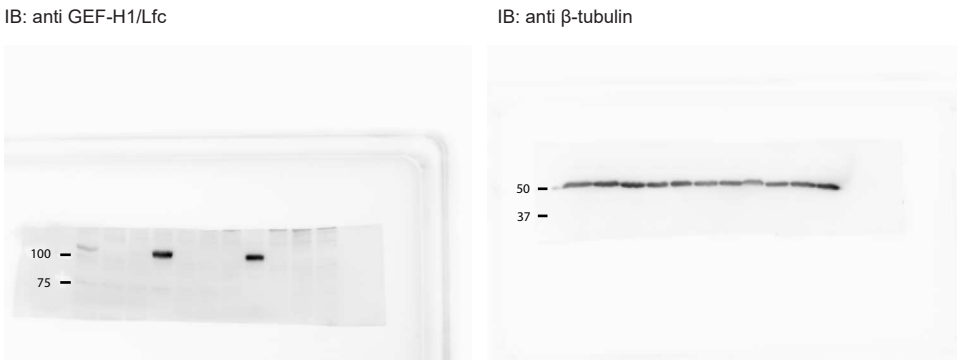


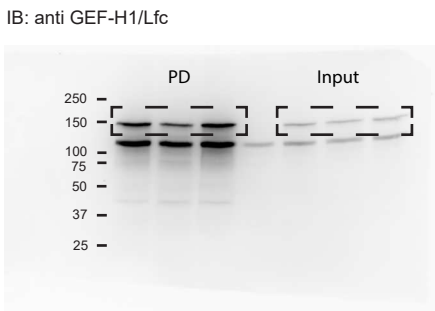
Figure 5C



Supplementary Figure 2A



Supplementary Figure 3B



Supplementary Figure 4B

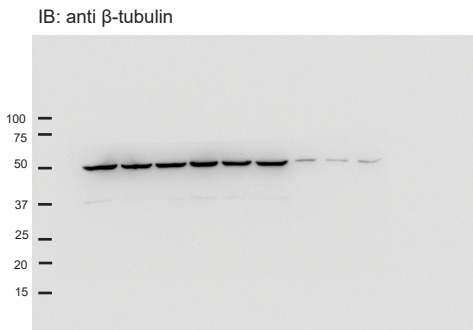
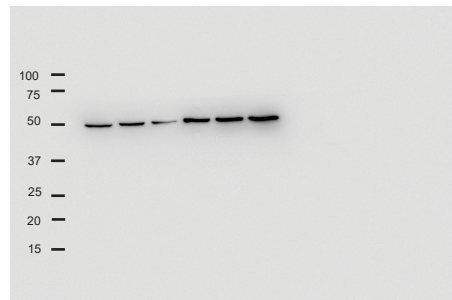


Fig. S7. Uncropped WBs. Dotted rectangles highlight the areas shown in the indicated figures.

Supplementary Figure 8

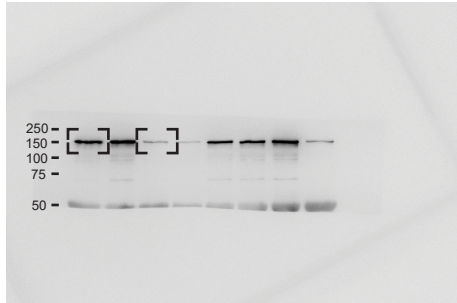
Supplementary Figure 4C

IB: anti β -tubulin



Supplementary Figure 5C

IB: anti GEF-H1/Lfc, RhoA G17A PD, A mutants



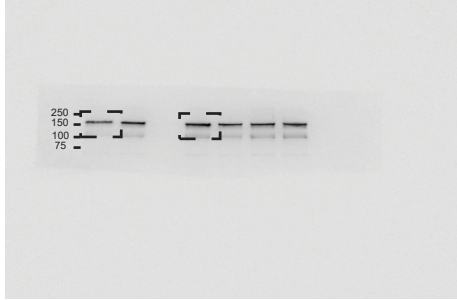
IB: anti GEF-H1/Lfc, RhoA G17A PD input, A mutants



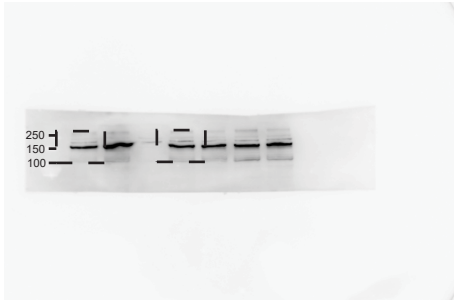
IB: anti GAPDH, RhoA G17A PD input, A mutants



IB: anti GEF-H1/Lfc, RhoA G17A PD, D mutants



IB: anti GEF-H1/Lfc, RhoA G17A PD input, D mutants

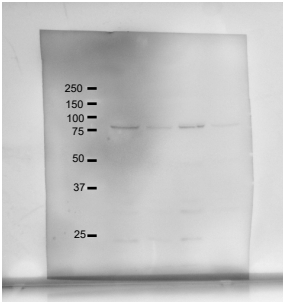


IB: anti GAPDH, RhoA G17A PD input, D mutants

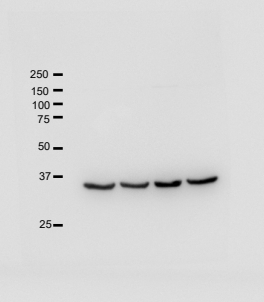


Supplementary Figure 7A

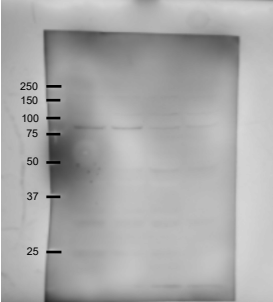
IB: anti MARK2



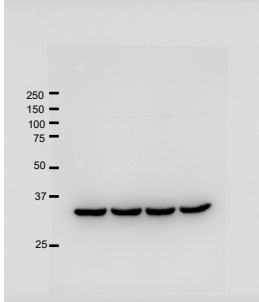
IB: anti GAPDH, MARK2 blot



IB: anti MARK3

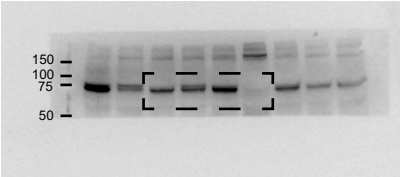


IB: anti GAPDH, MARK3 blot

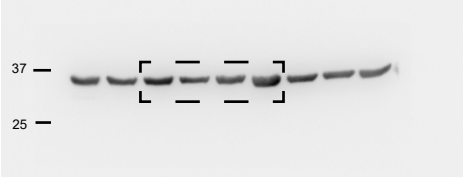


Supplementary Figure 7C

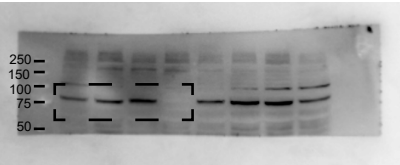
IB: anti MARK 2



IB: anti GAPDH, MARK2 blot



IB: anti MARK 3



IB: anti GAPDH, MARK3 blot

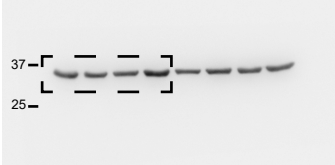
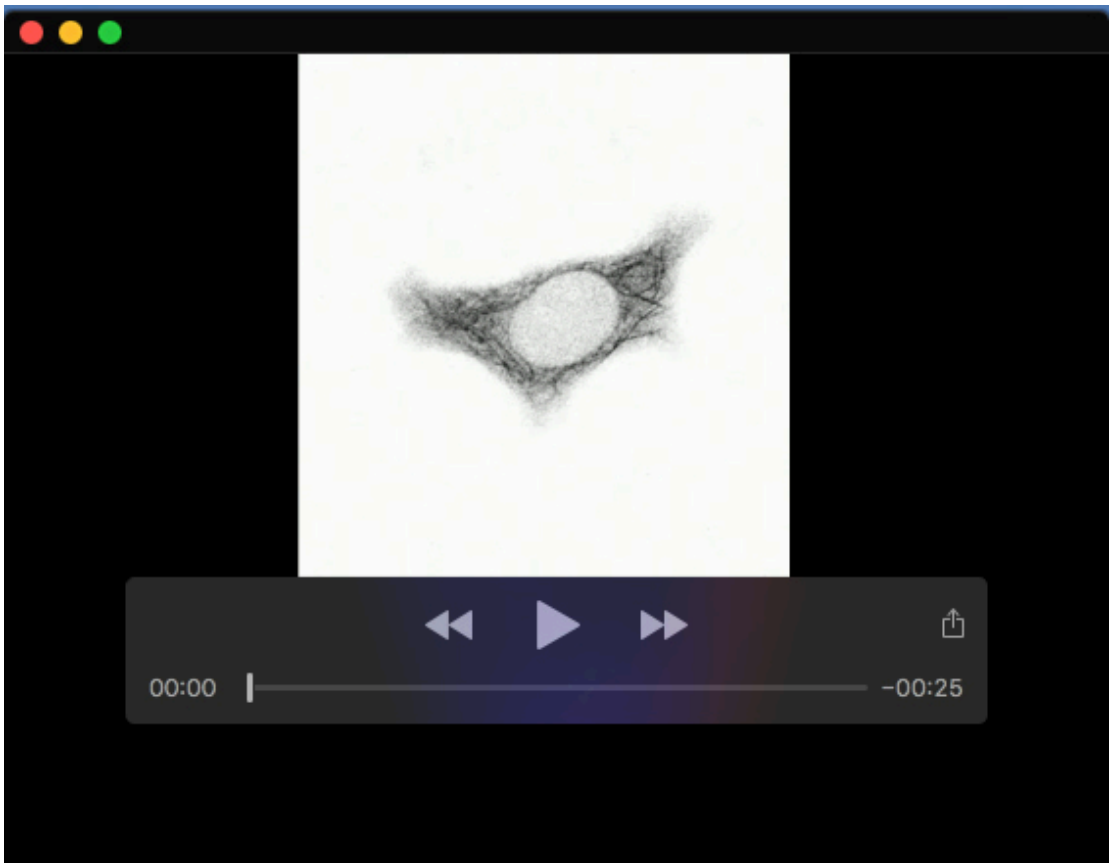


Fig. S8. Uncropped WBs. Dotted rectangles highlight the areas shown in the indicated figures.



Movie 1. Timelapse imaging of pKO- α v cells overexpressing GFP-Lfc on FN-coated glass without serum. Recording started immediately after cells were treated under the microscope with 1nM of Staurosporine. The recording time interval was 10sec/frame.